Models and numerical schemes for free surface flows. Beyond the Saint-Venant system

Jacques Sainte-Marie

UNIVERSITE PARIS VI - PIERRE et MARIE CURIE

Habilitation à diriger des recherches

Spécialité : Mathématiques Appliquées et Applications des Mathématiques

Présentée par

Jacques SAINTE-MARIE

Models and numerical schemes for free surface flows.

Beyond the Saint-Venant system

Soutenue le 2 décembre 2010

Jury :

Président :	Benoit Perthame	-	Professeur
Rapporteurs :	François Bouchut	-	Dir. Rech. CNRS
	Randall J. LeVeque	-	Professeur
	Carlos Pares	-	Professeur
Examinateurs :	Marie-Odile Bristeau	-	Dir. Rech. INRIA
	Dominique Chapelle	-	Dir. Rech. INRIA
	Bruno Després	-	Professeur
	Jean-Marc Hérard	-	Chercheur senior EDF R&D

Voici une maxime mémorable gravée au frontispice
de l'entrée d'une parcelle de vigne de la côte de Beaune
et située en bordure d'une route passagère.

Ami passant,
En te levant chaque matin,
Fête mon vin,
Tu auras ainsi santé parfaite.
Mais pour avoir félicité complète,
Ne manques pas en te couchant,
Le soir d'en faire autant.

Dixit et fecit Claudius Charleux.

Remerciements

Les remerciements constituent un point de passage obligé pour ce type de document. On éprouve *a priori* un certain plaisir à rédiger cette partie que l'on réserve donc pour un moment de lassitude par exemple, celui où l'on doute de l'intérêt d'être habilité à diriger des recherches voire de la pertinence et de l'utilité même des dites recherches.

Parmi les interrogations qui hantent l'esprit de l'auteur de ces lignes, la première est celle de la distinction entre les personnes que l'on ne peut pas ne pas citer, celles qui doivent être citées, celles qui mériteraient de l'être et celles qui pourraient l'être si l'opportunité se présente. Permettez-moi à ce stade de jeter un voile pudique sur les personnes que la bienséance incite à mentionner mais à qui l'on préfère refuser ce modeste satisfecit. Afin d'éviter de tels dilemmes cornéliens, j'ai choisi de ne citer aucune personne en espérant que les élus se reconnaîtront dans les lignes qui suivent.

Permettez-moi de commencer cette liste par les trois personnes qui ont accepté d'être rapporteur de ce travail. Les échanges que j'ai eu avec elles quant au contenu du document et aux perspectives sont très enrichissantes. Je tiens également à remercier très chaleureusement les autres membres du jury. J'ai énormément de plaisir à travailler avec plusieurs d'entre eux, ils sont des témoins de mon parcours.

J'ai une pensée émue pour deux personnes qui sont pour l'instant peu concernées par la recherche scientifique voire réfractaires aux mathématiques sauf quand il s'agit de compter les bonbons qu'ils auront à la fin du repas s'il sont sages. Dans ce premier cercle, figure également certaine personne qui m'accompagne, me supporte et m'encourage.

Je poursuivrais par ceux, de Bourgogne et d'ailleurs avec qui je ne parle ni de mathématiques ni d'interprétation cinétique mais de vigne, de jardinage, de chasse, d'un certain cinéma désuet, bref de choses tout aussi essentielles.

En ne dérogeant pas à la règle que je me suis imposée de ne citer personne, je voudrais remercier les personnes que j'ai cotoyée ces dernières années au bâtiment 16 de l'INRIA Rocquencourt. Au delà des compétences de chacun, c'est la qualité et la diversité des personnes rencontrées que je tiens à souligner. Règne dans cet endroit, tout comme au sein du laboratoire J.-L. Lions de l'université P.-M. Curie, une atmosphère faite de convivialité et de saine émulation. Cette alchimie me semble rare et précieuse.

Parmi ceux que j'ai cotoyés ces dernières années, il y a des gens qui m'ont accueilli dans leur équipe, qui m'ont guidé, conseillé et encouragé, qui m'ont patiemment écouté et corrigé. A ces personnes, je dis simplement merci.

Contents

Résumé étendu

Ce document est une synthèse des résultats obtenus par l'auteur au cours des dernières années. Ces recherches ont été menées au laboratoire Saint-Venant (laboratoire commun EDF R&D[1], ENPC[2], CETMEF[3]) et à l'INRIA[4] au sein des équipes MACS et BANG. La première partie du document traite des écoulements à surface libre : la dérivation de modèles, leur analyse et l'obtention de schémas numériques associés. Dans la seconde partie, des résultats concernant la modélisation de tissus biologiques et d'organes sont présentés.

Dans un souci d'homogénéité, ce document privilégie les travaux associés aux écoulements à surface libre. Il ne s'agit en aucune façon d'un jugement de valeur sur les autres résultats obtenus qui sont succintement présentés dans la seconde partie du document.

Chronologiquement, les activités concernant la modélisation cardiaque ont débuté en 2001 à l'INRIA au sein du projet MACS. Depuis 2006 au sein du laboratoire Saint-Venant et en collaboration avec l'équipe BANG, l'hydrodynamique à surface libre tient une place importante. Pour autant depuis 2006, les recherches en biomécanique se poursuivent principalement dans les domaines de la réduction de modèle et de la mécanique des milieux poreux (perfusion des muscles).

Les points clés des contributions de l'auteur sont précisés ci-dessous.

Synthèse des principaux résultats obtenus

Ecoulement à surface libre

Deux hypothèses principales – licites dans le cas des écoulements peu profonds – permettent d'obtenir les équations du modèle de Saint-Venant à partir des équations de Navier-Stokes

- la pression du fluide est hydrostatique ou bien de façon équivalente, l'accélération verticale du fluide peut être négligée par rapport aux effets de la gravité,
- la vitesse horizontale du fluide est bien représentée par sa moyenne verticale.

Le système de Saint-Venant est capable de rendre compte d'une large gamme de problèmes physiques mais dans le cas d'écoulements avec un fort frottement au fond, avec une hauteur d'eau significative où bien lorsque le fluide est stratifié selon la verticale, les hypothèses ci-dessus ne sont plus valables et la validité du système de Saint-Venant est dubitable.

L'objectif principal de ce travail est de proposer des modèles de complexité minimale – spécialement pour la discrétisation – et adaptés aux cas où les hypothèses ci-dessus ne sont plus valables. Une telle approche implique des approximations des équations de Navier-Stokes plus sophistiquées que le système de Saint-Venant. L'objectif est donc de s'appuyer sur

- certains résultats et certaines propriétés du système de Saint-Venant (formulation cinétique, existence d'une grande famille d'entropie, ...),
- les techniques numériques performantes disponibles pour la simulation des lois de conservation,

[1] Electricité de France (EDF)
[2] Ecole Nationale des Ponts et Chaussées (ENPC)
[3] Centre d'Etudes Technique Maritime et Fluvial (CETMEF)
[4] Institut National de Recherche en Informatique et Automatique (INRIA)

pour proposer des schémas numériques efficaces permettant de résoudre ces modèles plus complexes. Pour chaque modèle, des validations numériques dans diverses situations discriminantes sont proposées notamment des comparaisons avec des solutions analytiques et des mesures expérimentales, quand cela est possible.

Les contributions principales sur ces sujets sont brièvement décrites ci-dessous. Une liste complète des publications de l'auteur est donnée page 135.

Le système de Saint-Venant étendu (voir pages 29, 63 et 84, Refs : [8, 5, 7])

L'extension la plus immédiate et sans doute la plus simple – sous réserve que le schéma numérique ait les propriétés requises – est l'introduction de termes non-hydrostatiques. Une littérature très importante existe sur ce sujet, citons par exemple les modèles de type KdV (Korteweg-de Vries), le modèle BBM (Benjamin-Bona-Mahony) ou bien encore les équations de Serre-Boussinesq ou encore de Green-Nagdhi et pour finir le système de Peregrine. Bien entendu de nombreuses variantes de ces modèles ont été proposées.

Nous avons proposé une extension non-hydrostatique naturelle du système de Saint-Venant en utilisant une démarche analogue à celle utilisée pour la dérivation asymptotique des modèles d'écoulements peu profonds. L'originalité consiste à aller un peu plus loin dans le développement asymptotique et donc à retenir des termes que l'on néglige quand on se limite aux équations de Saint-Venant classiques. Le modèle ainsi obtenu ne suppose pas le fluide irrotationnel et satisfait un bilan d'énergie. Un schéma numérique stable et peu coûteux a été proposé, il peut être utilisé en complément de n'importe quel solveur – de type volumes finis – des équations de Saint-Venant. Diverses validations numériques sont également proposées avec des comparaisons expérimentales.

Le modèle a été implémenté et est utilisé dans le code industriel Mascaret [mas09]. Ce code est utilisé pour la simulation de crues, d'inondations ainsi que pour la simulation de rupture des barrages hydro-électriques (élaboration des plans de prévention des risques).

Les équations de Navier-Stokes hydrostatiques (voir pages 31, 49, 95, 100 et 107, Ref : [3])

Une approximation de type Galerkin (uniquement selon la verticale) des équations de Navier-Stokes hydrostatiques est proposée, elle conduit à un système de type Saint-Venant multi-couches mais avec échanges de masse, de quantités de mouvement et d'énergie entre les diverses couches. Le modèle ainsi obtenu possède d'intéressantes propriétés et soulève des problèmes largement ouverts (hyperbolicité). Il admet une interprétation cinétique. Un schéma numérique stable, *équilibre*, du second ordre en espace et en temps est donné avec de nombreuses validations numériques.

L'extension du système de Saint-Venant au cas des écoulements stratifiés selon la verticale a suscité beaucoup d'intérêts ces dernières années et de nombreux résultats ont été présentés sur ce sujet. La simplicité du modèle proposé ainsi que ses propriétés font de ces résultats une des contributions majeures de l'auteur. A noter que les modèles ainsi proposés ne font plus référence aux écoulements peu profonds.

Basé sur cette approche, un code 3d résolvant les équations de Navier-Stokes hydrostatique a été développé.

Ecoulements à densité variable (voir pages 37, 49 et 100, Refs : [2, 4])

On s'est intéressé également aux écoulements à densité variable c'est-à-dire à des situations où la densité du fluide dépend de la température, de la salinité,... ces dernières quantités étant elles-mêmes advectées par le flot.

La stratégie utilisée est similaire à ce qui a été décrit dans le paragraphe précédent. Mais les variations de densité introduisent certains couplages nonlinéaires et nécessitent également un

traitement spécifique des termes sources de pression. A noter que le modèle et le schéma numérique ne font pas l'hypothèse classique et simplificatrice dite de Boussinesq à savoir que la densité du fluide n'influe que sur les termes gravitationnels.

Le schéma numérique proposé est *équilibre*, positif et du second ordre en espace et en temps. De plus, la positivité de la concentration du traceur (température et/ou salinité) ainsi qu'un principe du maximum sur cette même concentration du traceur sont garantis. A noter que les variations de la densité du fluide entraînent que la matrice de masse du système est non-diagonale ce qui engendre des coûts de calcul élevés.

Les simulations démontrent que le modèle et le schéma numérique sont capables de reproduire des écoulements complexes, une comparaison avec une solution analytique est également donnée. Il apparaît que dans de nombreux cas, les variations de densité du fluide *a priori* très faibles ont une influence prépondérante sur la dynamique des écoulements considérés.

Les équations d'Euler (voir pages 39 et 52, Ref : [10])

L'hypothèse de pression hydrostatique présente dans les deux paragraphes ci-dessus peut s'avérer également limitante dans diverses situations. On s'est donc intéressé aux équations de Navier-Stokes complètes i.e. avec tous les termes non-hydrostatiques. L'idée est ici est de ne pas calculer simplement les moyennes verticales des équations de Navier-Stokes – tel que cela est fait pour obtenir les équations de Saint-Venant – mais de calculer les premiers moments selon la verticale de ces équations. On obtient ainsi un système d'équations de type transport-réaction. Cette approche peut également être couplée avec la discrétisation de type Galerkin sur la verticale décrite précédemment. On s'affranchit ainsi à nouveau de l'hypothèse des écoulements peu profonds.

Pour les modèles ainsi obtenus, une estimation formelle de la convergence des modèles vers les équations de Navier-Stokes ainsi qu'une interprétation cinétique est donnée.

On ne propose pas encore de schéma numérique pour ces modèles, le travail est actuellement en cours. Mais l'interprétation cinétique couplée aux approches volume finis déjà mentionnées offre des perspective prometteuses.

Remarque *La simulation d'écoulements sur des topographies mobiles et les phénomènes d'érosion qui sont associés sont également une préoccupation. Une première publication sur ce sujet a été soumise mais il s'agit de travaux préliminaires qui ne sont pas abordés dans ce document. Dans ce domaine, les travaux sont effectués en collaboration avec P.Y. Lagrée (UPMC), M. Seaid (univ. Manchester), F. Marche (univ. Montpellier) and F. Benkhaldoun (univ. Paris XIII).*

Points forts des résultats obtenus

Dérivation des modèles

Pour les écoulements peu profonds, nous avons utilisé les adimensionnements usuels ainsi que les développements asymptotiques classiques. On a pris soin de ne pas s'appuyer sur des hypothèses non physiques et d'éviter celles ayant des domaines de validité réduits telle que l'hypothèse d'écoulements potentiels.

Pour chaque modèle, les principales améliorations qu'il apporte ainsi qu'une comparaison avec les modèles existants sont données. Pour les modèles contenant des termes non-hydrostatiques, une équation d'énergie est donnée.

Décomposition sur la verticale des champs de vitesse

Un point important est que les modèles que nous proposons ne sont pas contraints par une

hypothèse de type écoulements peu profonds et sont utilisables pour des écoulements avec des hauteurs d'eau arbitraires. La discrétisation sur la verticale des variables de vitesse fait apparaître naturellement les échanges de masse entre les couches. Cette dernière propriété est cruciale et est une réelle avancée par rapport aux modèles existants.

A noter que contrairement à ce que l'on rencontre souvent, la définition du nombre de couches ainsi que leur répartition ne correspond pas à une partition physique de l'écoulement mais plutôt à la qualité de l'approximation souhaitée vis-à-vis du modèle initial.

Interprétation cinétique des modèles

Pour chacun des modèles proposés, une interprétation cinétique est donnée. Même si elle est plus restrictive que la formulation cinétique, l'interprétation cinétique donne à moindre coût des schémas numériques efficaces avec un décentrement des divers termes (conservatifs ou non). De plus cette description microscopique permet de démontrer diverses propriétés telles la conservativité, la stabilité, la positivité ou le principe du maximum qui sont souvent délicates à établir au niveau macroscopique.

Discrétisation des termes sources

Ce point est essentiel pour la discrétisation des systèmes hyperboliques (ou associés) tels ceux rencontrés en géophysique. L'obtention de schémas *équilibres* est cruciale et parfois délicate. Nous proposons une extension de la technique dite de *reconstruction hydrostatique* classiquement utilisée, voir paragraphe 5.4.5.

Maillages mobiles et maillages fixes

Pour les écoulements à surface libre, une des difficultés majeures au niveau discret est le traitement des maillages mobiles (apparition, disparition de zones sèches et topologie du domaine fluide). De même la géométrie de la surface libre peut avoir des variations rapides faisant apparaître des discontinuités. Tous les modèles présentés dans ce document utilisent uniquement des maillages fixes.

Modélisation cardiaque

La pratique médicale évolue de plus en plus vers des décisions personnalisées par exemple pour la prévention, le diagnostic ou encore la thérapie. Ces décisions sont prises sur la base d'un nombre toujours croissant de mesures (analyse, imagerie,...).

Cette évolution irréversible a ouvert la voie et rend maintenant nécessaire l'utilisation de modèles numériques de l'anatomie mais aussi de la physiologie capables de rendre compte des mesures effectuées mais aussi de détecter les anomalies, de prévoir les évolutions et de simulet et d'évaluer les thérapies.

Afin de construire un simulateur de l'activité cardiaque, quatre principaux processus physiologiques doivent être pris en compte simultanément

- l'électrophysiologie,
- la contraction et la relaxation mécanique du muscle,
- la perfusion,
- le métabolisme cardiaque.

Nous avons proposé des contributions ayant traits au second et au troisième phénomène. Ces travaux ont été principalement menés jusqu'en 2006 alors que l'auteur était en position de détachement à l'INRIA. Actuellement, ces sujets constituent toujours un centre d'intérêt pour l'auteur, ses préoccupations étant principalement tournées vers la perfusion et la réduction de modèle.

Activité mécanique du muscle cardiaque et simulations (voir pages 113 et 131, Refs : [11, 9, 12])

Un modèle mécanique complet et 3d de l'activité du myocarde a été proposé ainsi qu'un schéma numérique pour sa discrétisation. Une technique d'estimation pour le diagnostic de troubles de la contraction cardiaque a été également présentée et validée. Il est important de noter que le modèle en question est maintenant complètement validé et couramment utilisé, voir les publications de P. Moireau, R. Chabiniok and D. Chapelle [mac10].

Alors que la plupart des modèles d'excitation-contraction pour les fibres cardiaques sont basés sur des approches heuristiques et des tests expérimentaux, nous utilisons une loi contractile basée sur des considérations physiologiques et introduite par M. Sorine dans [BCS01b]. Pour ce modèle de fibre cardiaque, on a prouvé (en 1d) l'existence et l'unicité de solutions et on a étudié leur comportement en temps long. Une interprétation cinétique de cette loi de contraction a été obtenue récemment, see 7.1.4.

Perfusion dans le muscle cardiaque (voir pages 124, Ref : [6])

En dépit des avancées récentes sur la description anatomique et les mesures de l'arbre coronarien, la modélisation complète et la simulation de l'écoulement sanguin dans les coronaires depuis les artères jusqu'au veines en passant par les capillaires est toujours hors d'atteinte.

Ainsi, afin de modéliser la perfusion sanguine au travers du tissue cardiaque, nous devons limiter la description de l'écoulement à une certaine échelle. Pour cela, la prise en compte de l'interaction fluide-structure dans le cadre de la mécanique des milieux poreux semble appropriée.

La principale contribution dans ce domaine est l'obtention d'un modèle poroélastique en déformations finies valide pour les milieux quasi-incompressibles. Un schéma numérique résolvant de façon itérative l'écoulement poreux et le problème poro-visco-élastique non-linéaire. Des tests numériques en 3d sont présentés pour illustrer le comportement du modèle. Les résultats obtenus montrent les interactions entre le muscle et le sang et reproduisent des phénomènes clés observés lorsde la perfusion cardiaque.

Participation à des projets de recherche

Ces travaux ont été menés alors que l'auteur était impliqué dans divers projets de recherche, notamment

- le projet ANR "METHODE" (université d'Orléans, INRA, BRGM, INRIA and CERMICS), son objectif est d'étudier l'influence des hétérogénéités de surface sur les écoulements (2008-2011),
  `http://methode.netcipia.net`.

- l'action de recherche coopérative (ARC) "Nautilus"est un projet de recherche de 2 ans avec pour partenaires le CNRS, l'UPMC et l'INRIA et s'intéressant au couplage hydrodynamique-biologie (2010-2011),
  `http://www-sop.inria.fr/comore/ARC_Nautilus/index.html`.

- l'action d'envergure "CardioSense3d" d'une durée de 4 ans, ce projet a débuté en 2005 et traite

de la modélisation du muscle cardiaque et particulièrement du couplage excitation-contraction, `http://www-sop.inria.fr/CardioSense3D/`.

Thèses co-encadrées

- Lydie Nouvelière *Commande robuste pour l'assistance à la conduite : automatisation basse vitesse*, 1999-2002, actuellement maître de conférences à l'université d'Evry- Val d'Essonne, encadrement avec S. Mammar, prof. à l'université d'Evry.
- Sébastien Glaser *Modélisation et contrôle d'un véhicule en trajectoire limite : application au développement d'un système d'aide à la conduite*, 2001-2003, actuellement chargé de recherche aux Laboratoire Central des Ponts et Chaussées, encadrement avec S. Mammar, prof. à l'université d'Evry.
- Asven Gariah *Réduction de modèle pour les simulations en biomécanique*, 2008-., encadrement avec D. Chapelle, chef de l'équipe MACS.
- Anne-Céline Boulanger *Analyse théorique et numérique du couplage hydrodynamique-biologie*, 2010-., encadrement avec B. Perthame, prof. à l'université Pierre et Marie Curie.

Extended abstract

This document is an overview of the works carried out by the author at the Saint-Venant Laboratory (joint laboratory EDF R&D[5], ENPC[6], CETMEF[7]) and at INRIA[8] (MACS and BANG teams). The presented results, recently obtained, concern modeling and simulation in geophysics and life sciences. The first part of the document deals with free surface flows and their modeling, analysis and simulation. Then we present results on modeling and simulation of soft tissue mechanics.

Without value judgment over its contributions, the author has singled out the coherence of the document. Thus, the works dealing with cardiac modeling, data assimilation and model reduction presented in the second part of the document are not so detailed as those concerning geophysical flows presented in the first part.

The activities concerning the cardiac modeling have begun in 2001 at INRIA within the MACS team. Since 2006, at the Saint-Venant laboratory and in collaboration with the BANG team, the researches concerning free surface hydrodynamics are dominating. Despite, the author is still engaged and interested in soft tissue mechanics mainly model reduction and porous mechanics (muscle perfusion).

Overview of the main obtained results

We summarize hereafter the main contributions of the author.

Free surface flows

The derivation of the Saint-Venant system from the Navier-Stokes equations is based on two main approximations – valid because of the Shallow Water assumption – namely

- the pressure is hydrostatic or equivalently the vertical acceleration of the fluid can be neglected compared to the gravitational effects,
- the horizontal fluid velocity is well approximated by its vertical mean.

The Saint-Venant system is able to tackle a wide range of physical problems but considering density-stratified flows or flows with large friction coefficients, with significant water depth, with important wind effects, the two preceding approximations become questionable.

The main objective of these works is to derive models of minimal complexity – especially at the computational point of view – adapted to flows where these two approximations are no more valid. Of course this approach means more acurate approximations of the Navier-Stokes system but also more sophisticated models than the Saint-Venant system. Thus we aim at taking advantage of the known results for

- the analysis of the Saint-Venant system (kinetic formulation, hyperbolicity, entropies,...),
- the efficiency of the available numerical methods for solving conservation laws,

[5] Electricité de France (EDF)
[6] Ecole Nationale des Ponts et Chaussées (ENPC)
[7] Centre d'Etudes Technique Maritime et Fluvial (CETMEF)
[8] Institut National de Recherche en Informatique et Automatique (INRIA)

to propose efficient numerical techniques to solve these enriched models. For each model, we propose numerical validations in various situations with comparisons to analytical solutions and experimental data when they exist.

The main contributions of the author on this topic can be divided into several parts shortly described below. A complete publication list of the author is given page 135.

Extended Saint-Venant systems (see pages 29, 63 and 84, Refs : [8, 5, 7])

The first and simplest extension of the Saint-Venant system consists in the introduction of non-hydrostatic effects. A huge literature exists on this topic, let us mention the Korteweg-de Vries equation, Camassa-Holm equation, the Benjamin-Bona-Mahony (BBM) equation, the Serre or Green-Nagdhi equations and the Peregrine system and also all their slight modifications.

We have proposed a natural extension of the Saint-Venant using classical arguments for the asymptotic derivation of Shallow Water flows. In this model that is free from any irrotationality condition, the non-hydrostatic pressure terms are taken into account and an energy balance is obtained. A stable numerical scheme is proposed and various numerical validations are proposed.

This model has been integrated in the industrial code Mascret [mas09].

Hydrostatic Navier-Stokes system (see pages 31, 49, 95, 100 and 107, Ref : [3])

The Galerkin approximation (only in the vertical direction) of the hydrostatic Navier-Stokes system leading to a multilayer type Saint-Venant system with mass exchanges is one of the main contributions of the author. The obtained model is free from any Shallow Water assumption and has interesting properties (hyperbolicity, energy balance). It admits a kinetic interpretation. A well-balanced, positive, second order (in space and time) scheme is proposed with extensive numerical validations.

Based on this approach, a 3d code solving the free surface Navier-Stokes system has been developed.

Density-stratified flows (see pages 37, 49 and 100, Refs : [2, 4])

The strategy is similar to what is described in the preceding paragraph for the model derivation. But due to the density variations, the model exhibits pressure source terms and nonlinear couplings that have to be treated carefully. The numerical scheme is still well-balanced, positive and second order (in space and time) and has also a maximum principle on the tracer concentration. Still due to the density variations the system has a nontrivial mass matrix leading to increased computational costs. The numerical simulations demonstrate the model and the numerical scheme are able to reproduce complex physical flows and analytical solutions (when available). It also demonstrates the density gradients may involve large modifications in the hydrodynamical behavior.

The Euler system (see pages 39 and 52, Ref : [10])

Here we tackle the complete Navier-Stokes system and all the non-hydrostatic terms are considered. The keypoint is to calculate not only the vertical averages of the Navier-Stokes equations but also the vertical first order momenta of these equations. This leads to a transport-reaction type set of equations. As far as the author knows, such an approximation is new.

This process can be used to derive a single layer but also a multilayer type system using the Galerkin approximation mentioned below. Thus the obtained model is not omly devoted to Shallow Water flows. A formal estimate of the convergence of the multilayer system towards the Navier-Stokes system is given and a kinetic interpretation is obtained.

For this model we do not propose, at the moment, any numerical scheme. The definition of a suitable time scheme for the system is a work in progress of the author.

Remark *The simulation of flows over movable beds and the associated erosion phenomena are also interesting problems. A first publication has been proposed [1] but this remains preliminary results and this issue is not discussed in this document. On this subject, we work in collaboration with P.Y. Lagrée (UPMC), M. Seaid (univ. Manchester), F. Marche (univ. Montpellier) and F. Benkhaldoun (univ. Paris XIII).*

Strong points of the obtained results

Derivation process of the models

For Shallow Water flows, we have used classical rescalings and asymptotic analysis without any non physical assumption. In each case, a comparison with the existing models is given and we mention the improvements we have carried out. For several models, the hydrostatic assumption is dropped and some non-hydrostatic terms are included. For each of the proposed models, an energy balance has been obtained.

Vertical decomposition of the velocity fields

The models we propose are not only Shallow Water models for laminar flows but are suitable for flows with arbitrary water depths. The proposed discretization of the velocity fields along the vertical direction leads to multilayer type models with mass exchanges.

The crucial distinguishing feature of our model with respect to the classical multilayer approach is its property of allowing inter-layer fluid circulation.

The definition of the layers does not correspond to a physical partition of the flow but is related to the quality of the desired approximation over the variables.

Kinetic interpretation of the models

For all the derived models, a kinetic interpretation is obtained. Even if it is more restrictive than a kinetic formulation, the kinetic interpretation allows to derive efficient numerical schemes with natural upwindings. The microscopic description also gives important properties such as conservativity, stability, positivity, maximum principle that are far from being obvious at the macroscopic level.

Numerical treatment of the source terms

This topic is essential for the simulation of hyperbolic type problems as in geophysics. We have proposed an extension of the well-known hydrostatic reconstruction classically used, see paragraph 5.4.5.

Moving/fixed meshes

When dealing with free surface flows, one of the main difficulty encountered at the discrete level is the treatment of moving meshes. The models proposed in Sec. 3 have the advantage to use only fixed meshes.

Cardiac modeling

There is an irreversible evolution of medical practice toward more quantitative and personalized decision procedures for prevention, diagnosis and therapy, based on ever larger and more complex

sets of measurements.

This deep trend induces a crucial need for producing a new type of so-called computational models of the anatomy and the physiology of the human body, able to explain the observations, detect abnormalities, predict evolutions, as well as to simulate and evaluate therapies.

In order to build a cardiac simulator, four different physiological phenomena have to be coupled

- electrophysiology,
- mechanical contraction and relaxation,
- myocardium perfusion,
- cardiac metabolism.

We have proposed contributions for the second and third items. These researches have been mainly carried out by the author while he was at full time at INRIA i.e. until 2006. Now the author is still interested by this subject and involved in related research activities especially perfusion and model reduction.

Mechanical activity of the heart muscle and simulations (see pages 113 and 131, Refs : [11, 9, 12])

A full 3d mechanical model of the myocardium activity has been proposed with an associated numerical scheme. An estimation technique for the diagnosis of contraction troubles has also been proposed. It is worth being noticed that this model is now fully validated and extensively used, see the associated publications of P. Moireau, D. Chapelle and R. Chabiniok [mac10].

While most of existing models of myofibre excitation-contraction mainly rely on heuristic approaches and experimental testing, we use a physiologically-based law for the fibres of the myocardium originally introduced in [BCS01b]. In 1d, we prove global existence and uniqueness of solutions and we study their asymptotic behaviour in time. A kinetic type interpretation of the contraction law has been obtained, see 7.1.4.

Perfusion in the heart muscle (see pages 124, Ref : [6])

Despite recent advances on the anatomical description and measurements of the coronary tree the complete modeling and simulation of blood flows inside the coronaries from the arteries to the veins via the capillaries is still out of reach. Therefore, in order to model blood perfusion in the cardiac tissue, we must limit the description of the detailed flows at a given space scale. To that purpose, the modeling of the fluid-solid coupling within the framework of porous media appears appropriate.

The main contribution of this study is the derivation of a general poroelastic model valid for a nearly incompressible medium which experiences finite deformations. A numerical procedure is proposed to iteratively solve the porous flow and the nonlinear poroviscoelastic problems. Three-dimensional numerical experiments are presented to illustrate the model. Results show the complex temporal and spatial interactions of the muscle and blood, reproducing several key phenomena observed in cardiac perfusion.

Research projects

This work has been achieved while the author was involved in several projects

- the ANR project METHODE involves the university of Orléans, INRA, BRGM, INRIA and CERMICS, its objective is to study the influence of surface heterogeneity over flows (2008-2011),
  `http://methode.netcipia.net`.
- The ARC Nautilus is a 2-year research project involving teams from CNRS, UPMC and INRIA and dealing with the coupling between hydrodynamics and biology (2010-2011),
  `http://www-sop.inria.fr/comore/ARC_Nautilus/index.html`.
- The CardioSense3d is a 4-year Large Initiative Action launched in 2005 and which focuses on the electro-mechanical modeling of the heart,
  `http://www-sop.inria.fr/CardioSense3D/`.

Co-supervised Ph.D. students

- Lydie Nouvelière *Robust command for driving assistance : low speed automation*, 1999-2002, currently assistant professor at the university of Evry, supervision with S. Mammar, prof. at the university of Evry.
- Sébastien Glaser *Modeling and control of a vehicle in limit trajectory : application to the development of a driving assistance tool*, 2001-2003, currently research assistant at the Central Laboratory for roads and bridges, supervision with S. Mammar, prof. at the university of Evry.
- Asven Gariah *Model reduction for biomechanics simulations*, 2008-., supervision with D. Chapelle, head of the MACS team.
- Anne-Céline Boulanger *Theoretical and numerical analysis of the hydrodynamics-biology coupling*, 2010-., supervision with B. Perthame, prof. at the university Pierre et Marie Curie.

1 Introduction

In this section, we briefly present the two topics that we be tackled in this document. We begin with a rapid and informal overview of free surface flows problems in geophysics with a particular focus on sustainable development issues. Then we propose a list of challenges concerning the modeling and simulation of free surface flows and these scientific problems are confronted with the state of the art. Finally we give a quick overview of the aims of researches in soft tissue modeling and especially cardiac modeling.

1.1 Free surface flows in geophysics

Free surface flows study is a part of fluid mechanics and the fluid considered in geophysics, usually water, can be taken as incompressible, yet because of the presence of the free surface it has common points with compressible fluids. For this reason, the study of free surface flows is in-between compressible and incompressible fluids mechanics.

The epistemology of free surface flows in geophysics tells us this subject has been quickly divided into two parts

- hydrodynamics of oceans and seas where the free surface is almost flat and the major concern is the vertical description of the flow characteristics with external quantities such as temperature, salinity,...
- hydrodynamics of rivers where we are mainly interested in the values of water depth and flux.

From the mathematical point of view, this partitioning is natural. The first case corresponds to situations with large domains and rather smooth solutions whereas rivers flows can exhibit shocks and irregular solutions over more reduced domains.

For several reasons, this former division between rivers flows and hydrodynamics of oceans is less and less justified. Firstly, these systems are obviously coupled since water rivers reach the oceans after a certain period. The second reason concerns the used models. If originally the Saint-Venant like models were used in rivers and lakes whereas approximated versions of the Navier-Stokes equations were devoted to oceanography, the numerical models used in each discipline tend to meet since the requirements for the numerical codes are similar: accuracy, conservativity,...
Sustainable development brings us the last reason. More and more, the simulations of the hydrodynamics regime of a river or an estuary are not restricted to the determination of the water depth and the fluid velocity. They have to predict the distribution and evolution of external quantities such as pollutants or biological species. And these concerns of water quality, pollutant transports and biological life are encountered in rivers, lakes and oceans.

To be more precise, let us try to exhibit the concrete issues that will have a growing relevance in the years to come and requiring researches in the domain of geophysical flows.

1.1.1 Water management

When the water is available, its quality has to be checked with respect to its final use. It is especially restrictive for running water and swimming places. This aspect has been, to some extent, neglected – perhaps due to scientific difficulties to model and predict the water quality – but have now a growing importance. This issue is complex and challenging since the water has to be

considered as a multiphysics system with tracers and biological species being advected by the flow but also having their own dynamics (reaction terms, death, deposit).

Let us also notice that the fresh water is not only used for household consumption but also for agriculture, leisure and energy production as in nuclear power plant. The typical situation is a dam for electricity production downstream a lake. It is obvious that the management of the water ressource is a difficult, fragile and possibly moving compromise since it has to take into account the interests of swimmers, farmers, electricity manufacturers that are different and sometimes opposite.

1.1.2 Impact and prediction of natural disasters

Since they can be due to anthropic activities, more and more people consider that the precautionary principle also applies to natural disasters such as flooding, hurricane, earthquake, tidal waves. And since urbanism cannot only develop in areas free from such risks, natural disasters have to be predicted or at least their effects be anticipated.

Such a matter of course implies the availability of numerical simulations tools but the main difficulty lies in the small frequency of appearence of such events and in their unusual characteristics.

1.1.3 Seawater characteristics and their evolutions

Among all the consequences of climatic changes, we first mention the elevation of the sea level. The elevation of the sea level has strong influence over natural ecosystems (coasts or coral reefs) but also over artificial structures such as harbors, seawalls. The modeling of this phenomenon allows to adapt the embrittled structures or ecosystems.

Another aspect is the modification of the chemical composition and the biological activity of the oceans. An increase of the CO_2 concentration in the atmosphere moves the equilibrium between the ratio of CO_2 stored in the ocean and the part which is released in the atmosphere due to respiration.

1.2 Scientific challenges

The modeling, analysis and simulation of free surface flows are complex and challenging topics and this issue has been given extensive coverage in applied research and engineering. A attempt of presentation of the associated scientific challenges and of the state of the art is given hereafter.

The problems listed above deal with engineering, economy,... We now try to turn then into a scientific formulation. The difficulties arising in geophysics are threefold

- the models and equations encountered in fluid mechanics (typically the Navier-Stokes equations) are complex to analyse and solve.
- This first feature is reinforced by the fact that the considered phenomena often takes place over large domains and time periods. As an example, we mention coastal erosion, the elevation of temperature in oceans, the thaw of ice masses or the propagation of a tsunami.
- Last but not least, these problems are multiphysics with strong couplings and nonlinearities. Thus the green gazes effect induces an elevation of the sea surface but the rise of the temperature also involves chemical modifications in the ocean modifying the CO_2 absorption.

As often, efficient models and numerical tools are necessary to tackle these problems. Besides the simulation of fluid variables, the aim of researches is to be able to simulate external quantities such

as temperature, salinity, chlorophyll,... that are advected by the flow but also reacting within the fluid.

The objective of the modeling is not only to represent test cases, experiments corresponding to known events. Once a model is calibrated and validated for direct simulations, it is natural to use it for prediction and possibly for inverse problems. The coupling between geophysical models and control, stabilization and data assimilation techniques is also an important aim.

1.3 State of the art

1.3.1 The Navier-Stokes system

For the modeling and the simulation of free surface flows, the starting point is the free surface Navier-Stokes equations. It is not in the scope of this document to discuss the recent advances in analysis and simulation of the Navier-Stokes equations, we concentrate on specific aspects of fluid mechanics for geophysical flows. Hydrodynamics of rivers, lakes and oceans have three distinctive features

- *the free surface,*
- *the dissipative effects,*
- *the boundary conditions.*

Since the air viscosity is small, there is few dynamical stresses at the free surface. This implies the flows are often not very smooth and the shape of the free surface can be very complex as in the surf zone of a beach. Several techniques are available for the numerical treatment of the free surface : moving meshes, level set, volume of fluids, lagrangian techniques. A compromise between accuracy and computational costs is needed.

The parabolic feature of the Navier-Stokes equations coming from the viscous terms is often the basis of the analysis and discretization techniques. Unfortunately in practice the viscosity of the water in rivers, lakes and oceans is very small and the viscous effects are often negligible. A tsunami wave propagates over large distances with few loss of energy.

The inflow and outflow boundary conditions available in practice are usually flux and/or water depth. At the discrete level, it is far from being obvious to derive stable numerical schemes where such quantities are imposed.

For the numerical simulation of the Navier-Stokes equations, finite elements techniques are classically used. This is natural but not completely satisfactory for several reasons. Even if the state of the art of numerical techniques for the resolution of the Navier-Stokes system is not in the scope of this document, we point out the following difficulties. Indded, geophysical flows are characterized by

- non smooth solutions (shock waves, dam break) to capture,
- drying and flooding leading to topological modifications of the fluid domain,
- in presence of a tracer (temperature, salinity,...), properties such as conservativity and maximum principle have to be ensured,
- the water depth can tend to zero and in this situation, the numerical scheme has to remain stable.

Despite the numerous attempts (see [KM03, Her07] and references therein) and as far as the author knows, the above mentioned properties can hardly be satisfied using finite elements type discretizations.

1.3.2 Models of reduced complexity

The difficulties coming from the discretization and the simulation of the Navier-Stokes but also the scales – in space and time – of the considered problems in geophysics encourage to look for models of reduced complexity but able to represent complex flows.

The Saint-Venant system [BdSV71] is a well known and efficient approximation of the Navier-Stokes system for Shallow Water flows. For a large class of problems (dam break, flooding, debris flow) the Saint-Venant system is a very good approximation of the Navier-Stokes system [Sto58, GP01, Mar07, FS04, BW04]. For decades, it has been the cornerstone of river hydrodynamics studies.

Even if the Saint-Venant system is widely used, its discretization remains tricky and before to extend it, we propose a review of the numerical techniques for its resolution.

The *parabolic/finite elements* approach prevailed until early 80's where the advances in compressible fluid mechanics (especially in aeronautics) gave another point of view on the Shallow Water models since the Saint-Venant system is a special case of the Euler system for compressible gas dynamics. Thus the formulation of the Saint-Venant system under the form of a system of conservation law with shock waves, entropies,... makes way for significant progress.

As a natural consequence, finite volume techniques [Bou04b, LeV02, GR96, EGH00] converting divergence terms into surface integrals appear for the numerical resolution. Finite volume schemes offer two advantages compared to finite differences, these methods are conservative and can be – quite – easily implemented on unstructured meshes.

The difficulty to define accurate numerical schemes for such hyperbolic systems is related to their deep mathematical structure. We begin the story with the Godunov and Roe schemes [God59, Roe97] that are able to capture shocks. The notion of approximate Riemann solver [HLvL83] is a very general tool for the construction of numerical schemes. Among the widely used solvers, only the VFRoe [BGH00, BM08] does not belong to this family. The relaxation technique [Bou04c, CLL94, LP01] is the most recent proposed one and gives rise to very efficient solvers [BBC$^+$05, CGP$^+$01, JX95, Bou03].

For an analysis of the schemes for which nonlinear stability properties (preservation of invariant domain, existence of entropy inequality, ...) can be proved, see [Bou04b]. Here we concentrate on two fundamental stability properties: positivity and preservation of relevant equilibria.

For the analysis but also in practice [GM97], it is important to get schemes ensuring the positivity of the water depth. The positivity of the Roe scheme can not be demonstrated but Pelanti et al. propose a Roe-type scheme for shallow granular where the positivity of the computed flow depth is guaranteed [PBM08]. Likewise a discretization of the Saint-Venant system using the Discontinuous Galerkin method has been proposed in [EPD08], a slight modification of the momentum equation is needed to ensure the scheme is positive. Notice also that even if the positivity of some schemes is demonstrated, in practice some problems can occur as for the Godunov scheme, see [BGH98]. Since there exists a wide choice of positive schemes, we have chosen to neglect the others.

In the context of the discretization of hyperbolic systems of balance laws another fundamental point is to get schemes that satisfy the preservation of steady-states such as still water equilibrium in the context of the Saint-Venant system. The difficulty to build such schemes was pointed out by

several authors and led to the notion of *well-balanced* schemes. Different approaches to satisfy the well-balanced property have been proposed. The Roe solver has been modified in order to preserve steady-states by Bermudez and Vasquez [BV94]. A two-dimensional extension is performed by Bermudez et al. [BDDV98] and recent extensions to other types of homogeneous solvers can be found in [CRDN03a, CRDN03b]. Leveque [LeV98] and Jin [Jin01] propose other ways to adapt exact or approximate Riemann solver to the non-homogeneous case. Following the idea of Leroux and Greenberg [GL96] for the scalar case, Gosse [Gos00, Gos01] and Gallouët et al. [GHS03] construct numerical schemes based on the solution of the – exact or approximate – Riemann problem associated with a larger system where a third equation on the variable describing the bottom topography is added. Approaches based on central schemes are used in [KL02, NT90, KT00].

For the preservation of the static equilibria, the most popular reference is [ABB$^+$04] where a very flexible approach involving a hydrostatic reconstruction is proposed. Notice that this technique is generic, in the sense that it can be used in conjunction with any given numerical flux for the homogeneous Saint-Venant problem.

In [Bou04b], Bouchut proposes a comparison between several efficient solvers for the Saint-Venant system: Suliciu, kinetic and VFRoe. In the test cases considered, discontinuities and shocks appear. All the tested methods give similar results especially at the second order.

The kinetic schemes [PS01, Per99, AB03] that will be widely used in the following, belong to the family of approximate Riemann solver. Notice also that a kinetic system is a particular case of relaxation system [Bou99, Bou03].

When dealing with more complex models than the Saint-Venant system, the notion of hyperbolicity and conservation law quickly vanishes. Thus, the hydrostatic Euler system [Bre99, Gre99, Lio96] can not be written under the form of a conservation law because of the kinematic boundary condition at the free surface. We will see all along this document that kinetic solvers can face this difficulty whereas most of other solvers for hyperbolic systems fail.

Large slope & bottom friction In practice, Saint-Venant solvers are often used in situations relatively far away from the validity domain of the model. Typical cases are the simulation of a dam break in a valley and debris flows. In such situations, the bottom slope and the bottom friction can be large. We recall that for the derivation of the Saint-Venant system, the bottom friction and the bottom slope are supposed to be small [Mar07, GP01].

As far as the author knows, there is not any complete answer to these questions. An improved model, due to Savage-Hutter, is valid for large slopes and small slope variations [HKPS95, SH91a]. A new model relaxing all restrictions on the topography has been proposed by Bouchut et al. [BMCPV03] but its numerical resolution remains costly.

Even if the bottom friction induces dissipative effects and hence stabilizing, when it can not be considered as a small correction added to the hyperbolic part some instabilities can appear, see paragraphs 5.2.3 and 6.1.

Nowadays and except in some situations such as large slope or large bottom friction (see paragraph 1.3.2), numerical techniques exist and are mature for its resolution, see [Bou04b] and references therein.

Thus it is now possible to consider more sophisticated versions of the Saint-Venant system. There are two main directions of extension

- include non-hydrostatic terms,
- enrich the vertical discretization of the velocity field.

We propose several extensions of the Saint-Venant system in Sec. 3 for which a numerical scheme is given. For each extension, the bibliography is given in Sec. 3.

1.4 3d models and simulations

In this document, we mainly present models approximating the 2d Navier-Stokes equations written in coordinates (x, z). In 3d, their derivation and kinetic interpretation can be carried out without any difficulty. But, the writting in 3d makes the presentation unwieldy and does not enrich it. This remark does not hold at the discrete level since the design of numerical schemes for 3d problems and their implementation is often far more complex than in 2d. Even if the numerical results presented in this document are mainly in 2d, the author points out that a numerical code is also available integrating 3d versions of the proposed numerical schemes. Some 3d simulations using this tool are given at the end of the document.

The paragraphs dealing with numerical results contain illustrations of the proposed models and schemes. The author wants to emphasize that the simulation of complex flows – especially in 3d – and their comparison with experimental data are time consuming. And in applied science and especially in fluid mechanics, the ability for numerical codes and schemes to simulate complex test problems is crucial.

1.5 Cardiac modeling

The heart can be seen as an electrically activated pump providing the organs with oxygen-rich blood coming from the lungs. The modeling of the heart muscle is complex since it mainly results from the coupling of

- an electrical activation,
- a circulation of the blood inside the heart cavities but also inside the muscle (perfusion),
- an active law for the contraction of the cardiac fibres,
- a passive behavior of the elastic tissues surrounding the contractile fibres.

In Sec. 7, we address the last three items.

The modeling of the active mechanical behavior of muscle tissues, and of the myocardium in particular, has been the object of an abundant literature, see for example [Fun93, HNS97, NH41, Hum02, HO09] and references therein, with some detailed experimental validations in most instances, at the local (tissue) or global (organ) levels, or both, see e.g. [CCL$^+$09]. Of course, in order to adequately model the muscle physiology, energy considerations (balances and exchanges) are of utmost value, and such mechanisms are well-described at the cellular level [Hil38]. However, little attention has so far been devoted to carrying over these considerations to the macroscopic level in the muscular tissue models, whereas key phenomena such as adaptation to effort and oxygen consumption, and correspondingly pathologies associated with shortage of oxygen supply, such as ischemia and infarction – critically depend on energy mechanisms.

The objective of computational cardiac modeling and simulation is to contribute significantly to the understanding of heart physiology and disease.

2 Outline of the document

The document is organized as follows. Sections 1-6 are devoted to free surface flows. In Sec. 7, we detail the contributions in soft tissue modeling, porous mechanics and model reduction.

In Sec. 1, we present the scientific problems arising in free surface flows in geophysics and we give the state of the art for the modeling, analysis and simulation of such problems. In Sec. 3, the models we propose and their derivation is described. The key point for the numerical simulation of these models is their kinetic interpretations that are given in Sec. 4. Then for each model the milestones of the numerical scheme are given. Especially the main properties of the schemes such as stability, positivity, well-balancing are demonstrated. In Sec. 6, numerical simulations of each of the proposed models are presented.

In Sec. 7, we first describe the electro-mechanical modeling of the the heart muscle we have proposed. This 3d model has several ingredients : geometrical model, blood circulation, passive and active behavior of the cardiac fibres. In a simplified 1d case, the contraction law of the cardiac fibres is analysed. Then we present an enriched electro-mechanical model of the heart where the perfusion of the blood with the cardiac muscle is introduced. Of course the models of the cardiac activity we propose are complex with expensive computational costs especially for inverse problems, we have experimented several reduced order modeling strategies and results (*a priori* estimates and reduced simulations) based on the Proper Orthogonal Decomposition are finally described.

3 Some models between Navier-Stokes and Saint-Venant

In this section we present models of reduced complexity able to reproduce complex flows. After a presentation of the free surface Navier-Stokes system with the notations that will be used throughout the document, we propose four main models of growing complexity approximating the Navier-Stokes equations.

The strong points of these models have already been mentioned in the syllabus of this document. Until now, we have paid few attention to the mathematical analysis of the proposed models, nevertheless we take care they are in accordance with physical rules (principles of thermodynamics) and they have some mathematical properties such as hyperbolicty, entropies,...

3.1 Navier-Stokes, Euler and Saint-Venant systems

At the level of continuous mechanics, the Navier-Stokes equations model fluid motion accurately but the complicated nature of this nonlinear system of partial differential equations often needs simplifications to deal with real situations as in geophysics. A first simplification of the equations is obtained when considering an incompressible flow of a Newtonian fluid, that is done in the following.

We mainly restrict our presentation to two-dimensional flows – horizontal and vertical directions – but we claim that what is presented in this document in terms of models and numerical techniques can be adapted to three-dimensional case up to computational cost constraints. These constraints can not be neglected especially when dealing with real life applications as we intend to. We focus our attention on the accuracy, the stability and the efficiency of the numerical schemes but the optimization (high performance calculus, parallelization) is not in the scope of this document.

3.1.1 The free surface Navier-Stokes system

We begin by considering the two-dimensional Navier-Stokes system [Lio96] describing a free surface gravitational flow moving over a bottom topography $z_b(x,t)$. We denote with x and z the horizontal and vertical directions, respectively. The system has the form

$$\frac{\partial \rho}{\partial t} + \frac{\partial \rho u}{\partial x} + \frac{\partial \rho w}{\partial z} = 0, \tag{3.1}$$

$$\frac{\partial \rho u}{\partial t} + \frac{\partial \rho u^2}{\partial x} + \frac{\partial \rho uw}{\partial z} + \frac{\partial p}{\partial x} = \frac{\partial \Sigma_{xx}}{\partial x} + \frac{\partial \Sigma_{xz}}{\partial z}, \tag{3.2}$$

$$\frac{\partial \rho w}{\partial t} + \frac{\partial \rho uw}{\partial x} + \frac{\partial \rho w^2}{\partial z} + \frac{\partial p}{\partial z} = -\rho g + \frac{\partial \Sigma_{zx}}{\partial x} + \frac{\partial \Sigma_{zz}}{\partial z}, \tag{3.3}$$

and we consider solutions of the equations for

$$t > t_0, \quad x \in \mathbb{R}, \quad z_b(x,t) \leq z \leq \eta(x,t),$$

where $\eta(x,t)$ represents the free surface elevation, $\mathbf{u} = (u,w)^T$ the velocity vector, ρ the density and g the gravity acceleration. The water depth is $H = \eta - z_b$, see Fig. 1. We consider the bathymetry z_b can vary with respect to abscissa x and also with respect to time t, this allows to represent e.g. erosion type problems or wave generation by the bottom motions.

The chosen form of the viscosity tensor is

$$\Sigma_{xx} = 2\mu \frac{\partial u}{\partial x}, \qquad \Sigma_{xz} = \mu\Big(\frac{\partial u}{\partial z} + \frac{\partial w}{\partial x}\Big),$$
$$\Sigma_{zz} = 2\mu \frac{\partial w}{\partial z}, \qquad \Sigma_{zx} = \mu\Big(\frac{\partial u}{\partial z} + \frac{\partial w}{\partial x}\Big),$$

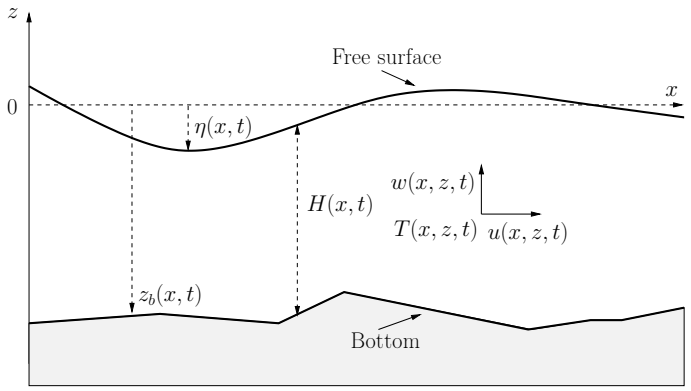

Figure 1: Notations: water height $H(x,t)$, free surface $\eta(x,t)$ and bottom $z_b(x,t)$.

where μ is a viscosity coefficient. The turbulence modeling and simulation is also out of the scope of this document so we consider a constant viscosity in the following.

Neglecting the viscous and friction effects, the Navier-Stokes system (3.1)-(3.3) reduces to the Euler system

$$\frac{\partial \rho}{\partial t} + \frac{\partial \rho u}{\partial x} + \frac{\partial \rho w}{\partial z} = 0, \tag{3.4}$$

$$\frac{\partial \rho u}{\partial t} + \frac{\partial \rho u^2}{\partial x} + \frac{\partial \rho uw}{\partial z} + \frac{\partial p}{\partial x} = 0, \tag{3.5}$$

$$\frac{\partial \rho w}{\partial t} + \frac{\partial \rho uw}{\partial x} + \frac{\partial \rho w^2}{\partial z} + \frac{\partial p}{\partial z} = -\rho g, \tag{3.6}$$

with an associated energy balance.

The fluid density $\rho(x,t)$ is supposed to depend on the spatial and temporal distribution of a given tracer $T(x,z,t)$, namely

$$\rho = \rho(T), \tag{3.7}$$

and T is governed by a transport-diffusion equation

$$\frac{\partial \rho T}{\partial t} + \frac{\partial \rho uT}{\partial x} + \frac{\partial \rho wT}{\partial z} = \mu_T \frac{\partial^2 T}{\partial x^2} + \mu_T \frac{\partial^2 T}{\partial z^2}, \tag{3.8}$$

where μ_T is the tracer diffusivity. In the case of several tracers e.g. temperature T and salinity S we write $\rho = \rho(S,T)$ and T, S satisfy a set of coupled transport-diffusion equations. When $\rho = \rho_0 = Cst$, we recover in (3.1)-(3.3) the classical formulation of the incompressible Navier-Stokes equations.

We recall the fondamental stability property related to the fact that the Navier-Stokes system admits an energy

$$E = \rho \frac{u^2 + w^2}{2} + \rho g z + p^a, \tag{3.9}$$

leading to the following equation

$$\frac{\partial}{\partial t}\int_{z_b}^{\eta}(E+p^a)\,dz+\frac{\partial}{\partial x}\int_{z_b}^{\eta}u\big(E+p-\mu\left(2u\frac{\partial u}{\partial x}+w\left(\frac{\partial u}{\partial z}+\frac{\partial w}{\partial x}\right)\right)\big)\,dz=$$
$$-\kappa(\mathbf{u_b},H)u_b^2-2\mu\int_{z_b}^{\eta}\left(\left(\frac{\partial u}{\partial x}\right)^2+\frac{1}{2}\left(\frac{\partial u}{\partial z}+\frac{\partial w}{\partial x}\right)^2+\left(\frac{\partial w}{\partial z}\right)^2\right)dz$$
$$+H\frac{\partial p^a}{\partial t}+(p|_b-p^a)\frac{\partial z_b}{\partial t},\tag{3.10}$$

where the friction law at the bottom involving $\kappa(\mathbf{u_b},H)$ is defined by (3.15). The last term in the preceding equation

$$(p|_b-p^a)\frac{\partial z_b}{\partial t},$$

comes from the time variations of the displacement $z_b(x,t)$ of the boundary at the bottom. Thus this term accounts for the work of the external force applied to the bottom and inducing the bottom displacements.

Boundary conditions The system (3.1)-(3.3) is completed with boundary conditions. The outward and upward unit normals to the free surface $\mathbf{n}_s$ and to the bottom $\mathbf{n}_b$ are given by

$$\mathbf{n}_s=\frac{1}{\sqrt{1+\left(\frac{\partial\eta}{\partial x}\right)^2}}\begin{pmatrix}-\frac{\partial\eta}{\partial x}\\1\end{pmatrix},\quad \mathbf{n}_b=\frac{1}{\sqrt{1+\left(\frac{\partial z_b}{\partial x}\right)^2}}\begin{pmatrix}-\frac{\partial z_b}{\partial x}\\1\end{pmatrix}.$$

Let Σ_T be the total stress tensor with

$$\Sigma_T=-pI_d+\begin{pmatrix}\Sigma_{xx}&\Sigma_{xz}\\\Sigma_{zx}&\Sigma_{zz}\end{pmatrix}.$$

At the free surface we have the kinematic boundary condition

$$\frac{\partial\eta}{\partial t}+u_s\frac{\partial\eta}{\partial x}-w_s=0,\tag{3.11}$$

where the subscript s denotes the value of the considered quantity at the free surface.

The wind forcing is denoted τ_w and we consider the following expression [Imb98]

$$\tau_w=C_D\frac{\rho_a}{\rho_0}|V_w|V_w\tag{3.12}$$

where the wind velocity is denoted V_w and the wind drag coefficient C_D. Assuming negligible the air viscosity, the continuity of stresses at the free boundary imposes

$$\Sigma_T\mathbf{n}_s=-p^a\mathbf{n}_s+\tau_w\mathbf{t}_s,\tag{3.13}$$

where $p^a=p^a(x,t)$ is a given function corresponding to the atmospheric pressure and $\mathbf{t}_s$ being orthogonal to $\mathbf{n}_s$. Relation (3.13) can be splitted into

$$\mathbf{n}_s.\Sigma_T\mathbf{n}_s=-p^a,\quad\text{and}\quad\mathbf{t}_s.\Sigma_T\mathbf{n}_s=\tau_w.$$

At the bottom, the kinematic boundary condition consists in

$$\frac{\partial z_b}{\partial t}+u_b\frac{\partial z_b}{\partial x}-w_b=0.\tag{3.14}$$

Note that Eq. (3.14) reduces to a classical no-penetration condition when z_b does not depend on time t.

For the stresses at the bottom we consider a wall law under the form

$$\mathbf{t}_b.\Sigma_T\mathbf{n}_b = \kappa(\mathbf{u}_b, H).\mathbf{t}_b, \tag{3.15}$$

where $\mathbf{t}_b$ a unit vector satisfying $\mathbf{t}_b \cdot \mathbf{n}_b = 0$ and $\mathbf{u}_b = (u_b, w_b)$. If $\kappa(\mathbf{u_b}, H)$ is constant then we recover a Navier friction condition as in [GP01]. Introducing laminar k_l and turbulent k_t friction, we use the expression

$$\kappa(\mathbf{u_b}, H) = k_l + k_t H|\mathbf{u_b}|,$$

corresponding to the boundary condition used in [Mar07]. Another form of $\kappa(\mathbf{u_b}, H)$ is used in [BW04] and for other wall laws, the reader can also refer to [MPV98]. Due to thermomechanical considerations, in the sequel we will suppose $\kappa(\mathbf{u_b}, H) \geq 0$ and $\kappa(\mathbf{u_b}, H)$ will be often simply denoted by κ.

Obviously initial conditions and inflow/outflow conditions need also be prescribed.

3.1.2 Turbulence and Coriolis effects

All along this document, we have singled out the Euler part of the Navier-Stokes sytem. Even if they can be of great importance in some specific cases for geophysical flows, we have paid few attention to turbulence effects and thus we only consider constant viscosity. Since we mainly consider limited domains, the Coriolis effects are also neglected. In the works in progress concerning hydrodynamics-biology coupling in the oceans, this assumption is no more valid and the Coriolis forces will be integrated.

3.1.3 Shallow Water type models

Because of the scales – in space and time – of the considered problems in geophysics, there exists a demand for models of reduced complexity such as Shallow Water type models but able to represent complex flows. This demand concerns either the simulation or the analysis. For example, considering the Saint-Venant or the Korteweg-de Vries (KdV) systems, the mathematical theory behind these Shallow Water systems is rich and interesting, and, in the broad sense, is a topic of active mathematical research.

Non-linear Shallow Water equations model the dynamics of a shallow, rotating layer of an homogeneous incompressible fluid and are typically used to describe vertically averaged flows in two or three dimensional domains in terms of horizontal velocity and depth variation. This set of equations is particularly well-suited for the study and numerical simulations of a large class of geophysical phenomena such as rivers, coastal domains, oceans or even run-off or avalanches when being modified with adapted source terms [BW04].

When considering Shallow Water flows, the physical system is rescaled using the quantities

- h and λ, two characteristic dimensions along the z and x axis respectively,
- a_s the typical wave amplitude, a_b the typical bathymetry variation,
- $C = \sqrt{gh}$ the typical horizontal wave speed.

Classically for the derivation of a Shalow Water system, we introduce the small parameter

$$\varepsilon = \frac{h}{\lambda}. \tag{3.16}$$

When considering long waves propagation, another important parameter needs be considered, namely

$$\delta = \frac{a_s}{h}, \tag{3.17}$$

and we consider for the bathymetry $\frac{a_b}{h} = \mathcal{O}(\delta)$. This rescaling is discussed in more details in [5].

When deriving Shallow Water type models, the game consists in finding asymptotic expansions of the Navier-Stokes equations and truncating them up to $\mathcal{O}(\varepsilon^n \delta^p)$ terms. For large values of n and p, the obtained models become often difficult to analyse and/or simulate and sometimes they seem even more complex than the original Navier-Stokes equations...

3.1.4 The Saint-Venant system

Among the large family of Shallow Water type models, the Saint-Venant system [BdSV71] plays an important role. Adhémar Jean Claude Barré de Saint-Venant introduces a set of hyperbolic partial differential equations that well approximates stiff phenomena such as river flows, hydraulic jumps, dam breaks...

The Saint-Venant system [FS04, GP01, Mar07] results from an asymptotic expansion for small ε of the Navier-Stokes equations. In 1d the Saint-Venant system with viscosity and friction has been obtained by Gerbeau and Perthame [GP01]. Similarly, the 2d Saint-Venant system has been derived by Marche [Mar07]. In the case of a channel with varying section, the asymptotic expansion has been obtained by Decoene [DBMS09]. The 1d Saint-Venant system with viscosity and friction reads

$$\frac{\partial H}{\partial t} + \frac{\partial}{\partial x}\big(H\bar{u}\big) = 0, \tag{3.18}$$

$$\begin{aligned}\frac{\partial (H\bar{u})}{\partial t} + \frac{\partial (H\bar{u}^2)}{\partial x} + \frac{g}{2}\frac{\partial H^2}{\partial x} = &-H\frac{\partial p^a}{\partial x} - gH\frac{\partial z_b}{\partial x} + \frac{\partial}{\partial x}\big(4\nu H\frac{\partial \bar{u}}{\partial x}\big) \\ &-\frac{\kappa(\overline{\mathbf{u}}_b, H)}{1+\frac{\kappa(\overline{\mathbf{u}}_b,H)}{3\nu}H}\bar{u},\end{aligned} \tag{3.19}$$

with $\nu = \mu/\rho$, $\rho = \rho_0$ and the mean horizontal velocity is defined by

$$\overline{u} = \frac{1}{H}\int_{z_b}^{\eta} u \; dz, \quad \text{with} \quad u = \overline{u} + \mathcal{O}(\varepsilon^2). \tag{3.20}$$

For smooth solutions, we also have the energy balance

$$\begin{aligned}\frac{\partial E_h}{\partial t} + \frac{\partial}{\partial x}\left(\overline{u}\big(E_h + g\frac{H^2}{2} + 4\nu H\frac{\partial \bar{u}}{\partial x}\big)\right) \; = \; &-\frac{\kappa(\overline{\mathbf{u}}_b, H)}{1+\frac{\kappa(\overline{\mathbf{u}}_b,H)}{3\nu}H}\bar{u}^2 \\ &-4\nu H\left(\frac{\partial \bar{u}}{\partial x}\right)^2 + H\frac{\partial p^a}{\partial t},\end{aligned} \tag{3.21}$$

with E_h given by

$$E_h = \frac{H}{2}\overline{u}^2 + \frac{g}{2}\left(\eta^2 - z_b^2\right) + Hp^a.$$

The Saint-Venant system without friction and viscosity can be viewed as a special case of the Euler system for compressible gas dynamics. Existence and uniqueness of solutions for this system has been demonstrated, see [LPS96] and references therein.

3.1.5 Validity of the Saint-Venant system and other applications

The Saint-Venant system initially proposed for free surface flows, is used in a wide range of applications such as trafic flow modeling [Hel96], blood flows in arteries [FLQ03a],....

It is worth being noticed that the Shallow Water assumption is necessary for the derivation of the Saint-Venant system but it is not a sufficient condition. And since its formulation (3.18)-(3.19) does not explictly emphasizes the assumptions allowing its derivation ($\varepsilon \ll 1$, $\frac{\partial z_b}{\partial x} \ll 1$, small bottom friction and small viscosity), it is sometimes used in situations where these requirements are no more valid.

For example, it is the case when considering large variations of an uneven bottom as appears in rain streaming or erosion phenomena [CDFNF08] or wave breaking problems. In these situations, the use a Savage-Hutter type model [BMCPV03] allowing larger values of the bottom gradient $\frac{\partial z_b}{\partial x}$ may be appropriate but significantly increases the computational costs.

In the following paragraphs, the proposed model extending the Saint-Venant system are shortly described. For a complete derivation, the reader can refer to the associated publications.

3.2 The section-averaged Saint-Venant system [8]

The derivation of this model is to some extent classical. The contribution of the author mainly consists in the kinetic interpretation (paragraph 5.2), the associated numerical scheme (paragraph 5.2), the simulation results and the comparison with analytical/experimental solutions (paragraph 6.1). The model formulation is only briefly recalled to emphasize the importance of the source terms.

For many applications involving natural rivers hydrodynamics, the extension of the Saint-Venant system to the case of non rectangular channels is necessary and this section-averaged Saint-Venant system that is cheaper than 2d simulations exhibits additional source terms. The main difficulty of these equations consists in the discretization of these source terms, see paragraph 5.2.

The section-averaged Shallow Water model usually applied in river and open channel hydrodynamics is also derived asymptotically starting from the three-dimensional Reynolds-averaged Navier-Stokes equations for incompressible free surface flows [DBMS09]. The derivation is carried out under quite general assumptions on the geometry of the channel and the characteristic dimensions of the flow, thus allowing for the application of the resulting equations to natural rivers with arbitrarily shaped cross sections.

The section-averaged Shallow Water model is often used for the simulation of the hydrodynamics of a whole river. It can be also inserted in a control loop for the regulation of a dam or coupled with a 2d code [MM09].

Using the notations of Fig. 2, water height $h(x,y,t)$, free surface $\eta(x,y,t)$, width $L(x,z)$ and bottom $z_b(x,y)$, let us introduce the following averaged quantities

$$\begin{aligned} S(x,t) &= \int_{l_1}^{l_2} h(x,y,t)\ dy = \int_{z_b}^{\eta} L(x,z)\ dz, \\ Q(x,t) &= \int_{l_1}^{l_2}\int_{z_b}^{\eta} u(x,y,z,t)\ dzdy = S(x,t)\bar{u}(x,t), \end{aligned} \tag{3.22}$$

corresponding respectively to the area of the fluid section at abscissa x and time t and the mass flux thought S. From the notations introduced in Fig. 2, we also define

$$\overline{z}_b(x) = \min_{y\in[l_1,l_2]} z_b(x,y), \tag{3.23}$$

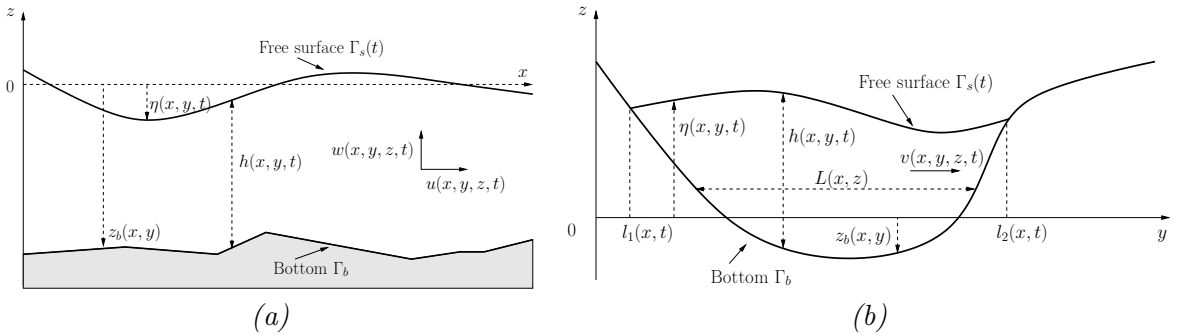

Figure 2: Channel profile, *(a)* side view and *(b)* front view.

and we assume

$$h(x,y,t) + z_b(x,y) := H(x) + \overline{z}_b(x).$$

From the previous relation we introduce $\overline{\eta}$ defined by

$$\overline{\eta} = H + \overline{z}_b. \tag{3.24}$$

3.2.1 The model

The derivation of the section-averaged Saint-Venant system for the 3d Navier-Stokes is classical. In particular, the reader can refer to [DBMS09]. So we give without any proof the following proposition

Proposition 1. *Written under a conservative form, the section-averaged Saint-Venant system defined by*

$$\frac{\partial S}{\partial t} + \frac{\partial S\overline{u}}{\partial x} = 0, \tag{3.25}$$

$$\frac{\partial S\overline{u}}{\partial t} + \frac{\partial}{\partial x}\left(S\overline{u}^2 + g\int_{\overline{z}_b}^{\overline{\eta}} L(x,z)(\overline{\eta} - z)\ dz\right) = -gHL(x,\overline{z}_b)\frac{\partial \overline{z}_b}{\partial x} + g\int_{\overline{z}_b}^{\overline{\eta}} (\overline{\eta} - z)\frac{\partial L}{\partial x}dz - S\frac{\partial p^a}{\partial x} - \kappa\overline{u}. \tag{3.26}$$

results from an approximation in $\mathcal{O}(\varepsilon^2)$ of the 3d Navier-Stokes equations, $\overline{\eta}$ and $\overline{z}_b$ are respectively defined by (3.24) and (3.23). Moreover the smooth solutions of (3.25)-(3.26) satisfy the following energy balance

$$\frac{\partial}{\partial t}\left(S\frac{\overline{u}^2}{2} + \int_{\overline{z}_b}^{\overline{\eta}} gL(x,z)z\ dz + Sp^a\right) + \frac{\partial}{\partial x}\left(\overline{u}\left(S\frac{\overline{u}^2}{2} + \int_{\overline{z}_b}^{\overline{\eta}} L(x,z)(\eta - z)\ dz + \int_{\overline{z}_b}^{\overline{\eta}} L(x,z)z\ dz + Sp^a\right)\right) = S\frac{\partial p^a}{\partial t} - \kappa\overline{u}^2. \tag{3.27}$$

3.2.2 The source terms

The discretization of the source terms of a conservation law is often tricky. In this paragraph and without loss of generality, we give another expression for each of the source terms appearing in Eq. (3.26). This new formulation will be used in the discrete scheme.

The section S is defined by (3.22), let us suppose the cross section profile satisfies

$$L(x,z) > 0, \qquad \text{for} \quad z > \overline{z}_b. \tag{3.28}$$

Then obviously, there exists an operator A such that forall x, t

$$A(S) = H, \tag{3.29}$$

and the operator A is invertible. Let us also suppose the section width $L(x,z)$ can be written under the form (see Fig. 3)

$$L(x,z) = L_b(x) + L_1(x)\left(\int_{\overline{z}_b}^{z} \alpha_l\big(\tilde{z} - \overline{z}_b(x)\big)d\tilde{z} + \int_{\overline{z}_b}^{z} \alpha_r\big(\tilde{z} - \overline{z}_b(x)\big)d\tilde{z}\right), \tag{3.30}$$

where $x \mapsto L_b(x)$ is a given positive function. The functions $x \mapsto L_1(x)$ and $z \mapsto \alpha_i(z)$ for $i = l, r$ are given smooth functions not necessarily positive but satisfying (3.28) with $\alpha_i(0) = 0$. In the case of constant slopes (Fig. 3-*(b)*), we recover

$$L(x,z) = L_b(x) + L_1(x)\left((\overline{\alpha}_l + \overline{\alpha}_r)\,(z - \overline{z}_b)\right).$$

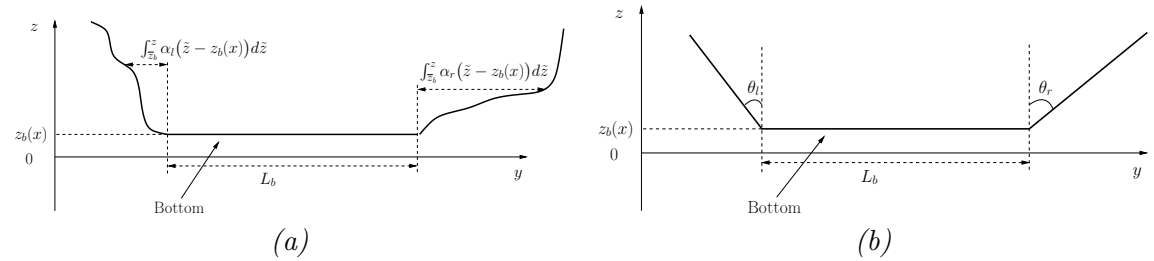

Figure 3: Section width $L(x,z)$. *(a)* general slopes and *(b)* constant slopes $\overline{\alpha}_l = \tan\theta_l$ and $\overline{\alpha}_r = \tan\theta_r$.

Remark 3.1. *A more general expression for $L(x,z)$ is*

$$L(x,z) = L_b(x) + \int_{\overline{z}_b}^{z} l_l\big(x, \tilde{z} - \overline{z}_b(x)\big)d\tilde{z} + \int_{\overline{z}_b}^{z} l_r\big(x, \tilde{z} - \overline{z}_b(x)\big)d\tilde{z}.$$

This expression is similar to our choice when we can separate the variables for functions $(x,z) \mapsto l_i(x,z)$ with $l_i(x,z) = L_1(x)\alpha_i(z)$ for $i = l, r$. Note that at the discrete level, this assumption is not restrictive.

Let us introduce $L_2(x,z)$ defined by

$$L_2(x,z) = \int_{\overline{z}_b}^{z} \alpha_l\big(\tilde{z} - \overline{z}_b(x)\big)d\tilde{z} + \int_{\overline{z}_b}^{z} \alpha_r\big(\tilde{z} - \overline{z}_b(x)\big)d\tilde{z}.$$

Then exists another operator B such that for any given x

$$\int_{\overline{z}_b}^{\overline{\eta}} (\overline{\eta} - z)L_2(x,z)\; dz = B\left(\int_{\overline{z}_b}^{\overline{\eta}} L_2(x,z)\; dz\right) = B(S,x).$$

As an example, if there exists an integer p such that $\frac{\partial^p L_2}{\partial z^p} = 0$ using an integration by parts we obtain

$$\int_{\overline{z}_b}^{\overline{\eta}} (\overline{\eta} - z) L_2(x,z)\ dz = \frac{\partial^{p-1} L_2}{\partial z^{p-1}} \frac{A(S)^{p+1}}{(p+1)!}.$$

From the chosen expression (3.30) for $L(x,z)$, we have

$$\begin{aligned}
\int_{\overline{z}_b}^{\overline{\eta}} (\overline{\eta} - z) \frac{\partial L}{\partial x} dz &= \frac{\partial L_b}{\partial x} \frac{H^2}{2} + \frac{\partial L_1}{\partial x} \int_{\overline{z}_b}^{\overline{\eta}} (\overline{\eta} - z) L_2(x,z) dz \\
&\quad - \frac{\partial \overline{z}_b}{\partial x} L_1(x) \int_{\overline{z}_b}^{\overline{\eta}} (\overline{\eta} - z) \int_{\overline{z}_b}^{z} \left. \frac{\partial(\alpha_l + \alpha_r)}{\partial z} \right|_{\tilde{z} - \overline{z}_b(x)} d\tilde{z} dz \\
&= \frac{\partial L_b}{\partial x} \frac{A(S)^2}{2} + \frac{\partial L_1}{\partial x} B(S,x) \\
&\quad - \frac{\partial \overline{z}_b}{\partial x} L_1(x) \int_{\overline{z}_b}^{\overline{\eta}} (\overline{\eta} - z) \left(\alpha_l\big(z - \overline{z}_b\big) + \alpha_r\big(z - \overline{z}_b\big) \right) dz \\
&= \frac{\partial L_b}{\partial x} \frac{A(S)^2}{2} + \frac{\partial L_1}{\partial x} B(S,x) \\
&\quad - \frac{\partial \overline{z}_b}{\partial x} L_1(x) \int_{\overline{z}_b}^{\overline{\eta}} \int_{\overline{z}_b}^{z} \left(\alpha_l\big(\tilde{z} - \overline{z}_b\big) + \alpha_r\big(\tilde{z} - \overline{z}_b\big) \right) d\tilde{z} dz,
\end{aligned}$$

so the source terms read

$$- gHL(x,\overline{z}_b) \frac{\partial \overline{z}_b}{\partial x} + g \int_{\overline{z}_b}^{\overline{\eta}} (\overline{\eta} - z) \frac{\partial L}{\partial x} dz = -g \frac{\partial \overline{z}_b}{\partial x} S + g \frac{\partial L_b}{\partial x} \frac{A(S)^2}{2} + g \frac{\partial L_1}{\partial x} B(S,x), \tag{3.31}$$

and the Saint-Venant system described in Prop. 1 can be rewritten under the form

$$\frac{\partial S}{\partial t} + \frac{\partial S\overline{u}}{\partial x} = 0, \tag{3.32}$$

$$\begin{aligned}
&\frac{\partial S\overline{u}}{\partial t} + \frac{\partial}{\partial x} \left(S\overline{u}^2 + g \left(L_b(x) \frac{(A(S))^2}{2} + L_1(x) B(S,x) \right) \right) = \\
&\qquad -g \frac{\partial \overline{z}_b}{\partial x} S + g \frac{\partial L_b}{\partial x} \frac{A(S)^2}{2} + g \frac{\partial L_1}{\partial x} B(S,x) - S \frac{\partial p^a}{\partial x} - \kappa \overline{u}.
\end{aligned} \tag{3.33}$$

When considering any geometry profile – non rectangular – but constant along x i.e. $\frac{\partial L_b}{\partial x} = \frac{\partial L_1}{\partial x} = 0$, the only remaining source term is $-g \frac{\partial \overline{z}_b}{\partial x} S$ corresponding to the one of the classical Saint-Venant system where H is replaced by S. When considering constant slopes in y direction, the system (3.32)-(3.33) reads

$$\begin{aligned}
&\frac{\partial S}{\partial t} + \frac{\partial S\overline{u}}{\partial x} = 0, \\
&\frac{\partial S\overline{u}}{\partial t} + \frac{\partial}{\partial x} \left(S\overline{u}^2 + g \frac{H^2}{2} \left(L_b(x) + L_1(x)(\overline{\alpha}_l + \overline{\alpha}_r) \frac{H}{3} \right) \right) = \\
&\quad g \frac{H^2}{2} \left(\frac{\partial L_b}{\partial x} + (\overline{\alpha}_l + \overline{\alpha}_r) \frac{H}{3} \frac{\partial L_1}{\partial x} \right) - gH \left(L_b(x) + (\overline{\alpha}_l + \overline{\alpha}_r) \frac{H}{2} L_1(x) \right) \frac{\partial \overline{z}_b}{\partial x} \\
&\quad - S \frac{\partial p^a}{\partial x} - \kappa \overline{u}.
\end{aligned}$$

In the case of a rectangular channel i.e. with $S = L_b H$, $L_1(x) = L_b(x) = 1$ and $\overline{\alpha}_l = \overline{\alpha}_r = 0$, we recover the classical Saint-Venant system.

3.3 Non-hydrostatic Shallow Water models [5, 7]

Much work has been done in the derivation of relatively simple mathematical models for Shallow Water flows and long non-linear water waves. Starting from the original works of Boussinesq [Bou71a, Bou71b, Bou72], let us mention the works of Serre ([Bar04] and references therein) and the Green-Naghdi model [GN76]. Often the modeling of these phenomena starts from the Euler equations ignoring rotational and dissipative effects [BBM72, CBB06a, CBB06b, Nwo93, Per67, Wal99, LB09]. In practice, the use of such models that ignore rotational and friction effects at the bottom may be restrictive. Furthermore, even when well posed the Boussinesq type models often exhibit a lack of conservation energy that is odd since they are derived from the Euler equations [BCS02, BCS04].

In [5] Bristeau and Sainte-Marie have proposed an extended version of the Saint-Venant system where the hydrostatic assumption is dropped. This model is obtained going one step further in the asymptotic development proposed by Gerbeau and Perthame [GP01]. A slight improvement of this model that is not based on any irrotationality assumption allows to exhibit an energy balance, see [7].

The proposed model can be seen as a Shallow Water approximation of the simplified Euler system

$$\frac{\partial u}{\partial x}+\frac{\partial w}{\partial z}=0, \tag{3.34}$$

$$\frac{\partial u}{\partial t}+\frac{\partial u^2}{\partial x}+\frac{\partial uw}{\partial z}+\frac{\partial p}{\partial x}=0, \tag{3.35}$$

$$\frac{\partial w}{\partial t}+\frac{\partial p}{\partial z}=-g, \tag{3.36}$$

with suitable boundary conditions and where, compared to the Euler system (3.4)-(3.6), the convective terms in the z-momentum equation are neglected. In Eq. (3.36), $\frac{\partial w}{\partial t}$ accounts for the non-hydrostatic effects and we have the following proposition

Proposition 2. *The non-hydrostatic Saint-Venant system defined by*

$$\frac{\partial H}{\partial t}+\frac{\partial}{\partial x}\big(H\overline{u}\big)=0, \tag{3.37}$$

$$\frac{\partial}{\partial t}(H\overline{u})+\frac{\partial}{\partial x}(H\overline{u}^2)+\frac{\partial}{\partial x}\left(H\overline{p}\right)=-\,\overline{p}|_b\,\frac{\partial z_b}{\partial x}+p^a\frac{\partial \eta}{\partial x}, \tag{3.38}$$

$$\overline{w}=-(z-z_b)\frac{\partial \overline{u}}{\partial x}+\frac{\partial z_b}{\partial x}\overline{u}, \tag{3.39}$$

$$H\overline{p}=Hp^a+\frac{g}{2}H^2+\frac{\partial}{\partial t}\int_{z_b}^{\eta}\int_{z}^{\eta}\overline{w}\;dz+\frac{\partial H^2}{\partial t}\left(H\frac{\partial \overline{u}}{\partial x}-\frac{\partial z_b}{\partial x}\overline{u}\right), \tag{3.40}$$

$$\overline{p}|_b=p^a+gH+\frac{\partial}{\partial t}\int_{z_b}^{\eta}\overline{w}\;dz+2\frac{\partial H}{\partial t}\left(H\frac{\partial \overline{u}}{\partial x}-\frac{\partial z_b}{\partial x}\overline{u}\right), \tag{3.41}$$

results from an approximation in $\mathcal{O}(\varepsilon^2\delta^2,\varepsilon^3\delta)$ of the Euler equations. Moreover the smooth solutions of (3.37)-(3.41) satisfy the following energy balance

$$\frac{\partial}{\partial t}\left(H\frac{\overline{u}^2}{2}+\int_{z_b}^{\eta}\frac{\hat{w}^2}{2}\;dz+\frac{g}{2}\left(\eta^2-z_b^2\right)+Hp^a\right)$$
$$+\frac{\partial}{\partial x}\left(\overline{u}\left(H\frac{\overline{u}^2}{2}+H\overline{p}+\frac{g}{2}\left(\eta^2-z_b^2\right)\right)\right)=H\frac{\partial p^a}{\partial t}. \tag{3.42}$$

Remark 3.2. *The non-hydrostatic terms we add to the Saint-Venant system come from the vertical acceleration term $\frac{\partial w}{\partial t}$ in the z-momentum equation. Thus they all contain time derivatives and they vanish when steady situations are considered.*

Remark 3.3. *The asymptotic approximation of the system and the proof of the preceding proposition are not detailed here but fully described in [5].*

Remark 3.4. *The starting model (3.34)-(3.36) for the derivation of this non-hydrostatic model can hardly admit an energy balance since the convective terms in the z-momentum equation are missing. Thus complementary terms approximating the neglected ones are introduced for the derivation of (3.37)-(3.42) and allows to ensure the thermo-mechanical compatibility, see [7].*

The analysis of the model is difficult since conservation properties, hyperbolicity,... can hardly been established. In some simplified cases, let us mention some interesting related works.

When the time derivative of the water height is neglected in the non-hydrostatic terms, the preceding model reduces to

$$\begin{aligned}
&\frac{\partial H}{\partial t} + \frac{\partial}{\partial x}\big(H\bar{u}\big) = 0,\\
&\frac{\partial}{\partial t}(H\bar{u}) + \frac{\partial}{\partial x}(H\bar{u}^2) + \frac{\partial}{\partial x}\left(\frac{g}{2}H^2 - \frac{\overline{H}^3}{6}\frac{\partial^2\bar{u}}{\partial x\partial t} + \frac{\overline{H}^2}{2}\frac{\partial^2(z_b\bar{u})}{\partial x\partial t}\right) =\\
&\qquad \frac{\partial z_b}{\partial x}\left(-gH - \frac{\overline{H}^2}{2}\frac{\partial^2\bar{u}}{\partial x\partial t} - \overline{H}\frac{\partial^2(z_b\bar{u})}{\partial x\partial t}\right) - H\frac{\partial p^a}{\partial x} - \frac{\overline{H}}{2}\frac{\partial^3 z_b}{\partial x\partial t^2},
\end{aligned}$$

with $\overline{H} = \eta_0 - z_b$ and $\eta_0 = Cst$, but the energy balance vanishes. This formulation is analogous to the expression obtained by Peregrine [Per67] in the simplified case of a flat steady bottom namely

$$\begin{aligned}
&\frac{\partial H}{\partial t} + \frac{\partial}{\partial x}\big(H\bar{u}\big) = 0,\\
&\frac{\partial}{\partial t}(H\bar{u}) + \frac{\partial}{\partial x}(H\bar{u}^2 + \frac{g}{2}H^2) + \frac{\overline{H}^3}{3}\frac{\partial^3\bar{u}}{\partial x^2\partial t} = 0.
\end{aligned}$$

The form of the x-momentum equation containing the non-hydrostatic terms has common features with the Sobolev equation

$$-\frac{\partial}{\partial x}(a(x)\frac{\partial^2 u}{\partial x\partial t}) + c(x)\frac{\partial u}{\partial t} = -\frac{\partial}{\partial x}(\alpha(x)\frac{\partial u}{\partial x}) + \beta(x)\frac{\partial u}{\partial x},$$

that is an alternative to the Korteweg-de Vries equations and has been studied by several authors [ADT81, BBM72]. Perotto and Saleri [PS00] proposed an *a posteriori* error analysis for the Peregrine formulation with constant bathymetry. Bona *et al.* [BCS02, BCS04] have studied the well-posedness of several high-order generalizations of the Boussinesq equations.

A numerical scheme for the discretization of the extended Saint-Venant system (3.37)-(3.41) will be proposed in paragraph 5.3. Simulations results and comparison with experimental data are given in paragraph 6.2.

3.3.1 Comparison with other existing models

As already mentioned, an important literature is available concerning non-hydrostatic Shallow Water models. Among all the existing models, the formulation (3.37)-(3.41) has four main advantages

- it is a natural extension of the Saint-Venant system since starting from the Navier-Stokes system, it is obtained going one step further in the asymptotic expansion.
- The irrotationality assumption of the fluid is not necessary.
- The model admits an energy balance.
- A slight adaptation of any existing solver for the Saint-Venant system allows to simulate the proposed model, see paragraph 5.3.

It is worth noticing that the formulations obtained by Nwogu [Nwo93], Walkley [Wal99], Saut *et al.* [BCS02] and Soares Frazao *et al.* [SFZ02] are different from the proposed one. The differences lie either in the continuity equation or in the momentum equation. Moreover none of these models admits an energy balance.

An important amont of works on this subject has been done by Lannes and co-authors, see for example [LB09] and references therein. In simplified situations, the models they propose are similar to the Green-Naghdi model [GN76].

3.3.2 More sophisticated non-hydrostatic models

More sophisticated non-hydrostatic models are proposed by the author in [5] where all the convective terms in the z-momentum equation are considered. But their formulations exhibit high order derivatives in space and their numerical treatment is much more complex than what is necessary for the system (3.37)-(3.41). It seems to the author that due to their numerical complexity, the practical interest of these complex models is reduced and the use of depth averaged versions of the full Euler system – as those proposed in [10] – is more interesting.

3.4 Hydrostatic Navier-Stokes system [3]

In this paragraph, we forget the non-hydrostatic effects in Shallow Water flows and we consider flows with large friction coefficients, with significant water depth or with important wind effects i.e. where the horizontal velocity can hardly be approximated – as in Saint-Venant type systems – by a vertically constant velocity [ST96]. To drop this limitation multilayer Saint-Venant models are often used. In these models each layer is described by its own height, its own velocity and is advected by the flow (see [Aud05, AB07, ABD08] and the references therein). This advection property induces that there is no mass exchanges between neighborhing layers and makes a close relation to models for non-miscible fluids (see [BMdL08, CGRGV$^+$04, CMP01] for instance). In [Aud05], introducing a vertical partitioning of the water height, a multilayer strategy was formally derived from the 2d Navier-Stokes system with hydrostatic hypothesis and it is extended to 3d computations in [ABD08].

Here, we derive another and simpler multilayer model where we prescribe the vertical discretization of the layers taking into account the (unknown) total water height. Using a Galerkin approximation in lagrangian formulation, we obtain a system where the only additional unknowns are the layers velocities. This leads to a global continuity equation and allows mass exchanges between layers. This model is interesting since it has the structure of a classical multilayer type Saint-Venant system with mass exchanges but it is also an approximation –without any Shallow Water assumption – of the hydrostatic Navier-Stokes system. The technique we propose is also simpler than methods involving moving meshes and sigma transform [DG09] since we only use here fixed meshes.

We briefly present the main steps of this approximation of the hydrostatic Navier-Stokes system and recall its main properties (hyperbolicity, energy equality,...). The kinetic interpretation of the model and some simulations in various situations are presented in paragraphs 5.4 and 6.3 where we demonstrate the accuracy and robustness of the model in-between the Navier-Stokes and Saint-Venant systems.

3.4.1 Model derivation

We start from the hydrostatic free surface Navier-Stokes equations with constant density $\rho = \rho_0 = Cst$ corresponding to

$$\frac{\partial u}{\partial x} + \frac{\partial w}{\partial z} = 0, \tag{3.43}$$

$$\frac{\partial u}{\partial t} + \frac{\partial u^2}{\partial x} + \frac{\partial uw}{\partial z} + \frac{\partial p}{\partial x} = \frac{\partial \Sigma_{xx}}{\partial x} + \frac{\partial \Sigma_{xz}}{\partial z}, \tag{3.44}$$

$$\frac{\partial p}{\partial z} = -\rho_0 g + \frac{\partial \Sigma_{zx}}{\partial x} + \frac{\partial \Sigma_{zz}}{\partial z}. \tag{3.45}$$

The varying density case will be examined in paragraph 3.5.

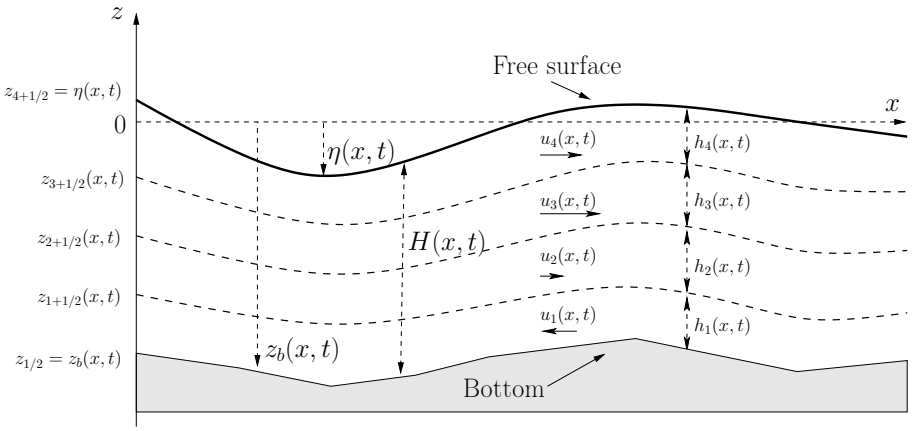

Figure 4: Notations for the multilayer approach.

The interval $[z_b, \eta]$ is divided into N layers $\{L_\alpha\}_{\alpha\in\{1,\dots,N\}}$ of thickness $l_\alpha H(x,t)$ where each layer L_α corresponds to the points satisfying $z \in L_\alpha(x,t) = [z_{\alpha-1/2}, z_{\alpha+1/2}]$ with

$$\begin{cases} z_{\alpha+1/2}(x,t) = z_b(x,t) + \displaystyle\sum_{j=1}^{\alpha} l_j H(x,t), \\ h_\alpha(x,t) = z_{\alpha+1/2}(x,t) - z_{\alpha-1/2}(x,t) = l_\alpha H(x,t), \end{cases} \tag{3.46}$$

with $l_j > 0, \quad \sum_{j=1}^{N} l_j = 1$, see Fig. 4. Such a partitioning can also be found in [RHI02] but leading to a different model.

Now let us consider the space $\mathbb{P}_{0,H}^{N,t}$ of piecewise constant functions defined by

$$\mathbb{P}_{0,H}^{N,t} = \left\{ \mathbb{I}_{z\in L_\alpha(x,t)}(z), \quad \alpha \in \{1,\dots,N\} \right\}, \tag{3.47}$$

where $\mathbb{I}_{z\in L_\alpha(x,t)}(z)$ is the characteristic function of the interval $L_\alpha(x,t)$. Using this formalism, the projection of u and w onto $\mathbb{P}_{0,H}^{N,t}$ is a piecewise constant function defined by

$$X^N(x,z,\{z_\alpha\},t) = \sum_{\alpha=1}^{N} 1_{[z_{\alpha-1/2},z_{\alpha+1/2}]}(z) X_\alpha(x,t), \tag{3.48}$$

for $X \in (u,w)$. We have the following result where for the sake of simplicity, we omit the viscous and friction terms, we refer to [3] for the treatment of these terms.

Proposition 3. *The weak formulation of Eqs. (3.43)-(3.45) on $\mathbb{P}_{0,H}^{N,t}$ leads to a system of the form*

$$\sum_{\alpha=1}^{N} \frac{\partial h_\alpha}{\partial t} + \sum_{\alpha=1}^{N} \frac{\partial h_\alpha u_\alpha}{\partial x} = 0, \tag{3.49}$$

$$\frac{\partial h_\alpha u_\alpha}{\partial t} + \frac{\partial}{\partial x}\left(h_\alpha u_\alpha^2 + h_\alpha p_\alpha\right) = u_{\alpha+1/2} G_{\alpha+1/2} - u_{\alpha-1/2} G_{\alpha-1/2} + \frac{\partial z_{\alpha+1/2}}{\partial x} p_{\alpha+1/2} - \frac{\partial z_{\alpha-1/2}}{\partial x} p_{\alpha-1/2}, \tag{3.50}$$

for $\alpha \in [1,\dots,N]$. The definitions of $p_\alpha, p_{\alpha+1/2}, u_{\alpha+1/2}, G_{\alpha+1/2}$ are given in the following. The system (3.49)-(3.50) results from a formal asymptotic approximation in $\mathcal{O}(\varepsilon^2\delta)$ (see (3.16),(3.17)) coupled with a vertical discretization of the Navier-Stokes equations (3.43)-(3.45) with hydrostatic pressure.

Without entering in details, we give hereafter a proof of this proposition since it allows to give the expression of the source terms in the right hand side of Eq. (3.50).

Proof of Prop. 3. Using the Leibniz rule, the Galerkin approximation of Eq. (3.43) on $\mathbb{P}_{0,H}^{N,t}$ gives the set of equations

$$\frac{\partial h_\alpha}{\partial t} + \frac{\partial}{\partial x}\left(h_\alpha u_\alpha\right) = G_{\alpha+1/2} - G_{\alpha-1/2}, \qquad \alpha \in [1,\dots,N] \tag{3.51}$$

with

$$G_{\alpha+1/2} = \left(\frac{\partial z_{\alpha+1/2}}{\partial t} + u_{\alpha+1/2}\frac{\partial z_{\alpha+1/2}}{\partial x} - w_{\alpha+1/2}\right), \tag{3.52}$$

$$G_{1/2} = G_{N+1/2} = 0. \tag{3.53}$$

The relations (3.52) give the mass flux leaving/entering each layer α whereas the relations (3.53) just express that the bottom and the top are interfaces without loss/supply of mass (see the boundary conditions (3.11),(3.14)).

Let us notice that the layer mass equation (3.51) can not be used per se since the layer height h_α is not an independent variable but is defined as a part of the whole water height $H(t,x)$, see relation (3.46). But using the first condition of (3.53), one can compute $G_{\alpha+1/2}$ just adding up the equations (3.51)

$$G_{\alpha+1/2} = \sum_{j=1}^{\alpha} \frac{\partial h_j}{\partial t} + \sum_{j=1}^{\alpha} \frac{\partial h_j u_j}{\partial x}, \quad , \alpha = 1,\dots,N. \tag{3.54}$$

Then the equation (3.54) written for $\alpha = N$ and the second condition of (3.53) give the equation (3.49). The need to consider only the global mass equation (3.49) is related to the fact that we

consider a single fluid possibly with varying density and not several layers of non-miscible fluids as in some other multilayer models [Ovs79, Vre79, CMP01, BZ10]. Then it is physically relevant to consider a single mass equation that authorizes in some sense a circulation of the fluid between the layers introduced in the discretization process. In the following, we use the formula (3.54) rather than (3.52), and thus we have not to define $w_{\alpha+1/2}$.

Similarly, the $\mathbb{P}^{N,t}_{0,H}$-approximation of the x-momentum equation (3.44) leads to (3.50). Indeed from (3.45) we can compute

$$p(x,z,t) = \int_z^\eta g \; dz,$$

so we have for $z \in L_\alpha$

$$p(x,z,t) = g\left(\sum_{j=\alpha+1}^{N} h_j + (z_{\alpha+1/2} - z)\right).$$

Using the notations

$$p_\alpha = \frac{1}{h_\alpha}\int_{z_{\alpha-1/2}}^{z_{\alpha+1/2}} p(x,z,t)dz, \qquad p_{\alpha+1/2} = p(x, z_{\alpha+1/2}, t), \tag{3.55}$$

we have

$$p_\alpha = g\left(\frac{h_\alpha}{2} + \sum_{j=\alpha+1}^{N} h_j\right), \qquad p_{\alpha+1/2} = g\sum_{j=\alpha+1}^{N} h_j \tag{3.56}$$

and applying the Leibniz rule to the pressure term of equation (3.2), we can write

$$\int_{z_{\alpha-1/2}}^{z_{\alpha+1/2}} \frac{\partial p}{\partial x}dz \;\; = \frac{\partial h_\alpha p_\alpha}{\partial x} - \frac{\partial z_{\alpha+1/2}}{\partial x}p_{\alpha+1/2} + \frac{\partial z_{\alpha-1/2}}{\partial x}p_{\alpha-1/2}. \tag{3.57}$$

To complete the definition of equation (3.50), the quantities $u_{\alpha+1/2}$, $\alpha = 1, \ldots, N-1$ are defined using an upwinding

$$u_{\alpha+1/2} = \begin{cases} u_\alpha & \text{if } G_{\alpha+1/2} \geq 0 \\ u_{\alpha+1} & \text{if } G_{\alpha+1/2} < 0. \end{cases} \quad \square \tag{3.58}$$

3.4.2 Energy

It is straightforward to obtain an energy equality for the model depicted in Prop. 3. Considering smooth solutions and multiplying the x-momentum equation (3.44) by u and performing the Galerkin approximation on $\mathbb{P}^{N,t}_{0,H}$.

For the layer α we have

$$\begin{aligned}\frac{\partial}{\partial t}E^N_{sv,\alpha} + \frac{\partial}{\partial x}\left(u_\alpha\left(E^N_{sv,\alpha} + \frac{g}{2}h_\alpha H\right)\right) = \\ + \left(\frac{u^2_{\alpha+1/2}}{2} + p_{\alpha+1/2} + gz_{\alpha+1/2}\right)G_{\alpha+1/2} \\ - \left(\frac{u^2_{\alpha-1/2}}{2} + p_{\alpha-1/2} + gz_{\alpha-1/2}\right)G_{\alpha-1/2} \\ - p_{\alpha+1/2}\frac{\partial z_{\alpha+1/2}}{\partial t} + p_{\alpha-1/2}\frac{\partial z_{\alpha-1/2}}{\partial t},\end{aligned} \tag{3.59}$$

with $E^N_{sv,\alpha} = \frac{h_\alpha u_\alpha^2}{2} + \frac{g(z^2_{\alpha+1/2} - z^2_{\alpha-1/2})}{2}$. Adding the preceding relations for $\alpha = 1, \ldots, N$, we obtain the global balance

$$\frac{\partial}{\partial t}\left(\sum_{\alpha=1}^{N} E^N_{sv,\alpha}\right) + \frac{\partial}{\partial x}\left(\sum_{\alpha=1}^{N} u_\alpha \left(E^N_{sv,\alpha} + \frac{g}{2} h_\alpha H\right)\right) = 0.$$

3.4.3 Pressure source terms

As often when considering hyperbolic type problems, the treatment of the source terms is subtle. We have written in (3.57) the inviscid part of the hydrostatic pressure terms of the layer α as the combination of a conservative part and two source terms, one for each interface.

It is obvious that (3.57) can be written under the simplified form

$$\int_{z_{\alpha-1/2}}^{z_{\alpha+1/2}} \frac{\partial p}{\partial x} dz \quad = g l_\alpha H \frac{\partial \eta}{\partial x} = \frac{g}{2}\frac{\partial h_\alpha H}{\partial x} + g h_\alpha \frac{\partial z_b}{\partial x}. \tag{3.60}$$

The two writtings (3.57) and (3.60) are obviously equivalent but at the discrete level they differ since in (3.57) the conservative part of the pressure term nonlinearly depends on the elevation. Indeed for equally spaced layers i.e. $l_\alpha = 1/N$, we have

$$h_\alpha p_\alpha = \frac{g}{2}\frac{N - \alpha + 1}{N^2} H^2,$$

that is very different from the corresponding expression in (3.60).

At the discrete level, we have singled out the formulation (3.57) that is more natural. For the discretization of the pressure source terms in (3.57), we have proposed an extension of the hydrostatic reconstruction technique proposed by Audusse *et al.* [ABB$^+$04].

3.4.4 Comparison with other multilayer systems

To illustrate the formulation of the model, we compare it with the system proposed in [Aud05] in the simple case of a two-layer formulation. Neglecting the viscosity and friction, the formulation obtained by Audusse [Aud05] corresponds to (3.51),(3.50) with $G_{\alpha+1/2} \equiv 0$, i.e.

$$\frac{\partial h_1}{\partial t} + \frac{\partial h_1 u_1}{\partial x} = 0, \qquad \frac{\partial h_2}{\partial t} + \frac{\partial h_2 u_2}{\partial x} = 0, \tag{3.61}$$

$$\frac{\partial h_1 u_1}{\partial t} + \frac{\partial h_1 u_1^2}{\partial x} + g h_1 \frac{\partial (h_1 + h_2)}{\partial x} = -g h_1 \frac{\partial z_b}{\partial x}, \tag{3.62}$$

$$\frac{\partial h_2 u_2}{\partial t} + \frac{\partial h_2 u_2^2}{\partial x} + g h_2 \frac{\partial (h_1 + h_2)}{\partial x} = -g h_2 \frac{\partial z_b}{\partial x}, \tag{3.63}$$

with $h_1 + h_2 = H$. The preceding formulation corresponds to a superposition of two single layer Saint-Venant systems (see also [BMdL08, CGRGV$^+$04, CMP01] where a very similar model is considered in a bi-fluid framework).

With our approach (3.49),(3.50), the two-layer formulation reads

$$\frac{\partial H}{\partial t} + \frac{\partial h_1 u_1}{\partial x} + \frac{\partial h_2 u_2}{\partial x} = 0, \tag{3.64}$$

$$\frac{\partial h_1 u_1}{\partial t} + \frac{\partial h_1 u_1^2}{\partial x} + \frac{g}{2}\frac{\partial H h_1}{\partial x} = -g h_1 \frac{\partial z_b}{\partial x} + u_{3/2}\left(l\frac{\partial H}{\partial t} + l\frac{\partial H u_1}{\partial x}\right), \tag{3.65}$$

$$\frac{\partial h_2 u_2}{\partial t} + \frac{\partial h_2 u_2^2}{\partial x} + \frac{g}{2}\frac{\partial H h_2}{\partial x} = -g h_2 \frac{\partial z_b}{\partial x} - u_{3/2}\left(l\frac{\partial H}{\partial t} + l\frac{\partial H u_1}{\partial x}\right), \tag{3.66}$$

$$\text{where } \; h_1 = lH, \quad h_2 = (1-l)H, \tag{3.67}$$

with $l \in (0,1)$ prescribed. The velocity at the interface, denoted $u_{3/2}$, is calculated using upwinding, following the sign of the mass exchange between the layers. It is important to notice that, in the new formulation (3.64)-(3.67), we obtain directly a left hand side term written in conservative form with the topography and the mass exchange as source terms whereas the pressure term of (3.61)-(3.63) has to be modified [Aud05] to get a conservative form. Moreover we prove in paragraph 3.4.5 that the system (3.64)-(3.67) is *often* hyperbolic, which is not the case for system (3.61)-(3.63).

The difference between (3.64)-(3.67) and (3.61)-(3.63) mainly comes from the physical definition of the layers. Audusse introduces a physical discretization where each layer has its own continuity equation. These N continuity equations mean the layers are isolated each other, this situation corresponds to the case of N non miscible fluids. In the formulation (3.64)-(3.67), the discretization corresponds to a semidiscretization in the vertical direction– of P_0 finite elements type – of the velocity u. In this case, the definition of the layers does not correspond to a physical partition of the flow but is related to the quality of the desired approximation over u. Thus we have only one continuity equation meaning the fluid can circulate from one layer to another.

3.4.5 Hyperbolicity

Let us first say some words about the two-layers case i.e. $N = 2$. It is proved in [3] that the two-layers version of the multilayer Saint-Venant system (3.49)-(3.50) is strictly hyperbolic when the total water height is strictly positive. When $N = 2$, the non-miscible multilayer system proposed by Audusse *et al.* [Aud05] was proved to be non-hyperbolic.

In the general case, the system (3.49)-(3.50) approximates the hydrostatic free surface Euler system which in general is not an hyperbolic system. Thus this is not surprising that numerically, the quasilinear form of (3.49)-(3.50) can exhibit complex eigenvalues.

We have performed various numerical evaluations of the eigenelements of the jacobian of (3.49)-(3.50) with numerous choices of the variables H, u_α, $u_{\alpha+1/2}$ and l_α. When the chosen values correspond to physical values for geophysical flows, these tests have always shown that the matrix is diagonalizable on $\mathbb{R}$. But when considering shear flows with very large velocities e.g. $|u_{i_0}| \gg 1$, $|u_{j_0}| \gg 1$ and $u_{i_0} u_{j_0} < 0$ for some $i_0 \neq j_0$, complex eigenvalues can appear corresponding to vibrations of the interfaces $z_{\alpha+1/2}$, see [Aud05, CGRGV$^+$04].

In the simple case where all the layers have the same velocity u, the barotropic eigenvalues $u + \sqrt{gH}$ and $u - \sqrt{gH}$ are simple and the baroclinic eigenvalue u has a multiplicity of $N-1$ but the matrix remains diagonalizable on $\mathbb{R}$.

Considering flows satisfying $u_\alpha \ll \sqrt{gH}$, it is observed numerically that the eigenvalues of the system belongs to the interval

$$\left[\min_\alpha\{|u_\alpha|\} - \sqrt{gH}, \max_\alpha\{|u_\alpha|\} + \sqrt{gH}\right].$$

The numerical discretization of the proposed model will be discussed later but we point out that the kinetic scheme instead of using discrete eigenvalues of the jacobian matrix, uses a continuum of eigenvalues and is able to deal with situations where some of the discrete eigenvalues are complex.

3.4.6 Vertical velocity

In Prop. 3, the vertical velocity w no more appears, but performing the Galerkin approximation of the divergence free condition multiplied by z leads to

$$\frac{\partial}{\partial t}\left(\frac{z_{\alpha+1/2}^2 - z_{\alpha-1/2}^2}{2}\right) + \frac{\partial}{\partial x}\left(\frac{z_{\alpha+1/2}^2 - z_{\alpha-1/2}^2}{2} u_\alpha\right) = h_\alpha w_\alpha + z_{\alpha+1/2} G_{\alpha+1/2} - z_{\alpha-1/2} G_{\alpha-1/2}, \tag{3.68}$$

where the w_α, $\alpha = 1, \ldots, N$ are the components of the Galerkin approximation of w on $\mathbb{P}_{0,H}^{N,t}$, see (3.48). And since all the quantities except w_α appearing in Eq. (3.68) are already defined by (3.49),(3.50), relation (3.68) allows to recover the value of w_α. Note that we use relation (3.68) rather than the divergence free condition for stability purpose. We refer the reader to [10] for more details.

3.5 Hydrostatic Navier-Stokes system with varying density [2]

In this paragraph, we extend the model presented in the preceding paragraph to the case of density stratified flows. The density stratifications due to e.g. temperature and salinity have often important effects in geophysical flows but are still computationally expensive because they rely on the full Navier-Stokes system. We are mainly interested in applications to geophysical flows such as lakes and estuarine waters that typically exhibit a significant density stratification. In these water bodies small variations of the density may involve large modifications in the hydrodynamical behavior. The modeling and simulation of these flows require stable, accurate, conservative schemes able to sharply resolve density gradients.

We present in this paragraph an enriched version of the multilayer Saint-Venant system (3.49)-(3.50),(3.59) suitable for free surface density-stratified flows over variable topography. Instead of starting from the hydrostatic Euler system (3.43)-(3.45) with constant density, we consider the set of equations

$$\frac{\partial \rho}{\partial t} + \frac{\partial \rho u}{\partial x} + \frac{\partial \rho w}{\partial z} = 0, \tag{3.69}$$

$$\frac{\partial \rho u}{\partial t} + \frac{\partial \rho u^2}{\partial x} + \frac{\partial \rho u w}{\partial z} + \frac{\partial p}{\partial x} = 0, \tag{3.70}$$

$$\frac{\partial p}{\partial z} = -\rho g, \tag{3.71}$$

$$\frac{\partial \rho T}{\partial t} + \frac{\partial \rho u T}{\partial x} + \frac{\partial \rho w T}{\partial z} = 0, \tag{3.72}$$

with $\rho = \rho(T)$ a given function. Once again, the viscous and friction effects are neglected in this presentation but considered in the associated publication [2].

We still adopt the discretization defined by (3.46) and (3.47) and the notations including the discretized tracer are depicted in Fig. 5. Except for the tracer equation, the model derivation is similar to what has been presented in paragraph 3.4.1 so we give without any proof the model formulation

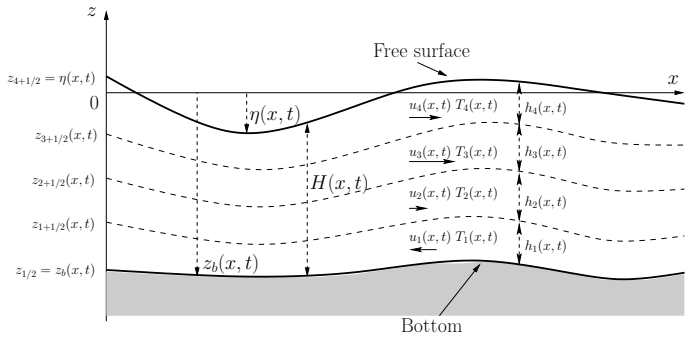

Figure 5: Notations for the multilayer approach with varying density.

Proposition 4. *The weak formulation of Eqs. (3.69)-(3.72) on $\mathbb{P}^{N,t}_{0,H}$ leads to a system of the form*

$$\sum_{\alpha=1}^{N} \frac{\partial \rho_\alpha h_\alpha}{\partial t} + \sum_{\alpha=1}^{N} \frac{\partial \rho_\alpha h_\alpha u_\alpha}{\partial x} = 0. \tag{3.73}$$

$$\frac{\partial \rho_\alpha h_\alpha u_\alpha}{\partial t} + \frac{\partial}{\partial x}\left(\rho_\alpha h_\alpha u_\alpha^2 + h_\alpha p_\alpha\right) = u_{\alpha+1/2} G_{\alpha+1/2} - u_{\alpha-1/2} G_{\alpha-1/2} + \frac{\partial z_{\alpha+1/2}}{\partial x} p_{\alpha+1/2} - \frac{\partial z_{\alpha-1/2}}{\partial x} p_{\alpha-1/2}, \tag{3.74}$$

$$\frac{\partial \rho_\alpha h_\alpha T_\alpha}{\partial t} + \frac{\partial}{\partial x}\left(\rho_\alpha h_\alpha T_\alpha u_\alpha\right) = T_{\alpha+1/2} G_{\alpha+1/2} - T_{\alpha-1/2} G_{\alpha-1/2}, \tag{3.75}$$

$$\alpha \in [1, \ldots, N].$$

The quantities $p_\alpha, p_{\alpha+1/2}, u_{\alpha+1/2}, T_{\alpha+1/2}, G_{\alpha+1/2}$ are defined by

$$\begin{aligned}
p_\alpha &= g\left(\frac{\rho_\alpha h_\alpha}{2} + \sum_{j=\alpha+1}^{N} \rho_j h_j\right), \\
p_{\alpha+1/2} &= g \sum_{j=\alpha+1}^{N} \rho_j h_j, \\
G_{\alpha+1/2} &= \sum_{j=1}^{\alpha} \frac{\partial \rho_j h_j}{\partial t} + \sum_{j=1}^{\alpha} \frac{\partial \rho_j h_j u_j}{\partial x}, \\
v_{\alpha+1/2} &= \begin{cases} v_\alpha & \text{if } G_{\alpha+1/2} \geq 0 \\ v_{\alpha+1} & \text{if } G_{\alpha+1/2} < 0 \end{cases} \quad \text{for } v = u, T.
\end{aligned} \tag{3.76}$$

As in paragraph 3.4.2, we have for the smooth solutions of the system (3.73)-(3.75) an energy equality having the form

$$\frac{\partial}{\partial t}\left(\sum_{\alpha=1}^{N} E^N_{\rho,\alpha}\right) + \frac{\partial}{\partial x}\left(\sum_{\alpha=1}^{N} u_\alpha \left(E^N_{\rho,\alpha} + \frac{g}{2}\rho_\alpha h_\alpha H\right)\right) = 0, \tag{3.77}$$

with $E^N_{\rho,\alpha} = \frac{\rho_\alpha h_\alpha u_\alpha^2}{2} + \frac{g\rho_\alpha (z^2_{\alpha+1/2} - z^2_{\alpha-1/2})}{2}$.

3.5.1 Vertical velocity

The components of the vertical velocity w_α are not variables of the problem but quantities calculated *a posteriori* for post-processing purpose.

As in paragraph 3.4.6 the components of Galerkin projection of the vertical velocity w onto $\mathbb{P}_{0,H}^{N,t}$ defined by Eq. (3.47) satisfy

$$\frac{\partial}{\partial t}\left(\rho_\alpha \frac{z_{\alpha+1/2}^2 - z_{\alpha-1/2}^2}{2}\right) + \frac{\partial}{\partial x}\left(\rho_\alpha \frac{z_{\alpha+1/2}^2 - z_{\alpha-1/2}^2}{2} u_\alpha\right) = \rho_\alpha h_\alpha w_\alpha + z_{\alpha+1/2} G_{\alpha+1/2} - z_{\alpha-1/2} G_{\alpha-1/2}. \tag{3.78}$$

This relation is used to recover the components w_α of the vertical velocity w.

3.5.2 The boussinesq assumption

In geophysical water flows the density variations are often small. Assuming homogeneous chemical composition, and identifying here T with the temperature, the state equation of water can be expressed by the classical relation

$$\rho(T) = \rho_0 \left(1 - \alpha (T - T_0)^2\right),$$

with $T_0 = 4\,^o\mathrm{C}$, $\alpha = 6.63\,10^{-6}\,^o\mathrm{C}^2$ (volume coefficient of thermal expansion) and $\rho_0 = 10^3\,\mathrm{kg.m}^{-3}$. For example, the relative density variation corresponding to two temperatures with $T_1 = 25\,^o\mathrm{C}$ and $T_2 = 10\,^o\mathrm{C}$ is

$$\frac{\rho(25) - \rho(10)}{\rho(10)} \approx 0.0026\,.$$

Such small variations allow to justify the Boussinesq assumption which consists in considering the density variations only in the gravitational force. This leads to the following incompressible hydrostatic Navier-Stokes system

$$\frac{\partial u}{\partial x} + \frac{\partial w}{\partial z} = 0, \tag{3.79}$$

$$\frac{\partial u}{\partial t} + \frac{\partial u^2}{\partial x} + \frac{\partial uw}{\partial z} + \frac{1}{\rho_0}\frac{\partial p}{\partial x} = \frac{1}{\rho_0}\left(\frac{\partial \Sigma_{xx}}{\partial x} + \frac{\partial \Sigma_{xz}}{\partial z}\right), \tag{3.80}$$

$$\frac{\partial p}{\partial z} = -\rho g + \frac{\partial \Sigma_{zx}}{\partial x} + \frac{\partial \Sigma_{zz}}{\partial z}, \tag{3.81}$$

$$\frac{\partial T}{\partial t} + \frac{\partial uT}{\partial x} + \frac{\partial wT}{\partial z} = \nu_T \frac{\partial^2 T}{\partial x^2} + \nu_T \frac{\partial^2 T}{\partial z^2} \tag{3.82}$$

with $\nu_T = \frac{\mu_T}{\rho_0}$. Notice that the divergence free condition (3.79) means a conservation of volume rather than a conservation of mass as in Eqs. (3.69).

In the model we propose, this assumption is not made and its validity will be emphasized in the numerical simulations, see paragraph 6.4. Notice that this assumption significantly simplifies the numerical cost of the simulations since it leads, at the discrete level, to an identity mass matrix for the system i.e. without any nonlinear coupling between the state variables, see paragraph 5.4.

3.6 The Euler system [10]

In this paragraph, we couple the improvements presented in the previous paragraphs, namely all the non-hydrostatic pressure terms are considered and a vertical distribution of the velocity fields is also introduced. The two models we present now are approximations of the Euler system (3.4)-(3.6).

3.6.1 Shallow Water approximation of the Euler system

The first model can be seen as another extension of the non-hydrostatic Saint-Venant system but still under the Shallow Water assumption.

When non-hydrostatic terms are integrated in Shallow Water type models, the strategy often consists in a vertical integration of the z-momentum equation in order to have the expression of the fluid pressure p. Then, this expression is replaced in the x-momentun equation. This corresponds to what has been done in model (3.37)-(3.41), see especially Eqs. (3.38) and (3.40). This is the most natural approach but it leads to formulations where the contribution of the non-hydrostatic terms (acceleration, convection,...) is not fully meaningful. Then the analysis and the discretization of such formulations are often difficult.

We propose here another strategy consisting in an integration of the Euler equations (3.4)-(3.6) with $\rho = \rho_0 = 1$ against z^i for $i = 0, 1$, i.e.

$$\int_{z_b}^{\eta} z^i \left(\frac{\partial u}{\partial x} + \frac{\partial w}{\partial z} \right) dz = 0, \tag{3.83}$$

$$\int_{z_b}^{\eta} z^i \left(\frac{\partial u}{\partial t} + \frac{\partial u^2}{\partial x} + \frac{\partial uw}{\partial z} + \frac{\partial p}{\partial x} \right) dz = 0, \tag{3.84}$$

$$\int_{z_b}^{\eta} z^i \left(\frac{\partial w}{\partial t} + \frac{\partial uw}{\partial x} + \frac{\partial w^2}{\partial z} + \frac{\partial p}{\partial z} + g \right) dz = 0. \tag{3.85}$$

The vertical average $\overline{A}$ of a given quantity A is defined by

$$\overline{A} = \frac{1}{H} \int_{z_b}^{\eta} A \, dz. \tag{3.86}$$

We also suppose in each point of the fluid region – including at the bottom – we have

$$p - p^a \geq 0. \tag{3.87}$$

The analysis below and especially the kinetic interpretation of the model given below (see paragraph 4.4.4) are restricted to this situation. Notice that in the case of the hydrostatic Euler equations since we have

$$p - p^a = g(\eta - z),$$

this assumption reduces to the non-negativity of the water height H.

Remark 3.5. *In the model presented in paragraph 3.3, only the unsteady non-hydrostatic terms are considered, here they are all taken into account.*

We have the following proposition

Proposition 5. *The averaged Euler system defined by*

$$\frac{\partial H}{\partial t} + \frac{\partial}{\partial x}\big(H\overline{u}\big) = 0, \tag{3.88}$$

$$\frac{\partial}{\partial t}(H\overline{u}) + \frac{\partial}{\partial x}(H\overline{u}^2) + \frac{\partial}{\partial x}\left(H\overline{p}\right) = -p_b\frac{\partial z_b}{\partial x} + p^a\frac{\partial \eta}{\partial x}, \tag{3.89}$$

$$\frac{\partial}{\partial t}(H\overline{w}) + \frac{\partial}{\partial x}(H\overline{w}\,\overline{u}) = p_b - p^a - gH, \tag{3.90}$$

$$\frac{\partial}{\partial t}\left(\frac{\eta^2 - z_b^2}{2}\right) + \frac{\partial}{\partial x}\left(\frac{\eta^2 - z_b^2}{2}\overline{u}\right) - H\overline{w} = 0, \tag{3.91}$$

$$\begin{aligned}\frac{\partial}{\partial t}\left(\frac{\eta^2 - z_b^2}{2}\overline{u}\right) + \frac{\partial}{\partial x}\left(\frac{\eta^2 - z_b^2}{2}\overline{u}^2\right) + \frac{\partial}{\partial x}\int_{z_b}^{\eta} zp\ dz - H\overline{w}\,\overline{u} = \\ \frac{1}{2}\frac{\partial \eta^2}{\partial x}p^a - \frac{1}{2}\frac{\partial z_b^2}{\partial x}p_b,\end{aligned} \tag{3.92}$$

$$\begin{aligned}\frac{\partial}{\partial t}\int_{z_b}^{\eta} z\hat{w}\ dz + \frac{\partial}{\partial x}\overline{u}\int_{z_b}^{\eta} z\hat{w}\ dz - \int_{z_b}^{\eta}\hat{w}^2\ dz - H\overline{p} = \\ -\eta p^a + z_b p_b - g\frac{\eta^2 - z_b^2}{2},\end{aligned} \tag{3.93}$$

where $\overline{u}$, $\overline{w}$ and $\overline{p}$ are defined by (3.86), results from an approximation in $\mathcal{O}(\varepsilon^2)$ of the Euler equations (3.4)-(3.6). Moreover the smooth solutions of (3.88)-(3.93) satisfy the energy balance

$$\frac{\partial E}{\partial t} + \frac{\partial}{\partial x}\left(\overline{u}\big(E + H\overline{p}\big)\right) = H\frac{\partial p^a}{\partial t}, \tag{3.94}$$

with

$$E = \frac{H\overline{u}^2}{2} + \int_{z_b}^{\eta}\frac{\hat{w}^2}{2}\ dz + \frac{gH(\eta + z_b)}{2} + Hp^a.$$

In the preceding formulation, $\hat{w}$ is the vertical velocity associated to the mean velocity $\overline{u}$, it satisfies a sort of *mean* divergence free condition

$$\frac{\partial \overline{u}}{\partial x} + \frac{\partial \hat{w}}{\partial z} = 0,$$

that is equivalent to

$$\hat{w} = -(z - z_b)\frac{\partial \overline{u}}{\partial x} + \frac{\partial z_b}{\partial x}\overline{u}. \tag{3.95}$$

A simplified case Let consider $p^a = 0$ and $\frac{\partial z_b}{\partial x} = 0$. It is interesting to mention that the set of equations (3.88)-(3.94) can be written under the noteworthy form of a transport-reaction type system

$$\frac{\partial X}{\partial t} + \frac{\partial}{\partial x}F(X) - R(X) = 0,$$

with

$$X = \begin{pmatrix} H \\ H\overline{u} \\ H\overline{w} \\ \frac{\eta^2 - z_b^2}{2} \\ \frac{\eta^2 - z_b^2}{2}\overline{u} \\ \overline{z\hat{w}} \\ E \end{pmatrix}, \qquad R(X) = \begin{pmatrix} 0 \\ 0 \\ p_b - gH \\ H\overline{w} \\ H\overline{w}\,\overline{u} \\ H(\overline{\hat{w}^2} + \overline{p - gz}) - z_b p_b \\ 0 \end{pmatrix},$$

$$F(X) = \begin{pmatrix} H\overline{u} \\ H\overline{u} + H\overline{p} \\ H\overline{w}\,\overline{u} \\ \frac{\eta^2 - z_b^2}{2}\overline{u} \\ \frac{\eta^2 - z_b^2}{2}\overline{u}^2 + H\overline{zp} \\ H\overline{u}\,\overline{z\hat{w}} \\ \overline{u}(E + H\overline{p}) \end{pmatrix}.$$

Remarks In the system (3.88)-(3.93), the eight unknowns are

$$H, \overline{u}, \overline{w}, \overline{p}, p_b, \int_{z_b}^{\eta} \hat{w}^2 dz, \int_{z_b}^{\eta} z\hat{w} dz, \int_{z_b}^{\eta} zp dz,$$

whereas we only have six equations. But due to the shallow water approximation (3.20), the vertical velocity $\hat{w}$ is linear in z (see Eq. (3.95)) and this induces several relations between these eight unknowns. Namely, we have

$$\int_{z_b}^{\eta} z\hat{w}\ dz = \left(\frac{2}{3}H + z_b\right) H\overline{w} - \frac{1}{6}\frac{\partial z_b}{\partial x} H\overline{u}, \tag{3.96}$$

$$\int_{z_b}^{\eta} \hat{w}^2\ dz = H\overline{w}^2 + \frac{H^3}{12}\left(\frac{\partial \overline{u}}{\partial x}\right)^2 = H\overline{w}^2 + \frac{H}{3}\left(\overline{w} - \frac{\partial z_b}{\partial x}\overline{u}\right)^2. \tag{3.97}$$

For the pressure term $\int_{z_b}^{\eta} zp\ dz$, we use the following arguments: due to relation (3.95), the z-momentum equation involving $\frac{\partial p}{\partial z}$ is linear in z with $p_s = p^a$. This means we can write p under the form

$$p = a_1(z - z_b)(z - z_b - H) + \frac{z - z_b}{H}(p^a - p_b) + p_p,$$

leading to the formula

$$\int_{z_b}^{\eta} zp\ dz = \left(z_b + \frac{1}{2}H\right) H\overline{p} - \frac{1}{12}H^2\left(p_b + p^a\right). \tag{3.98}$$

The relations (3.96),(3.98) mean that in fact we only have five independant variables with six equations. Fortunately up to $\mathcal{O}(\varepsilon^2)$ terms, the two equations (3.89) and (3.92) are identical. Indeed, written in a non conservative form they read

$$\frac{\partial \overline{u}}{\partial t} + \overline{u}\frac{\partial \overline{u}}{\partial x} = -\frac{1}{H}\frac{\partial}{\partial x}\left(H\overline{p}\right) - \frac{1}{H}p_b\frac{\partial z_b}{\partial x} + \frac{p^a}{H}\frac{\partial \eta}{\partial x},$$
$$\frac{\partial \overline{u}}{\partial t} + \overline{u}\frac{\partial \overline{u}}{\partial x} = -\frac{2}{\eta^2 - z_b^2}\frac{\partial}{\partial x}\int_{z_b}^{\eta} zp\ dz + \frac{1}{\eta^2 - z_b^2}\frac{\partial \eta^2}{\partial x}p^a - \frac{1}{\eta^2 - z_b^2}\frac{\partial z_b^2}{\partial x}p_b,$$

and the right hand side of the two previous equations are equal up to $\mathcal{O}(\varepsilon^2)$ terms since from (3.85) we have

$$H\overline{p} = \frac{g}{2}H^2 + \mathcal{O}(\varepsilon^2), \quad \text{and} \quad p_b = gH + \mathcal{O}(\varepsilon^2).$$

3.6.2 General formulation of the free surface Euler system

Now we drop the Shallow Water assumption $\varepsilon \ll 1$ and we decompose the water height H into N layers with N possibly large. This means we have shallow layers instead of a global Shallow Water assumption. Using the notations defined in paragraph 3.4.1 and depicted over Fig. 4, the variables are discretized using (3.48) that is

$$X^N(x,z,\{z_\alpha\},t) = \sum_{\alpha=1}^{N} 1_{[z_{\alpha-1/2},z_{\alpha+1/2}]}(z) X_\alpha(x,t),$$

for (u,w,p), and we derive a system approximating the Euler system up to $\mathcal{O}(1/N)$ terms.

We suppose there exist piecewise constant – in z – approximate solutions (u^N,w^N,p^N) given by (3.48) and satisfying the free surface Euler equations. We are first interested in the formal limit as $1/N$ vanishes in the quantities

$$\|u^N - u\|, \quad \|w^N - w\| \quad \text{and} \quad \|p^N - p\|,$$

where (u,w,p) are solutions of (3.1)-(3.3) and $\|.\|$ is a convenient norm. We suppose u is enough smooth and we have for each $\alpha \in \{0,\dots,N\}$

$$l_\alpha = \mathcal{O}\left(\frac{1}{N}\right),$$

the form of the vertical expansion (3.48) ensures

$$\left\|u^N - u\right\| = \mathcal{O}\left(\frac{1}{N^2}\right). \tag{3.99}$$

Likewise we obtain

$$\left\|(u^N)^2 - u^2\right\| = \mathcal{O}\left(\frac{1}{N^2}\right). \tag{3.100}$$

Concerning the vertical velocity we have for $z \in [z_{\alpha-1/2}, z_{\alpha+1/2}]$

$$\left\|w^N - w\right\| = \left\|\frac{\partial}{\partial x}\int_{z_b}^{z}(u^N - u)\ dz\right\| = \left\|\frac{\partial}{\partial x}\int_{z_{\alpha-1/2}}^{z}(u_\alpha - u)\ dz\right\| = \mathcal{O}\left(\frac{1}{N^2}\right). \tag{3.101}$$

In the Euler system, integrating the momentum equation along z gives

$$p = p^a + g(\eta - z) + \frac{\partial}{\partial t}\int_z^\eta w\ dz + \frac{\partial}{\partial x}\int_z^\eta (uw)\ dz - w^2,$$

so we obtain for $z \in [z_{\alpha-1/2}, z_{\alpha+1/2}]$

$$\begin{aligned}\left\|p^N - p\right\| &= \left\|\frac{\partial}{\partial t}\int_z^\eta (w^N - w)\ dz + \frac{\partial}{\partial x}\int_z^\eta (u^N w^N - uw)\ dz - (w^N)^2 + w^2\right\| \\ &= \mathcal{O}\left(\frac{1}{N}\right).\end{aligned} \tag{3.102}$$

Due to the chosen form of the vertical discretization, we have

$$\int_{z_{\alpha-1/2}}^{z_{\alpha+1/2}} X^N(x,z,\{z_\alpha\},t)dz = h_\alpha X_\alpha,$$

so using (3.99), (3.101) and (3.102) and up to $\mathcal{O}(1/N)$ terms, the velocities u_α, w_α and the pressures p_α, $\alpha = 1,\dots,N$ satisfy

$$X_\alpha(x,t) = \frac{1}{h_\alpha}\int_{z_{\alpha-1/2}}^{z_{\alpha+1/2}} X(x,z,t)dz, \tag{3.103}$$

for $X = (u,w,p)$. We also denote $X_{\alpha+1/2} = X(x,z_{\alpha+1/2},t)$, the value of the velocities u, w and of the pressure p at the interface $z_{\alpha+1/2}$.

Using the discretizations (3.46),(3.48) and the estimates (3.100)-(3.103) and integrating the Euler equations (3.1)-(3.3) over the layers $[z_{\alpha-1/2}, z_{\alpha+1/2}]$, $\alpha = 1,...,N$, we claim that

Proposition 6. *The multilayer formulation of the averaged Euler system defined for $\alpha = 1,\dots,N$ by*

$$\sum_{\alpha=1}^{N}\frac{\partial h_\alpha}{\partial t} + \sum_{\alpha=1}^{N}\frac{\partial h_\alpha u_\alpha}{\partial x} = 0, \tag{3.104}$$

$$\begin{aligned}\frac{\partial h_\alpha u_\alpha}{\partial t} + \frac{\partial}{\partial x}\left(h_\alpha u_\alpha^2 + h_\alpha p_\alpha\right) &= p_{\alpha+1/2}\frac{\partial z_{\alpha+1/2}}{\partial x} - p_{\alpha-1/2}\frac{\partial z_{\alpha-1/2}}{\partial x}\\ &+u_{\alpha+1/2}G_{\alpha+1/2} - u_{\alpha-1/2}G_{\alpha-1/2},\end{aligned} \tag{3.105}$$

$$\begin{aligned}\frac{\partial h_\alpha w_\alpha}{\partial t} + \frac{\partial}{\partial x}\left(h_\alpha w_\alpha u_\alpha\right) &= -p_{\alpha+1/2} + p_{\alpha-1/2} - gh_\alpha\\ &+w_{\alpha+1/2}G_{\alpha+1/2} - w_{\alpha-1/2}G_{\alpha-1/2},\end{aligned} \tag{3.106}$$

$$\begin{aligned}\frac{\partial}{\partial t}\left(\frac{z_{\alpha+1/2}^2 - z_{\alpha-1/2}^2}{2}\right) + \frac{\partial}{\partial x}\left(\frac{z_{\alpha+1/2}^2 - z_{\alpha-1/2}^2}{2}u_\alpha\right) &= h_\alpha w_\alpha\\ &+z_{\alpha+1/2}G_{\alpha+1/2} - z_{\alpha-1/2}G_{\alpha-1/2},\end{aligned} \tag{3.107}$$

$$\begin{aligned}\frac{\partial}{\partial t}\left(\frac{z_{\alpha+1/2}^2 - z_{\alpha-1/2}^2}{2}u_\alpha\right) + \frac{\partial}{\partial x}\left(\frac{z_{\alpha+1/2}^2 - z_{\alpha-1/2}^2}{2}\left(u_\alpha^2 + p_\alpha\right)\right) &=\\ h_\alpha w_\alpha u_\alpha + \frac{1}{2}\frac{\partial z_{\alpha+1/2}^2}{\partial x}p_{\alpha+1/2} - \frac{1}{2}\frac{\partial z_{\alpha-1/2}^2}{\partial x}p_{\alpha-1/2}&\\ +z_{\alpha+1/2}u_{\alpha+1/2}G_{\alpha+1/2} - z_{\alpha-1/2}u_{\alpha-1/2}G_{\alpha-1/2},&\end{aligned} \tag{3.108}$$

$$\begin{aligned}\frac{\partial}{\partial t}\left(\frac{z_{\alpha+1/2}^2 - z_{\alpha-1/2}^2}{2}w_\alpha\right) + \frac{\partial}{\partial x}\left(\frac{z_{\alpha+1/2}^2 - z_{\alpha-1/2}^2}{2}u_\alpha w_\alpha\right) &= h_\alpha(w_\alpha^2 + p_\alpha)\\ -z_{\alpha+1/2}p_{\alpha+1/2} + z_{\alpha-1/2}p_{\alpha-1/2} - g\frac{z_{\alpha+1/2}^2 - z_{\alpha-1/2}^2}{2}&\\ +z_{\alpha+1/2}w_{\alpha+1/2}G_{\alpha+1/2} - z_{\alpha-1/2}w_{\alpha-1/2}G_{\alpha-1/2},&\end{aligned} \tag{3.109}$$

results from a formal asymptotic approximation in $\mathcal{O}(1/N)$ coupled with a vertical discretization of the free surface Euler equations.

The quantity $G_{\alpha+1/2}$ still corresponds to the kinematic of the interface $z_{\alpha+1/2}$ given for $\alpha = 0,\dots,N$ by relation (3.54).

The proof of this proposition is simple and relies on simple calculus. We use the same strategy as in proposition 5 namely, an integration similar to (3.83)-(3.85) but over each interval $[z_{\alpha-1/2}, z_{\alpha+1/2}]$ of the Euler equations against z^i for $i = 0, 1$.

Energy equality The multilayer Euler system admits an energy equality and we have the following proposition

Proposition 7. *The smooth solutions of system (3.104)-(3.109) satisfy the energy balance*

$$\frac{\partial}{\partial t}\left(\sum_{\alpha=1}^{N} E_\alpha^N\right) + \frac{\partial}{\partial x}\left(\sum_{\alpha=1}^{N} u_\alpha \left(E_\alpha^N + h_\alpha p_\alpha\right)\right) = -p^a \frac{\partial H}{\partial t} + (p_b - p^a)\frac{\partial z_b}{\partial t},$$

with

$$E_\alpha^N = \frac{h_\alpha u_\alpha^2}{2} + \frac{h_\alpha w_\alpha^2}{2} + g\frac{z_{\alpha+1/2}^2 - z_{\alpha-1/2}^2}{2}.$$

Remarks The system (3.104)-(3.109) corresponds to $5N + 1$ equations with $4N + 1$ unknowns, namely

$$H, u_\alpha, w_\alpha, p_\alpha, p_{\alpha-1/2}.$$

Fortunately and as in the single layer case, the two equations (3.105),(3.108) are identical. Indeed, written in a non conservative form they read

$$\begin{aligned}
\frac{\partial u_\alpha}{\partial t} + u_\alpha \frac{\partial u_\alpha}{\partial x} &= -\frac{1}{h_\alpha}\frac{\partial}{\partial x}\left(h_\alpha p_\alpha\right) + \frac{p_{\alpha+1/2}}{h_\alpha}\frac{\partial z_{\alpha+1/2}}{\partial x} - \frac{p_{\alpha-1/2}}{h_\alpha}\frac{\partial z_{\alpha-1/2}}{\partial x} \\
&\quad + \frac{u_{\alpha+1/2} - u_\alpha}{h_\alpha} G_{\alpha+1/2} - \frac{u_{\alpha-1/2} - u_\alpha}{h_\alpha} G_{\alpha-1/2} \\
\frac{\partial u_\alpha}{\partial t} + u_\alpha \frac{\partial u_\alpha}{\partial x} &= -\frac{2}{z_{\alpha+1/2}^2 - z_{\alpha-1/2}^2}\frac{\partial}{\partial x}\int_{z_{\alpha-1/2}}^{z_{\alpha+1/2}} zp\, dz \\
&\quad + \frac{1}{z_{\alpha+1/2}^2 - z_{\alpha-1/2}^2}\frac{\partial z_{\alpha+1/2}^2}{\partial x} p_{\alpha+1/2} - \frac{1}{z_{\alpha+1/2}^2 - z_{\alpha-1/2}^2}\frac{\partial z_{\alpha-1/2}^2}{\partial x} p_{\alpha-1/2} \\
&\quad + \frac{2z_{\alpha+1/2}(u_{\alpha+1/2} - u_\alpha)}{z_{\alpha+1/2}^2 - z_{\alpha-1/2}^2} G_{\alpha+1/2} - \frac{2z_{\alpha-1/2}(u_{\alpha-1/2} - u_\alpha)}{z_{\alpha+1/2}^2 - z_{\alpha-1/2}^2} G_{\alpha-1/2},
\end{aligned}$$

for $\alpha = 1, \ldots, N$. And the right hand sides of the two previous equations are equal up to $\mathcal{O}(1/N)$ terms since from $z_{\alpha+1/2} = z_{\alpha-1/2} + h_\alpha = z_{\alpha-1/2} + \mathcal{O}(1/N)$ we have

$$\frac{1}{h_\alpha} = \frac{2z_{\alpha+1/2}}{z_{\alpha+1/2}^2 - z_{\alpha-1/2}^2} + \mathcal{O}(\frac{1}{N^2}) = \frac{2z_{\alpha-1/2}}{z_{\alpha+1/2}^2 - z_{\alpha-1/2}^2} + \mathcal{O}(\frac{1}{N^2}).$$

Notice that the quantities $u_{\alpha+1/2}$ and $w_{\alpha+1/2}$ for $\alpha = 0, \ldots, N$ are defined using an upwinding already discussed in (3.58) i.e.

$$G_{\alpha+1/2} \geq 0 \Rightarrow \left\{ \begin{array}{l} u_{\alpha+1/2} = u_{\alpha+1} \\ w_{\alpha+1/2} = w_{\alpha+1} \end{array} \right. \quad \text{and} \quad G_{\alpha+1/2} < 0 \Rightarrow \left\{ \begin{array}{l} u_{\alpha+1/2} = u_\alpha \\ w_{\alpha+1/2} = w_\alpha. \end{array} \right.$$

Due to physical considerations, this choice is the only possible choice.

4 Kinetic approach

We briefly present the kinetic theory applied to the formulation/interpretation of conservation laws. For a complete overview, the reader can refer to [Per02].

The idea we would like to emphasize is that the kinetic approach has two levels. First, the *kinetic formulations* where a full description is given when a large enough family of entropies is available, and the more general *kinetic representation* which is based on a single entropy.

Notice that the *kinetic formulation* is not restricted to hyperbolic problems, it can be obtained for parabolic problems such as parabolic scalar conservation laws, see [Per02, chap. 1].

4.1 Kinetic formulation

The so-called kinetic formulation of nonlinear hyperbolic systems of conservation laws is a method which reduces them to a linear equation, with an additional kinetic variable, on a nonlinear quantity related to the conserved unknowns. It represents all the entropy inequalities in a single equation depending on an additional variable. It was introduced by Lions, Perthame and Tadmor for scalar conservation laws (see [LPT94a, PT91]) and for isentropic gas dynamics (see [LPT94b]). It turns out to be a powerful tool to derive mathematical properties – and also numerical schemes.

4.2 Kinetic interpretation

A kinetic interpretation is much weaker than the kinetic formulation since it only uses the single entropy given by the energy. Moreover in a kinetic representation, the collision term in the right hand side carries little information.

And yet, a kinetic interpretation are in practice very useful since it allows to construct efficient numerical schemes.

4.3 Advantages of the kinetic approach

In the following of the document, the discretization of the models presented in Sec. 3 will be carried out almost exclusively using kinetic representations. A natural question is : is it possible to consider other techniques to obtain efficient numerical schemes ?

For the section averaged Saint-Venant system and the non-hydrostatic Saint-Venant system, the answer is clearly positive. The references are given in the corresponding paragraphs.

For the other proposed models where the velocity is not reduced to its vertical mean and as far as the authors knows, no numerical techniques ensuring properties such as conservativity, positivity, stability, maximum principle have been proposed.

4.4 Kinetic interpretation of the proposed models

In this paragraph we give the kinetic interpretation of three different models presented in Sec. 3, namely

- the section-averaged Saint-Venant system,
- the hydrostatic Navier-Stokes system with varying density (the interpretation is also valid for the constant density case),

- the Euler system.

Since the proposed kinetic interpretations are extensions of what is done for the classical Saint-Venant system (in this case this is also a kinetic formulation), we first briefly recall the kinetic formalism for the Saint-Venant system.

For the sake of simplicity and without any loss of generality we consider in the following the atmospheric pressure at the free surface vanishes i.e. $p^a = 0$. The friction and viscous effects are omitted at the kinetic level.

4.4.1 The Saint-Venant system

We introduce a distribution function $M(x,t,\xi)$ of fictitious particles with microscopic velocity ξ in order to obtain a linear microscopic kinetic equation equivalent to the macroscopic model (3.18)-(3.19).

We also introduce a real function χ defined on $\mathbb{R}$, compactly supported and which has the following properties

$$\begin{cases} \chi(-w) = \chi(w) \geq 0 \\ \int_{\mathbb{R}} \chi(w)\ dw = \int_{\mathbb{R}} w^2 \chi(w)\ dw = 1, \end{cases} \tag{4.1}$$

we also define $k_3 = \int_{\mathbb{R}} \chi^3(w)\ dw$.

Now let us construct the density of particles $M(x,t,\xi)$ defined by a Gibbs equilibrium: the microscopic density of particles present at time t, abscissa x and with velocity ξ is given by

$$M(x,t,\xi) = \frac{H}{c}\chi\left(\frac{\xi - \overline{u}}{c}\right),$$

with $c = \sqrt{\frac{gH}{2}}$. Then we have the following proposition

Proposition 8. *The functions $(H, \overline{u})$ are strong solutions of the Saint-Venant system described in (3.18)-(3.19) if and only if the equilibrium $M(x,t,\xi)$ is solution of the kinetic equation*

$$(\mathcal{B}) \qquad \frac{\partial M}{\partial t} + \xi \frac{\partial M}{\partial x} - g\frac{\partial z_b}{\partial x}\frac{\partial M}{\partial \xi} = Q(x,t,\xi), \tag{4.2}$$

where $Q(x,t,\xi)$ is a "collision term" satisfying

$$\int_{\mathbb{R}} Q\ d\xi = \int_{\mathbb{R}} \xi Q\ d\xi = 0. \tag{4.3}$$

The solution is an entropy solution if additionally

$$\int_{\mathbb{R}} \left(\xi^2 + \frac{3g^2}{4k_3}M^2\right) Q d\xi \leq 0. \tag{4.4}$$

Proof of Prop. 8. The proof is very simple and relies on simple integrations of the Gibbs equilibrium. Since we have

$$\int_{\mathbb{R}} M\ d\xi = H, \qquad \int_{\mathbb{R}} \xi M\ d\xi = H\overline{u}, \qquad \int_{\mathbb{R}} \xi^2 M\ d\xi = H\overline{u}^2 + \frac{g}{2}H^2.$$

the proof is obtained using integrations in ξ of the equation (4.2). More precisely, an integration of (4.2) against 1 and ξ gives the continuity and momentum equations (3.18)-(3.19). The energy balance for smooth solutions (3.21) comes from

$$\int_{\mathbb{R}} \left(\frac{\xi^2}{2} + \frac{3g^2}{8k_3} M^2 \right) (\mathcal{B}) d\xi = 0. \quad \square$$

4.4.2 The section-averaged Saint-Venant system [8]

Now we propose a kinetic interpretation for the section-averaged Saint-Venant system defined in Prop. 1 (page 26). We keep the notations introduced in paragraph 3.2 (page 25) and the properties of the function χ defined by (4.1). Thus we construct the new density of particles $M_s(x,t,\xi)$ given by

$$M_S(x,t,\xi) = \frac{S}{c} \chi \left(\frac{\xi - \bar{u}}{c} \right), \tag{4.5}$$

where the water depth H is replaced by the channel section S and with

$$c = \sqrt{\frac{g(\frac{L_b(x)}{2}(A(S))^2 + L_1(x)B(S,x))}{S}}.$$

The additional source terms coming from the section width variations require we define the new Gibbs equilibria

$$M_B(x,t,\xi) = \frac{B(S,x)}{c} \chi \left(\frac{\xi - \overline{u}}{c} \right), \quad M_{A^2}(x,t,\xi) = \frac{A^2(S)}{c} \chi \left(\frac{\xi - \overline{u}}{c} \right).$$

Then we have the following proposition

Proposition 9. *The functions $(S, \bar{u})$ are strong solutions of the section-averaged Saint-Venant system described in Prop. 1 if and only if $M_s(x,t,\xi)$, $M_{A^2}(x,t,\xi)$ and $M_B(x,t,\xi)$ are solutions of the kinetic equation*

$$(\mathcal{B}) \quad \frac{\partial M_S}{\partial t} + \xi \frac{\partial M_S}{\partial x} - g \frac{\partial \overline{z}_b}{\partial x} \frac{\partial M_S}{\partial \xi} + g \frac{\partial L_b}{\partial x} \frac{\partial M_{A^2}}{\partial \xi} + g \frac{\partial L_1}{\partial x} \frac{\partial M_B}{\partial \xi} = Q_S(x,t,\xi), \tag{4.6}$$

where $Q_S(x,t,\xi)$ is a "collision term" satisfying for a.e. values of (x,t)

$$\int_{\mathbb{R}} Q_S d\xi = 0, \qquad \int_{\mathbb{R}} \xi Q_S d\xi = 0. \tag{4.7}$$

The Boltzmann type equation (4.6) is similar to (4.2) used for the classical Saint-Venant system but additional Vlasov type terms are necessary to represent the source terms induced by the section variations.

For the energy balance of the system (see Eq. (3.42)) we have the following proposition

Proposition 10. *Let us introduce the new equilibrium $\widetilde{M}$ defined by*

$$\widetilde{M}(x,t,\xi) = \frac{gSH - \frac{c^2}{2}}{c} \chi \left(\frac{\xi - \bar{u}}{c} \right).$$

If we assume the equilibria M_{A^2}, M_B and $\widetilde{M}$ satisfy

$$(\mathcal{B}_{A^2}), \quad \frac{\partial M_{A^2}}{\partial t} + \xi \frac{\partial M_{A^2}}{\partial x} = Q_{A^2}(x,t,\xi), \tag{4.8}$$

$$(\mathcal{B}_S), \quad \frac{\partial M_S}{\partial t} + \xi \frac{\partial M_S}{\partial x} = Q_S(x,t,\xi), \tag{4.9}$$

$$(\widetilde{\mathcal{B}}), \quad \frac{\partial \widetilde{M}}{\partial t} + \xi \frac{\partial \widetilde{M}}{\partial x} = \widetilde{Q}(x,t,\xi), \tag{4.10}$$

with

$$\int_{\mathbb{R}} \left(\left(\frac{\xi^2}{2} + g z_b \right) Q_S + Q_{A^2} + Q_B + \widetilde{Q} \right) d\xi \leq 0, \tag{4.11}$$

then the solution is an entropy solution.

Proofs of Props. 9 and 10. Since we have

$$\int_{\mathbb{R}} M_S \, d\xi = S, \qquad \int_{\mathbb{R}} \xi M_S \, d\xi = S\overline{u} \tag{4.12}$$

$$\int_{\mathbb{R}} \xi^2 M_S d\xi = S\overline{u}^2 + g\frac{L_b(x)}{2} A(S)^2 + g L_1(x) B(S,x), \tag{4.13}$$

$$\int_{\mathbb{R}} \frac{\partial M_S}{\partial \xi} \, d\xi = \int_{\mathbb{R}} \frac{\partial M_B}{\partial \xi} \, d\xi = \int_{\mathbb{R}} \frac{\partial M_{A^2}}{\partial \xi} \, d\xi = 0, \quad \int_{\mathbb{R}} \xi \frac{\partial M_B}{\partial \xi} \, d\xi = B(S),$$

$$\int_{\mathbb{R}} \xi \frac{\partial M_{A^2}}{\partial \xi} \, d\xi = A(S)^2, \quad \int_{\mathbb{R}} \frac{\xi^2}{2} \frac{\partial M_B}{\partial \xi} \, d\xi = B(S)\overline{u},$$

$$\int_{\mathbb{R}} \frac{\xi^2}{2} \frac{\partial M_{A^2}}{\partial \xi} \, d\xi = A(S)^2 \overline{u}$$

the proofs are obtained using (4.7),(4.11) and calculating the quantities

$$\int_{\mathbb{R}} (\mathcal{B}) \, d\xi, \quad \int_{\mathbb{R}} \xi (\mathcal{B}) \, d\xi, \quad \text{and} \quad \int_{\mathbb{R}} \left(\left(\frac{\xi^2}{2} + g z_b \right) (\mathcal{B}) + (\mathcal{B}_{A^2}) + (\mathcal{B}_B) + (\widetilde{\mathcal{B}}) \right) d\xi. \quad \square$$

4.4.3 The hydrostatic Navier-Stokes system with varying density [3, 2]

In the preceding paragraph the kinetic interpretation was only a slight modification of what is usually done for the Saint-Venant system. For the model obtained in paragraph 3.5 (page 37), the situation is more complex since the model takes into account vertical circulations of the fluid.

Notice that the process detailed below to obtain the kinetic interpretation of the model with varying density can be adapted to the case of a flow with a passive tracer i.e. a tracer whose concentration does not influence the fluid density. This is done simply assuming the fluid density is constant $\rho = Cst$. Obviously it is also valid when no tracer is considered.

Keeping the notations of paragraphs 3.4 and 3.5 (pages 31 and 37), for a given layer α, a distribution function $M_\alpha(x,t,\xi)$ of fictitious particles with microscopic velocity ξ is introduced to obtain a linear kinetic equation equivalent to the macroscopic model presented in Prop. 4.

Now let us construct a density of particles $M_\alpha(x,t,\xi)$ defined by a Gibbs equilibrium: the microscopic density of particles present at time t, in layer α, at abscissa x and with velocity ξ given by

$$M_\alpha = \frac{\rho_\alpha h_\alpha(x,t)}{c_\alpha} \chi\left(\frac{\xi - u_\alpha(x,t)}{c_\alpha} \right), \tag{4.14}$$

with

$$c_\alpha^2 = \frac{p_\alpha}{\rho_\alpha},$$

and p_α defined by (3.56).

Likewise, we define $N_{\alpha+1/2}(x,t,\xi)$ and $S_{\alpha+1/2}(x,t,\xi)$ by

$$N_{\alpha+1/2}(x,t,\xi) = G_{\alpha+1/2}(x,t)\ \delta\left(\xi - u_{\alpha+1/2}(x,t)\right), \tag{4.15}$$

$$S_{\alpha+1/2}(x,t,\xi) = p_{\alpha+1/2}(x,t)\frac{\partial z_{\alpha+1/2}}{\partial x}\frac{\partial}{\partial \xi}\delta\left(\xi - \left(u_{\alpha+1/2}(x,t) - \frac{w_{\alpha+1/2}(x,t)}{\frac{\partial z_{\alpha+1/2}}{\partial x}}\right)\right), \tag{4.16}$$

for $\alpha = 0,\dots,N$ and where δ denotes the Dirac distribution.

The quantities $G_{\alpha+1/2}$, $0 \le \alpha \le N$ represent the mass exchanges between layers α and $\alpha+1$, they are defined in (3.76) and satisfy the conditions (3.53), so $N_{1/2}$ and $N_{N+1/2}$ also satisfy

$$N_{1/2}(x,t,\xi) = N_{N+1/2}(x,t,\xi) = 0. \tag{4.17}$$

For the temperature, we have the equilibria

$$U_\alpha(x,t,\xi) = T_\alpha(x,t)M_\alpha(x,t,\xi), \tag{4.18}$$

$$V_{\alpha+1/2}(x,t,\xi) = T_{\alpha+1/2}(x,t)N_{\alpha+1/2}(x,t,\xi), \tag{4.19}$$

for $\alpha = 0,\dots,N$. With the previous definitions we write a kinetic representation of the system described in Prop. 4 and we have the following proposition

Proposition 11. *The functions (H, u^N, T^N) are strong solutions of the system (3.73) -(3.75) if and only if the set of equilibria $\{M_\alpha(x,t,\xi), U_\alpha(x,t,\xi)\}_{\alpha=1}^N$ are solutions of the kinetic equations*

$$(\mathcal{B}_{M_\alpha}),\quad \frac{\partial M_\alpha}{\partial t} + \xi\frac{\partial M_\alpha}{\partial x} - N_{\alpha+1/2} - S_{\alpha+1/2} + N_{\alpha-1/2} + S_{\alpha-1/2} = Q_{M_\alpha}, \tag{4.20}$$

$$\frac{\partial U_\alpha}{\partial t} + \xi\frac{\partial U_\alpha}{\partial x} - V_{\alpha+1/2} + V_{\alpha-1/2} = Q_{U_\alpha}, \tag{4.21}$$

for $\alpha = 1,\dots,N$ with $\{N_{\alpha+1/2}(x,t,\xi), S_{\alpha+1/2}(x,t,\xi), V_{\alpha+1/2}(x,t,\xi)\}_{\alpha=0}^N$ satisfying (4.15)-(4.19).

The quantities $Q_{M_\alpha} = Q_{M_\alpha}(x,t,\xi)$ and $Q_{U_\alpha} = Q_{U_\alpha}(x,t,\xi)$ are "collision terms" equal to zero at the macroscopic level i.e. which satisfy for a.e. values of (x,t)

$$\int_{\mathbb{R}} Q_{M_\alpha} d\xi = 0, \quad \int_{\mathbb{R}} \xi Q_{M_\alpha} d\xi = 0, \quad \textit{and} \qquad \int_{\mathbb{R}} Q_{U_\alpha} d\xi = 0. \tag{4.22}$$

The proof of this proposition is simple and given in the following with the proof of the proposition concerning the energy balance.

Vertical velocity kinetic equation In order to capture the macroscopic vertical velocities w_α that are necessary for the energy balance and for post-processing purpose, the kinetic interpretation has to take into account the microscopic vertical velocity γ of the particles. For a given layer $\alpha \in [1,\dots,N]$, we construct the new densities of particles $R_\alpha(x,t,\xi,\gamma)$ defined by the Gibbs equilibria: the microscopic density of particles present at time t, abscissa x and with microscopic horizontal (resp. vertical) velocity ξ (resp. γ) given by

$$R_\alpha(x,t,\xi,\gamma) = \rho_\alpha \frac{z_{\alpha+1/2}^2 - z_{\alpha-1/2}^2}{2}\delta\left(\xi - u_\alpha\right)\delta\left(\gamma - w_\alpha\right), \tag{4.23}$$

and satisfying the kinetic equations

$$(\mathcal{B}_{R_\alpha}), \quad \frac{\partial R_\alpha}{\partial t} + \xi \frac{\partial R_\alpha}{\partial x} - \delta\left(\gamma - w_\alpha\right)\left(\gamma M_\alpha - z_{\alpha+1/2} N_{\alpha+1/2} + z_{\alpha-1/2} N_{\alpha-1/2}\right) = Q_{R_\alpha}, \tag{4.24}$$

for $\alpha = 1, \ldots, N$ where $Q_{R_\alpha} = Q_{R_\alpha}(x, t, \xi, \gamma)$ is a collision term satisfying

$$\int_{\mathbb{R}^2} Q_{R_\alpha} d\xi d\gamma = 0. \tag{4.25}$$

Using (4.25) a simple integration in ξ and γ of Eq. (4.24) gives (3.78).

Remark 4.1. *The use of the vertical microscopic velocity γ will be one of the key point of the kinetic interpretation of the complete Euler system (see paragraph 4.4.4) i.e. with all the non-hydrostatic terms.*

Kinetic interpretation of energy equation In order to recover for smooth solutions, the energy balances (3.77), we also introduce for $\alpha = 1, \ldots, N$ the densities $\widetilde{M}_\alpha(x, t, \xi)$ defined by

$$\widetilde{M}_\alpha = \frac{l_\alpha(x,t) H p_\alpha(x,t)}{2} \delta\left(\xi - u_\alpha(x,t)\right),$$

and we have the following proposition

Proposition 12. *The solutions of (4.20), (4.21) and (4.24) are entropy solutions if additionally*

$$(\widetilde{\mathcal{B}}_\alpha), \quad \frac{\partial \widetilde{M}_\alpha}{\partial t} + \xi \frac{\partial \widetilde{M}_\alpha}{\partial x} = \widetilde{Q}_\alpha(x, t, \xi), \quad \alpha = 1, \ldots, N, \tag{4.26}$$

with for smooth solutions

$$\sum_{\alpha=1}^{N} \left(\int_{\mathbb{R}} \left(\frac{\xi^2}{2} Q_{M_\alpha} - \widetilde{Q}_\alpha \right) d\xi + g \int_{\mathbb{R}^2} Q_{R_\alpha} d\xi d\gamma \right) = 0. \tag{4.27}$$

Proofs of Props. 11,12. Using the definitions (4.14),(4.18) and the properties of the function χ, we have

$$\rho_\alpha l_\alpha H = \int_{\mathbb{R}} M_\alpha(x, t, \xi) d\xi, \qquad \rho_\alpha l_\alpha H u_\alpha = \int_{\mathbb{R}} \xi M_\alpha(x, t, \xi) d\xi, \tag{4.28}$$

$$\rho_\alpha l_\alpha H T_\alpha = \int_{\mathbb{R}} U_\alpha(x, t, \xi) d\xi, \qquad \rho_\alpha l_\alpha H T_\alpha u_\alpha = \int_{\mathbb{R}} \xi U_\alpha(x, t, \xi) d\xi. \tag{4.29}$$

From the definitions (4.15),(4.16) of $N_{\alpha+1/2}$ and $S_{\alpha+1/2}$, we also have

$$\int_{\mathbb{R}} N_{\alpha+1/2}(x, t, \xi) d\xi = G_{\alpha+1/2}, \tag{4.30}$$

$$\int_{\mathbb{R}} \xi N_{\alpha+1/2}(x, t, \xi) d\xi = u_{\alpha+1/2} G_{\alpha+1/2}, \tag{4.31}$$

$$\int_{\mathbb{R}} S_{\alpha+1/2}(x, t, \xi) d\xi = 0, \tag{4.32}$$

$$\int_{\mathbb{R}} \xi S_{\alpha+1/2}(x, t, \xi) d\xi = p_{\alpha+1/2} \frac{\partial z_{\alpha+1/2}}{\partial x}. \tag{4.33}$$

Then, using (4.22),(4.30),(4.32), the equation (4.20) integrated in ξ gives, for each layer α, the equation (3.51) but in the non constant density case i.e.

$$\frac{\partial \rho_\alpha h_\alpha}{\partial t} + \frac{\partial}{\partial x}\left(\rho_\alpha h_\alpha u_\alpha\right) = G_{\alpha+1/2} - G_{\alpha-1/2}.$$

And, with the conditions (4.17), the sum of the equations (4.20) gives the continuity equation (3.73). Likewise the equations (4.20) integrated in ξ against ξ give the momentum equations (3.74). And a simple integration in ξ of the equations (4.21), always using (4.22), gives the tracer equations (3.75).

For the energy balance and due to the definitions of the Gibbs equilibria we have

$$\begin{aligned}
&\rho_\alpha l_\alpha H u_\alpha^3 + \frac{l_\alpha H}{2} p_\alpha u_\alpha = \int_{\mathbb{R}} \xi^3 M_\alpha(x,t,\xi) d\xi,\\
&\rho_\alpha l_\alpha H w_\alpha = \int_{\mathbb{R}^2} \gamma\delta(\gamma - w_\alpha) M_\alpha(x,t,\xi) d\xi d\gamma,\\
&l_\alpha H p_\alpha u_\alpha = \int_{\mathbb{R}} \xi \widetilde{M}_\alpha(x,t,\xi) d\xi, \quad u_{\alpha+1/2}^2 = \int_{\mathbb{R}} \xi^2 N_{\alpha+1/2}(x,t,\xi) d\xi,\\
&G_{\alpha+1/2} = \int_{\mathbb{R}^2} \delta(\gamma - w_\alpha) N_{\alpha+1/2}(x,t,\xi) d\xi d\gamma,\\
&\rho_\alpha \frac{z_{\alpha+1/2}^2 - z_{\alpha-1/2}^2}{2} = \int_{\mathbb{R}^2} R_\alpha(x,t,\xi,\gamma) d\xi d\gamma,\\
&\rho_\alpha \frac{z_{\alpha+1/2}^2 - z_{\alpha-1/2}^2}{2} u_\alpha = \int_{\mathbb{R}^2} \xi R_\alpha(x,t,\xi,\gamma) d\xi d\gamma,\\
&2 p_{\alpha+1/2} \frac{\partial z_{\alpha+1/2}}{\partial x} u_{\alpha+1/2} = \int_{\mathbb{R}} \xi^2 S_{\alpha+1/2}(x,t,\xi) d\xi.
\end{aligned}$$

Then the calculus of

$$\sum_{\alpha=1}^{N} \left(\int_{\mathbb{R}} \left(\frac{\xi^2}{2} (\mathcal{B}_{M_\alpha}) - (\widetilde{\mathcal{B}}_\alpha) \right) d\xi + g \int_{\mathbb{R}^2} (\mathcal{B}_{R_\alpha}) d\xi d\gamma \right) = 0,$$

gives the energy balance (3.77) that completes the proofs. □

4.4.4 The Euler system [10]

The last kinetic interpretation we propose concerns the Euler system with constant density. A Shallow Water approximation of this system has been proposed in paragraph 3.6.1 and a more complete formulation corresponding to a multilayer type approximation of the complete Euler equations has been derived in paragraph 3.6.2.

The averaged Euler system In this paragraph, we propose a kinetic interpretation for the averaged Euler system defined in Prop. 5.

We keep the definition and the properties of the function χ (see Eq. (4.1)) and we introduce another real function ψ with compact support, defined on $\mathbb{R}$ and which has the following properties

$$\begin{cases} \psi(-w) = \psi(w) \geq 0 \\ \int_{\mathbb{R}} \psi(w)\ dw = \int_{\mathbb{R}} w^2 \psi(w)\ dw = 1. \end{cases}$$

Since we take into account the non-hydrostatic effects of the pressure, the microscopic vertical velocity γ of the particles has to be considered and we now construct the new density of particles $M^e(x,t,\xi,\gamma)$ defined by a Gibbs equilibrium: the microscopic density of particles present at time t and abscissa x and with microscopic horizontal (resp. vertical) velocity ξ (resp. γ) is given by

$$M^e(x,t,\xi,\gamma) = \frac{H}{c_1 c_2}\chi\left(\frac{\xi-\overline{u}}{c_1}\right)\psi\left(\frac{\gamma-\overline{w}}{c_2}\right),$$

with

$$c_1 = \sqrt{\overline{p}}, \quad \text{and} \quad c_2 = \sqrt{\frac{1}{H}\int_{z_b}^{\eta}\hat{w}^2 dz - \overline{w}^2 + \overline{p}}.$$

Notice that from relation (3.97) one also has

$$c_2 = \sqrt{\frac{1}{3}\left(\overline{w} - \frac{\partial z_b}{\partial x}\overline{u}\right)^2 + \overline{p}}.$$

We also define the new Gibbs equilibrium $R^e(x,t,\xi,\gamma)$

$$R^e(x,t,\xi,\gamma) = \frac{\eta^2 - z_b^2}{2}\chi\left(\frac{\xi-\overline{u}}{c_3}\right)\delta\left(\gamma - \check{w}\right),$$

where using (3.96) we have

$$\check{w} = \frac{2}{\eta^2 - z_b^2}\int_{z_b}^{\eta} z\hat{w}\, dz = \frac{2}{\eta + z_b}\left(\left(\frac{2}{3}H + z_b\right)\overline{w} - \frac{1}{6}\frac{\partial z_b}{\partial x}\overline{u}\right),$$

and

$$c_3 = \sqrt{\frac{2}{\eta^2 - z_b^2}\int_{z_b}^{\eta} zp\, dz}.$$

Notice that from relation (3.98), one has

$$c_3 = \sqrt{\overline{p} - \frac{H}{6(\eta + z_b)}p_b},$$

Notice also that according to the assumptions concerning the non-negativity of the fluid pressure p (see Eq. (3.87)) we have

$$c_1 \geq 0, \quad c_2 \geq 0, \quad \text{and} \quad c_3 \geq 0.$$

Then we have the following proposition

Proposition 13. *The functions $(H, \overline{u}, \overline{w})$ are strong solutions of the averaged Euler system described in (3.88)-(3.93) if and only if the equilibria $M^e(x,t,\xi,\gamma)$ and $R^e(x,t,\xi,\gamma)$ are solutions of the kinetic equations*

$$(B_M^e) \qquad \frac{\partial M^e}{\partial t} + \xi\frac{\partial M^e}{\partial x} - g\frac{\partial M^e}{\partial \gamma} = Q_1, \tag{4.34}$$

$$(B_{R^e,M^e}) \qquad \frac{\partial R^e}{\partial t} + \xi\frac{\partial R^e}{\partial x} - \gamma M^e - g\frac{\partial R^e}{\partial \gamma} = Q_2, \tag{4.35}$$

where $Q_1 = Q_1(x,t,\xi,\gamma)$ and $Q_2 = Q_2(x,t,\xi,\gamma)$ are "collision terms" satisfying

$$\int_{\mathbb{R}^2} Q_1 \; d\xi d\gamma = \int_{\mathbb{R}^2} Q_2 \; d\xi d\gamma = 0, \tag{4.36}$$

$$\int_{\mathbb{R}^2} \left(\xi + \gamma \frac{\partial z_b}{\partial x}\right) Q_1 \; d\xi d\gamma = 0, \tag{4.37}$$

$$\int_{\mathbb{R}^2} \left(\xi Q_2 + z_b \frac{\partial z_b}{\partial x} \gamma Q_1\right) d\xi d\gamma = 0, \tag{4.38}$$

$$\int_{\mathbb{R}^2} \left(\gamma Q_2 - z_b \gamma Q_1\right) d\xi d\gamma = 0. \tag{4.39}$$

We also introduce the density $\widetilde{M}^e(x,t,\xi,\gamma)$ defined by

$$\widetilde{M}^e(x,t,\xi,\gamma) = H c_1^2 \delta\left(\xi - \overline{u}\right) \delta\left(\gamma - \overline{w}\right), \tag{4.40}$$

where δ denotes the Dirac distribution and satisfying the kinetic equation

$$(\widetilde{B}) \qquad \frac{\partial \widetilde{M}^e}{\partial t} + \xi \frac{\partial \widetilde{M}^e}{\partial x} = \widetilde{Q}(x,t,\xi,\gamma).$$

The solution of (4.34),(4.35) is an entropy solution if additionally

$$\int_{\mathbb{R}^2} \left(\frac{\xi^2 + \gamma^2}{2} Q_1 - \widetilde{Q}\right) d\gamma d\xi \leq 0. \tag{4.41}$$

Proof. of Prop. 13. The proof relies on simple integrations in ξ,γ of the Gibbs equilibria M^e, R^e and $\widetilde{M}^e$ using the properties (4.36)-(4.39),(4.41). □

The kinetic interpretation (4.34)-(4.35) reduces the averaged Euler system to a fully linear system of transport-reaction equations as obtained at the macroscopic level page 41. The nonlinearities appear in the expressions of the Gibbs equilibria M^e and R^e. Such a formulation could be useful for the analysis of the free surface Euler system and the derivation of efficient numerical schemes.

For hydrostatic or nearly hydrostatic flows such as the classical Saint-Venant system, the contribution of the vertical acceleration is neglected. So at the kinetic level, only appears the horizontal microscopic velocity ξ whereas the vertical microscopic velocity γ is not considered. This simplification is no more valid for non-hydrostatic flows and a transport-reaction type equation (4.35) has to be added to the classical Boltzmann equation (4.34). The Vlasov term

$$g \frac{\partial z_b}{\partial x} \frac{\partial M}{\partial \xi},$$

in the kinetic interpretation of the Saint-Venant system (4.20) and accounting for the topographic source term is now replaced by

$$g \frac{\partial M^e}{\partial \gamma}.$$

Under this form, the influence of the topography at the kinetic level is well understood since the averaged x-momentum equation (3.89) corresponds to

$$\int_{\mathbb{R}^2} (\mathbf{v_m})^t \mathbf{t_b} \left(B_M^e\right) d\xi d\gamma,$$

where $(\mathbf{v_m})^t\mathbf{t_b}$ with $\mathbf{v_m} = (\xi, \gamma)^t$ corresponds to the projection of the microscopic velocity vector $\mathbf{v_m}$ on the tangent $\mathbf{t_b}$ to the topography.

It is also important to notice that the system (4.34)-(4.35) is coupled. It is not possible to solve (4.34) and then to calculate the momenta of R^e from (4.35) knowing the momenta of M^e. Indeed, the contribution of the non-hydrostatic pressure terms in the Gibbs equilibrium M^e – that also correspond to the dispersive terms – are given by the wave velocity c_1. And c_1 is obtained from c_2 that is given by (4.35) using (4.38) and (4.39). At the discrete level, a finite volume discretization of the averaged Euler system (3.88)-(3.93) based on the kinetic equations (4.34)-(4.35) can easily be adapted from what is done for the classical Saint-Venant system, see [AB07]. The two main difficulties to overcome arise from

- the time scheme to use in presence of the reactions terms,
- the relevant equilibria that have to be satisfied at the discrete level.

The Euler system In this paragraph we give a kinetic interpretation for the model presented in propositions 6 and 7 i.e. without any Shallow Water assumption. We construct a density of particles $M^e_\alpha(x,t,\xi,\gamma)$ defined by a Gibbs equilibrium: the microscopic density of particles present at time t, abscissa x and in layer α, with microscopic horizontal velocity ξ and microscopic vertical velocity γ given by

$$M^e_\alpha(x,t,\xi,\gamma) = \frac{h_\alpha}{c_\alpha^2}\chi\left(\frac{\xi - u_\alpha}{c_\alpha}\right)\psi\left(\frac{\gamma - w_\alpha}{c_\alpha}\right),$$

with

$$c_\alpha = \sqrt{p_\alpha},$$

Likewise for $\alpha = 0, \dots, N$, we define $N^e_{1,\alpha+1/2}(x,t,\xi,\gamma)$ and $S^e_{1,\alpha+1/2}(x,t,\xi,\gamma)$ by

$$N^e_{1,\alpha+1/2} = G_{\alpha+1/2}\,\delta\left(\xi - u_{\alpha+1/2}\right)\delta\left(\gamma - w_{\alpha+1/2}\right), \tag{4.42}$$

$$S^e_{1,\alpha+1/2} = p_{\alpha+1/2}\frac{\partial z_{\alpha+1/2}}{\partial x}\frac{\partial}{\partial \xi}\left(\chi\left(\xi - v_{\alpha+1/2}\right)\right)\chi\left(\frac{\xi}{\frac{\partial z_{\alpha+1/2}}{\partial x}} + \gamma\right), \tag{4.43}$$

where

$$v_{\alpha+1/2} = \frac{\left(\frac{\partial z_{\alpha+1/2}}{\partial x}\right)^2\left(u_{\alpha+1/2} - \frac{w_{\alpha+1/2}}{\frac{\partial z_{\alpha+1/2}}{\partial x}}\right)}{1 + \left(\frac{\partial z_{\alpha+1/2}}{\partial x}\right)^2}.$$

As in the hydrostatic cases, the quantities $G_{\alpha+1/2}$, $0 \le \alpha \le N$ represent the mass exchanges between layers α and $\alpha+1$, they are defined in (3.54) and satisfy the conditions (3.53), so $N^e_{1,1/2}$ and $N^e_{1,N+1/2}$ also satisfy

$$N^e_{1,1/2}(x,t,\xi,\gamma) = N^e_{1,N+1/2}(x,t,\xi,\gamma) = 0.$$

For each $\alpha \in \{0, \dots, N\}$, the quantity $p_{\alpha+1/2}$ represents the pressure term applied on the interface $z_{\alpha+1/2}$.

We introduce the equilibria

$$N^e_{2,\alpha+1/2}(x,t,\xi,\gamma) = z_{\alpha+1/2}N^e_{1,\alpha+1/2}(x,t,\xi,\gamma), \tag{4.44}$$

$$S^e_{2,\alpha+1/2}(x,t,\xi,\gamma) = z_{\alpha+1/2}S^e_{1,\alpha+1/2}(x,t,\xi,\gamma), \tag{4.45}$$

for $\alpha = 0, \dots, N$. For the sake of clarity, the equilibria $N^e_{i,\alpha+1/2}(x,t,\xi,\gamma)$ and $S^e_{i,\alpha+1/2}(x,t,\xi,\gamma)$ associated with the source terms at the interfaces $z_{\alpha+1/2}$ are replaced by

$$T^e_{i,\alpha}(x,t,\xi,\gamma) = N^e_{i,\alpha}(x,t,\xi,\gamma) - S^e_{i,\alpha}(x,t,\xi,\gamma). \tag{4.46}$$

We also define the new set of Gibbs equilibria $R^e_\alpha(x,t,\xi,\gamma)$ defined by

$$R^e_\alpha(x,t,\xi,\gamma) = \frac{z^2_{\alpha+1/2} - z^2_{\alpha+1/2}}{2} \chi\left(\frac{\xi - u_\alpha}{c_\alpha}\right) \delta\left(\gamma - w_\alpha\right).$$

With the previous definitions, we have the following proposition

Proposition 14. *The functions $H, u_\alpha, w_\alpha, p_\alpha, p_{\alpha-1/2}$, $\alpha = 1, \dots, N$ are strong solutions of the multilayer Euler system (3.104)-(3.109) if and only if the set of equilibria $\{M^e_\alpha(x,t,\xi,\gamma), R^e_\alpha(x,t,\xi,\gamma)\}_{\alpha=1}^N$ is solution of the kinetic equations*

$$(B_{M^e_\alpha}) \qquad \frac{\partial M^e_\alpha}{\partial t} + \xi \frac{\partial M^e_\alpha}{\partial x} - g \frac{\partial M^e_\alpha}{\partial \gamma} - T^e_{1,\alpha+1/2} + T^e_{1,\alpha-1/2} = Q_{1,\alpha}, \tag{4.47}$$

$$(B_{R_\alpha, M_\alpha}) \qquad \frac{\partial R^e_\alpha}{\partial t} + \xi \frac{\partial R^e_\alpha}{\partial x} - \gamma M^e_\alpha - g \frac{\partial R^e_\alpha}{\partial \gamma} - T^e_{2,\alpha+1/2} + T^e_{2,\alpha-1/2} = Q_{2,\alpha}, \tag{4.48}$$

for $\alpha = 1, \dots, N$ with $\{T^e_{i,\alpha+1/2}(x,t,\xi,\gamma)\}_{\alpha=0}^N$ satisfying (4.42)-(4.46). The quantities $Q_{1,\alpha}(x,t,\xi,\gamma)$ and $Q_{2,\alpha}(x,t,\xi,\gamma)$ are "collision terms" satisfying

$$\int_{\mathbb{R}^2} Q_{1,\alpha}\, d\xi d\gamma = \int_{\mathbb{R}^2} Q_{2,\alpha}\, d\xi d\gamma = 0, \tag{4.49}$$

$$\int_{\mathbb{R}^2} \xi Q_{1,\alpha}\, d\xi d\gamma = \int_{\mathbb{R}^2} \xi Q_{2,\alpha}\, d\xi d\gamma = 0, \tag{4.50}$$

$$\int_{\mathbb{R}^2} \gamma Q_{1,\alpha} d\xi d\gamma = \int_{\mathbb{R}^2} \gamma Q_{2,\alpha} d\xi d\gamma = 0. \tag{4.51}$$

We also introduce the densities $\widetilde{M}^e_\alpha(x,t,\xi,\gamma)$ defined by

$$\widetilde{M}^e_\alpha(x,t,\xi,\gamma) = H c^2_\alpha \delta\left(\xi - u_\alpha\right) \delta\left(\gamma - w_\alpha\right), \tag{4.52}$$

and satisfying the kinetic equation

$$(\widetilde{B}^e_\alpha) \qquad \frac{\partial \widetilde{M}^e_\alpha}{\partial t} + \xi \frac{\partial \widetilde{M}^e_\alpha}{\partial x} = \widetilde{Q}_\alpha(x,t,\xi,\gamma).$$

The solution of (4.47),(4.48) is an entropy solution if additionally

$$\int_{\mathbb{R}^2} \left(\frac{\xi^2 + \gamma^2}{2} \sum_{\alpha=1}^N Q_{1,\alpha} - \sum_{\alpha=1}^N \widetilde{Q}_\alpha \right) d\gamma d\xi \leq 0.$$

Proof. of Prop. 14. The proof of this proposition is similar to what is done in the single layer case, see Prop. 13. □

5 Numerical schemes

In this section we describe the numerical schemes we propose for the resolution of the derived models.

For each model, its kinetic interpretation obtained in Sec. 4 gives the framework of the discretization. All the schemes we propose share common properties

- stable and positive,
- well-balanced,
- consistent,
- 2^{nd} order in space and time.

5.1 General framework

To approximate the solution of these models, we use a finite volume framework. We assume that the computational domain is discretized by I nodes x_i. We denote C_i the cell of length $\Delta x_i = x_{i+1/2} - x_{i-1/2}$ with $x_{i+1/2} = (x_i + x_{i+1})/2$. For the time discretization, we denote $t^n = \sum_{k \leq n} \Delta t^k$ where the time steps Δt^k will be precised for each model through a CFL condition.

5.1.1 Boundary conditions

The treatment of the boundary conditions is not detailed in this paper. For the section-averaged Saint-Venant system and the non-hydrostatic Saint-Venant system, it consists in a natural adaptation of the technique proposed by Bristeau and Coussin, see [BC01].

For models with a vertical distribution of the velocities, the original work of Bristeau and Coussin has to be extended. The extension is not presented here.

5.1.2 Second order scheme

The second-order accuracy in time is usually recovered by the Heun method [Bou04a] that is a slight modification of the second order Runge-Kutta method. The advantage of the Heun scheme is that it preserves the invariant domains without any restrictive limitation on the CFL.

We also apply a formally second order scheme in space by a limited reconstruction of the variables [ABB$^+$04]. These new variables are classically obtained with three ingredients: prediction of the gradients in each cell, linear extrapolation, and limitation procedure. The process is detailed in [AB05a].

5.2 The section-averaged Saint-Venant system [8]

First, we propose a discretization of the section-averaged Saint-Venant system derived in paragraph 3.2 (page 25). As already mentioned, the main difficulty of these equations consists in the discretization of the unusual source terms. Up to now, a stable and efficient numerical treatment of these equations with the source terms is still challenging [GM02, Gla05, YKW04]. Recently, a semi-implicit method has been proposed by Deponti *et al.* [DBRG07] and a central scheme has been derived by Balbàs *et al.* [BK09].

The numerical treatment of the source terms is based on an extension of the hydrostatic reconstruction technique. Notice that the presented numerical scheme improves previous results proposed by Goutal *et al.* [GM02] and implemented in the simulation tool "Mascaret" [mas09].

Introducing $X = (S, S\overline{u})^T$, we rewrite the system (3.32)-(3.33) under the form

$$\frac{\partial X}{\partial t} + \frac{\partial F(X)}{\partial x} = S_b(X) + S_f(X), \tag{5.1}$$

with $F(X)$ the flux of the hyperbolic part, $S_b(X)$ the topography source terms and $S_f(X)$ the friction term.

We denote $X_i^n = (S_i^n, q_i^n)$ the approximate solution at time t^n on the cell C_i with $q_i^n = S_i^n \overline{u}_i^n$.

5.2.1 Time scheme

For the time discretization, we apply time splitting to the equation (5.1) and we write

$$\frac{\tilde{X}^{n+1} - X^n}{\Delta t^n} + \frac{\partial F(X^n)}{\partial x} = S_b(X^n), \tag{5.2}$$

$$\frac{X^{n+1} - \tilde{X}^{n+1}}{\Delta t^n} - S_f(X^n, X^{n+1}) = 0. \tag{5.3}$$

Classically we first compute the hyperbolic part (5.2) of the system by an explicit scheme. This first computation includes the topographic source terms in order to preserve relevant equilibria [ABB+04]. Concerning the friction terms that are dissipative, three strategies are available. The first one consists in a semi-implicit scheme (5.3) having good stability properties. The second way is to write the bottom friction law as a modification of the topography $\overline{z}_b$ [Bou04b]. The third possibility is to use a simple Euler explicit time scheme. These three approaches are explained in paragraph 5.2.3.

5.2.2 Numerical scheme : explicit part

To perform the explicit step we deduce a finite volume kinetic scheme from the kinetic interpretation of the section-averaged system. The kinetic solver used here has several advantages among which is the nonnegativity of the water height.

Starting from a piecewise constant approximation of the initial data, the general form of a finite volume method is

$$\tilde{X}_i^{n+1} - X_i^n + \sigma_i^n \left[F_{i+1/2}^n - F_{i-1/2}^n \right] = \sigma_i^n S_{b,i}^n, \tag{5.4}$$

where $\sigma_i^n = \Delta t^n / \Delta x_i$ is the ratio between time and space steps and the numerical flux $F_{i+1/2}^n$ is an approximation of the exact flux estimated at point $x_{i+1/2}$.

The topographic source term $S_{b,i}^n$ is not deduced from the kinetic interpretation (see [PS01]) but computed by a generalisation of the hydrostatic reconstruction presented in [ABB+04], see prop. 15.

Hyperbolic part As in [AB05a, ABD08] the kinetic interpretation (4.6) is used to precise the expression of the fluxes $F_{i+1/2}^n$ in (5.4). First, by analogy with (4.5) we define the discrete densities of particles $M_{S,i}^n$ by

$$M_{S,i}^n(\xi) = \frac{A^{-1}(H_i^n)}{c_i^n} \chi\left(\frac{\xi - \overline{u}_i^n}{c_i^n} \right),$$

with

$$c_i^n = \sqrt{g\frac{L_{b,i}H_i^n + L_{1,i}B(A^{-1}(H_i^n))}{A^{-1}(H_i^n)}},$$

where A^{-1} denotes the inverse of the operator A introduced in (3.29).

Then Eq. (4.6) without the topographic source terms is discretized by applying a simple upwind scheme for the advection term

$$f_i^{n+1}(\xi) = M_{S,i}^n(\xi) - \xi\sigma_i^n\left(M_{S,i+1/2}^n(\xi) - M_{S,i-1/2}^n(\xi)\right), \tag{5.5}$$

where

$$M_{S,i+1/2}^n = \begin{cases} M_{S,i}^n & \text{if } \xi \geq 0 \\ M_{S,i+1}^n & \text{if } \xi < 0. \end{cases}$$

Each new density function f_i^{n+1} is not an equilibrium but thanks to the property of the collision term (see Eq. (4.7)) and by analogy with (4.12)-(4.13) we can recover the macroscopic quantities at time t^{n+1}. We write

$$S_i^{n+1} = \int_{\mathbb{R}} f_i^{n+1}(\xi)d\xi,$$

and by a simple integration in ξ of (5.5) against the vector $\mathcal{K}(\xi)$ given by $\mathcal{K}(\xi) = (1,\xi)^T$, we can precise the macroscopic formula (5.4) (without the topographic term)

$$\tilde{X}_i^{n+1} = \int_{\mathbb{R}} \mathcal{K}(\xi)\ f_i^{n+1}(\xi)d\xi. \tag{5.6}$$

If we denote

$$F_{i+1/2}^n = F(X_i^n, X_{i+1}^n) = F^+(X_i^n) + F^-(X_{i+1}^n),$$

we define

$$F^-(X_i^n) = \int_{\xi\in\mathbb{R}^-} \xi\mathcal{K}(\xi)\ M_{S,i}^n(\xi)\ d\xi, \quad F^+(X_i^n) = \int_{\xi\in\mathbb{R}^+} \xi\mathcal{K}(\xi)\ M_{S,i}^n(\xi)\ d\xi. \tag{5.7}$$

More precisely the expression of $F^+(X_i)$ can be written

$$F^+(X_i) = \begin{pmatrix} F_S^+(X_i) \\ F_q^+(X_i) \end{pmatrix}, \tag{5.8}$$

with

$$F_S^+(X_i) = A^{-1}(H_i)\int_{-\frac{\overline{u}_i}{c_i}}^{\infty} (\overline{u}_i + wc_i)\chi(w)dw,$$
$$F_q^+(X_i) = A^{-1}(H_i)\int_{-\frac{\overline{u}_i}{c_i}}^{\infty} (\overline{u}_i + wc_i)^2\chi(w)dw.$$

We denote also

$$\mathcal{F}_{S,i} = F_{S,i+1/2} - F_{S,i-1/2} = F_S^+(X_i) + F_S^-(X_{i+1}) - \left(F_S^+(X_{i-1}) + F_S^-(X_i)\right).$$

This kinetic method is interesting because it gives a very simple and natural way to propose a numerical flux through the kinetic interpretation. If we can perform analytically the integration in (5.8), i.e. if the probability function χ defined in (4.1) is chosen to be simple enough, it is also

numerically powerfull because the kinetic level disappears and the scheme is written directly as a macroscopic scheme for which only very simple computations are needed. For instance the simplest choice is

$$\chi(w) = \frac{1}{2\sqrt{3}} 1_{|w|\leq\sqrt{3}}(w), \tag{5.9}$$

and we use it in the following. Then the numerical fluxes are explicitly given by

$$F_S^+(X) = \frac{A^{-1}(H)}{4\sqrt{3}c}\left(M_+^2 - M_-^2\right), \quad F_q^+(X) = \frac{A^{-1}(H)}{6\sqrt{3}c}\left(M_+^3 - M_-^3\right),$$

with $M_+ = \max\{0, \bar{u} + \sqrt{3}c\}$ and $M_- = \max\{0, \bar{u} - \sqrt{3}c\}$.

Topographic source terms Cell-centered evaluations of the source term in (5.2) and (5.4) will generally not be able to maintain the steady states of a lake at rest, which are characterized by (see [GL96])

$$\bar{u}_i^n = 0, \quad H_i^n + z_{b,i} = Cst \in \mathbb{R}, \qquad \forall i, \quad \forall n. \tag{5.10}$$

The source term $S_{b,i}^n = (S_{b,S,i}^n, S_{b,q,i}^n)$ is an approximation of the topographic source terms and we follow the technique proposed by Audusse *et al.* [ABB$^+$04] that consists in locally representing the cell-averaged source term as the discrete gradient of the hydrostatic momentum flux. This ansatz is motivated by the balancing requirement as follows. For nearly hydrostatic flows, one has $\overline{u} \ll \sqrt{gH}$. In the associated asymptotic limit the leading order water height H adjusts so as to satisfy the balance of momentum flux and momentum source terms, i.e.

$$\frac{\partial}{\partial x}\int_{\overline{z}_b}^{\overline{\eta}} (gL(x,z)(\eta - z))\, dz = -gHL(x,\overline{z}_b)\frac{\partial \overline{z}_b}{\partial x} + g\int_{\overline{z}_b}^{\overline{\eta}} (\overline{\eta} - z)\frac{\partial L}{\partial x} dz.$$

Integrating over the ith grid cell we obtain an approximation of the source term under the form

$$\begin{aligned}\int_{x_{j-1/2}}^{x_{j+1/2}} \left(-gHL(x,\overline{z}_b)\frac{\partial \overline{z}_b}{\partial x} + g\int_{\overline{z}_b}^{\overline{\eta}} (\overline{\eta} - z)\frac{\partial L}{\partial x} dz\right) dx = \\ \int_{\overline{z}_b}^{\overline{\eta}} (gL(x,z)(\eta - z))\, dz\Big|_{x_{j+1/2}} - \int_{\overline{z}_b}^{\overline{\eta}} (gL(x,z)(\eta - z))\, dz\Big|_{x_{j-1/2}}.\end{aligned} \tag{5.11}$$

Following (5.11) and using relation (3.31), we adopt the following discretization

$$\begin{aligned} S_{b,S,i}^n &= 0, \\ S_{b,q,i}^n &= g\left(L_{b,i+1/2}\frac{(H_{i+1/2-}^n)^2}{2} + L_{1,i+1/2}B_{i+1/2}(A^{-1}(H_{i+1/2-}^n))\right) \\ &\quad - g\left(L_{b,i-1/2}\frac{(H_{i-1/2+}^n)^2}{2} + L_{1,i-1/2}B_{i-1/2}(A^{-1}(H_{i-1/2+}^n))\right). \end{aligned} \tag{5.12}$$

with $\overline{z}_{b,i+1/2} = \max\{\overline{z}_{b,i}, \overline{z}_{b,i+1}\}$ and

$$\begin{aligned} &H_{i+1/2-}^n = H_i^n + \overline{z}_{b,i} - \overline{z}_{b,i+1/2}, \quad H_{i+1/2+}^n = H_{i+1}^n + \overline{z}_{b,i+1} - \overline{z}_{b,i+1/2}, \\ &L_{b,i+1/2} = L_{b,i} + \frac{1}{2}(L_{b,i+1} - L_{b,i}), \quad L_{1,i+1/2} = L_{1,i} + \frac{1}{2}(L_{1,i+1} - L_{1,i}), \\ &\overline{\alpha}_{i+1/2} = \overline{\alpha}_i + \frac{1}{2}(\overline{\alpha}_{i+1} - \overline{\alpha}_i), \quad B_i(S_i) = B(S_i, x_i). \end{aligned}$$

We can now precise the first-order well-balanced finite volume scheme (5.4) with

$$
\begin{aligned}
&F_{i+1/2} = \mathcal{F}(X_{i+1/2-}, X_{i+1/2+}),\\
&X_{i+1/2-} = \begin{pmatrix} H_{i+1/2-} \\ H_{i+1/2-}\bar{u}_i \end{pmatrix}, \quad X_{i+1/2+} = \begin{pmatrix} H_{i+1/2+} \\ H_{i+1/2+}\bar{u}_{i+1} \end{pmatrix},\\
&H_{i+1/2\pm} = \max\{0, H_{i+1/2\pm}\}, \quad S_{b,i} = S_{b,i+1/2-} + S_{b,i-1/2+},
\end{aligned}
$$

and

$$
S^n_{b,i+1/2-} = -\begin{pmatrix} 0 \\ C(H^n_{i+1/2-}, H^n_i) \end{pmatrix},
$$

$$
S^n_{b,i-1/2+} = \begin{pmatrix} 0 \\ C(H^n_{i-1/2+}, H^n_i) \end{pmatrix},
$$

where

$$
\begin{aligned}
C(H^n_{i+1/2-}, H^n_i) &= g\left(L_{b,i+1/2}\frac{(H^n_{i+1/2-})^2}{2} + L_{1,i+1/2}B_{i+1/2}(A^{-1}(H^n_{i+1/2-}))\right)\\
&\quad -g\left(L_{b,i}\frac{(H^n_i)^2}{2} + L_{1,i}B_i(A^{-1}(H^n_i))\right),\\
C(H^n_{i-1/2+}, H^n_i) &= g\left(L_{b,i-1/2}\frac{(H^n_{i-1/2+})^2}{2} + L_{1,i-1/2}B_{i-1/2}(A^{-1}(H^n_{i-1/2+}))\right)\\
&\quad -g\left(L_{b,i}\frac{(H^n_i)^2}{2} + L_{1,i}B_i(A^{-1}(H^n_i))\right).
\end{aligned}
$$

With this re-interpretation of the source terms in mind, we may also rewrite the scheme (5.4) as

$$
\frac{1}{\sigma^n_i}\left(\tilde{X}^{n+1}_i - X^n_i\right) + \left[\mathcal{F}^n_{i+1/2} - \mathcal{F}^n_{i-1/2}\right] = 0, \tag{5.13}
$$

with $\mathcal{F}^n_{i+1/2} = F^n_{i+1/2} - S^n_{b,i+1/2-}$, $\mathcal{F}^n_{i-1/2} = F^n_{i-1/2} + S^n_{b,i-1/2+}$. The latter expression for the source terms is equivalent to the earlier (5.12), it shows that the source may be considered as being distributed to the cell interfaces. Then we have the following proposition

Proposition 15. *The discretization of the source terms given by (5.12) preserves the steady states of the "lake at rest" (5.10) of the section averaged Saint-Venant system.*

Proof. On a steady state of a lake at rest, we have $H_{i+1/2-} = H_{i+1/2+}$ and $\bar{u}_{i+1} = \bar{u}_i$ thus $X_{i+1/2-} = X_{i+1/2+}$ and the kinetic scheme gives

$$
F^n_{i+1/2} = \begin{pmatrix} 0 \\ g\left(L_{b,i+1/2}\frac{\left(H^n_{i+1/2-}\right)^2}{2} + L_{1,i+1/2}B_{i+1/2}(A^{-1}(H^n_{i+1/2-}))\right) \end{pmatrix},
$$

and

$$
F^n_{i-1/2} = \begin{pmatrix} 0 \\ g\left(L_{b,i-1/2}\frac{\left(H^n_{i-1/2+}\right)^2}{2} + L_{1,i-1/2}B_{i-1/2}(A^{-1}(H^n_{i-1/2+}))\right) \end{pmatrix}.
$$

So we have $F^n_{i+1/2} - F^n_{i-1/2} = S^n_{b,i+1/2-} - S^n_{b,i-1/2+}$ that completes the proof. □

5.2.3 Friction and viscous terms

Even if the bottom friction corresponds to dissipative and hence stabilizing effects, its numerical discretization is not always straightforward, see paragraph 6.1.1 and all the literature concerning Roll waves. In practice in cases of dry areas, large Froude numbers or when dealing with large friction effects, a stable treatment of the friction source term is necessary and hence an implicit scheme is often used. Unfortunately, such a centered discretization can be inaccurate for transcritical flows and the preservation of stationnary states. In such situations, the apparent topography [Bou04b] procedure can be useful.

Semi-implicit treatment Since the friction terms only appear in the momentum equation, this implicit step does not affect the discrete wet surface and water height therefore $S_i^{n+1} = \tilde{S}_i^{n+1}$ and $H_i^{n+1} = \tilde{H}_i^{n+1}$. So the computation of the new velocitiy $\bar{u}^{n+1}$ leads to solve the discrete equation

$$q_i^{n+1} = q_i^n - \Delta t^{n+1} S_{f,i}^{n+1}. \tag{5.14}$$

Several friction laws can be used among which are Navier, Chezy, Darcy-Weisbach, Manning and Strickler laws.

For stationnary solutions, since we have $S_i^{n+1} = S_i^n$, the continuity equation ensures at the discrete level $\frac{\partial q^n}{\partial x} = 0$. But the discretization used in (5.14) does not ensure at the discrete level $\frac{\partial q^{n+1}}{\partial x} = 0$. The reconstruction of an apparent topography, presented hereafter, allows to avoid this difficulty.

Apparent topography Another possibility to discretize the bottom friction term is to write it as an apparent topography source term. The key point of the apparent topography method proposed by Bouchut [Bou04b] is to write the friction term as

$$S_f(X) = \frac{\partial F_r}{\partial x}.$$

Then the steady states of the lake at rest become $u = 0, \quad H + \overline{z}_b - F_r = Cste$ and the apparent topography is given by

$$\overline{z}_{mod} = \overline{z}_b - F_r. \tag{5.15}$$

And we apply the scheme (5.13) with this new topography. This approach has been tested in [8], see the obtained results depicted in paragraph 6.1.

Explicit scheme Using a simple explicit scheme

$$q_i^{n+1} = q_i^n - \Delta t^n S_{f,i}^n,$$

a stability condition appears on Δt^n ensuring $q_i^{n+1} q_i^n \geq 0$.

Viscous terms As for the friction terms, the viscous terms do not affect the continuity equation. The use of an implicit scheme requires to solve a linear system

$$q_i^{n+1} = q_i^n - \Delta t^{n+1} S_{v,i}^{n+1},$$

since S_v^{n+1} is linear in $(q_1, \ldots, q_N)$. When an explicit scheme is singled out

$$q_i^{n+1} = q_i^n - \Delta t^n S_{v,i}^n,$$

no linear system has to be solved but a stability condition depending on the viscosity coefficient, appears on Δt^n that could be more restrictive than the usual CFL condition given herafter.

For the viscous terms, we have not encountered any phenomenon similar instabilities between friction terms and topography source terms.

5.2.4 Stability of the scheme

We now establish the stability property of the kinetic scheme. Classically for the Saint-Venant system, a CFL condition ensures the water height is non negative. This CFL condition means that the quantity of water leaving a given cell during a time step Δt^n is less than the actual water in the cell.

Proposition 16. *Assume that the function χ has a compact support of length $2w_M$ then under the CFL condition*

$$\Delta t^n \leq \min_{i \in I} \frac{\Delta x_i}{|u_i^n| + w_M c_i^n}, \tag{5.16}$$

the kinetic scheme (5.4), (5.8) and (5.12) keeps the water height positive i.e. $S_i^n \geq 0$ and $H_i^n \geq 0$ if it is true initially. Notice that this condition does not depend on the section profile variations $\frac{\partial z_b}{\partial x}$, $\frac{\partial L_b}{\partial x}$ and $\frac{\partial L_1}{\partial x}$.

Proof. The proof has been adapted from those given in [AB03, PS01] and is not presented here. □

5.2.5 Second order scheme

The second-order extension is globally described in paragraph 5.1.2. For a detailed presentation, the reader can refer to [8].

Concerning the friction terms, the second order extension can be applied with the apparent topography (5.15) presented in paragraph 5.2.3, see also paragraph 6.1.1. But due to the nonlinearities appearing in classical friction laws, a second order extension of the implicit step procedure presented in paragraph 5.2.3 is not straightforward.

Notice that we only give a formal proof of the efficiency of the second order reconstruction by calculating, for a test problem, the convergence order of the 1^{st} and 2^{nd} order scheme, see paragraph 6.1.3.

5.3 Non-hydrostatic Saint-Venant system [5, 7]

Now we are interested in finding an efficient numerical scheme for the non-hydrostatic Saint-Venant system derived in paragraph 3.3. Several works recently appeared where the scheme for the resolution of such non-hydrostatic systems is based on a mixed finite volume/finite differences approaches [BBC$^+$10, CLM10, LMGH10].

The strong point of the scheme we propose is the following. As its name indicates, an extended Saint-Venant system is an extension of the usual Saint-Venant system so we propose a numerical scheme that only consists in a slight modification of any existing solver for the Saint-Venant system. In this paragraph we present how, starting from a numerical scheme solving the classical Saint-Venant system, the non-hydrostatic terms can be added. To illustrate this property, a finite volume kinetic solver and a Roe solver [GM02] are used to obtain the numerical simulations presented in paragraph 6.2.

Notice that the presented numerical scheme is implemented in the industrial code Mascaret [mas09] that solves the section-averaged Saint-Venant system using a Roe scheme. The Mascaret modeing system is used for dam breaks simulations, flooding,...

If we compare the system (3.37)-(3.41) with the usual Saint-Venant system, we notice that the complementary terms arising from the non-hydrostatic pressure terms have no influence over the mass conservation equation. In a condensed form, the x-momentum equation (3.38) becomes

$$\frac{\partial}{\partial t}\left(H\overline{u}+\mathcal{M}_2(X,\frac{\partial}{\partial x})\right)+\frac{\partial}{\partial x}\left(H\overline{u}^2+\frac{g}{2}H^2\right)+\mathcal{N}_2(X,\frac{\partial}{\partial t},\frac{\partial}{\partial x})= -gH\frac{\partial z_b}{\partial x}+p^a\frac{\partial \eta}{\partial x},$$

with

$$\begin{aligned}\mathcal{M}_2(X,\frac{\partial}{\partial x}) &= \frac{\partial}{\partial x}\left(-\frac{H^3}{3}\frac{\partial \overline{u}}{\partial x}+\frac{H^2}{2}\frac{\partial z_b}{\partial x}\overline{u}\right)+\frac{\partial z_b}{\partial x}\left(-\frac{H^2}{2}\frac{\partial \overline{u}}{\partial x}+\frac{\partial z_b}{\partial x}H\overline{u}\right),\\ \mathcal{N}_2(X,\frac{\partial}{\partial t},\frac{\partial}{\partial x}) &= \frac{\partial}{\partial x}\left(\frac{\partial H^2}{\partial t}\left(H\frac{\partial \overline{u}}{\partial x}-\frac{\partial z_b}{\partial x}\overline{u}\right)\right)+2\frac{\partial z_b}{\partial x}\frac{\partial H}{\partial t}\left(H\frac{\partial \overline{u}}{\partial x}-\frac{\partial z_b}{\partial x}\overline{u}\right)\\ &\quad -\frac{\partial^2 z_b}{\partial t\partial x}\left(-\frac{H^2}{2}\frac{\partial \overline{u}}{\partial x}+\frac{\partial z_b}{\partial x}H\overline{u}\right).\end{aligned}$$

So, the system (3.37)-(3.41) we have to solve can be written under the form

$$\frac{\partial X}{\partial t}+\frac{\partial}{\partial t}\mathcal{M}(X,\frac{\partial}{\partial x})+\frac{\partial}{\partial x}F(X)+\mathcal{N}(X,\frac{\partial}{\partial t},\frac{\partial}{\partial x})=S_b(X)+S_{f,v}(X), \tag{5.17}$$

where X, $F(X)$, $S_b(X)$ and $S_{f,v}(X)$ defined by

$$X=\begin{pmatrix} H \\ H\overline{u}\end{pmatrix},\quad F(X)=\begin{pmatrix} H\overline{u} \\ H\overline{u}^2+\frac{g}{2}H^2\end{pmatrix},$$
$$S_b(X)=\begin{pmatrix} 0 \\ -gH\frac{\partial z_b}{\partial x}+p^a\frac{\partial \eta}{\partial x}\end{pmatrix},\qquad S_{f,v}(X)=\begin{pmatrix} 0 \\ -4\frac{\partial}{\partial x}\left(\nu\frac{\partial \overline{u}}{\partial x}\right)-\kappa(X)\overline{u}\end{pmatrix},$$

are respectively the state vector, the conservative part, the topography source terms and the friction/viscous terms. We also denote

$$\mathcal{M}=\begin{pmatrix} 0 \\ \mathcal{M}_2\end{pmatrix},\quad \mathcal{N}=\begin{pmatrix} 0 \\ \mathcal{N}_2\end{pmatrix}.$$

When $\mathcal{M}$ and $\mathcal{N}$ are neglected, Eq. (5.17) reduces to the classical Saint-Venant system.

Remark 5.1. *For the sake of simplicity, the derivation of the non-hydrostatic model has been carried out in paragraph 3.3 starting from the Euler equations so the viscous and friction terms do not appear in the model proposed in Prop. 2. Obviously, the dissipative terms appearing in the Saint-Venant system derivated from the Navier-Stokes system (see [GP01]) are still valid, this explains the chosen expression for $S_{f,v}(X)$. For a more complete asymptotic derivation of the dissipative terms, the reader can refer to [5].*

5.3.1 Time discretization

For the time discretization, we apply a time splitting to the equation (5.17) and we write

$$\frac{\tilde{X}^{n+1} + \mathcal{M}(\tilde{X}^{n+1}, \frac{\partial}{\partial x}) - \left(X^n + \mathcal{M}(X^n, \frac{\partial}{\partial x})\right)}{\Delta t^n} + \frac{\partial F(X^n)}{\partial x} + \mathcal{N}(\tilde{X}^{n+1}, X^n, \frac{\partial}{\partial x}) = S_b(X^n), \tag{5.18}$$

$$\frac{X^{n+1} - \tilde{X}^{n+1}}{\Delta t^n} - S_{f,v}(X^n, X^{n+1}) = 0, \tag{5.19}$$

where $\mathcal{N}(\tilde{X}^{n+1}, X^n, \frac{\partial}{\partial x})$ is a time approximation of the quantity $\mathcal{N}(X, \frac{\partial}{\partial t}, \frac{\partial}{\partial x})$

$$\mathcal{N}(\tilde{X}^{n+1}, X^n, \frac{\partial}{\partial x}) \approx \frac{1}{\Delta t^n} \int_{t^n}^{t^{n+1}} \mathcal{N}(X, \frac{\partial}{\partial t}, \frac{\partial}{\partial x}) dt,$$

precised later.

We first compute the conservative part of (5.18) by an explicit scheme. This first step also includes the topography source terms S_b in order to preserve relevant equilibria [ABB$^+$04]. Concerning the viscous and friction terms $S_{f,v}$ in (5.19), they have been omitted in the derivation and their numerical treatment do not differ from earlier works of the authors [3]. Since these terms are dissipative, we prefer a semi-implicit scheme for reasons of stability (see paragraph 5.2.3).

Classically for the solution of the Saint-Venant system, a finite volume scheme is used so the discretization of the system (5.18) leads to

$$\tilde{X}_i^{n+1} + \mathcal{M}_i^{n+1} - (X_i^n + \mathcal{M}_i^n) + \frac{\Delta t^n}{\Delta x_i}\left(F_{i+1/2}^n - F_{i-1/2}^n\right) + \mathcal{N}_i^{n+1/2} = \Delta t^n S_b(X_i^n), \tag{5.20}$$

where the numerical flux $F_{i+1/2}^n$ is an approximation of the exact flux of the conservative part estimated at point $x_{i+1/2}$, see paragraph 5.3.2. In the sequel we precise the space discretization of the non-hydrostatic terms involving $\mathcal{M}$ and $\mathcal{N}$ and appearing in Eq. (5.20), i.e.

$$\mathcal{M}_i^{n+1} \approx \frac{1}{\Delta x_i} \int_{C_i} \mathcal{M}(\tilde{X}^{n+1}, \frac{\partial}{\partial x}) dx,$$

$$\mathcal{N}_i^{n+1/2} \approx \frac{1}{\Delta x_i} \int_{C_i \times [t_n, t_{n+1}]} \mathcal{N}(\tilde{X}^{n+1/2}, \frac{\partial}{\partial t}, \frac{\partial}{\partial x}) dx dt.$$

5.3.2 Numerical fluxes

The numerical fluxes appearing in Eq. (5.20) are obtained from any finite volume solver for the Saint-Venant equations and no special requirement is made for this solver. In paragraph 6.2, the authors have tested a Roe solver [GM02] and a kinetic solver [ABP00, PS01]. It appears that the accuracy of the simulations greatly depends on the accuracy of the used finite volume solver.

5.3.3 Well-balanced scheme and second order extension

The second-order accuracy is recovered as described in paragraph 5.1.2. To get a positive preserving and well-balanced scheme, the quantities H and z_b appearing the conservative part $F(X)$ and in the source term $S_b(X)$ are discretized using the classical hydrostatic reconstruction procedure [ABB$^+$04].

5.3.4 Space discretazition of the non-hydrostatic terms

Since the non-hydrostatic pressure terms of the system (5.17) have no influence on the conservative part, the numerical scheme used to solve the continuity equation for the Saint-Venant system remains unchanged.

For the space discretization of the non-hydrostatic terms, we use a first order centered scheme. More precisely, we detail below the numerical discretization only for $\mathcal{M}_2^1$ the leading term of $\mathcal{M}_2$

$$\mathcal{M}_2^{1,n+1} = \frac{\partial}{\partial x}\left(\frac{(H^{n+1})^3}{3}\frac{\partial \overline{u}^{n+1}}{\partial x}\right),$$

and we have

$$\begin{aligned}\mathcal{M}_{2,i}^{1,n+1} &\approx \left.\frac{(H_{i+1/2}^{n+1})^3}{3}\frac{\partial \overline{u}^{n+1}}{\partial x}\right|_{i+1/2} - \left.\frac{(H_{i-1/2}^{n+1})^3}{3}\frac{\partial \overline{u}^{n+1}}{\partial x}\right|_{i-1/2} \\ &= \frac{(H_{i+1/2}^{n+1})^3}{3\Delta x_{i+1/2}}\left(\overline{u}_{i+1}^{n+1} - \overline{u}_i^{n+1}\right) - \frac{(H_{i-1/2}^{n+1})^3}{3\Delta x_{i-1/2}}\left(\overline{u}_i^{n+1} - \overline{u}_{i-1}^{n+1}\right),\end{aligned}$$

with $H_{i+1/2}^{n+1} = 1/2(H_{i+1}^{n+1} + H_i^{n+1})$, $\overline{u}_i^{n+1} = (H\overline{u})_i^{n+1}/H_i^{n+1}$ and $\Delta x_{i+1/2} = x_{i+1} - x_i$. Because we use an explicit time scheme and since the mass conservation equation does not contain any non-hydrostatic term, it is solved before the x-momentum equation. So the quantities H_i^{n+1} for $i \in I$ are known when discretizing $\mathcal{M}_i^{n+1}$. For the other non-hydrostatic terms appearing in $\mathcal{M}$ we perform the same type of discretization as for $\mathcal{M}_2^1$, then the solution of the x-momentum equation needs the inversion of a tridiagonal mass matrix.

Similarly, for $\mathcal{N}_2^1$ the leading term of $\mathcal{N}_2$

$$\mathcal{N}_2^1 = \frac{\partial}{\partial x}\left(\frac{\partial H^2}{\partial t}\left(H\frac{\partial \overline{u}}{\partial x}\right)\right),$$

we write

$$\begin{aligned}\mathcal{N}_{2,i}^{1,n+1/2} &= \left((H_{i+1/2}^{n+1})^2 - (H_{i+1/2}^n)^2\right)\frac{H_{i+1/2}^n}{\Delta x_{i+1/2}}\left(\overline{u}_{i+1}^n - \overline{u}_i^n\right) \\ &\quad - \left((H_{i-1/2}^{n+1})^2 - (H_{i-1/2}^n)^2\right)\frac{H_{i-1/2}^n}{\Delta x_{i-1/2}}\left(\overline{u}_i^n - \overline{u}_{i-1}^n\right).\end{aligned}$$

5.3.5 Boundary conditions

Two types of boundary conditions appear in the model (3.37)-(3.41), those associated with the classical Saint-Venant system, that are not detailed here, and those coming from the non-hydrostatic terms.

For the non-hydrostatic terms, we have to prescribe boundary conditions for quantities like

$$\frac{\partial^2 \overline{u}}{\partial x^2}, \quad \text{and} \quad \frac{\partial \overline{u}}{\partial x}.$$

Since there is no natural way to proceed, we assume at each boundary we have

$$\frac{\partial \overline{u}}{\partial \underline{n}} = 0,$$

$\underline{n}$ being the outward normal at the inflow and outflow boundaries. For the test cases presented in paragraph 6.2, this assumption is valid but in more complex physical situations the numerical treatment of the boundary conditions should be improved.

5.3.6 Stability of the scheme

Classically, a stability property of the scheme has to be established through a CFL condition ensuring the water height remains non negative. As already mentioned, the non-hydrostatic terms do not appear in the mass conservation equation so the stability property for the used Saint-Venant solver remains valid when the non-hydrostatic terms are added.

5.4 Hydrostatic Navier-Stokes system with varying density [3, 2, 4]

Last but not least, we present a numerical scheme for the hydrostatic Navier-Stokes system with varying density given in paragraph 3.5 (page 37). Notice that this scheme is also valid for the simulation of the model proposed in paragraph 3.4 i.e. when the fluid density is constant and/or when the transport/diffusion equation of the tracer is not considered.

The discrete scheme is based on the kinetic interpretation obtained in paragraph 4.4.3 (page 49). This choice is motivated by several arguments. First the kinetic interpretation is a good starting point to build stable numerical schemes. We prove in paragraph 5.4.8 that the presented kinetic scheme preserves the positivity of the water height and ensures a discrete local maximum principle for the tracer concentration (temperature, salinity...). Second the construction of the kinetic scheme does not need the computation of the eigenvalues of the conservative part of the system. This point is very important here since these eigenvalues are hardly accessible, see paragraph 3.4.5 where the hyperbolicity is discussed. Finally we insist on the fact that the kinetic scheme is no more expensive than the usual solvers (Roe, HLL...). The kinetic interpretation allows us to derive efficient numerical fluxes and is the cornerstone of the stability proof but the practical computation is entirely made at the macroscopic level.

The multilayer system obtained in Prop. 3 is of the form

$$\frac{\partial X}{\partial t} + \frac{\partial F(X)}{\partial x} = S_e(X) + S_p(X) + S_{v,f}(X), \tag{5.21}$$

with $X = \left(\sum_{\alpha=1}^{N} \rho_\alpha l_\alpha H, q_1, \dots, q_N, k_1, \dots, k_N\right)^T$ and $q_\alpha = \rho_\alpha l_\alpha H u_\alpha$, $k_\alpha = \rho_\alpha l_\alpha H T_\alpha$. We denote $F(X)$ the flux of the conservative part, $S_e(X)$, $S_p(X)$ and $S_{v,f}(X)$ the source terms, respectively the mass transfer, the pressure at the interfaces and the viscous and friction effects. The viscous and friction terms do not depend on the fluid density. Their expressions are not recalled here, see [3].

We introduce a $(2N+1) \times 2N$ matrix $\mathcal{K}(\xi)$ defined by $\mathcal{K}_{1,j} = 1$, $\mathcal{K}_{1,j+N} = 0$ for $j = 1, \dots, N$, $\mathcal{K}_{i+1,j} = \delta_{i,j}\ \xi$, $\mathcal{K}_{i+N+1,j+N} = \delta_{i,j}$ for $i, j = 1, \dots, N$ with $\delta_{i,j}$ the Kronecker symbol. Then, using Prop. 11, we can write

$$X = \int_\xi \mathcal{K}(\xi) \begin{pmatrix} M(\xi) \\ U(\xi) \end{pmatrix} d\xi, \quad F(X) = \int_\xi \xi \mathcal{K}(\xi) \begin{pmatrix} M(\xi) \\ U(\xi) \end{pmatrix} d\xi, \tag{5.22}$$

$$S_e(X) = \int_\xi \mathcal{K}(\xi) \begin{pmatrix} N(\xi) \\ V(\xi) \end{pmatrix} d\xi, \quad S_p(X) = \int_\xi \mathcal{K}(\xi) \begin{pmatrix} P(\xi) \\ 0 \end{pmatrix} d\xi, \tag{5.23}$$

with $M(\xi) = (M_1(\xi), \dots, M_N(\xi))^T$, $U(\xi) = (U_1(\xi), \dots, U_N(\xi))^T$ and

$$P(\xi) = \begin{pmatrix} S_{3/2}(\xi) - S_{1/2}(\xi) \\ \vdots \\ S_{N+1/2}(\xi) - S_{N-1/2}(\xi) \end{pmatrix},$$
$$W(\xi) = \begin{pmatrix} W_{3/2}(\xi) - W_{1/2}(\xi) \\ \vdots \\ W_{N+1/2}(\xi) - W_{N-1/2}(\xi) \end{pmatrix}, \quad \text{for} \quad W = N, V.$$

We denote $X_i^n = \left(\sum_{\alpha=1}^N \rho_{\alpha,i}^n l_\alpha H_i^n, q_{1,i}^n, \dots, q_{N,i}^n, k_{1,i}^n, \dots, k_{N,i}^n\right)^T$ the approximate solution at time t^n on the cell C_i with $q_{\alpha,i}^n = \rho_{\alpha,i}^n l_\alpha H_i^n u_{\alpha,i}^n$, $k_{\alpha,i}^n = \rho_{\alpha,i}^n l_\alpha H_i^n T_{\alpha,i}^n$ and $\rho_{\alpha,i}^n = \rho(T_{\alpha,i}^n)$. Notice that to deduce the primitive variables $H_i^n, u_{1,i}^n, \dots, u_{N,i}^n, T_{1,i}^n, \dots, T_{N,i}^n$ from X_i^n, a non-linear problem has to be solved (see paragraph 5.4.7).

5.4.1 Time discretization

For the time discretization, we apply a time splitting to the equation (5.21) and we write

$$\frac{\tilde{X}^{n+1} - X^n}{\Delta t^n} + \frac{\partial F(X^n)}{\partial x} = \mathcal{S}_e(X^n, \tilde{X}^{n+1}) + \mathcal{S}_p(X^n), \tag{5.24}$$
$$\frac{X^{n+1} - \tilde{X}^{n+1}}{\Delta t^n} - \mathcal{S}_{v,f}(X^n, X^{n+1}) = 0. \tag{5.25}$$

Because of the multilayer approach, the numerical scheme is more complex than the one described in paragraph 5.2 and we detail hereafter its key points. We first compute the conservative part of (5.24) by an explicit kinetic scheme (paragraphs 5.4.2 and 5.4.3). The mass exchange terms are also deduced of the kinetic interpretation (paragraph 5.4.4). The first step also includes the pressure source terms at the interfaces in order to preserve relevant equilibria [ABB$^+$04]. Concerning the viscous and friction terms $S_{v,f}$ in (5.25), their numerical treatment do not differ from what is proposed in paragraph 5.2.3.

5.4.2 Discrete kinetic equations

To perform the first step (5.18) we deduce a finite volume kinetic scheme from the kinetic interpretation (4.20)-(4.21) of the system (3.73)-(3.75). Notice that the hyperbolicity of the multilayer system remains an open problem, see paragraph 3.4.5. Moreover the eigenvalues of the matrix of the quasilinear form of the dynamical system can not be computed analytically and are hardly accessible. Thus any solver requiring the knowledge of the eigenvalues would face difficulties while the kinetic scheme is easily extended [AB07]. Notice also that the kinetic scheme instead of using discrete eigenvalues of the matrix, uses a continuum of eigenvalues and is able to deal with situations where some of the discrete eigenvalues are complex.

Starting from a piecewise constant approximation of the initial data and with the usual notations, the general form of a finite volume discretization of system (5.18) is

$$\tilde{X}_i^{n+1} - X_i^n + \sigma_i^n \left[F_{i+1/2}^n - F_{i-1/2}^n\right] = \Delta t^n \mathcal{S}_{e,i}^{n+1/2} + \sigma_i^n \mathcal{S}_{p,i}^n. \tag{5.26}$$

We propose an interesting progress for the numerical treatment of the pressure source terms $\mathcal{S}_{p,i}^n$ at the layers interfaces. It uses an extended version of the hydrostatic reconstruction, see paragraph. 5.4.5 combined with the kinetic equation. As in [AB05a, ABD08] the kinetic interpretation (4.20)-(4.21) is used to precise the expression of the fluxes $F_{i+1/2}^n$ in (5.26). Assuming that the primitive variables $H_i^n, u_{1,i}^n, \ldots, u_{N,i}^n, T_{1,i}^n, \ldots, T_{N,i}^n$ are known, by analogy with (4.14) we first define the discrete densities of particles $M_{\alpha,i}^n$ by

$$M_{\alpha,i}^n(\xi) = \rho_{\alpha,i}^n l_\alpha \frac{H_i^n}{c_{\alpha,i}^n} \chi\left(\frac{\xi - u_{\alpha,i}^n}{c_{\alpha,i}^n}\right), \qquad \text{with} \quad c_{\alpha,i}^n = \sqrt{\frac{p_{\alpha,i}^n}{\rho_{\alpha,i}^n}}, \tag{5.27}$$

and following (3.56)

$$p_{\alpha,i}^n = g\left(\frac{\rho_{\alpha,i}^n l_\alpha H_i^n}{2} + \sum_{j=\alpha+1}^{N} \rho_{j,i}^n l_j H_i^n\right).$$

Then the equation (4.20) is discretised for each α by applying a simple upwind scheme

$$\begin{aligned} f_{\alpha,i}^{n+1}(\xi) = M_{\alpha,i}^n(\xi) - \xi\sigma_i^n \left(M_{\alpha,i+1/2}^n(\xi) - M_{\alpha,i-1/2}^n(\xi)\right) + \\ \Delta t^n \left(N_{\alpha+1/2,i}^{n+1/2}(\xi) - N_{\alpha-1/2,i}^{n+1/2}(\xi) + S_{\alpha+1/2,i}^n(\xi) - S_{\alpha-1/2,i}^n(\xi)\right), \end{aligned} \tag{5.28}$$

where

$$M_{\alpha,i+1/2}^n = \begin{cases} M_{\alpha,i}^n & \text{if } \xi \geq 0 \\ M_{\alpha,i+1}^n & \text{if } \xi < 0. \end{cases}$$

The terms $N_{\alpha+1/2,i}^{n+1/2}$ (resp. $S_{\alpha+1/2,i}^n$) will be defined in paragraph 5.4.4 (resp. 5.4.5).

Notice that the discrete scheme (5.28) does not take into account the collision term Q_{M_α} which relaxes $f_{\alpha,i}^{n+1}$ to a Gibbs equilibrium so the quantity $f_{\alpha,i}^{n+1}$ can not be written under the form (5.27). The collision term is used in a second step introducing a discontinuity at time t^{n+1} on M_α and replacing $f_{\alpha,i}^{n+1}$ by an equilibrium

$$M_{\alpha,i}^{n+1}(\xi) = \rho_{\alpha,i}^{n+1} l_\alpha \frac{H_i^{n+1}}{c_{\alpha,i}^{n+1}} \chi\left(\frac{\xi - u_{\alpha,i}^{n+1}}{c_{\alpha,i}^{n+1}}\right).$$

Then

$$\rho_{\alpha,i}^{n+1} l_\alpha H_i^{n+1} = \int_{\mathbb{R}} f_{\alpha,i}^{n+1}(\xi) d\xi, \tag{5.29}$$

and

$$\rho_{\alpha,i}^{n+1} l_\alpha H_i^{n+1} u_\alpha^{n+1} = \int_{\mathbb{R}} \xi f_{\alpha,i}^{n+1}(\xi) d\xi. \tag{5.30}$$

and so we recover the macroscopic quantities at time t^{n+1}.

An upwind scheme similar to (5.28) is applied to Eq. (4.21) giving with obvious notations

$$\begin{aligned} g_{\alpha,i}^{n+1}(\xi) &= U_{\alpha,i}^n(\xi) - \xi\sigma_i^n \left(U_{\alpha,i+1/2}^n(\xi) - U_{\alpha,i-1/2}^n(\xi)\right) \\ &\quad + \Delta t^n \left(V_{\alpha+1/2,i}^{n+1/2}(\xi) - V_{\alpha-1/2,i}^{n+1/2}(\xi)\right), \end{aligned} \tag{5.31}$$

and allowing to recover the macroscopic quantities

$$\rho_{\alpha,i}^{n+1} l_\alpha H_i^{n+1} T_{\alpha,i}^{n+1} = \int_{\mathbb{R}} g_{\alpha,i}^{n+1}(\xi) d\xi. \tag{5.32}$$

The equations (5.29),(5.30),(5.32) are summarized by

$$\tilde{X}_i^{n+1} = \int_\xi \mathcal{K}(\xi) \begin{pmatrix} f_i^{n+1}(\xi) \\ g_i^{n+1}(\xi) \end{pmatrix} d\xi, \tag{5.33}$$

with $f_i^n(\xi) = (f_{1,i}^n(\xi), \dots, f_{N,i}^n(\xi))^T$, $g_i^n(\xi) = (g_{1,i}^n(\xi), \dots, g_{N,i}^n(\xi))^T$.

5.4.3 Numerical fluxes of the conservative part

In this section, we give some details for the computation of the fluxes introduced in the discrete equation (5.26). If we denote

$$F_{i+1/2}^n = F(X_i^n, X_{i+1}^n) = F^+(X_i^n) + F^-(X_{i+1}^n), \tag{5.34}$$

following (5.22), we define

$$F^-(X_i^n) = \int_{\xi\in\mathbb{R}^-} \xi\mathcal{K}(\xi) \begin{pmatrix} M_i^n(\xi) \\ U_i^n(\xi) \end{pmatrix} d\xi, \quad F^+(X_i^n) = \int_{\xi\in\mathbb{R}^+} \xi\mathcal{K}(\xi) \begin{pmatrix} M_i^n(\xi) \\ U_i^n(\xi) \end{pmatrix} d\xi \tag{5.35}$$

with $M_i^n(\xi) = (M_{1,i}^n(\xi), \dots, M_{N,i}^n(\xi))^T$, $U_i^n(\xi) = (U_{1,i}^n(\xi), \dots, U_{N,i}^n(\xi))^T$.

More precisely the expression of $F^+(X_i)$ can be written

$$F^+(X_i) = \left(F_H^+(X_i), F_{q_1}^+(X_i), \dots, F_{q_N}^+(X_i), F_{k_1}^+(X_i), \dots, F_{k_N}^+(X_i)\right)^T, \tag{5.36}$$

with

$$\begin{aligned} F_H^+(X_i) &= \sum_{\alpha=1}^N F_{h_\alpha}^+(X_i) = \sum_{\alpha=1}^N \rho_{\alpha,i} l_\alpha H_i \int_{w\geq -\frac{u_{\alpha,i}}{c_i}} (u_{\alpha,i} + wc_{\alpha,i})\chi(w)\, dw, \\ F_{q_\alpha}^+(X_i) &= \rho_{\alpha,i} l_\alpha H_i \int_{w\geq -\frac{u_{\alpha,i}}{c_i}} (u_{\alpha,i} + wc_{\alpha,i})^2\chi(w)\, dw, \\ F_{k_\alpha}^+(X_i) &= T_{\alpha,i} F_{h_\alpha}^+(X_i). \end{aligned} \tag{5.37}$$

We denote also

$$\mathcal{F}_{h_\alpha,i} = F_{h_\alpha,i+1/2} - F_{h_\alpha,i-1/2} = F_{h_\alpha}^+(X_i) + F_{h_\alpha}^-(X_{i+1}) - \left(F_{h_\alpha}^+(X_{i-1}) + F_{h_\alpha}^-(X_i)\right). \tag{5.38}$$

This kinetic method is interesting because it gives a very simple and natural way to propose a numerical flux through the kinetic interpretation. Indeed, choosing – as in Eq. (5.9) –

$$\chi(w) = \frac{1}{2\sqrt{3}} 1_{|w|\leq\sqrt{3}}(w),$$

the integration in (5.36) can be done analytically.

5.4.4 Discrete mass exchange terms

Let us now define the mass exchange term $\mathcal{S}_{e,i}^{n+1/2}$ in the equation (5.26) or more precisely the terms $N_{\alpha+1/2,i}^{n+1/2}$ in Eq. (5.28). From the conditions (4.17) we prescribe

$$N_{1/2,i}^{n+1/2}(\xi) = N_{N+1/2,i}^{n+1/2}(\xi) = 0, \tag{5.39}$$

and, using the discrete analoguous of Eq. (4.32) (see Eq. (5.46) in paragraph 5.4.5), the sum for all α of Eqs. (5.29) defines explicitly $\sum_{\alpha=1}^{N} \rho_{\alpha,i}^{n+1} l_\alpha H_i^{n+1}$.

Likewise, by partial summation of (5.28), we have

$$\Delta t^n N_{\alpha+1/2,i}^{n+1/2}(\xi) + \Delta t^n S_{\alpha+1/2,i}^{n+1/2}(\xi) = \sum_{j=1}^{\alpha} \left(f_{j,i}^{n+1}(\xi) - M_{j,i}^n(\xi) + \xi \sigma_i^n \left(M_{j,i+1/2}^n(\xi) - M_{j,i-1/2}^n(\xi) \right) \right), \tag{5.40}$$

for $\alpha = 1, \ldots, N-1$. By analogy with (4.30), we define

$$G_{\alpha+1/2,i}^{n+1/2} = \int_{\mathbb{R}} N_{\alpha+1/2,i}^{n+1/2}(\xi) d\xi, \qquad \alpha = 0, \ldots, N, \tag{5.41}$$

so, using (5.29) and (5.46), we can write

$$\Delta t^n G_{\alpha+1/2,i}^{n+1/2} = \sum_{j=1}^{\alpha} \left[l_j (\rho_{j,i}^{n+1} H_i^{n+1} - \rho_{j,i}^n H_i^n) + \sigma_i^n (F_{hj,i+1/2}^n - F_{hj,i-1/2}^n) \right], \tag{5.42}$$

for $\alpha = 1, \ldots, N$. We have to notice that this definition is compatible with the free surface condition of (5.39). Moreover this definition depends on $\rho_{\alpha,i}^{n+1} H_i^{n+1}$. These values are unknown at this stage since only the global quantity $\sum_{\alpha=1}^{N} \rho_{\alpha,i}^{n+1} l_\alpha H_i^{n+1}$ can be explicitely computed. It is the reason why we choose to denote the term as $G_{\alpha+1/2,i}^{n+1/2}$, and also $N_{\alpha+1/2}^{n+1/2}$, $V_{\alpha+1/2}^{n+1/2}$ and $\mathcal{S}_{e,i}^{n+1/2}$. The main consequence is that we will have to solve a nonlinear system to compute the quantities of interest at time t^{n+1}, see paragraph 5.4.7.

We define

$$N_{\alpha+1/2,i}^{n+1/2}(\xi) = G_{\alpha+1/2,i}^{n+1/2} \, \delta \left(\xi - u_{\alpha+1/2,i}^n \right), \quad V_{\alpha+1/2,i}^{n+1/2}(\xi) = T_{\alpha+1/2,i}^n N_{\alpha+1/2,i}^{n+1/2}(\xi) \tag{5.43}$$

with, according to (3.58)

$$v_{\alpha+1/2,i}^n = \begin{cases} v_{\alpha+1,i}^n & \text{if } G_{\alpha+1/2,i}^{n+1/2} \geq 0, \\ v_{\alpha,i}^n & \text{if } G_{\alpha+1/2,i}^{n+1/2} < 0, \end{cases} \tag{5.44}$$

for $v = u, T$. Here also, we insist on the fact that the quantity $G_{\alpha+1/2,i}^{n+1/2}$ can not be computed explicitely since it involves unknown quantities at time t^{n+1}. The way to overcome this difficulty will be precised when we describe the numerical solution of the nonlinear system in paragraph 5.4.7. Nevertheless we can now consider that the exchange term $\mathcal{S}_{e,i}^{n+1/2}$ in (5.26) is completely defined.

5.4.5 Numerical treatment of pressure source terms

We focus on the source term $\mathcal{S}_{p,i}^n$ associated with the pressure and appearing in (5.26), namely the discretization of $S_{\alpha+1/2}(x,t,\xi)$ defined by (3.56),(4.16). The numerical treatment of this term that we propose here is significantly different from what is usually done in hydrostatic reconstruction [ABB$^+$04] and what has been proposed by the author in [3]. Nevertheless in the case of a single layer and with a constant density, the source discretization we present is similar, for the first order scheme, to the formulation given in [ABB$^+$04].

From the kinetic interpretation (4.20) and using the definition (4.16), we point out that we can write

$$\mathcal{S}_{p,i}^n = \int_\xi \mathcal{K}(\xi) \begin{pmatrix} P_i^n(\xi) \\ 0 \end{pmatrix} d\xi, \tag{5.45}$$

with

$$P^n_{\alpha,i}(\xi) = S^n_{\alpha+1/2,i}(\xi) - S^n_{\alpha-1/2,i}(\xi).$$

We have the discrete analoguous of Eq. (4.32)

$$\int_{\mathbb{R}} S^n_{\alpha+1/2,i}(\xi)d\xi = 0. \tag{5.46}$$

The term

$$\int_{\mathbb{R}} \xi S^n_{\alpha+1/2,i}(\xi)d\xi,$$

that is an approximation of

$$\int_{x_{i-1/2}}^{x_{i+1/2}} \frac{\partial z_{\alpha+1/2}(x,t^n)}{\partial x} p_{\alpha+1/2}(x,t^n)dx,$$

is defined hereafter. The basis of the numerical treatment of the pressure source term is simply to rewrite it under the form

$$\frac{\partial z_{\alpha+1/2}(x,t)}{\partial x} p_{\alpha+1/2}(x,t) = \frac{\partial}{\partial x}\int_{x_0}^{x} \frac{\partial z_{\alpha+1/2}(\tilde{x},t)}{\partial \tilde{x}} p_{\alpha+1/2}(\tilde{x},t)\ d\tilde{x}.$$

This leads at the discrete level to the formula

$$\begin{aligned}\int_{x_{i-1/2}}^{x_{i+1/2}} & \frac{\partial z_{\alpha+1/2}(x,t^n)}{\partial x} \quad p_{\alpha+1/2}(x,t^n)dx \\ &= \int_{x_i}^{x_{i+1/2}} \frac{\partial z_{\alpha+1/2}(x,t^n)}{\partial x} p_{\alpha+1/2}(x,t^n)\ dx \\ &\quad - \int_{x_i}^{x_{i-1/2}} \frac{\partial z_{\alpha+1/2}(x,t^n)}{\partial \tilde{x}} p_{\alpha+1/2}(x,t^n)\ d\tilde{x},\end{aligned}$$

where the cell-averaged source term is locally represented as a discrete gradient. Then we write for $\alpha = 1, \ldots, N$

$$\int_{\mathbb{R}} \xi S^n_{\alpha+1/2,i}(\xi)d\xi = S^n_{\alpha+1/2,i+1/2-} - S^n_{\alpha+1/2,i-1/2+}, \tag{5.47}$$

with the definitions

$$S^n_{\alpha+1/2,i+1/2-} = p^n_{\alpha+1/2,i+1/4}\left(z^n_{\alpha+1/2,i+1/2-} - z^n_{\alpha+1/2,i}\right), \tag{5.48}$$

$$p^n_{\alpha+1/2,i+1/4} = \frac{p^n_{\alpha+1/2,i+1/2-} + p^n_{\alpha+1/2,i}}{2}, \tag{5.49}$$

$$p^n_{\alpha+1/2,i+1/2-} = g\sum_{j=\alpha+1}^{N} \rho^n_{j,i+1/2-} h^n_{j,i+1/2-}, \tag{5.50}$$

$$p^n_{\alpha+1/2,i} = g\sum_{j=\alpha+1}^{N} \rho^n_j h^n_{j,i}, \tag{5.51}$$

$$z^n_{\alpha+1/2,i+1/2-} = z_{b,i+1/2} + \sum_{j=1}^{\alpha} h^n_{\alpha,i+1/2-}, \tag{5.52}$$

$$z^n_{\alpha+1/2,i} = z_{b,i} + \sum_{j=1}^{\alpha} h^n_{\alpha,i}, \tag{5.53}$$

$$z_{b,i+1/2} = \max\{z_{b,i}, z_{b,i+1}\}, \tag{5.54}$$

$$H^n_{i+1/2-} = H^n_i + z_{b,i} - z_{b,i+1/2}, \tag{5.55}$$

$$H^n_{i+1/2+} = H^n_{i+1} + z_{b,i+1} - z_{b,i+1/2}, \tag{5.56}$$

$$h^n_{\alpha,i+1/2\pm} = l_\alpha H^n_{i+1/2\pm}, \tag{5.57}$$

$$\rho^n_{\alpha,i+1/2-} = \rho(T^n_{\alpha,i}), \tag{5.58}$$

$$\rho^n_{\alpha,i+1/2+} = \rho(T^n_{\alpha,i+1}). \tag{5.59}$$

Notice that Eqs. (5.48)-(5.53) are classical relations/definitions allowing to obtain approximate quadrature formula for the right hand side of (5.47) whereas Eqs. (5.54)-(5.57) correspond to an upwind discretization of the bottom topography using the hydrostatic reconstruction strategy. It has to be noticed that the definitions (5.58)-(5.59) which give the values of the fluid density at each interfaces i.e. $\rho^n_{\alpha,i+1/2\pm}$ are not the same as the one used for the pollutant value i.e. $T^n_{\alpha,i+1/2\pm}$, see (5.63). We also notice that the flux (5.34) is no more computed using the cell centered values $h^n_{\alpha,i}$ and $h^n_{\alpha,i+1}$ but the reconstructed interface values $h^n_{\alpha,i+1/2-}$ and $h^n_{\alpha,i+1/2+}$.

One of the major concern for the discretization of the pressure source terms $\mathcal{S}_{p,i}(X^n)$ is the preservation of relevant equilibria. At the continuous level, the static equilibrium of the lake at rest is given by

$$u(x,z) = 0, \quad \int_z^\eta \rho(x,\tilde{z}\ d\tilde{z} = Cst(z), \qquad \forall x, z,$$

that implies

$$u = 0, \quad \eta = Cst, \quad \text{and } T = T(z). \tag{5.60}$$

We first consider the density is constant i.e. $T(x,z,t) = T_0$ and we have the following proposition

Proposition 17. *When the density is constant, the discretization of the source terms given by (5.45) preserves the steady states of the "lake at rest" (5.60) for the system.*

Proof of Prop. 17. On a steady state of a lake at rest, we have by construction $H^n_{i+1/2-} = H^n_{i+1/2+}$, $u^n_{\alpha,i+1} = u^n_{\alpha,i} = 0$ and $S^{n+1/2}_{e,i} = 0$ for $\alpha = 1,\dots,N$, $i \in I$ thus $X^n_{i+1/2-} = X^n_{i+1/2+}$ and a simple calculus shows the expression of the source terms (5.45) coupled with the flux calculated with

the kinetic scheme gives $F^n_{i+1/2} - F^n_{i-1/2} = S^n_{p,i+1/2-} - S^n_{p,i-1/2+}$ with $S^n_{p,i+1/2-} = (S^n_{3/2,i+1/2-} - S^n_{1/2,i+1/2-}, \ldots, S^n_{N+1/2,i+1/2-} - S^n_{N-1/2,i+1/2-})^T$ that completes the proof. □

5.4.6 Static equilibrium and variable density

When the fluid density varies, the preservation of the equilibrium at rest is more tricky. In the case of a static equilibrium with a flat bottom, all the interfaces are horizontal so at the continuous and discrete level we have

$$\frac{\partial z_{\alpha+1/2}}{\partial x} = 0, \qquad \alpha = 1, \ldots, N.$$

It follows that $S_p = 0$ and the equilibrium is obviously preserved.

In the situation of a non flat bottom, the equilibrium at rest is more difficult to characterize since this corresponds to

$$\frac{\partial h_\alpha p_\alpha}{\partial x} = \frac{\partial z_{\alpha+1/2}}{\partial x} p_{\alpha+1/2} - \frac{\partial z_{\alpha-1/2}}{\partial x} p_{\alpha-1/2}$$

but with an inhomogeneous distribution of the tracer T.

Instead of proving that our scheme preserves such equilibria, we will numerically demonstrate in paragraph 6.4.1 that starting from a given initial condition and without any forcing term or energy supply, the system evolves to a static equilibrium satisfying

$$\eta_i = Cst, \quad u_{\alpha,i} = 0, \quad \text{and} \quad T(x_i, \{z_\alpha\}) = Cst_\alpha, \qquad \alpha = 1, \ldots, N, \quad i \in I,$$

that is the discrete equivalent of continuous equilibrium (5.60).

5.4.7 Nonlinear coupling

In paragraphs 5.4.2-5.4.5, we have described how to evaluate from the kinetic scheme and an extended hydrostatic reconstruction the quantities

$$\sum_{\alpha=1}^{N} \rho^{n+1}_{\alpha,i} l_\alpha H^{n+1}_i, \quad \rho^{n+1}_{\alpha,i} l_\alpha H^{n+1}_i u^{n+1}_{\alpha,i} \quad \text{and} \quad \rho^{n+1}_{\alpha,i} l_\alpha H^{n+1}_i T^{n+1}_{\alpha,i}. \tag{5.61}$$

From (5.29) and (5.39), we have deduced that the first term is computed explicitly. It is not the case for the third term since the evaluation of the interface flux $G^{n+1/2}_{\alpha+1/2,i}$ (5.42) involves quantities computed at time t^{n+1}. Moreover the density $\rho_{\alpha,i}$ is a non trivial function of the temperature $T_{\alpha,i}$. It follows that a $(N+1)$ nonlinear problem has to be solved to completely define H^{n+1}_i and $T^{n+1}_{\alpha,i}$. This nonlinear problem stands

$$\begin{aligned}
\sum_{\alpha=1}^{N} \rho^{n+1}_{\alpha,i} l_\alpha H^{n+1}_i &= \sum_{\alpha=1}^{N} \rho^{n}_{\alpha,i} l_\alpha H^{n}_i \\
&\quad + \frac{\Delta t^n}{\Delta x_i} \left(F^+_H(X^n_{i-1}) + F^-_H(X^n_i) - F^+_H(X^n_i) - F^-_H(X^n_{i+1}) \right), \\
\rho^{n+1}_{\alpha,i} l_\alpha H^{n+1}_i T^{n+1}_{\alpha,i} &= \rho^{n}_{\alpha,i} l_\alpha H^{n}_i T^{n}_{\alpha,i} \\
&\quad + \frac{\Delta t^n}{\Delta x_i} \left(F^+_{k_\alpha}(X^n_{i-1}) + F^-_{k_\alpha}(X^n_i) - F^+_{k_\alpha}(X^n_i) - F^-_{k_\alpha}(X^n_{i+1}) \right) \\
&\quad + \Delta t^n \left(T^{k,n}_{\alpha+1/2,i} G^{n+1/2}_{\alpha+1/2,i} - T^{k,n}_{\alpha-1/2,i} G^{n+1/2}_{\alpha-1/2,i} \right),
\end{aligned}$$

for $\alpha = 1, \ldots, N$, where the fluxes $F^{\pm}$ and G can be evaluated through formula (5.38) and (5.42) and interface values $T_{\alpha+1/2,i}$ are given by (5.44). This system can be written under the form

$$\mathcal{R}(H_i^{n+1}, T_{1,i}^{n+1}, \ldots, T_{N,i}^{n+1}) = C_i^n \tag{5.62}$$

where the term C_i^n contains all the data, i.e. the quantities that are evaluated at time t^n, and the function $\mathcal{R}$ from $\mathbb{R}^{N+1}$ to $\mathbb{R}^{N+1}$ is given by

$$\mathcal{R}(x, y_1, \ldots, y_n) = \begin{pmatrix} x \sum_{\alpha=1}^{N} l_\alpha \rho(y_\alpha) \\ x l_\alpha y_\alpha \rho(y_\alpha) - T_{\alpha+1/2,i}^{k,n} x \sum_{j=1}^{\alpha} l_j \rho(y_j) + T_{\alpha-1/2,i}^{k,n} x \sum_{j=1}^{\alpha-1} l_j \rho(y_j) \end{pmatrix}.$$

The nonlinear system (5.62) is solved by using an iterative procedure that defines a sequence of quantities $(H_i^{k,n}, T_{\alpha,i}^{k,n})$ where the superscript k refers to the advance in the iterative process. We notice that in the definition of the function $\mathcal{R}$ the interface value of the tracer $T_{\alpha+1/2,i}^{k,n}$ is explicitely related to the actual iteration. Indeed formula (5.44) which was said to be non explicit since the quantity $G_{\alpha+1/2,i}^{n+1/2}$ is implicitely defined, is replaced in the iterative process by the explicit formula

$$T_{\alpha+1/2,i}^{k,n} = \begin{cases} T_{\alpha+1,i}^{n} & \text{if } G_{\alpha+1/2,i}^{k-1,n} \geq 0, \\ T_{\alpha,i}^{n} & \text{if } G_{\alpha+1/2,i}^{k-1,n} < 0, \end{cases}$$

where the explicit quantity $G_{\alpha+1/2,i}^{k-1,n}$ is computed using the previous estimation of the unknown quantities

$$\Delta t^n G_{\alpha+1/2,i}^{k-1,n} = \sum_{j=1}^{\alpha} \left[l_j (\rho_{j,i}^{k-1,n} H_i^{k-1,n} - \rho_{j,i}^{n} H_i^{n}) + \sigma_i^n (F_{hj,i+1/2}^n - F_{hj,i-1/2}^n) \right].$$

This nonlinear problem is solved for example using a Newton-type algorithm. This is a small size problem but that has to be solved at each time step and for each cell C_i. In practice, this step is the most CPU time-consuming. Once H_i^{n+1} and $T_{\alpha,i}^{n+1}$ are computed, $u_{\alpha,i}^{n+1}$ is deduced from (5.30).

As mentionned in paragraph 3.5.2, the Boussinesq assumption simplifies the model since in this case, the density only appears in the wave velocity $c_{\alpha,i}$. Then we have

$$\tilde{X}_i^{n+1} = \begin{pmatrix} H_i^{n+1} \\ l_\alpha H_i^{n+1} u_{\alpha,i}^{n+1} \\ l_\alpha H_i^{n+1} T_{\alpha,i}^{n+1} \end{pmatrix},$$

and we easily recover the unknowns of interest without the solution of a nonlinear system : the global water height H_i^{n+1} is explicitely defined by the sum of relations (5.29) and then quantities $T_{\alpha,i}^{n+1}$ and $u_{\alpha,i}^{n+1}$ can be computed using (5.30) and (5.32).

5.4.8 Stability of the scheme and maximum principle

Classically, the stability property of the kinetic scheme can be established through a CFL condition ensuring the water height remains non negative. This CFL condition means that the quantity of water leaving a given cell during a time step Δt^n is less than the actual water in the cell. Notice that due to the vertical discretization, the water can leave the cell C_i of the layer α either by the boundaries $x_{i\pm1/2}$ or by the interfaces $z_{\alpha\pm1/2}$. This makes the CFL condition more restrictive. In the case of a constant density, the result is proved in [3]. Its adaptation to the situation where the density varies is straightforward and leads to the following proposition

Proposition 18. *Assume that the function χ has a compact support of length $2w_M$ then under the CFL condition*

$$\Delta t^n \leq \min_{1\leq\alpha\leq N}\min_{i\in I}\frac{\rho_\alpha l_\alpha H_i^n \Delta x_i}{\rho_\alpha l_\alpha H_i^n\left(|u_{\alpha,i}^n| + w_M c_{\alpha,i}^n\right) + \Delta x_i\left(\left[G_{\alpha+1/2,i}^{n+1/2}\right]_- + \left[G_{\alpha-1/2,i}^{n+1/2}\right]_+\right)}$$

the kinetic scheme defined in paragraphs 5.4.2-5.4.7 keeps the water height positive i.e. $H_i^n \geq 0$ if it is true initially.

Remark 5.2. *It can be proved that*

$$\left[G_{\alpha+1/2,i}^{n+1/2}\right]_- = \left[G_{\alpha-1/2,i}^{n+1/2}\right]_+ = \mathcal{O}(H_i^n),$$

so the preceding CFL condition does not become singular when H_i^n tends to zero.

For the concentration of pollutant we have the two following propositions. Their proofs are omitted, see [2].

Proposition 19. *Under the CFL condition defined in Prop. 18, the kinetic scheme defined in paragraphs 5.4.2-5.4.7 preserves the positivity of the concentration of pollutant.*

Proposition 20. *Under the CFL condition defined in Prop. 18, the kinetic scheme defined in Sec. 5.4.2-5.4.7 ensures a maximum principle for the concentration of pollutant. Indeed it satisfies*

$$\forall n,\ \forall i,\ \forall \alpha \qquad T_{\alpha,i}^{n+1} \leq \max\{T_{\alpha,i}^n, T_{\alpha+1,i}^n, T_{\alpha-1,i}^n, T_{\alpha,i+1}^n, T_{\alpha,i-1}^n\}.$$

5.4.9 Specific upwinding of the tracer

In practice the natural upwinding of the tracer equation defined by Eq. (5.37) is modified (see [AB03]) and we rather introduce an upwinding depending on the sign of the total mass flux. Then the pollutant flux vanishes with the total mass flux. It is done with the introduction of the new pollutant flux $F_k(X_i, X_{i+1})$ defined in the following formula that replaces (5.37)

$$F_{k_\alpha}(X_i, X_{i+1}) = T_{\alpha,i+1/2} F_{h_\alpha}(X_i, X_{i+1}),$$

where

$$T_{\alpha,i+1/2} = \begin{cases} T_{\alpha,i} & \text{for } F_{h_\alpha}(X_i, X_{i+1}) \geq 0, \\ T_{\alpha,i+1} & \text{for } F_{h_\alpha}(X_i, X_{i+1}) < 0. \end{cases} \tag{5.63}$$

Notice this upwinding preserves the properties demonstrated in the previous propositions.

5.4.10 Boundary conditions

For the treatment of the boundary conditions, see paragraph 5.1.1 and [BC01]. Notice that for a given boundary, the type of prescribed condition – water height, inflow, ... – can vary with the considered layer.

5.4.11 Second order scheme

Notice that using the second order scheme (see paragraph 5.1.2) even in the case of a single layer with constant density, the numerical scheme we propose does not adopt the same discretization for the pressure source terms but gives similar results compared to what has been proposed in [ABB$^+$04]. But, the convergence orders of the scheme in situations where an analytical solution is available are the same. Nevertheless, our discretization of the topographic source term seems more natural and for the second order extension, no additional centered source term is needed.

6 Simulations of complex flows

All the simulations presented in this section have been obtained with the same numerical code developed by the author and able to simulated all the models and the associated numerical schemes depicted in Sec. 5.

We do not present in this section any simulation of the classical Saint-Venant system. Even if there is still interesting questions associated with the simulation of the Saint-Venant system e.g. flows with large bottom friction, large bottom slope, roll waves, debris flows,... For all these questions, the reader can refer to the publications of F. Bouchut. In this section, we prefer to concentrate on test cases involving models more complex than the saint-Venant system.

6.1 The section-averaged Saint-Venant system [8]

In this paragraph, several simulations of test problems are described illustrating the accuracy of the numerical scheme for the section-averaged Saint-Venant system presented in paragraph 5.2. The notations correspond to those introduced in paragraph 5.2. We compare our simulations first with analytic solutions proposed by MacDonald [MBNS95a, MBNS95b] and then with experimental data.

All the results presented in this paragraph have been obtained with the second order scheme except when explicitly mentionned. The results have been obtained using the apparent topography reconstruction and its second order extension. In paragraph 6.1.3, we formally analyse the convergence order of the 1^{st} and 2^{nd} order schemes.

6.1.1 Rectangular channel

Example 1 The first test problem concerns a 1 km long rectangular channel of width 10 m with a discharge of 20 $m^3.s^{-1}$. The flow is fixed at inflow and the water height is prescribed at outflow. The flow is subcritical at inflow and at outflow but the Froude number is around 1.01 at mid length of the domain. The depth at the downstream boundary is 0.748409 m. The Manning roughness coefficient for the channel is 0.03 and the bed slope is given by

$$\frac{\partial z_b}{\partial x} = \left(1 - \frac{4}{gH^3}\right)\frac{\partial H}{\partial x} + 0.36\frac{(10+2H)^{\frac{4}{3}}}{(10H)^{\frac{10}{3}}},$$

where the water depth H is given by

$$H = \left(\frac{4}{g}\right)^{\frac{1}{3}}\left(1 + \frac{1}{2}e^{-16\left(\frac{x}{1000}-\frac{1}{2}\right)^2}\right).$$

The simulation results and the comparison with the analytic solutions are given in Figs. 6,7. This test problem corresponds to the example 1 in [MBNS95b]. The used mesh has 150 nodes. The error between the analytic and simulated water height is defined by

$$Er_H \ : \ x \mapsto \frac{|H^{simu}(x) - H^{anal}(x)|}{H^{anal}(x)}.$$

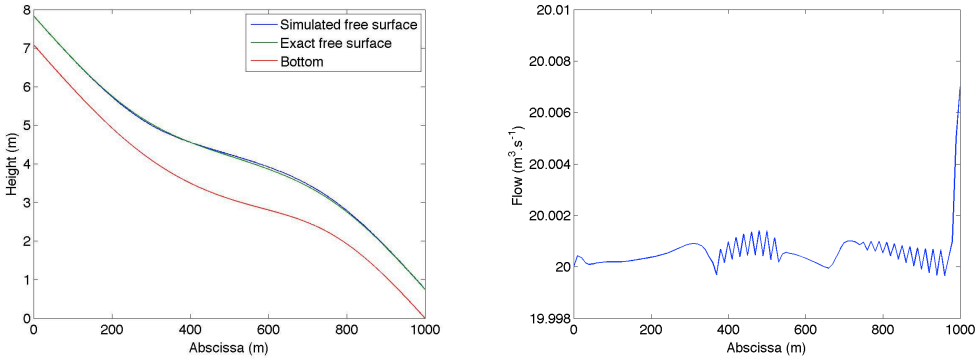

(a) *(b)*

Figure 6: Example 1: *(a)* Surface level and bed level, *(b)* Flow.

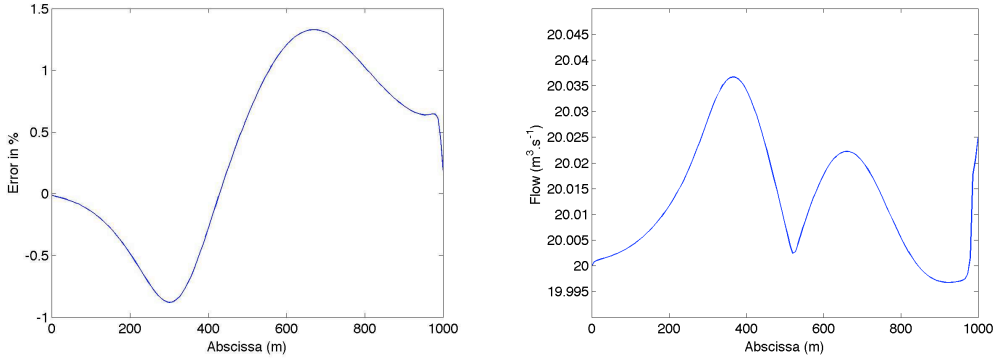

(a) *(b)*

Figure 7: Example 1: *(a)* Error $x \mapsto Er_H(x)$ and *(b)* flow (same test problem as in Fig. 6 but using the 1^{st} order scheme with 150 nodes).

The instabilities appearing in Fig. 6-*(b)* come from the apparent topography reconstruction described in paragraph 5.2.3 since $\overline{z}_{mod}$ in relation (5.15) cannot be evaluated in a consistent way. Indeed, the water height $H_{i+1/2\pm}$ has to be upwinded using

$$\begin{aligned}
\overline{z}_{mod,i+1/2} &= \max\{\overline{z}_{b,i} - F_{r,i}, \overline{z}_{b,i+1} - F_{r,i+1}\},\\
H^n_{i+1/2-} &= H^n_i + \overline{z}_{mod,i} - \overline{z}_{mod,i+1/2},\\
H^n_{i+1/2+} &= H^n_{i+1} + \overline{z}_{mod,i+1} - \overline{z}_{mod,i+1/2},
\end{aligned}$$

but since $F_r = F_r(H, \overline{u})$, it is necessary to know $H_{i+1/2\pm}$ in order to evaluate $F_{r,i+1} - F_{r,i}$. Notice that these instabilities are no more observed when using the 1^{st} order scheme, see Fig. 7-*(b)*. In supercritical cases, the implicit treatment of the friction terms and the apparent topography give similar results. As far as the author knows, there exists no ultimate solution to overcome this difficulty.

Example 2: Varying rectangular channel A 5 km long rectangular channel has a discharge of 20 $m^3.s^{-1}$. In this example, the channel width is described by the function

$$L_b(x) = 10 - 5e^{-64\left(\frac{x}{5000} - \frac{1}{3}\right)^2} - 5e^{-64\left(\frac{x}{5000} - \frac{2}{3}\right)^2},$$

where $L_b(x)$ is the given width at distance x. The bed slope of the channel is given by the formula

$$\frac{\partial z_b}{\partial x} = \left(1 - \frac{Q_0^2}{gL_b(x)^2H(x)^3}\right)\frac{\partial H}{\partial x} + Q_0^2 n^2 \frac{(2H(x) + L_b(x))^{\frac{4}{3}}}{(L_b(x)H(x))^{\frac{10}{3}}} - Q_0^2 \frac{\frac{\partial L_b}{\partial x}}{gL_b(x)^3H^2},$$

and the corresponding analytic solution is given by

$$H = 1 + \frac{1}{2}e^{-64\left(\frac{x}{5000} - \frac{1}{3}\right)^2} + \frac{1}{2}e^{-64\left(\frac{x}{5000} - \frac{2}{3}\right)^2}.$$

The depth at the downstream boundary is 1.000408 m and the Manning roughness coefficient for the channel is 0.03. The flow is subcritical. This test problem corresponds to the example denoted 'VR1' in [MBNS95a]. The results using a mesh with 150 nodes are given in Figs. 8 and 9.

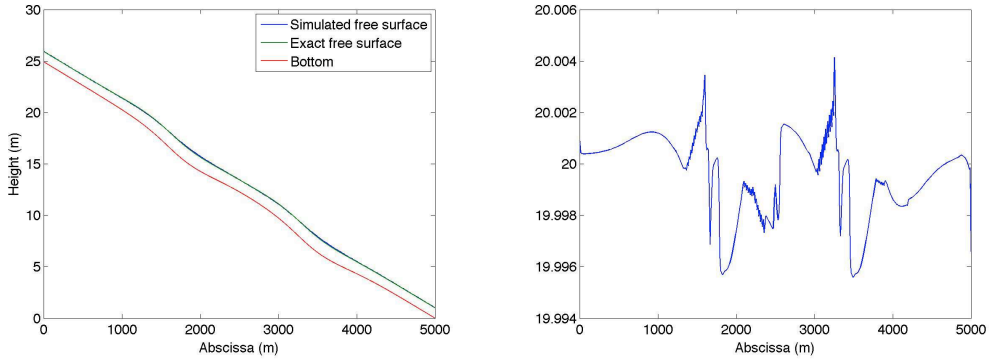

(a) *(b)*

Figure 8: Example 2: *(a)* surface level and bed level, *(b)* flow.

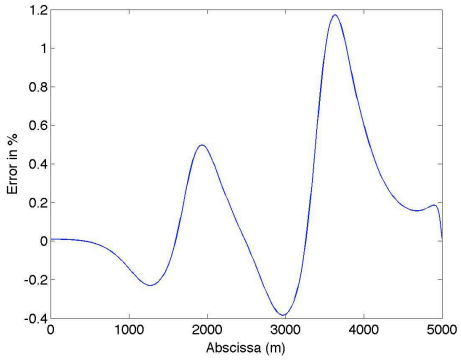

Figure 9: Example 2: error between the analytic and simulated solution (water height).

6.1.2 Trapezoidal channel

A 1 km long trapezoidal channel (with channel width $T = 10 + 2H$ and wetted perimeter $P = 10 + 2\sqrt{2}H$) has a discharge of 20 $\mathrm{m}^3.\mathrm{s}^{-1}$. The flow is subcritical at inflow and is subcritical at outflow with depth 1.349963 m. The Manning roughness coefficient for the channel is 0.02 and the bed slope is given by

$$\frac{\partial z_b}{\partial x} = \left(1 - \frac{400(10+2H)}{g(10+H)^3H^3}\right)\frac{\partial H}{\partial x} + 0.16\frac{(10+2\sqrt{2}H)^{\frac{4}{3}}}{(10+H)^{\frac{10}{3}}H^{\frac{10}{3}}},$$

where the water depth H is given by

$$H = \begin{cases} 0.723449\left(1 - \tanh\left(\frac{x}{1000} - \frac{3}{10}\right)\right) & 0 \le x \le 300 \\ 0.723449\left(1 - \frac{1}{6}\tanh\left(6\left(\frac{x}{1000} - \frac{3}{10}\right)\right)\right) & 300 \le x \le 600 \\ \frac{3}{4} + \sum_{k=1}^{3} a_k e^{-20k\left(\frac{x}{1000} - \frac{3}{5}\right)} + \frac{3}{5}e^{\frac{x}{1000}-1} & 600 \le x \le 1000, \end{cases}$$

with $a_1 = -0.111051$, $a_2 = 0.026876$ and $a_3 = -0.217567$. This test problem corresponds to the example 6 in [MBNS95b]. The used mesh has 150 nodes and the results are given in Fig. 10.

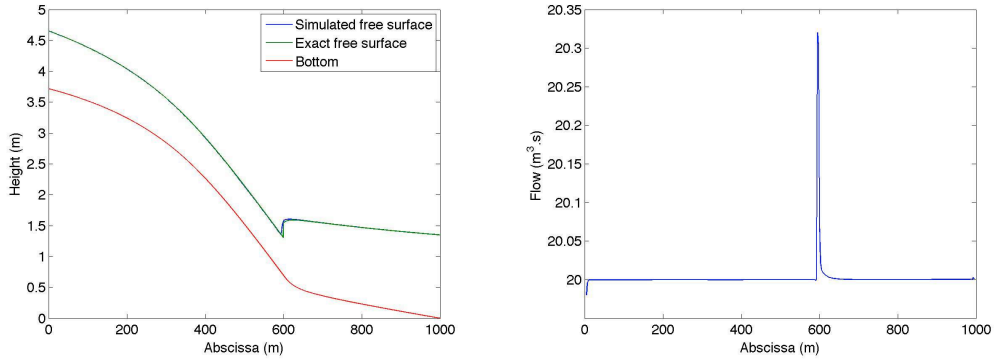

(a) *(b)*

Figure 10: Example 3: *(a)* surface level and bed level, *(b)* flow.

6.1.3 Convergence orders of the scheme

We consider a 1 km long channel with the following geometrical profile

- $\overline{z}_b(x) = e^{-5.10^{-5}(x-500)^2}$,
- $L_b(x) = 10 - 7e^{-8.10^{-5}(x-350)^2} - 10e^{-10^{-4}(x-800)^2}$,
- $\alpha(x) = 1 - 3\sin\left(\frac{2\pi x}{1000}\right)$.

Notice that $\alpha(x) < 0$ in some areas. A view of the channel profile is given in Fig. 11 where a rescaling in the y and z direction has been applied.

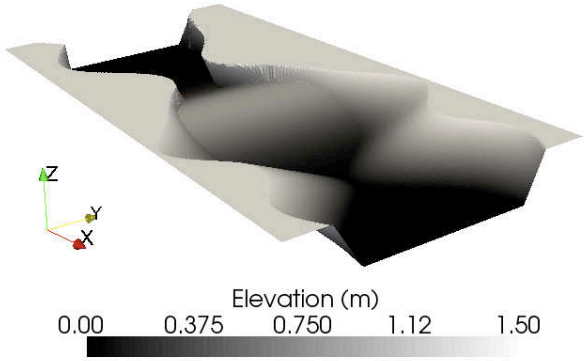

Figure 11: Channel profile

The discharge is fixed equal to $Q_0 = 5$ m^3.s^{-1} and the outflow depth is 1.5 m. The flow is subcritical and we have considered first a no friction condition at the bottom (Fig. 12) then a Navier friction law is used (Fig. 13). The reference solution satifies the ordinary differential equation (ODE)

$$-Q_0^2\frac{\partial S}{\partial x} + gS^3\frac{\partial \eta}{\partial x} = -\kappa S Q_0, \tag{6.1}$$

where κ is the Navier friction coefficient and with

$$\frac{\partial S}{\partial x} = L_s\frac{\partial \eta}{\partial x} + H\frac{\partial L_b}{\partial x} + \frac{\partial \alpha}{\partial x}\frac{H^2}{2} - L_s\frac{\partial z_b}{\partial x},$$

and $S = L_bH + \frac{\alpha}{2}H^2$, $L_s = L_b + \alpha H$. The ODE (6.1) has been solved using a 2^{nd} order Runge-Kutta scheme.

In order to show the improvement due to the formally second-order reconstruction, we plot the rate of error versus the space discretization. We have plotted in Fig. 12 the $\log(L^1 - error)$ of the water depth versus $\log(h_0/h_i)$ for the first and second-order scheme and they are compared to the theoretical order. We denote by h_i the average cell length, h_0 is the average cell length of the coarser mesh. These errors have been computed on 6 meshes with 50, 100, 150, 200, 300 and 400 cells. It appears that the computed convergence rates are closed to the theoretical ones. The formal second-order scheme provides an effective convergence up to the second order when the flow is sufficiently smooth. As already mentionned, the 2^{nd} order accuracy reduces to first-order near discontinuities, see [AB05a]. In case of large friction coefficients, the friction effects are no longer small corrections added to the hyperbolic part and the apparent topography – that admit 2^{nd} order extension – is useful.

The results have been obtained for an example where all the source terms are simultaneously non zero. Figure 12 presents the results obtained with the no friction condition and we recover the expected convergence rate. With $\kappa = 0.02\,\mathrm{m}^2$ and as explained in paragraph 6.1.1, the 2^{nd} order is lost, see Fig. 13

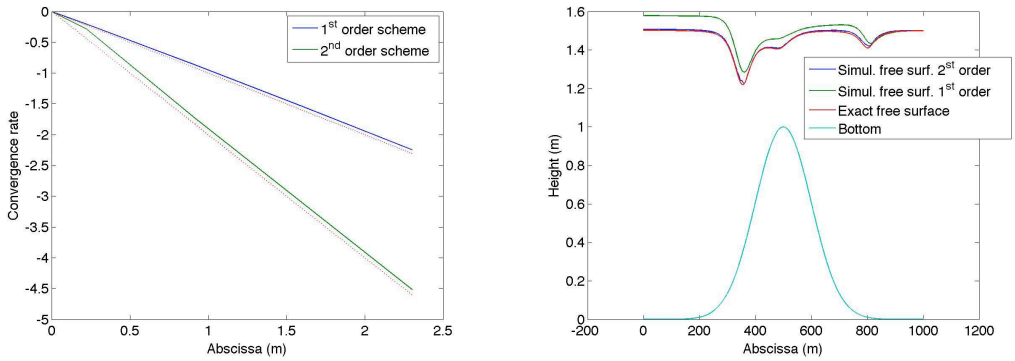

(a) *(b)*

Figure 12: *(a)* Convergence rate (no friction) and *(b)* Surface level and bed level for the 1^{st} and 2^{st} order schemes (the mesh used has 150 nodes).

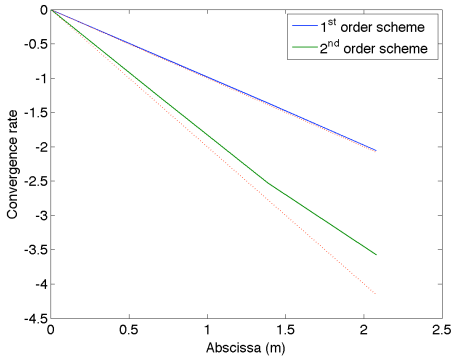

Figure 13: Convergence rate ($\kappa = 0.02$ m^2).

6.1.4 Experimental test case

Finally we confront the numerical results with experimental measurements. The aim is not to evaluate the validity of the section averaged Saint-Venant system – that has been widely done in the literature – but to compare, in a physical situation, the numerical scheme we propose with other existing schemes and codes.

The test case consists in a dam break in a channel with locally rectangular section. The experimental conditions are fully described in [GS98]. The channel section is described by $S(x,t) = L_b(x)H(x,t)$ where the width L_b is given and described in Fig. 14.

Measured values of the water level are available. The location of the four measurements points S_i, $i = 1,\ldots,4$ are presented in Fig. 14. The friction Strickler coefficient is equal to 100 $\mathrm{m}^{1/3}.\mathrm{s}^{-1}$. There is no bottom slope. Initially, the water is at rest. Ahead the gate, the water level is 0.3 m

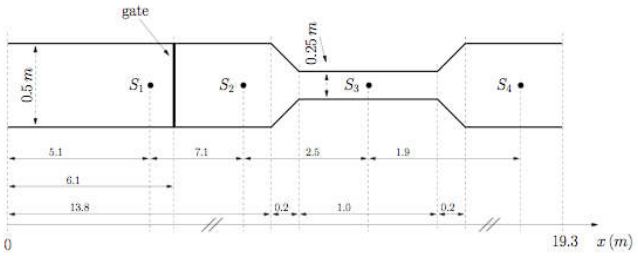

Figure 14: Geometry of the physical model (upper view).

and below it the bottom is dry. At time t_0, the gate opens. Because the calculation time is shorter than the time for the wave front to reach the outflow, the boundaries of the channel are treated as closed boundaries i.e. inflow and outflow equal zero.

The mesh used for the calculations has 400 nodes. Figure 15 presents the simulations results and the experimental measurements of the water depth at different measurement points. The results are in agreement with the experimental data concerning the wave propagation and also the hydraulic jump. The simulations are also in agreement with the numerical results obtained using other finite volume schemes in 1d ([GM02]) and in 2d ([GS98]). Notice that the difference in Fig. 15-*(c)* between the simulations and the experimental data mainly comes from 2d effects and non-hydrostatic pressure terms that are not taken into account in the 1d section-averaged Saint-Venant system.

6.2 Non-hydrostatic effects [7]

This paragraph is devoted to the numerical simulation of the non-hydrostatic model obtained in 3.3 with the discretizaton obtained in 5.3.

In paragraphs 6.2.1 and 6.2.2, we confront the model and the numerical scheme to experimental data. In these two paragraphs the simulations are carried out except when explicitly mentioned, with the second order extension – in space and time – of the scheme whereas in paragraph 6.2.4 the first and second order schemes are compared. In paragraph 6.2.3, we test our model and numerical scheme in situations involving solitary waves propagation.

For each simulation (except those in paragraph 6.2.3 where no viscosity is used), we have used a viscosity $\nu = 0.001\,\mathrm{m}^2.\mathrm{s}^{-1}$. Except in paragraph 6.2.1 no bottom friction is prescribed.

6.2.1 Favre waves

Favre waves are secondary free surface undulations appearing after a sudden change in discharge of a channel for example due to the opening/closing of a sluice gate [SFZ02, Tre94].

We consider a closed basin with vertical shores as depicted in Fig. 16. The width of the basin is 0.4 m and the slope of the bottom is constant with

$$\frac{\partial z_b}{\partial x} = -0.004.$$

The same flow $\overline{Q}$ is fixed at the inflow Q_{in} and the outflow Q_{out} with $\overline{Q} = 0.035\,\mathrm{l.s}^{-1}$. Thus the system reaches a stationnary regime with $H_0 \approx 0.2$ m. After time t_0, the outflow Q_{out} quickly

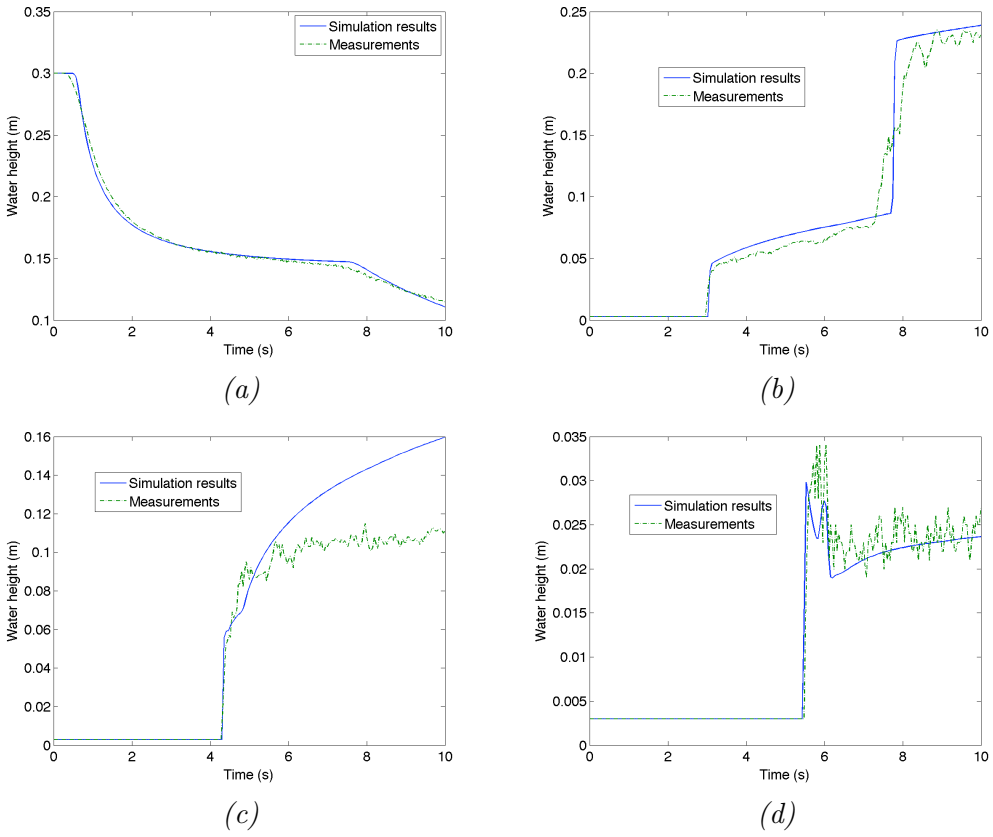

Figure 15: Surface level, (–) simulation results and (- -) experimental data. *(a)* probe S_1, *(b)* probe S_2, *(c)* probe S_3 and *(d)* probe S_4.

decreases

$$\begin{cases} Q_{out} = \overline{Q} & \text{for } t \leq t_0 \\ Q_{out} = 0 & \text{for } t \geq t_0 + T \end{cases}$$

with $T = 0.07\,\mathrm{s}$. At the bottom, a Strickler friction law is used with coefficient $\kappa = 102\,\mathrm{m}^{1/3}.\mathrm{s}^{-1}$.

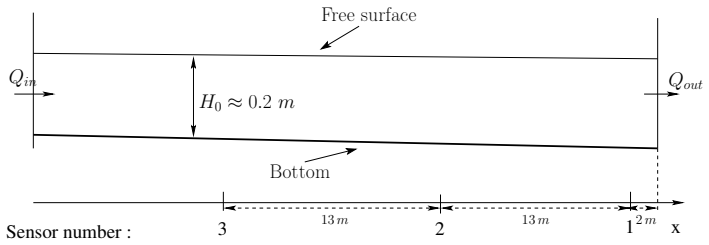

Figure 16: Channel profile for the experiments and location of the sensors.

Because of the sudden closure of the exit, a shock wave propagates for $t \geq t_0 + T$ from the exit to the left boundary of the domain and three sensors (see Fig. 16) record the free surface elevation along time.

We present simulations results obtained with the Roe scheme and the kinetic scheme in order to emphasize that the non-hydrostatic terms can be added to any finite volume solver for the usual Saint-Venant system. We first present (see Fig. 17) the simulations results obtained with the classical Saint-Venant and with the extended Saint-Venant system discretized using the kinetic and the Roe schemes (1^{st} order in space and time). Notice that, in this test case, the Roe scheme and the kinetic scheme give similar results for the simulation of the classical Saint-Venant system. For these simulations with the kinetic and the Roe solvers, the horizontal mesh has 3000 nodes.

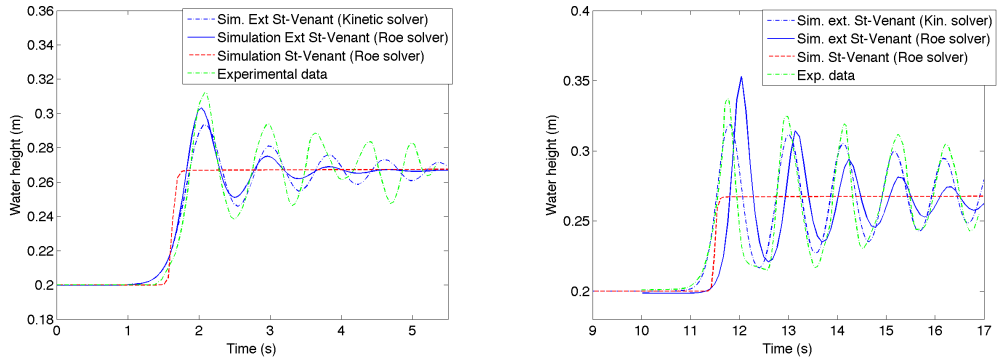

(a) *(b)*

Figure 17: Comparisons between the simulations of the extended Saint-Venant system: kinetic (-.), Roe (–), the classical Saint-Venant system (- -) and the experimental measurements (-.) for sensors 1 and 2. *(a)*: sensor 1 and *(b)*: sensor 2.

In Fig. 18, we present the simulation results of the extended Saint-Venant system obtained with the numerical scheme based on the kinetic solver with the 2^{nd} order in space and time. Notice the important improvement of the solution due to the 2^{nd} order scheme (in space), this improvement can not be obtained by the 1^{st} order schemes even on refined meshes, see paragraph 6.2.4. For the simulations with the 2^{nd} order scheme, the horizontal mesh has only 1500 nodes.

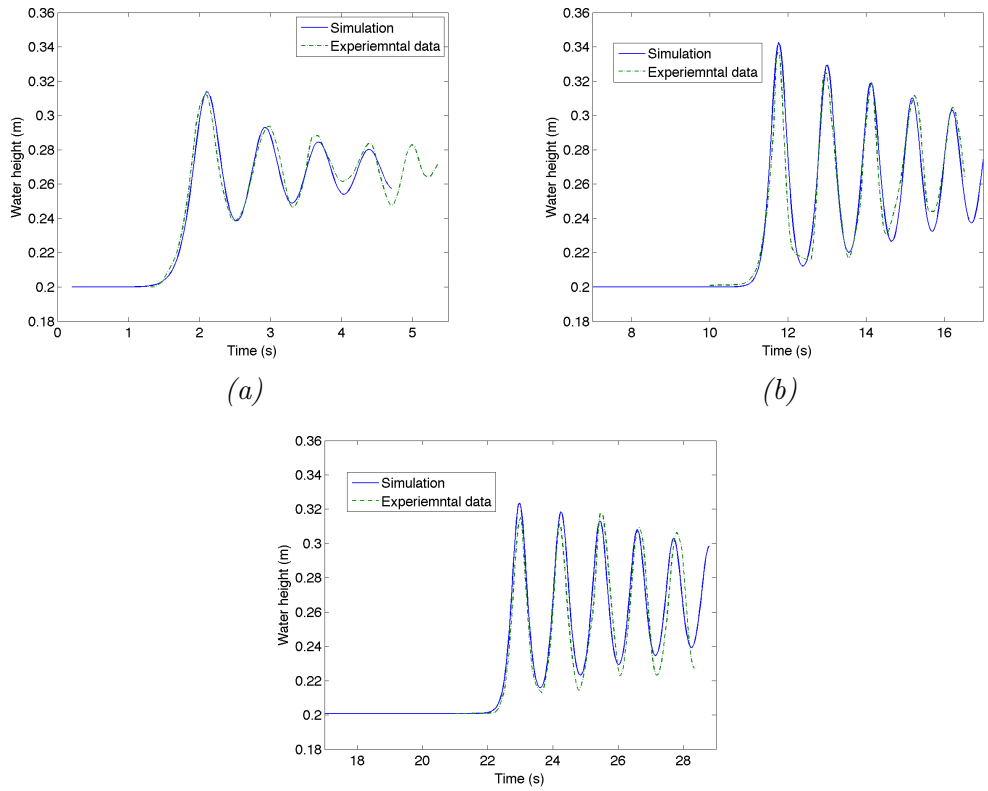

Figure 18: Comparisons between the simulations of the extended Saint-Venant system (solid line) and the experimental measurements (dasheddotted line) for each sensor. Kinetic solver *(a)*: sensor 1, *(b)*: sensor 2 and *(c)*: sensor 3.

Notice that in this situation, the parameter δ defined in paragraph 3.1.3 and representing the ratio between the typical wave amplitude and the typical water depth has a value around 0.7. Even if we are far from the assumption $\delta \ll 1$ allowing to justify that the convective terms can be neglected in the pressure expression (see Eqs. (3.36), the simulations of Fig. 18 are in good agreement with the experimental data provided by EDF (Electricité de France, [Cau68]).

The table 1 gives the computational cost in terms of CPU time corresponding to the simulations with the kinetic scheme in various situations. The simulations have been carried out on a Linux PC (processor AMD Phenom X4 820). For all the simulations presented in table 1, we have used the 2^{nd} order time scheme.

	Saint-Venant		Extended Saint-Venant	
	1^{st} order	2^{nd} order	1^{st} order	2^{nd} order
1500 nodes	41.5	97.2	52.3	118.4
3000 nodes	171.5	413.8	211.6	490.8

Table 1: CPU time (in s) corresponding to various simulations for the test case of the Favre waves.

Remark 6.1. *In order to capture the non-hydrostatic effetcs, fine meshes are necessary when using the 2^{nd} order schemes.*

Remark 6.2. *The Favre undulations as depicted in Figs. 17 and 18 are clearly an extension of the Rankine-Hugoniot jump condition. A quasi-analytical solution (for flat bottom) for the undulations can be found. This is not detailed in this document.*

6.2.2 Dinguemans experiments

The experiments carried out by Dingemans [Din97] at Delft Hydraulics deal with the wave propagation over uneven bottoms. A small amplitude wave (0.02 m) is generated at the left boundary of a closed basin with vertical shores, see Fig. 19. Eight sensors recording the free surface elevation are located at abscissa 2 m, 4 m, 10.5 m, 12.5 m, 13.5 m, 14.5 m, 15.7 m and 17.3 m. The simulations depicted in Figs. 20 and 21 have been obtained with 1000 nodes.

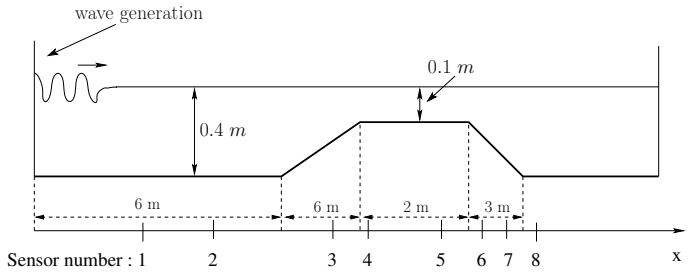

Figure 19: Channel profile for the experiments and location of the sensors.

We first compare the simulations obtained with the classical Saint-Venant system and the experimental measurements, see Fig 20. The wave propagation is non-dispersive when the bottom is flat (sensors 1 and 2) and becomes dispersive around the trapezoidal step.

Then we compare the experimental data with the simulations of the extended Saint-Venant system. Even if the considered geometry (see Fig. 19) corresponds to the shallow water assumption,

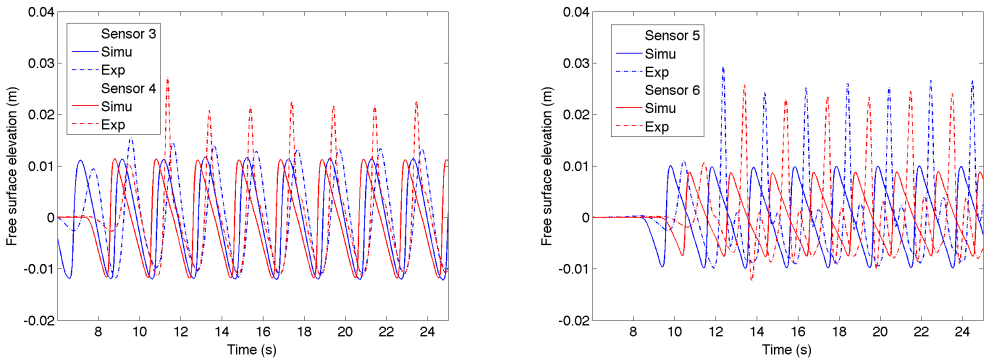

(c) *(d)*

Figure 20: Comparisons between the simulations of the classical Saint-Venant system (solid line) and the experimental measurements (dashed line) for sensors 3,4,5 and 6.

the gradient of the topography around the step is large and the assumption (see paragraph 3.1.3)

$$\frac{a_b}{h} \ll 1,$$

is not fully satisfied. Nevertheless, the simulations (Fig. 21) are in good agreement with the experimental data particularly for sensors 1 to 6. As expected, the discrepancy between the simulations obtained with the classical Saint-Venant system and its extended version is important.

It has to be noticed that for sensors 7 and 8 i.e. Fig. 21-*(d)* some significant differences appear between the simulations and experimental measurements. In this part of the channel, the topography gradient is large and possibly some non-hydrostatic effects coming from the convective terms

$$u\frac{\partial w}{\partial x} + w\frac{\partial w}{\partial z},$$

play an important role.

6.2.3 Solitary wave propagation

A solitary wave is a single elevation of water surface above an undisturbed surrounding, which is neither preceded nor followed by any free surface disturbances. Neglecting dissipation, as well as bottom and lateral boundary shear, a solitary wave travels over a horizontal bottom without changing its shape and velocity. Therefore, it is a good test case for testing the capability of free surface algorithms to describe the propagation of finite amplitude non-linear waves. The accuracy of the model can be evaluated by comparing the amplitude and the celerity of the wave with its theoretical values, as well as the deformation of the wave as it travels.

There are numerous analytical studies of this form of non-linear finite-amplitude wave. We refer to [Jan99] and more recent works [BBC+10, CLM10, LMGH10] and references therein for the simulation of a solitary wave in free surface flows. Notice that the analytical or approximated solutions of solitary waves propagating in free surface flows are generally obtained in the case of potential flows (irrotational) or Green-Naghdi model. So these solutions are not exact/approximated solutions for our extended Saint-Venant system but we show that our model well behaves with these particular solutions.

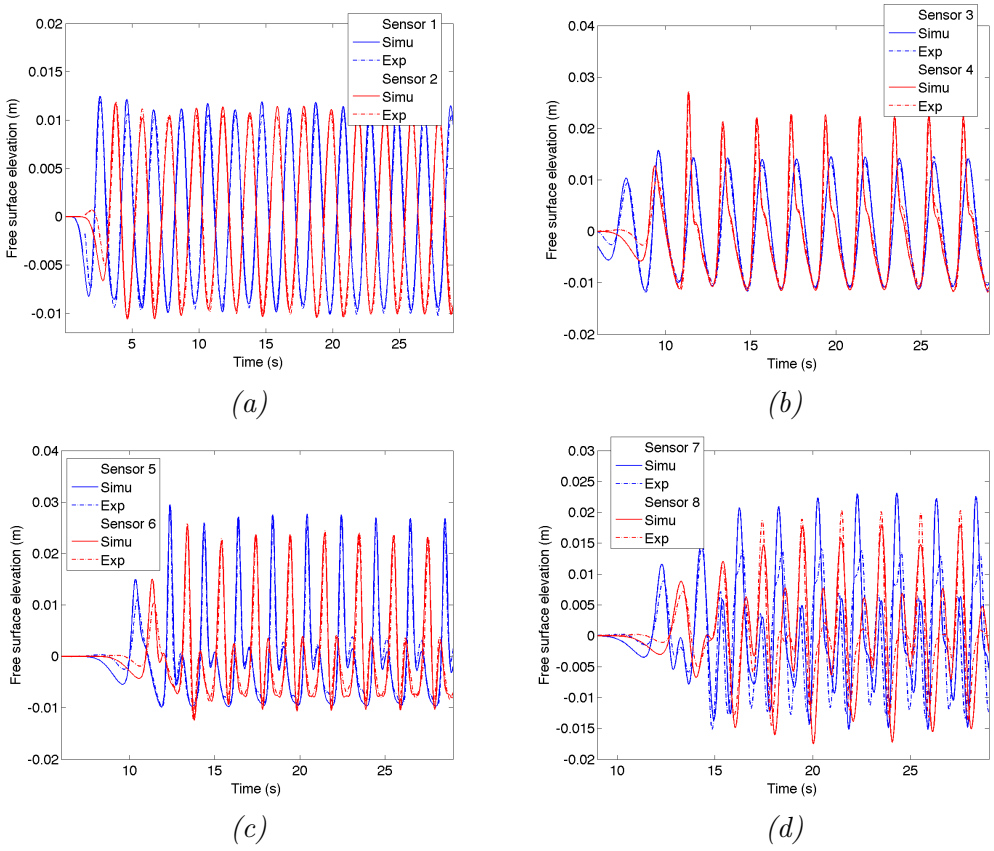

Figure 21: Comparisons between the simulations of the extended Saint-Venant system (solid line) and the experimental measurements (dashed line) for each sensor. *(a)* sensors 1 and 2, *(b)* sensors 3 and 4, *(c)* sensors 5 and 6, *(d)* sensors 7 and 8,

For a vertical section of an infinitely long channel with a water height H_0 (at rest), the following formulae give the free surface elevation η and the velocity u of a solitary wave with a height a propagating in the fluid with the celerity $c = \sqrt{g(H_0 + a)}$, see [Jan99, BBC+10, LMGH10]

$$\eta = H_0 + z_b + a\,\mathrm{sech}\left(\sqrt{\frac{3a}{4H_0^3}}(x - ct)\right), \tag{6.2}$$

$$u = \frac{\sqrt{gH_0}a}{H_0}\mathrm{sech}^2\left(\sqrt{\frac{3a}{4H_0^3}}(x - ct)\right). \tag{6.3}$$

Figure 22 clearly shows that the wave amplitude as well as the wave shape is preserved during the calculation with the extended Saint-Venant system (Figs. 22-*(b)* and 22-*(d)*) whereas the wave evolves towards a shock wave with the classical Saint-Venant system (Figs. 22-*(a)* and 22-*(c)*).

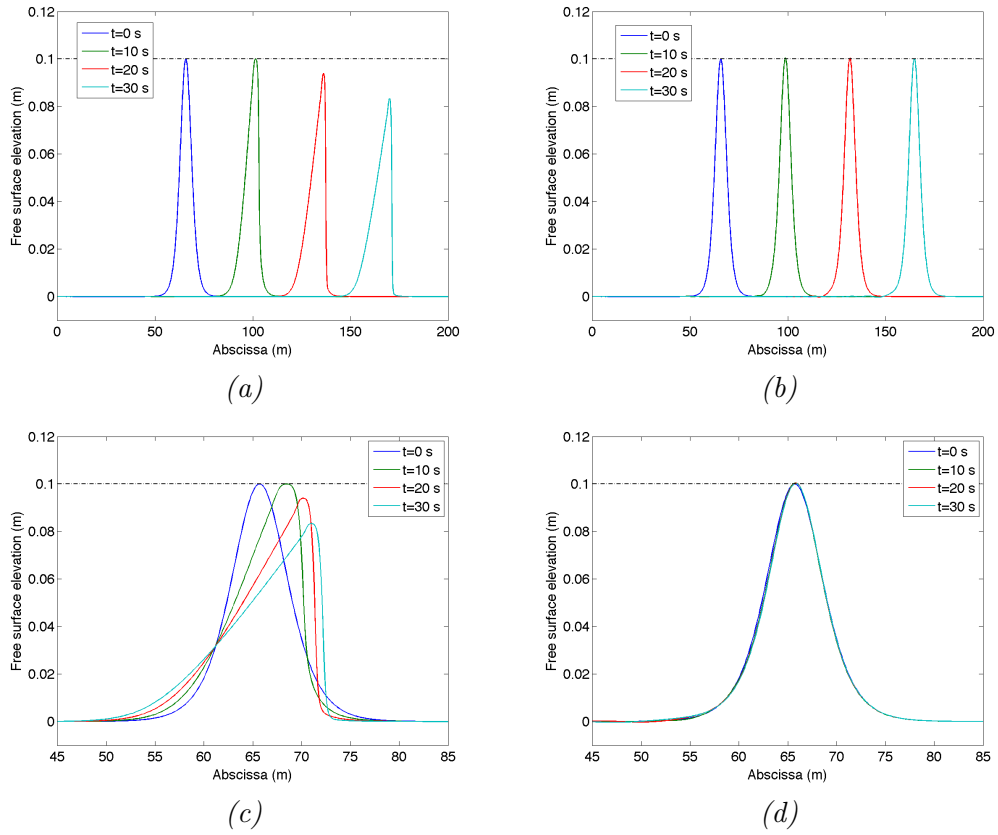

Figure 22: Solitary wave propagation in a long channel with a flat bottom when $a = 0.1H_0$ for various time steps, *(a)* Saint-Venant system and *(b)* Extended Saint-Venant system. *(c)* and *(d)* are analogous to respectively *(a)* and *(b)* but the snapshots of the free surface are translated to emphasize the shape modifications of the free surface along time.

6.2.4 First and second order schemes

It is not easy to give any convergence order for the numerical scheme since we have not at our disposal any analytical solution for our non-hydrostatic system. Indeed, the solitary wave given by

Eqs. (6.2),(6.3) is an exact solution of the Green-Nagdhi model but only an approximated solution for our non-hydrostatic model. Nevertheless assuming the numerical scheme converges, we can estimate a theoretical convergence order as follows: we simulate a test case with a very fine mesh and taking the obtained results as a reference solution, we compare them with the simulations results obtained with coarser meshes. Such a process has been used to obtain Fig. 23 where the reference solution corresponds to the simulation depicted in Fig. 18-*(c)* with 8000 nodes. In Fig. 23, we plot the rate of error versus the horizontal discretization, namely the number of nodes. We have plotted the $\log(L^1 - error)$ of the water height versus $\log(h_0/h_i)$. We denote by h_i the average cell length, h_0 is the average cell of the coarser mesh. These errors have been computed on 5 meshes with 250, 500, 1000, 2000 and 4000 nodes with the second order (in space and time) scheme. It appears on Fig. 23 that the convergence order of the scheme is around 1.5 that is satisfactory since even if the conservative and topography terms are approximated at the second order, the non-hydrostatic terms are discretized using a first order scheme.

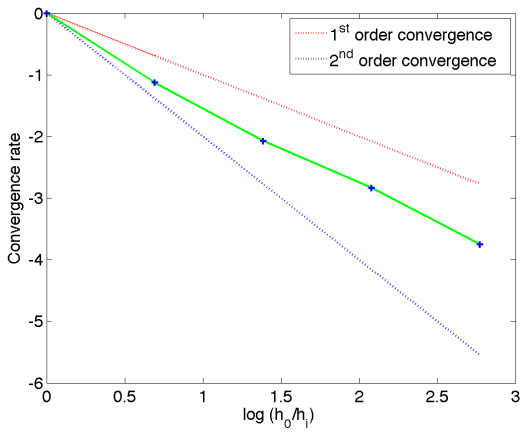

Figure 23: Convergence rate to a reference solution.

In order to evaluate the benefit of the 2^{nd} order approximation in space, we compare the simulation results of the Dinguemans experiment for the 6^{th} sensor obtained with 1500 nodes and the 2^{nd} order scheme to the simulation results with the 1^{st} order scheme for several meshes, see Fig. 24. The results depicted in Fig. 24 demonstrate the second order extension is crucial to capture the complex phenomena arising around the trapezoidal step. Even with 4000 nodes, the solution obtained with the 1^{st} order scheme is far from the experimental results.

Likewise we evaluate the benefit of the Heun scheme i.e. the 2^{nd} order time scheme, see Fig. 25. For the 6^{th} sensor, we compare the results obtained with the 2^{nd} order scheme (in space and time) with the results obtained with the first order scheme in time (but 2^{nd} order in space) under various CFL conditions.

6.2.5 Influence of the non-hydrostatic terms

All the non-hydrostatic terms are given in (3.40)-(3.41) but the rescaling associated with the Shallow Water assumption shows they do not have the same importance with respect to the small parameters ε, δ. In this paragraph, we examine the relative importance of these terms.

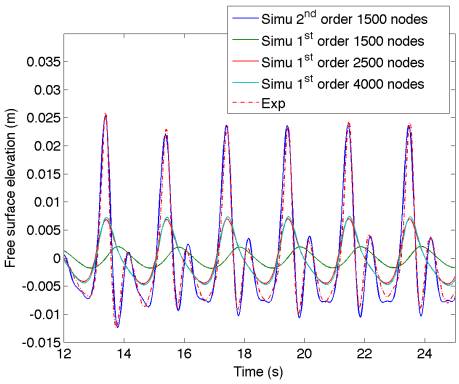

Figure 24: Comparisons between the experimental data and the simulation results with the 1^{st} and 2^{nd} order scheme for various mesh coarsity.

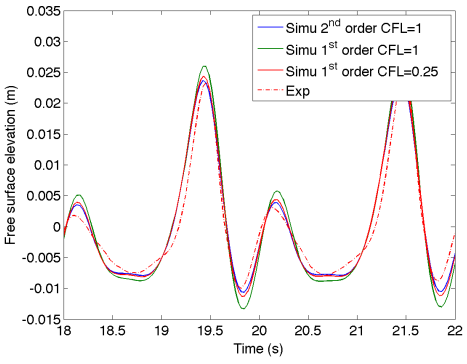

Figure 25: Comparisons between the experimental data (sensor 6) and the simulation results with the 1^{st} and 2^{nd} order in time scheme for various CFL conditions.

Thermo-mechanical compatibility The influence of the complementary terms ensuring the thermo-mechanical compatibility (see Remark 3.4) has been estimated. These terms have few influence when considering test cases –as in paragraph 6.2.1 –where the non-hydrostatic effects only consist in harmonic oscillations. In situations where the dispersive effects are more complex –as in paragraph 6.2.2 – the improvement can be meaningful, see Fig. 26.

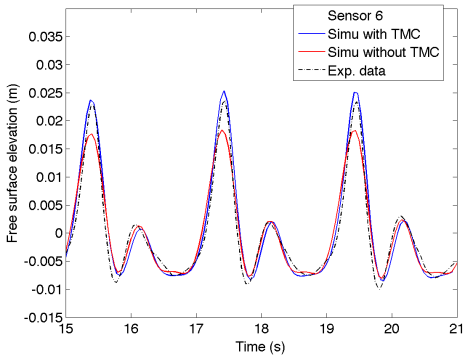

Figure 26: For the Dinguemans experiment, comparisons between the experimental data (sensor 6) and the simulation results with and without the thermo-mechanical compatibility (TMC).

In various situations – not only those depicted in this paper – the influence of the complementary terms ensuring the thermo-mechanical compatibility has been evaluated. In any case these complementary terms seem to have a significant influence over the simulation results. Thus, we have not encountered any case where the absence of these therms ensuring the thermo-mechanical compatibility leads to unrealistic results or failure of the code (e.g. due to negative water height) and even in stiff cases (dam break simulations, dry bottom,...).

Bathymetry gradient Even if the Saint-Venant system can be used to simulate shallow water flows with an arbitrary topography, its derivation from the Navier-Stokes equations is theoretically only valid when the bottom gradient is small (see [GP01, 5]) i.e.

$$\frac{\partial z_b}{\partial x} \ll 1.$$

In this paragraph we investigate the contribution of the non-hydrostatic terms depending on the bottom gradient over the simulation results.

When the slope is neglected in the non-hydrostatic terms i.e. $\frac{\partial z_b}{\partial x} = 0$ in Eqs. (3.40)-(3.41), then the pressure terms $H\overline{p}$ and $\overline{p}|_b$ reduce to

$$H\overline{p} = Hp^a + \frac{g}{2}H^2 - \frac{\partial}{\partial t}\left(\frac{H^3}{3}\frac{\partial \overline{u}}{\partial x}\right) + \frac{2}{3}\frac{\partial H^3}{\partial t}\frac{\partial \overline{u}}{\partial x}, \tag{6.4}$$

$$\overline{p}|_b = p^a + gH - \frac{1}{2}\frac{\partial}{\partial t}\left(H^2\frac{\partial \overline{u}}{\partial x}\right) - \frac{\partial H^2}{\partial t}\frac{\partial \overline{u}}{\partial x}. \tag{6.5}$$

Notice that the previous assumption does not imply the topography source terms coming from the hydrostatic part of the pressure vanish. If such a term is neglected, it obviously leads to unrealistic results.

We consider the test case depicted in paragraph 6.2.2 where the geometry given in Fig. 19 exhibits bottom slopes of 5% before the step and of 10% after the step. In Fig. 27, we compare

the simulation results with and without the previous assumption i.e. with the complete expression of the pressure terms given in Eqs. (3.40)-(3.41) and with the reduced version corresponding to Eqs. (6.4)-(6.5).

Surprisingly Fig. 27 shows the influence of the non-hydrostatic terms involving the bottom slope can be neglected. It seems more important to take into account the thermomechanical compatibility than the bottom slope (see Fig. 26). When considering larger slopes than in this test case, the validity of the Saint-Venant system in itself is questionable so the influence of the bottom slope over the non-hydrostatic terms has not been studied.

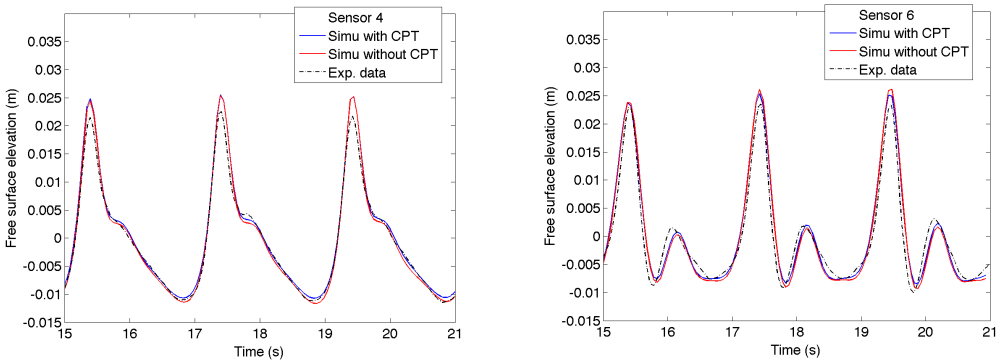

(a) *(b)*

Figure 27: Comparisons between the experimental data and the simulation results with and without the complete pressure terms (CPT). *(a)* sensor 4 and *(b)* sensor 6.

6.3 Hydrostatic Navier-Stokes system [3]

In this paragraph we give several validations of the model and numerical scheme respectively described in paragraphs 3.4 and 5.4. In this paragraph, the fluid density is kept constant. Flows with varying density will considered in paragraph 6.4.

We first consider a wind driven flow where a local analytical solution is available. Then we use the model in the classical test case of a supercritical regime with important variations of the free surface. Finally we compare the multilayer model with a 2d-(x, z) hydrostatic Navier-Stokes system based on a finite elements discretization and developed in FreeFem++ [fre09].

6.3.1 Analytical solution

We claim several times that the great interest of the new multilayer formulation that we proposed here is to allow mass exchanges between layers. This effect is exhibited in the numerical test that we present now. We consider a fluid in a rectangular closed bassin with vertical shores and we impose a constant wind stress (from left to right) at the free surface. The flow is then supposed to reach a stationary state with a recirculation in the lake. Notice that this kind of stationary flows is clearly impossible to compute with the classical one-layer Shallow Water system since the velocity is imposed to be constant along the vertical. They are also out of the domain of application of the former multilayer shallow water system that was introduced by Audusse [Aud05] since they clearly involve large mass transfers (at least near the shores) between the layers. It is easy to deduce from

the mass conservation equations that the only stationary regime of the former multilayer model for a flow in a closed bassin is the flow at rest, as for the classical Saint-Venant model.

The domain is 16 m long with an initial water height of 2 m. The mesh has 160 nodes in the x direction and 20 layers. The wind velocity (from left to right) is 20 $\mathrm{m.s}^{-1}$. We show the results on a postprocessing 2d mesh that is presented in Fig. 28. In Fig. 29 we also present the two dimensional velocity vectors on this 2d mesh. The results exhibit a global recirculation. Since we consider a Shallow Water type system, the vertical velocity is not a variable of the computation. But it is possible to recover it for postprocessing purpose using the kinetic relation proposed in paragraph 4.4.3 and especially a discrete version of Eq. (4.24).

For this test case, the bottom velocity is imposed to be zero by prescribing a very large Navier friction coefficient. Then there exists an analytical solution of the velocity profile at mid-length of the lake. This calculation is detailed in [SCS97]. In Fig. 30-*(a)* we compare the analytical solution with the results obtained with the multilayer model for different vertical discretizations. We have used a viscosity of $\nu = 0.01$ $\mathrm{m}^2.\mathrm{s}^{-1}$. In Fig. 30-*(b)*, we plot the rate of error versus the vertical discretization, namely the number of layers. We have plotted the $\log(L^1 - error)$ of the horizontal velocity – at mid-length of the domain – versus $\log(h_0/h_i)$. We denote by h_i the average cell height, h_0 is the average cell height of the coarser mesh. These errors have been computed on 4 meshes with 5, 10, 20 and 30 layers. For each mesh, the horizontal discretization is taken very precise meaning the error associated with the horizontal discretization can be neglected. Even if we use a second order scheme (see paragraph 5.1.2) for the hyperbolic part of the model, the friction and exchange terms are discretized using a 1^{st} order scheme. So it appears that the computed convergence rates are closed to 1.7.

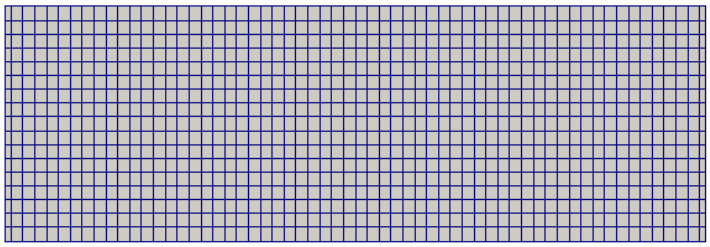

Figure 28: The geometrical model with the horizontal mesh and the vertical discretization by layers. In the horizontal direction, only 60 nodes are shown.

6.3.2 Transcritical flow over a bump

Then we consider an academic test case that is very commonly used for the validation of classical one-layer Shallow Water solvers. Here we add some friction at the bottom in order to compare solutions of one-layer and multilayer Shallow Water systems with the solution of hydrostatic incompressible Navier-Stokes equations. We impose an inflow (left boundary) of 1.0 $m^2.s^{-1}$ and the water height at the exit (right boundary) is prescribed to be equal to 0.6 m. The Strickler friction coefficient at the bottom is 30 $m^{1/3}.s^{-1}$ and the kinematic viscosity is 0.01 $m^2.s^{-1}$. The data are chosen such that the flow is supposed to reach a stationary regime that presents some transitions between sub- and supercritical parts and an hydraulic jump. Notice that an analytical solution exists for this test in the case of a single layer [AB05a, PS01].

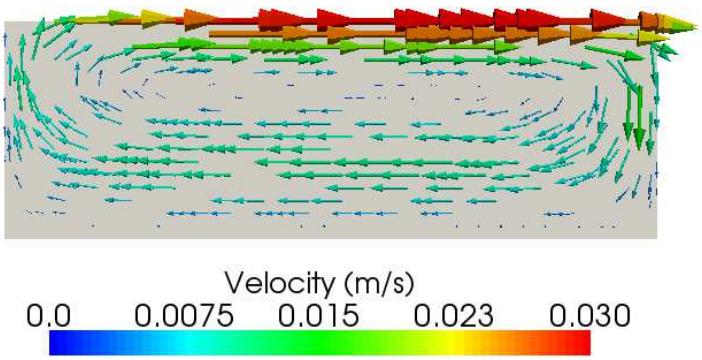

Figure 29: The wind blows from the left part of the domain to the right part. The arrows represent the velocity field in the lake.

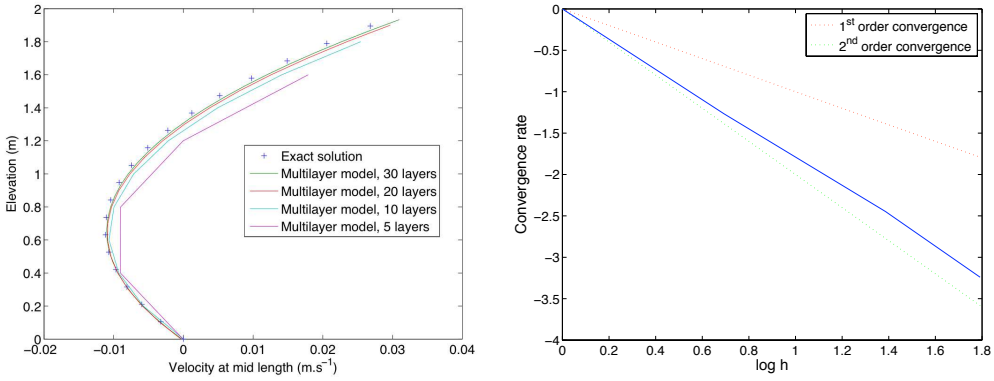

(a) *(b)*

Figure 30: *(a)* Comparison between the analytical and simulated solutions and *(b)* convergence rate.

The simulation results are depicted in Figs. 31, 32 and 33. Notice that the actual computations are purely one dimensional. Hence Figs. 31 and 32 present velocity results on a postprocessing mesh that is constructed departing from the 1d mesh by the use of the computed layer water heights. The presented results correspond to an instant t_f where the permanent regime is achieved.

The results depicted in Figs. 31 and 32 are consistent with computations performed using the hydrostatic Navier-Stokes equations of TELEMAC3d [ABD08, DG09] and also using the former multilayer Saint-Venant system [ABD08]. The results depicted in Fig. 33 exhibit that the presented solver is quite robust since it is able to compute transcritical solutions and shock waves even when a large number of layers is considered. This kind of robustness is far from being obvious for 3d Navier-Stokes solvers where the mesh has to follow the movements of the free surface. Notice also that the hydraulic jump appears to be overestimated by the one-layer computation when compared with other results - see Fig. 33.

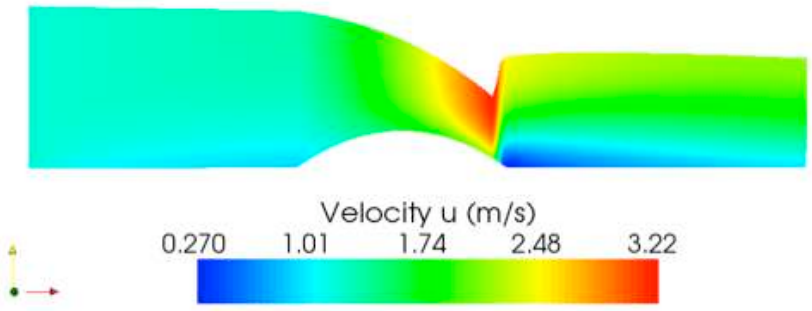

Figure 31: Horizontal velocities $\{u_\alpha(x,t_f)\}_{\alpha=1}^N$ with $N = 15$ layers.

6.3.3 Comparison with a finite element simulations of the hydrostatic Navier-Stokes system

We have also compared our simulations with results obtained using a finite element discretization of the hydrostatic Navier-Stokes system. The finite element formulation is P_1/P_1 for the velocity and the pressure and uses a stabilization technique. The formulation is available in the FreeFem++ code [fre09].

We still consider a wind driven flow with vertical shores but with a non trivial bottom. The domain is 6 m long with an initial water height of 2 m. The mesh has 160 nodes in the x direction and 20 layers. The wind velocity (from left to right) is 10 m.s^{-1}. We have used a viscosity of $\nu = 0.1$ $\text{m}^2\text{.s}^{-1}$ and a Navier type bottom friction with $\kappa = 0.1$ m.s^{-1}. For each simulation (multilayer approach or finite elements approximation), the mesh has approximatively 1000 nodes. For the multilayer approach, the results on a postprocessing 2d mesh (see Fig. 34) are presented in Fig. 35 where we have plotted the two dimensional velocity vectors $(u,w)^T$. In Fig. 36 the results obtained with the finite elements code are shown. The results exhibit a global recirculation that is combined with two local recirculations that are induced by the topography of the lake. The qualitative aspect of the solution is consistent with the previsions.

The FreeFem++ code, solving the full Navier-Stokes system serves as a reference. It is however not straightforward to analyze the origin of the differences because the boundary conditions are not imposed in the same way. But in the examples presented in Figs. 35 and 36 whereas the viscosity and the bottom friction are large, the simulations are in agreement. The vertical velocity

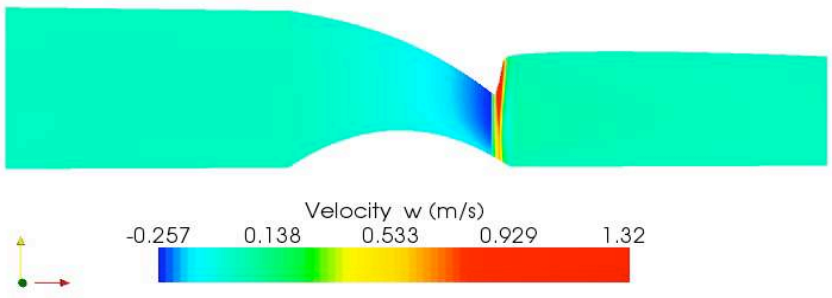

Figure 32: Vertital velocity $\{w_\alpha(x,t_f)\}_{\alpha=1}^N$ with $N = 15$ layers.

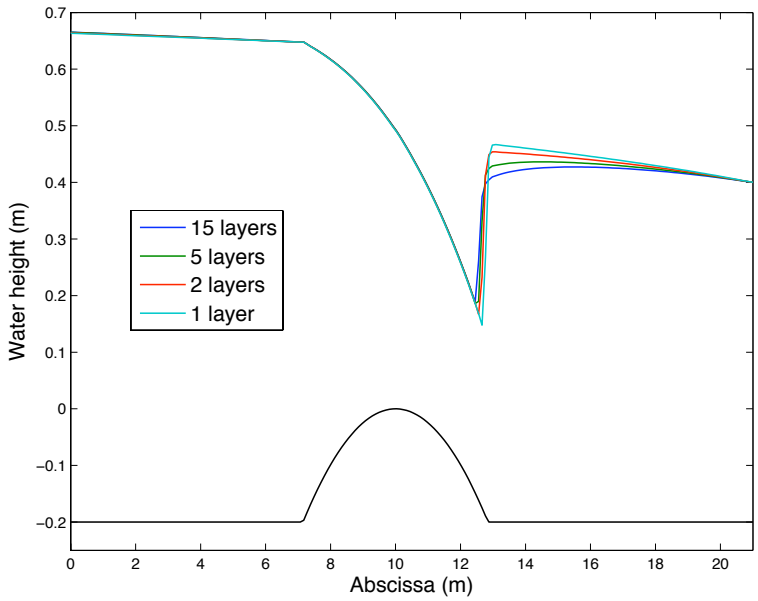

Figure 33: Shape of the free surface for simulations carried out with different number of layers.

w is overestimated by the multilayer code. This mainly comes from the fact that in the multilayer approach, w is calculated offline using u and the divergence free condition whereas in the finite element formulation, w follows a dynamical equation

$$\tilde{\epsilon}\left(\frac{\partial w}{\partial t}+u\frac{\partial w}{\partial x}+w\frac{\partial w}{\partial z}\right)+\frac{\partial p}{\partial z}=-g+\tilde{\epsilon}\frac{\partial \Sigma_{zx}}{\partial x}+\tilde{\epsilon}\frac{\partial \Sigma_{zz}}{\partial z},$$

with $\tilde{\epsilon}\ll 1$. Notice also that the difference of shape for the step in Figs. 35 and 36 only comes from the mesh reconstruction/interpolation procedure in the multilayer approach.

It is also difficult to compare the computational costs of the multilayer model and of the FE discretization since the simulations uses different tools. Nevertheless, if the simulation cost of a single layer Saint-Venant system is T, it is worth being noticed that without any parallelisation, the computational cost of a N layers system is only NT.

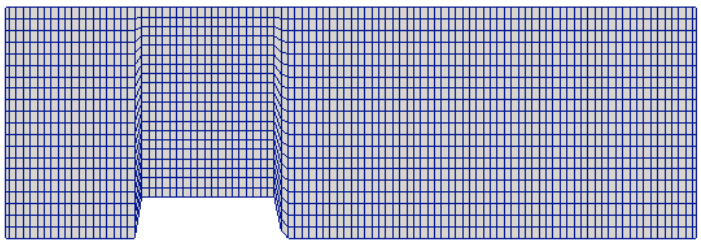

Figure 34: The geometrical model with the horizontal mesh and the vertical discretization by layers.

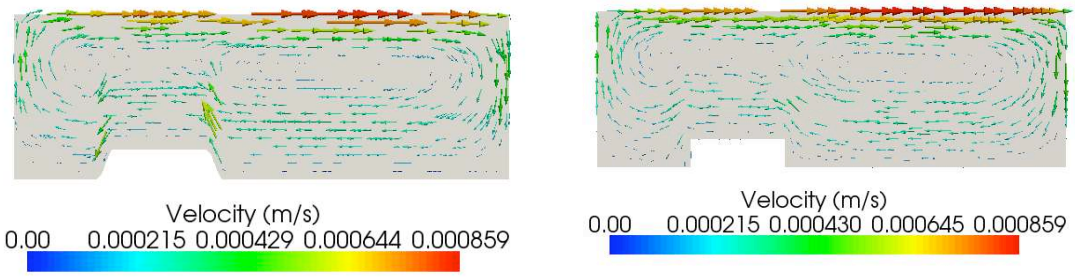

(a) *(b)*

Figure 35: The wind blows from the left part of the domain to the right part. The arrows represent the velocity field in the lake. *(a)* multilayer code and *(b)* finite element code.

6.4 Stratified flows [2, 4]

In this paragraph, we concentrate on situations where the density variations have crucial influence over the hydrodynamics.We consider the Navier-Stokes ystem with varying density described in paragraphs 3.5 and 5.4.

First we illustrate the behavior of the scheme in front of a non trivial static equilibria and then we present numerical experiments simulating density-stratified flows subjected to wind surface stress

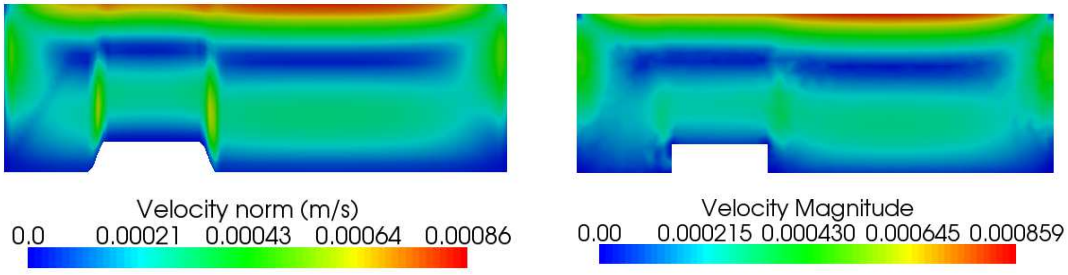

(a) *(b)*

Figure 36: Same as Fig. 35 but we plot the velocity norm $\sqrt{u^2+w^2}$.

and internal waves. The density is considered a function of the water temperature, and we adopt the classical state equation (as in Eq. (3.7))

$$\rho(T) = \rho_0 \left(1 - \alpha(T - T_0)^2\right), \tag{6.6}$$

with $T_0 = 4\,^o\mathrm{C}$, $\alpha = 6.63\,10^{-6}\,^o\mathrm{C}^2$ (volume coefficient of thermal expansion) and $\rho_0 = 10^3\,\mathrm{kg\,m^{-3}}$.

6.4.1 Static equilibria with non flat bottom

Here we illustrate the properties associated with the preservation of equilibria for stratified flows, see paragraph 5.4.6.

When considering diffusion on the pollutant i.e. $\mu_T \neq 0$ in relation (3.8), the only possible static equilibria are trivial and correspond to

$$\frac{\partial T}{\partial x} = Cst, \quad \text{and} \quad \frac{\partial T}{\partial z} = Cst, \qquad \forall x, z, t.$$

To avoid these simplified situations, we consider in this paragraph $\mu_T = \nu_T = 0$. However our numerical schemes having small numerical dissipation, a Navier type bottom friction is considered in each simulation in order to reach a static equilibrium more quickly.

We consider a 3 meters long closed basin with vertical shores and an initial water level of $H_0 + z_b = 1$ meter with the bottom geometry $z_b(x)$ defined by the parabolic bump

$$z_b(x) = \max(-1, -0.75 - 1.246(x - 1.2)^2),$$

The mesh has 100 nodes in the x direction.

In Figs. 37 and 38, we illustrate in the case of a non flat bottom the behavior of the scheme when starting from an unstable state. For the first example, presented in Fig. 37, at $t = t_0$ the temperature is distributed as follows

$$T^0(x,z) = \begin{cases} 25\,^oC & \text{if } z - z_b \geq 2H_0/3 \\ 8\,^oC & \text{otherwise} \end{cases}$$

For the simulation we have used a vertical discretization with 20 equally spaced layers i.e. $l_\alpha = 1/20$ for $\alpha = 1, \ldots, 20$. The postprocessing visualization tool performs a linear interpolation of the constant cell data that explains the small diffusion which is observed at initial time.

With the same geometry, still with a flow initially at rest but starting from an initial temperature distribution far from any equilibrium, see Fig. 38-*(a)*, the system also reaches a stable static equilibrium, see Fig. 38-*(b)*.

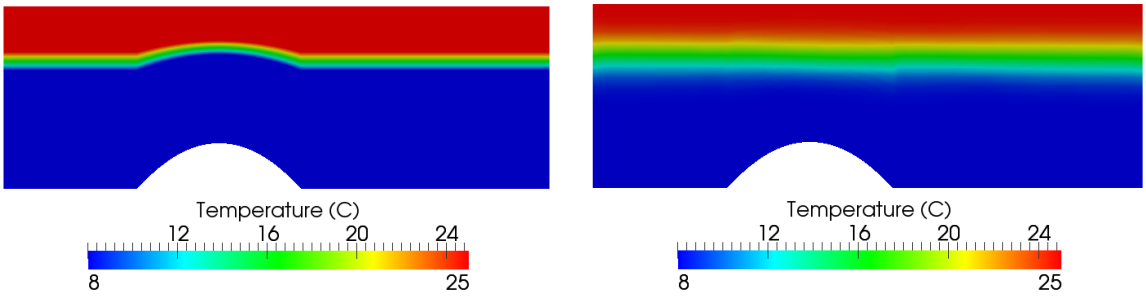

(a) *(b)*

Figure 37: *(a)* initial state and *(b)* static equilibrium reached after 10 minutes.

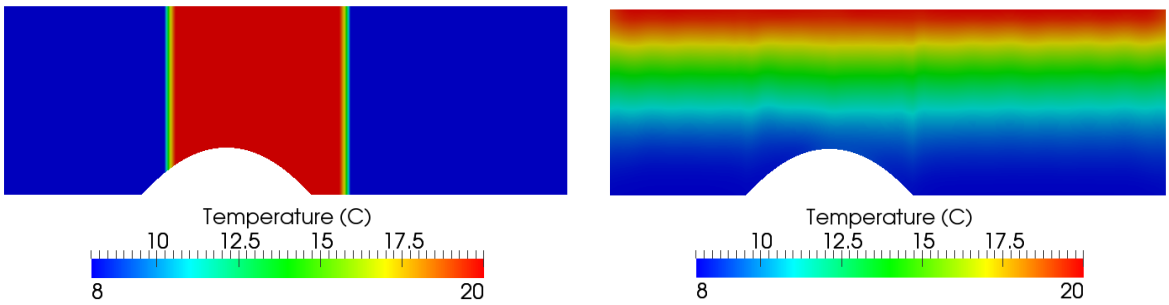

(a) *(b)*

Figure 38: *(a)* initial state and *(b)* static equilibrium reached after 20 minutes.

6.4.2 Internal gravity waves

Starting from an unstable initial condition and due to the fluid and tracer diffusivity, a stratified flow with two miscible fluids asymptotically evolves in presence of dissipative effects (bottom friction, viscosity), towards an equilibrium minimizing the potential energy E_p of the fluid volume V defined by

$$E_p = \int_V \rho(T) g z \; dz,$$

and corresponding to $\frac{\partial T}{\partial x} = 0$. So the interface between the two fluids is asymptotically horizontal. This corresponds exactly to the situations depicted in paragraph 6.4.1 with Figs. 37,38.

In this paragraph we show that there is few numerical diffusivity in our numerical scheme. In absence of physical diffusivity and friction and still starting from an unstable initial condition, the potential energy has now no reason to decrease and oscillations will appear in the fluid domain. The preservation of the interface between two miscible fluids for such gravity waves is an interesting challenge for numerical schemes since in practice numerical diffusion coming from the scheme is often observed leading the simulation to an artificial equilibrium.

Concerning gravity wave simulations, we mainly refer to [FAS05] and references therein. In [FAS05] various numerical schemes are confronted with a test case corresponding to a finite amplitude deep-water standing wave. The interface is defined in [Tho68] and given by

$$\zeta(x) = a \left(\left(1 - \frac{(ka)^2}{64} \right) \cos kx - \frac{(ka)^2}{8} \cos 3kx \right),$$

where $ka = 0.1$ is the initial steepness, $k = 2\pi/L$ and L is the length of the domain.

In the same situation as the one described in [FAS05] where the interface thickness is $k\delta = 0.01\pi$, we obtain the following results. In Fig. 39 we show the profile of the density field at the initial instant and after two periods of oscillation. The period of oscillation is $T = 9.82$ seconds. We have used 80 nodes in the horizontal direction and 100 equally-spaced layers in the vertical direction. This corresponds to the geometrical model used by Fringer *et al.* [FAS05] even if in [FAS05] a refined mesh near the interface is used.

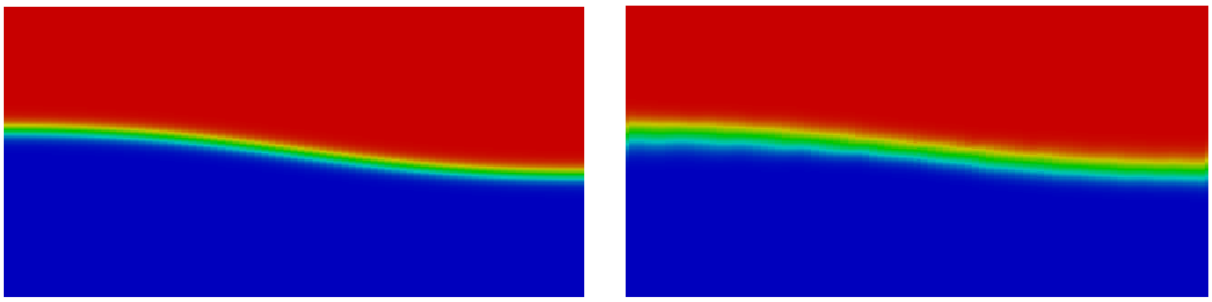

(a) *(b)*

Figure 39: Density field for the interfacial standing wave, *(a)* initial condition and *(b)* after two periods of oscillation.

6.4.3 Validity of the Boussinesq assumption

In the literature, the Boussinesq assumption (see paragraph 3.5.2) is very often considered but its validity is sometimes not so clear [MGL02, GLC01]. As far as the authors know, no numerical scheme exists with validated results and working without this assumption but there exist ocean models using various approximated versions of the non-Boussinesq equations [GLC01]. It seems to the authors that in most of the test cases they have simulated, this assumption is valid. However in case of internal waves with stratified flows and for long term simulations, the validity of this assumption is not always satisfied. The following test case ilustrates this behavior.

We consider the same geometry and initial conditions as in the first example of paragraph 6.4.1 and we compare in Fig. 40 the results that are obtained with and without the Boussinesq assumption. It appears that even if the system reaches in both situation the same static equilibrium, the transient velocity fields are different.

The differences induced by the Boussinesq assumption over the simulations are reinforced, in our case, by the numerous reflections against the vertical shores. For an overview of the physical situations where the Boussinesq assumption leads to significant errors, the reader can refer to [MGL02, GLC01].

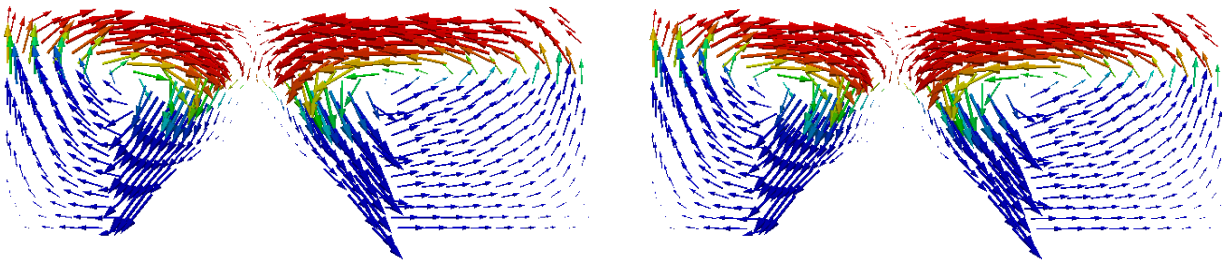

At time $t_1 = 1$ minute

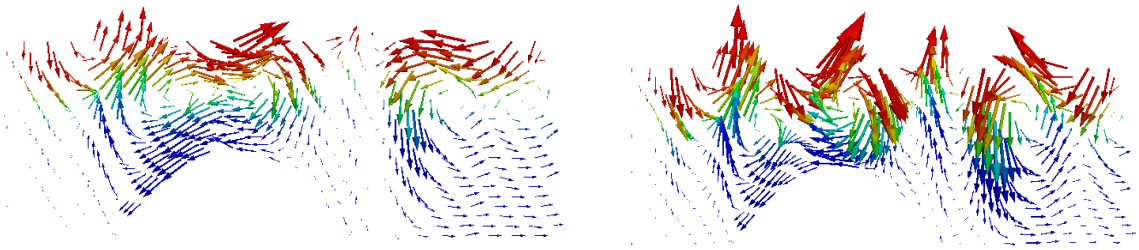

At time $t_2 = 2$ minutes

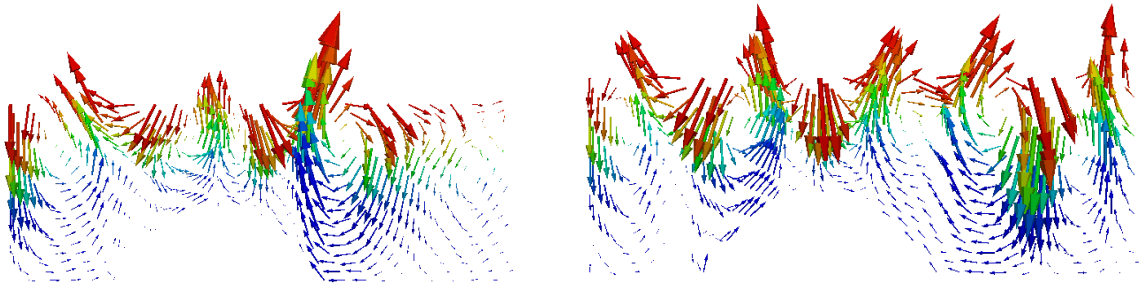

At time $t_3 = 3$ minutes

Figure 40: Numerical velocity field, left column: without the Boussinesq assumption and right column with the Boussinesq assumption.

6.4.4 Wind forced flows

The response of stratified flows to wind forcing is a typical situation in geophysical flows modeling. In this paragraph we first compare our numerical scheme to a local analytical solution then reproduce upwelling phenomena.

The typical thermal stratification of natural lakes and hydraulic reservoirs consists of a warmer less dense surface layer, a colder denser bottom layer, and a middle layer characterized by a steep vertical thermal gradient, the center of which is the thermocline. Thermo-hydrodynamical phenomena in lakes subject to the action of wind have been studied since a long time, by means of observations and measurements *in situ* [Wed12, Mor52], laboratory experiments [Mor52, Kra85, Mon86, SI96], theoretical analysis [HR66, Mon85, IP90], and, more recently, numerical simulations [TI80, CS97, HISW00, OI07]. Classically, in the literature the lake temperature distribution is schematized by a two-layer or three-layer thermal stratification.

When wind blows over these stratified systems, the thermocline is deflected upward in the upwind region. The thermocline behaves as a barrier between an upper region with circular fluid motion that has the same direction as the wind at the surface, and a lower region with fluid rotating in the opposite sense. If the wind is sufficiently strong then the thermocline reaches the surface at the upwind end of the basin and *upwelling* of deep fluid in the windward region occurs. This is quite different from the effect of wind forcing a homogeneous basin, where wind induces a simple circular motion of the fluid mass.

Analytical validation In this paragraph, we confront our numerical scheme to a local analytical solution. We consider a fluid in an enclosed rectangular basin, and we impose a constant uniform wind stress from left to right at the free surface. The simulations start with a basin at rest with the following two-layer temperature distribution (see Fig. 41)

$$T_0(x,z) = \begin{cases} 25\,^oC & \text{if } z - z_b \geq 2H_0/3 \\ 8\,^oC & \text{else} \end{cases}$$

where H_0 is the initial water height. Notice that since at $t_0 = 0$ we have

$$\frac{\partial \rho}{\partial z} \leq 0,$$

the initial state corresponds to a stable equilibrium. In such a situation, the system is supposed to reach a stationary regime described schematically by Fig. 41.

In the case of constant density, there exists an analytical solution of the horizontal velocity vertical profile at mid-length of the lake that is compatible with stationary Navier-Stokes equations. This calculation is detailed in [SCS97], see also paragraph 6.3.1. Here we extend this local analytical solution to the case of varying density. The calculus of this analytical solution is not described here, see Appendix A in [2].

We have used a viscosity of $\nu = 0.003$ m^2.s^{-1}, a Navier friction coefficient of $\kappa = 0.1$ m.s^{-1} and a wind velocity of 6 m.s^{-1}.

Notice that we have $\frac{\partial H}{\partial x}\frac{\partial H_1}{\partial x} < 0$ meaning the slope of the interface $z = H_1$ is significant and in the opposite direction compared to the free surface variations.

In Fig. 42-*(a)* we compare the analytical solution with the results obtained with the multilayer model for different vertical discretizations. Fig. 42-*(a)* presents the results obtained with 10, 30 and 50 layers. For each mesh, the horizontal discretization is taken very precise meaning the error

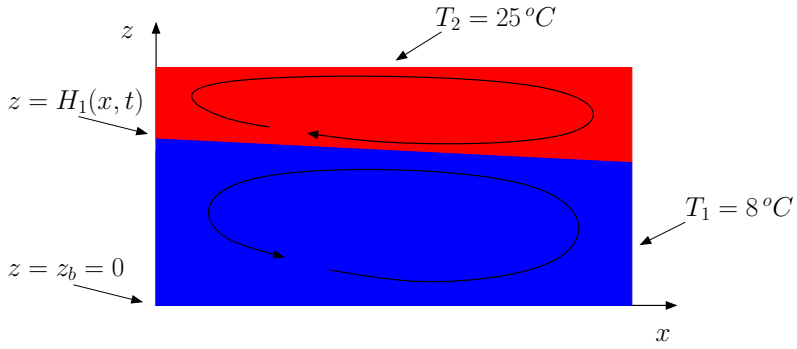

Figure 41: Flow domain with water height $H(x,t)$, interface $H_1(x,t)$ and with the double-gyre phenomenon. At t_0 we have $H_1(x,t_0) = 2H_0/3$.

associated with this discretization can be neglected. The results presented in Fig. 42-*(a)* are in good agreement with the analytical solution.

In Fig. 42-*(b)*, we plot the rate of error versus the vertical discretization, namely the number of layers. We have plotted the $\log(L^1 - error)$ of the horizontal velocity – at mid-length of the domain – versus $\log(h_0/h_i)$. We denote by h_i the average cell height, h_0 is the average cell height of the coarser mesh. These errors have been computed on 5 meshes with 5, 10, 20, 30 and 50 layers. It has to be noticed that the expression of the analytical solution gives $\frac{\partial H_1}{\partial x} < 0$. But since the velocity at the interface is tangent to $z = H_1$, this means we have $w \neq 0$ near $z = H_1$ so the initial assumption $w \approx 0$ is not completly true. For these reasons, the analytical solution and the simulated velocity at mid-length of the basin are not completly consistent and the convergence rate appearing in Fig. 42-*(b)* is not completely meaningful.

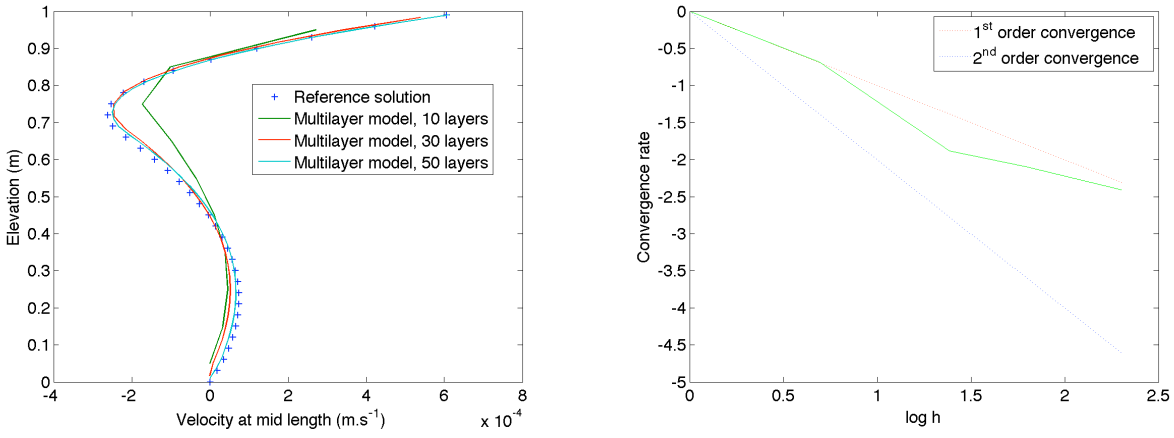

(a) *(b)*

Figure 42: Comparison between the analytical and numerical velocities at mid length of the basin.

Response to wind stress and upwelling Here we consider the test case depicted in the previous paragraph but with a larger wind velocity. The domain is a closed basin of 3 meters long with an

initial water height of 1 meter. The mesh has 100 nodes in the x direction and 30 layers. The wind velocity (from left to right) is $20\,\mathrm{m.s}^{-1}$. We have used a viscosity of $\nu = \nu_T = 0.001\,\mathrm{m}^2.\mathrm{s}^{-1}$ and a Navier type bottom friction with $\kappa = 0.1\mathrm{m.s}^{-1}$. In Fig. 43, we show at different times the computed temperature distribution and the velocity field. The right column corresponds to the case of a variable density obeying to the equation of state (see Eqs. (3.7) and (6.6)). The left column has been obtained with analogous configuration and initial conditions except that we have considered constant density: $\rho(T) \equiv \rho_0$. This means that T is merely a passive tracer that does not affect the density. Then, the differences between the right and left columns highlight the influence of the density variations on the flow response to wind forcing.

Notice that when the density variations are not considered the velocity profile along the vertical axis satisfies – far from the shores –

$$\frac{\partial^2 u}{\partial z^2} > 0,$$

whereas when the density variations are taken into account this quantity changes of sign when z varies from the bottom to the free surface. Because of the viscosity, this induces large dissipation and thus explains why the velocities are smaller on the left column than on the right one, see especially Fig. 43 (last picture on the left column). In the varying density case, the velocity field of the flow has reached a stationary state after $t = t_2$. In the constant density case, it is clear that no stationary state exists for the temperature distribution except an homogenous situation $T(x, z, t) = \bar{T}$. The shear stress coming from the wind induces a gradient of the free surface. Since the corresponding deformations of the free surface are small, they are not visible in Fig. 43.

Due to the simplicity of our physical model (uniform diffusivity, hydrostatic pressure), the aim of our numerical tests here is not attempting to reproduce realistic limnological processes on a long time scale. Rather, we emphasize the influence of density variations on the hydrodynamical response of the water body. In particular, the results of the simulations with variable density show that the numerical model is able to describe the tilting of the thermocline and upwelling of deeper fluid to the surface. Thus we are able to capture the essential features of the expected hydrodynamical behavior until the occurrence of upwelling. The post-upwelling flow dynamics cannot be modeled effectively by the present simplified model, mainly because of the lack of a turbulent mixing model.

More realistic upwelling simulations have been obtained by M. Pelanti and the author where turbulence models are introduced in the hydrostatic system with varying density. These simulations have been obtained with the industrial code Ophélie (EDF R&D) and compared with experimental data measured on the lakes of Parreloup and Sainte-Croix. The results will be published in a forthcoming paper. The industrial code Ophélie is developed in the framework of collaborative researches with EDF R&D especially M.J. Salençon (LNHE department).

6.5 3d simulations

We have claimed our model and numerical scheme can be extended to 3d flows. We present in this paragraph some 3d simulations with a 3d hydrostatic Navier-Stokes system with varying density. The 3d Navier-Stokes code has been built using a 3d extension of the model and numerical scheme presented in paragraphs 3.4, 3.5 and 5.4.

The derivation of the 3d model is straightforward. The dscretization is more tricky to obtain and we have followed the results proposed by Audusse et al. [AB05a]. The scheme we have used is positive, well-balanced and satisfies a maximum principle for the tracer. The second order extension in space and time is not yet implemented.

Since analytical solutions of the 3d hydrostatic Navier-Stokes are hardly accessible, we have

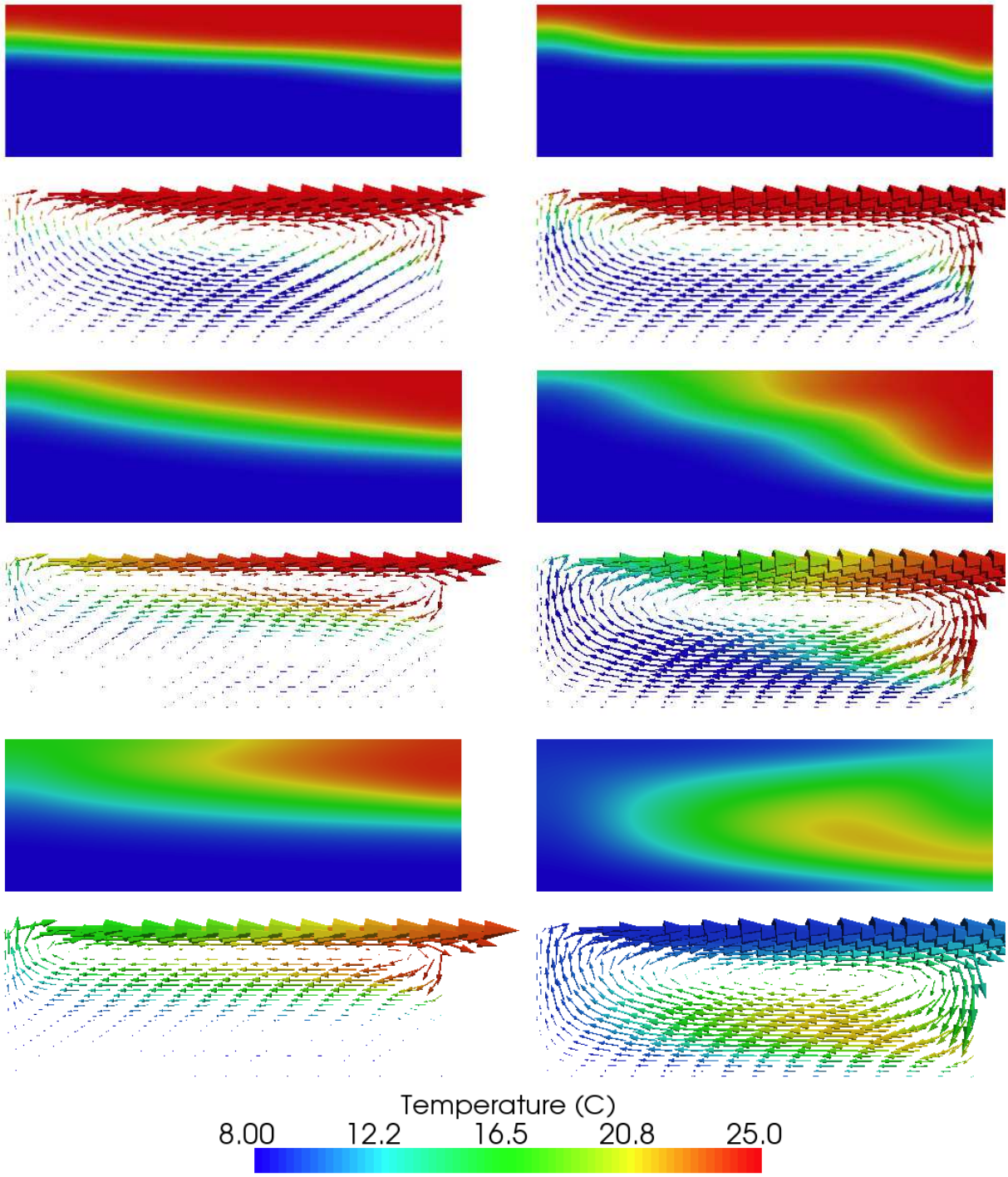

Figure 43: Influence of the density variations, left column with $\rho = \rho(T)$, right : same simulation but with $\rho = \rho_0$. First line, at time $t_1 = 10\,\text{s}$, second line at time $t_2 = 70\,\text{s}$ and third line at time $t_3 = 140\,\text{s}$.

confronted our code with situations reducing to 2d phenomena

- in the directions (x, z) such as those given in paragraphs 6.3 and 6.4,
- in the directions (x, y). In this case, we use our 3d code with only 1 layer ($N = 1$) and we compare it with existing codes solving the (x, y) Saint-Venant system.

In these two situations, the 3d code gives results that are similar to those obtained with

- the code developed by the author for the other proposed models,
- the 2d Saint-Venant code presented in [AB05a].

Obviously our 3d model with 1 layer reduces to the 2d (x, y) Saint-Venant system. The computational cost of the 3d model with N layers and constant density is exactly N times the cost of the simple 2d (x, y) Saint-Venant code.

6.5.1 Dam break simulation

We consider the case of a dam break in a channel with locally rectangular section. This simple geometry has been already used to confront the numerical scheme of the section-averaged Saint-Venant system with experimental measurements (see paragraph 6.1.4) and exhibits few variations of the variables in the y direction. For this reason, we have added a bump before the shortening of the channel width (the bump is not in the middle of channel in the y direction), see Fig. 44. The flow charateristics at four different instants are depicted in Fig. 45. We have used the 3d model with 10 layers. The mesh has 3500 nodes. The boundary and initial conditions are those described in paragraph 6.1.4.

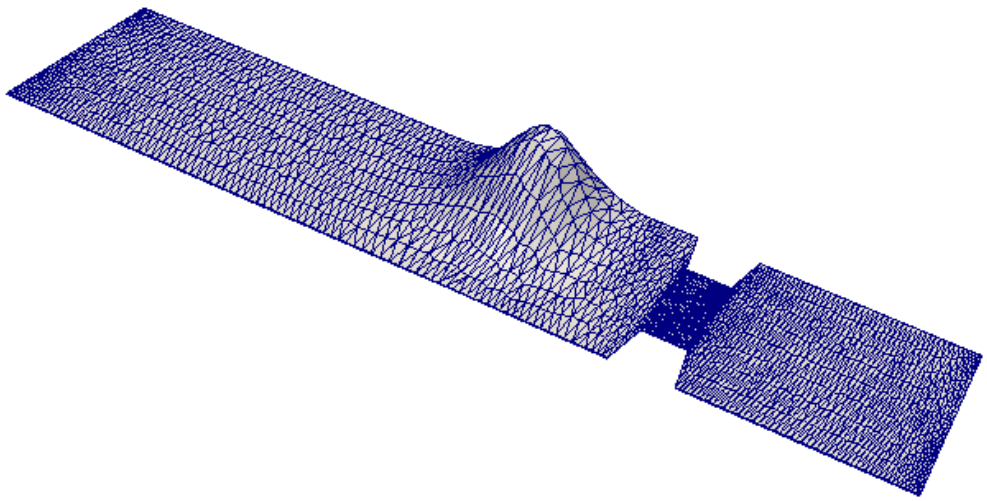

Figure 44: Mesh representing the channel geometry.

When the bump is removed, the geometry corresponds exactly to the test case given in paragraph 6.1.4 and for which experimental measurements are available. Thus, considering a flat bottom we can compare the 3d results with the experimental data and with the results coming from the

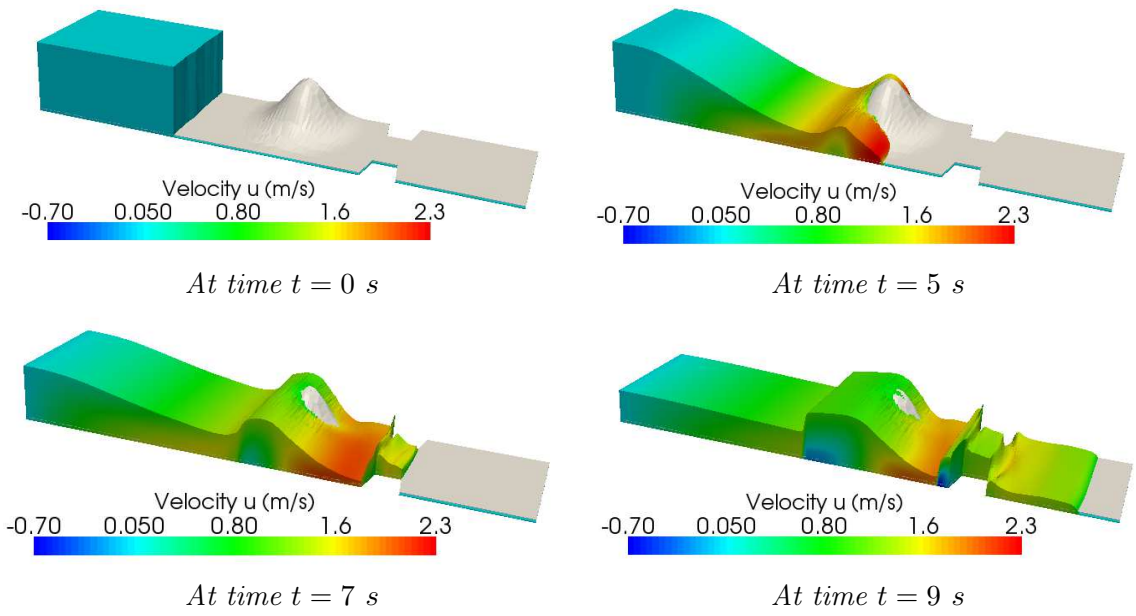

Figure 45: Dam break simulation over dry bottom with an uneven topography. Water depth and velocity u at different instants.

section-averaged Saint-Venant system. The comparison is given in Fig 48 where we can see the 3d simulation is in good agreement with the experimental data and improves the results coming from the section-averaged system.

6.5.2 Wind driven stratified flows

In this test case, we consider the same channel geometry as depicted in Fig. 44. The bassin is initially at rest with hot water near the free surface and colder water near the bottom, see Fig. 47.

The water density is kept constant i.e. it does not depend on the temperature. The wind blows (25 m.s^{-1}) parallel to the long axis of the bassin (x-axis). At two different instants we give the temperature distribution and the velocity field, see Fig. 48. In the case of a rectangular bassin with flat bottom, we recover that the velocity field corresponds to the analytical solution given in paragraph 6.3.1.

We do not present here any simulation where the fluid density depends on the tracer concentration. When the Boussinesq assumption is considered (see paragraph 3.5.2), our 3d code is able to treat such situations but we do not obtain more significant results than in the 2d case.

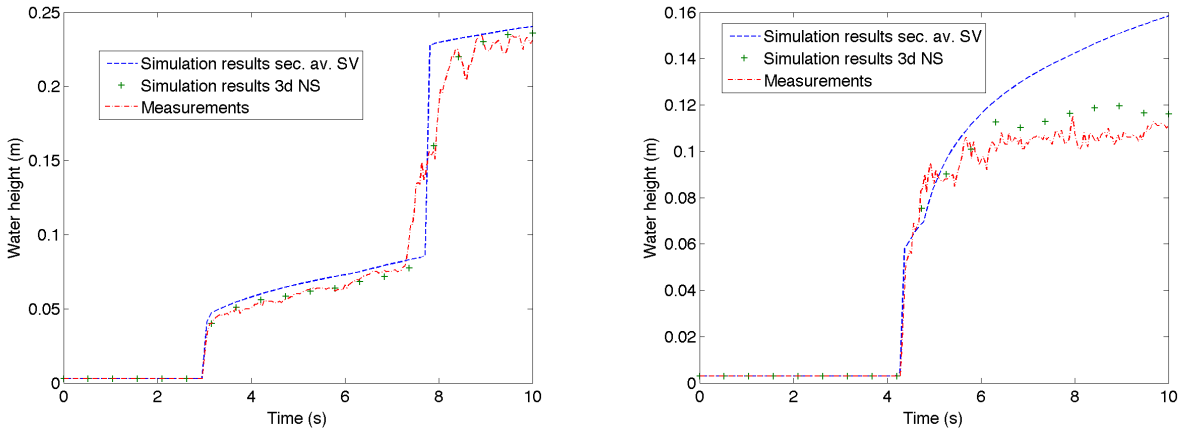

Sensor 2 *Sensor 3*

Figure 46: Comparison of the simulations obtained with the 3d code and with the section-averaged code, results for sensors 2 and 3.

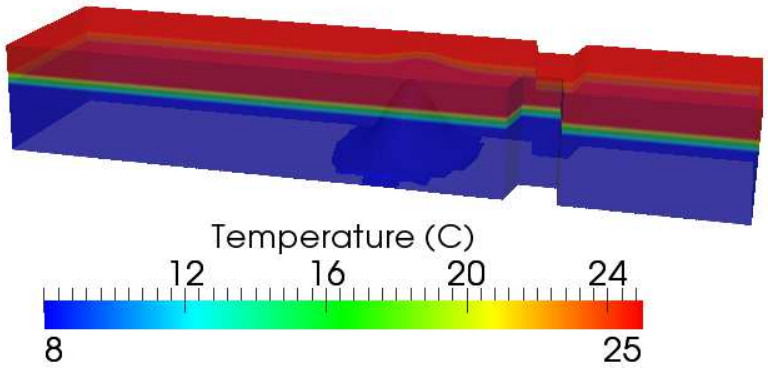

Figure 47: Geometry and initial conditions.

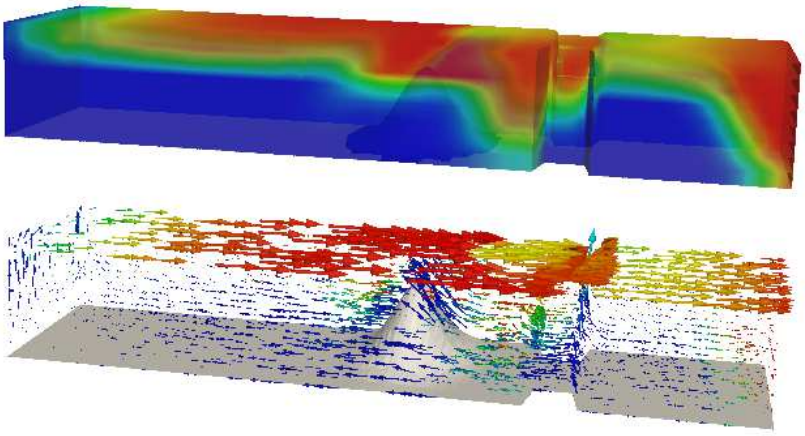

At time $t_1 = 100\ s$

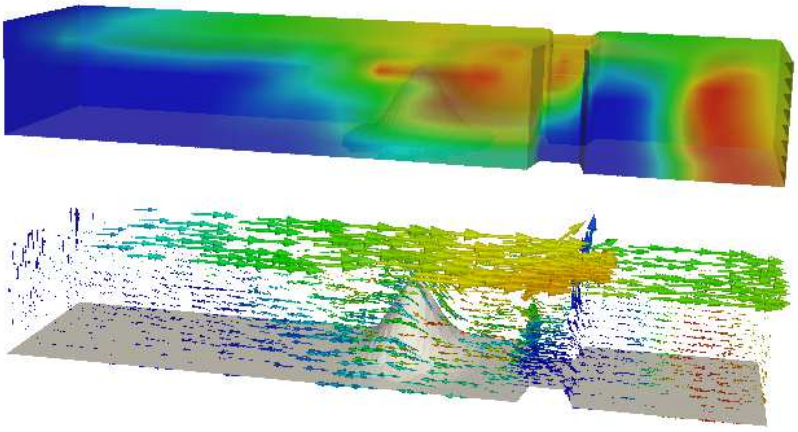

At time $t_2 = 200\ s$

Figure 48: Wind driven flow. Temperature and velocity field.

7 Cardiac modeling

Even if these activities are, to some extent, different from free surface flows modeling and simulation, they share common points namely, applied mathematics : modeling, analysis and numerical techniques for problems related to life sciences.

7.1 Modeling of soft tissue [11, 9, 12]

The knowledge of the heart behavior and the power of data acquisition techniques (ECG, ultrasound or MRI images,...) have greatly improved during the last decades. In-vivo measurements of the cardiac activity are very valuable for clinical purposes, but some crucial biological quantities are hardly – or not at all – accessible, as for example stresses, pressures or constitutive parameters that may reflect pathologies. In order to reach these quantities modeling is required.

In [11], we propose to model the electromechanical behavior of the heart, and to use the model in a data assimilation procedure in order to perform an identification of the parameters and state. The modeling of the heart tissue is based on an electrically-activated contraction law formulated via multiscale considerations and is consistent with various physiological and thermomechanical key requirements. The global heart system also incorporates a simplified lumped modeling of the blood compartments. We report on numerical simulations and on validations of our 3d model in reference and pathological conditions. Furthermore, the data assimilation procedure is intended to give access to quantities of interest for diagnosis purposes, and we present some promising results in this direction.

The focus and originality of this work mainly lies in the following two ideas:

- We propose an active, electrically activated, large displacements and large strains model of cardiac tissue rigorously derived from physiological multiscale considerations and consistent with key thermomechanical requirements.
- The formulation and complexity of the proposed model is adjusted to the nature and amount of available measurements necessary for its calibration, with a view to data assimilation.

In order to construct a model describing the threedimensional (3d) electromechanical behavior of the heart, the following major ingredients are required:

- a constitutive law accounting for both the active and passive aspects in the behavior of the muscle fibres;
- a representation of the electrical activation – the input in the constitutive law – that can be obtained from modeling approaches of various types and complexities;
- a geometrical (or "anatomical") description of the myocardium incorporating the fibre directions;
- a model of the blood circulation inside and outside of the heart cavities, and also a model describing the opening and closure of the valves that separate the cavities from each other and from the external circulation.

Each of these items is discussed in details in [11]. In [9] the mathematical analysis of the 1d electrically activated muscle fibre equation is performed. We have proved global existence and

uniqueness of solutions and we have studied their asymptotic behaviour in time. In particular we show that under vanishing external forcing solutions asymptotically converge to an equilibrium.

In the following, we present the cornerstones of the full 3d model. A kinetic interpretation of the fibres active contraction law – not published for the moment – is also given.

7.1.1 An excitation-contraction law for the myofibres

Most existing models of myofibre excitation-contraction mainly rely on heuristic approaches and experimental testing, whether directly at the macroscopic level [HNS97], or in order to identify the attachment and detachment rates of the actin-myosin bridges in the sarcomeres [WH99].

By contrast, our approach follows the path opened by Huxley [Hux57] – who has shown how actin-myosin bridge dynamics allows to describe the muscle contraction phenomena on the sarcomere scale – and Zahalak [Zah81] – who used the method of moments with bridge dynamics in order to describe muscle contraction on the myofibre scale. Our model is based on a chemically-controlled constitutive law of cardiac myofibre mechanics introduced in [BCS01a] and consistent with the behavior of myosin molecular motors [JAP97b]. The resulting sarcomere dynamics – derived by applying the moment-scaling method with the first two moments corresponding to active stiffness and stress, see [BCS01a] – is in agreement with the "sliding filament hypothesis" introduced in [Hux57]. A particular choice of the attachment and detachment rates is made so that Hill's force-velocity relations for isotonic contraction become closure equations for the method of moments. This choice is a slight modification of that made in [Hux57] or [Zah81]: here these rates are not only dependent upon the sarcomere strain but also upon the strain rate. We recall this model briefly.

On a microscopic scale, the sarcomere is made up of thin and thick parallel filaments. When ATP (the fuel of the cell) is available and the level of intracellular calcium bound on troponin C (the control of the contraction and relaxation in the sarcomeres) reaches a threshold ($Ca_{TnC} \geq \bar{C}$), the myosin heads of the thick filament that are not too far from actin sites on the thin filament ($\zeta \in [0,1]$ for some microscopic strain), become likely to bind with the binding rate f.

Unbinding is due to the macroscopic strain rate $\dot{\varepsilon}_c$, or to the action of the calcium pumps under the threshold $\bar{C}$, or to large values of ζ. The unbinding rate is g. The previous conditions are translated into the following formulae (where $\mathbb{I}_S$ is the characteristic function of the set S) [BCS01a]:

$$\begin{aligned} f(\zeta,t) &= k_{ATP}.\mathbb{I}_{Ca_{TnC}\geq\bar{C}}.\mathbb{I}_{\zeta\in[0,1]}, \\ g(\zeta,t) &= \alpha|\dot{\varepsilon}_c| + k_{SR}.\mathbb{I}_{Ca_{TnC}<\bar{C}} + k_{ATP}.\mathbb{I}_{Ca_{TnC}\geq\bar{C}}.\mathbb{I}_{\zeta\notin[0,1]}. \end{aligned}$$

The parameter k_{ATP} represents the rate of the chemical reaction providing energy from the hydrolysis of ATP to the molecular motors in the sarcomere, whereas k_{SR} denotes the rate of bridge destruction due to sarcoplasmic reticulum pumps removing calcium ions from the troponin. The parameter α is dimensionless and positive.

It will be convenient to define a new control variable

$$u(t) = k_{ATP}.\mathbb{I}_{Ca_{TnC}(t)\geq\bar{C}} - k_{SR}.\mathbb{I}_{Ca_{TnC}(t)<\bar{C}}$$

so that $f(\zeta,t) = |u(t)|_+.\mathbb{I}_{\zeta\in[0,1]}$ and $f(\zeta,t) + g(\zeta,t) = \alpha|\dot{\varepsilon}_c| + |u(t)|$ where $|u|_+ = \max(0,u) = k_{ATP}.\mathbb{I}_{Ca_{TnC}(t)\geq\bar{C}}$ and $|u|_- = \max(0,-u) = k_{SR}.\mathbb{I}_{Ca_{TnC}(t)<\bar{C}}$ are ATP consumption rates during contraction and active relaxation respectively.

The interaction potential W^{am} of the actin-myosin system is responsible for muscle contraction corresponding to the negative values of the macroscopic strain ε_c describing the relative sliding of

the actin over the myosin filament. Let $n(\zeta, t)$ be the density of cross-bridges with strain ζ at time t. Then, Huxley's model is:

$$\begin{aligned} &\frac{\partial n}{\partial t} + \dot{\varepsilon_c} \frac{\partial n}{\partial \zeta} = (1-n)f - ng, \\ &\sigma_c(t) = -d(\varepsilon_c) \int_{-\infty}^{+\infty} \frac{\partial W^{am}}{\partial \zeta} n d\zeta + \mu_c \dot{\varepsilon_c}. \end{aligned} \tag{7.1}$$

A parabolic W^{am} is chosen in [BCS01a]: $-\frac{\partial W^{am}}{\partial \zeta} = k_0 \zeta_0 + \sigma_0 \zeta$. The parameters k_0 and σ_0 are related to the number and stiffness of available actin-myosin cross-bridges in the sarcomere, μ_c is a viscosity parameter and ζ_0 is a strain constant. The scaling technique to compute σ_c leads to introducing k_c and τ_c, respectively proportional to the zero and first-order moments of n:

$$k_c(t) = k_0 \int_{-\infty}^{+\infty} n(\zeta, t) d\zeta \quad \text{and} \quad \tau_c(t) = \sigma_0 \int_{-\infty}^{+\infty} \zeta n(\zeta, t) d\zeta. \tag{7.2}$$

The resulting constitutive relation is given by the following system of ordinary differential equations:

$$\begin{cases} \dot{\tau}_c = k_c \dot{\varepsilon}_c - (\alpha \, |\dot{\varepsilon}_c| + |u|)\tau_c + \sigma_0 |u|_+, & \tau_c(0) = \tau_{c_0}, \\ \dot{k}_c = -(\alpha |\dot{\varepsilon}_c| + |u|)k_c + k_0 |u|_+, & k_c(0) = k_{c_0}, \\ \sigma_c = d(\varepsilon_c)(\tau_c + k_c \zeta_0) + \mu_c \dot{\varepsilon}_c, \end{cases} \tag{7.3}$$

where u denotes the electrical input – corresponding to a normalized concentration of calcium bound on the troponin-C – with $u > 0$ during contraction and $u < 0$ during active relaxation. For the sake of simplicity, we have chosen to denote the time derivative of a quantity x as $\dot{x}$.

Remark 7.1. *In the literature and in [11], the microscopic strain appearing in the Huxley model is often denoted ξ. In order to avoid any confusion with the microscopic velocity used the kinetic interpretations and schemes presented in Secs. 4 and 6, this microscopic strain is denoted here ζ.*

Remark 7.2. *An improved description of the contraction law (7.3) is now available in [CLTMS11].*

7.1.2 Starling effect

The Starling effect is one of the most important regulatory mechanisms of the heart activity. By this mechanism, when the preload increases the heart is able to also increase its contraction. The preload corresponds to the stretching of the cardiac fibres at the end of the previous diastolic filling, hence it is related to the veinous return and the pressure in the atria. Thus, increasing the ventricular end-diastolic pressure leads to an increased stroke volume, see Fig. 49. The Starling effect can also be interpreted by saying that the heart adapts its contraction so that the stroke volume compensates the end-diastolic volume.

The underlying physiological mechanism is as follows. When the stretching of the sarcomere increases, the troponin-C calcium sensitivity also increases leading to a growth of the cross-bridge attachment availability. This means that when the stretching of the sarcomere increases we move from point (a) to (b) on the curve presented in Fig. 50-(i), in which I denotes the normal range for the sarcomere length. This phenomenon is no more valid for very large stretching of the sarcomere, as represented by (c) in the figure. These various states of deformation are also schematically depicted in Fig. 51. It appears that for large deformations fewer actin-myosin cross-bridges can be created. This leads to the factor $d(\varepsilon_c)$ introduced in [MMS02]. This factor is a function with values in the interval $[0, 1]$ and behaving as represented in Fig. 50-(ii).

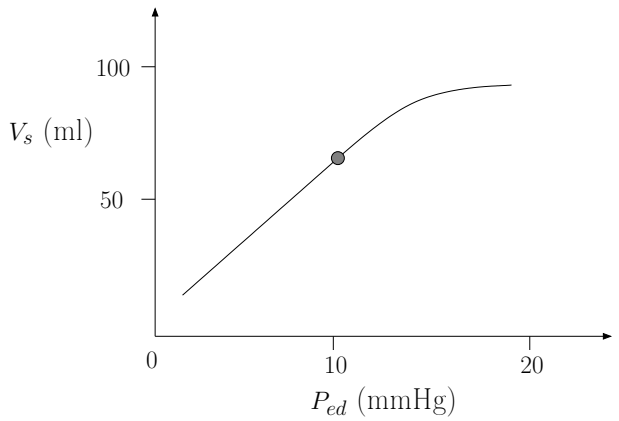

Figure 49: The Franck-Starling curve (V_s: stroke volume, P_{ed}: left ventricular end-diastolic pressure).

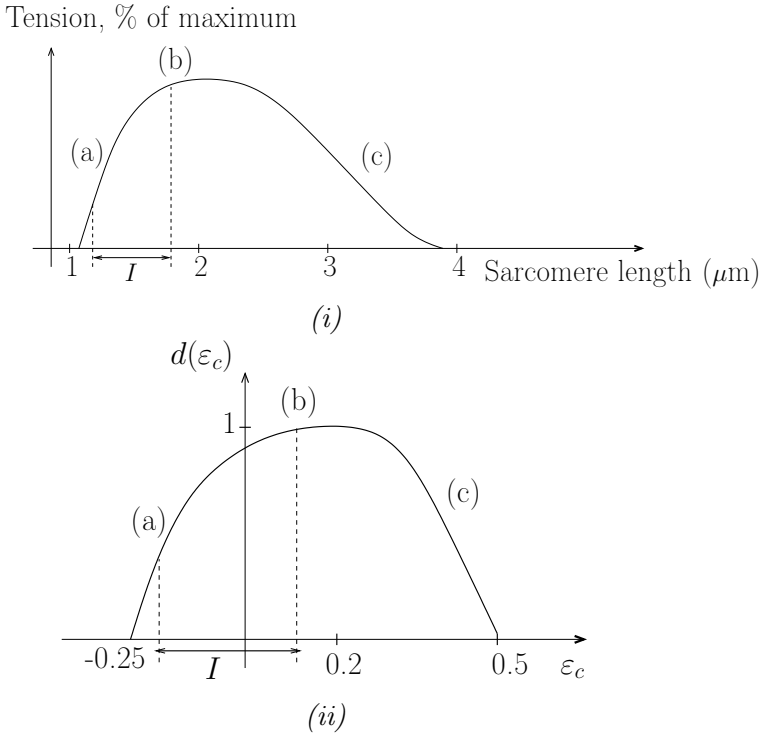

Figure 50: *(i)* the "length-tension" curve of a muscle with the three different configurations of the sarcomere shown in Fig. 51 and *(ii)* the corresponding modulation $d(\varepsilon_c)$ of the active stress σ_c.

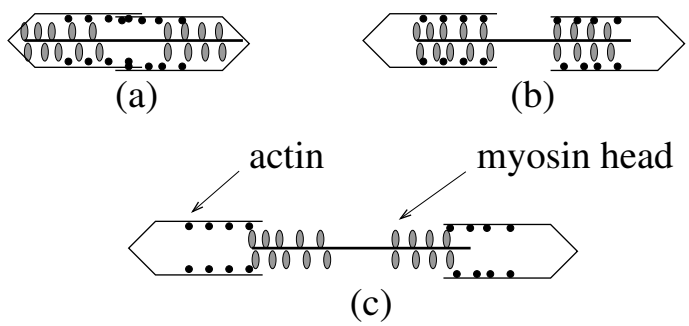

Figure 51: Three different sarcomere deformations.

7.1.3 Thermomechanical compatibilityof the contraction law

The stress in the myofibre is σ_c as given in System (7.3). Taking $0 \leq k_c(0) \leq k_0$, Eq. (7.3-b) ensures that $0 \leq k_c \leq k_0$ at all times. In fact, k_c can be seen as the progress of the chemical reactions governing the creation (resp. destruction) of cross-bridges via the calcium/troponin-C binding (resp. ATP hydrolysis). For small values of k_c, few cross-bridges are fastened whereas for $k_c \approx k_0$ the majority of the actin-myosin bridges are attached.

Let us introduce the quantity r defined by

$$r = |u| + \alpha|\dot{\varepsilon_c}|,$$

homogeneous to a time rate. Then the first equation of (7.3) can be rewritten in the form

$$\dot{\tau_c} = r\left(\frac{k_c\dot{\varepsilon}_c + \sigma_0|u|_+}{r} - \tau_c\right). \tag{7.4}$$

Assuming that $\dot{\varepsilon}_c$ is bounded ($|\dot{\varepsilon}_c| \leq a$), we can show that σ_c is also bounded by using (7.4) to obtain

$$|\tau_c| \leq \max\left\{\sup_t \frac{|k_c\dot{\varepsilon}_c + \sigma_0|u|_+|}{\alpha|\dot{\varepsilon}_c| + |u|}, |\tau_c(0)|\right\} \leq \max\{\sigma_0 + \frac{k_0}{\alpha}, |\tau_c(0)|\}.$$

Taking in particular $|\tau_c(0)| \leq \sigma_0 + k_0/\alpha$ we see that $|\tau_c| \leq \sigma_0 + k_0/\alpha$ always holds.

We can further interpret the active constitutive law by considering $\tilde{\tau}_c = \tau_c + k_c\zeta_0$, and rewriting System (7.3) as

$$\begin{cases} \dot{\tilde{\tau}}_c = k_c\dot{\varepsilon}_c - (\alpha|\dot{\varepsilon}_c| + |u|)\tilde{\tau}_c + (\sigma_0 + k_0\zeta_0)|u|_+, & \tilde{\tau}_c(0) = \tau_{c_0} + k_{c_0}\zeta_0, \\ \dot{k}_c = -(\alpha|\dot{\varepsilon}_c| + |u|)k_c + k_0|u|_+, & k_c(0) = k_{c_0}, \\ \sigma_c = d(\varepsilon_c)\tilde{\tau}_c + \mu_c\dot{\varepsilon}_c. \end{cases}$$

This shows that an appropriate redefinition of σ_0 allows to consider $\zeta_0 = 0$ in (7.3), which we henceforth do consider. Introducing ε_c^e defined by $\tau_c = k_c\varepsilon_c^e$ – note that ε_c^e can be seen as the elastic part of ε_c – and substituting in the first equation of (7.3) we obtain

$$\dot{\varepsilon}_c^e = \dot{\varepsilon}_c + \frac{\sigma_0}{k_c}|u|_+ - \frac{k_0}{k_c}|u|_+\varepsilon_c^e. \tag{7.5}$$

Now, defining $\varepsilon_c = \varepsilon_c^e + \varepsilon_c^p$ we have

$$\dot{\varepsilon}_c^p = -\frac{\sigma_0}{k_c}|u|_+ + \frac{k_0}{k_c}|u|_+\varepsilon_c^e. \tag{7.6}$$

Consider first the case $d(\varepsilon_c) = 1$. The internal mechanical power corresponding to the constitutive law (7.3) is given by

$$\begin{aligned}\sigma_c\dot{\varepsilon}_c &= \frac{\partial\left(\frac{k_c}{2}(\varepsilon_c^e)^2\right)}{\partial t} + \mu_c\dot{\varepsilon}_c^2 + k_c\varepsilon_c^e\dot{\varepsilon}_c^p - \dot{k}_c\frac{(\varepsilon_c^e)^2}{2} \\ &= \frac{\partial\left(\frac{k_c}{2}(\varepsilon_c^e)^2\right)}{\partial t} + \mu_c\dot{\varepsilon}_c^2 + k_c\varepsilon_c^e\dot{\varepsilon}_c^p + \frac{(\varepsilon_c^e)^2}{2}\Big((\alpha|\dot{\varepsilon}_c| + |u|)k_c - k_0|u|_+\Big).\end{aligned}$$

By (7.6) we have

$$k_c\varepsilon_c^e\dot{\varepsilon}_c^p = k_0|u|_+(\varepsilon_c^e)^2 - \sigma_0|u|_+\varepsilon_c^e,$$

hence the following expression holds for the mechanical power

$$\begin{aligned}\sigma_c\dot{\varepsilon}_c &= \frac{\partial\left(\frac{k_c}{2}(\varepsilon_c^e)^2\right)}{\partial t} + \mu_c\dot{\varepsilon}_c^2 \\ &\quad + \frac{(\varepsilon_c^e)^2}{2}\Big(k_0|u|_+ + (\alpha|\dot{\varepsilon}_c| + |u|)k_c\Big) - \sigma_0|u|_+\varepsilon_c^e. \qquad (7.7)\end{aligned}$$

We have the following thermomechanical interpretation: $\frac{1}{2}k_c(\varepsilon_c^e)^2$ appears as a free energy, whereas $\mu_c\dot{\varepsilon}_c^2 + \alpha|\dot{\varepsilon}_c|k_c\frac{(\varepsilon_c^e)^2}{2}$ is a nonnegative pseudo-potential of dissipation. Therefore the second principle of thermodynamics is satisfied. Furthermore the terms $(k_0|u|_+ + |u|k_c)\frac{(\varepsilon_c^e)^2}{2} - \sigma_0|u|_+\varepsilon_c^e$ represent "exogenous energy" due to the electrical input. More precisely, since $\varepsilon_c^e = \frac{\tau_c}{k_c}$ we can rewrite (7.7) as

$$\sigma_c\dot{\varepsilon}_c - \frac{\partial\left(\frac{k_c}{2}(\varepsilon_c^e)^2\right)}{\partial t} = \mu_c\dot{\varepsilon}_c^2 + \frac{(\tau_c)^2}{2k_c}(\alpha|\dot{\varepsilon}_c| + |u|) + \left(\frac{k_0}{2}\frac{\tau_c^2}{k_c^2} - \sigma_0\frac{\tau_c}{k_c}\right)|u|_+, \qquad (7.8)$$

where it appears that some energy can be supplied to the system only when $u > 0$ and $0 < \tau_c \leq 2\sigma_0\frac{k_c}{k_0+k_c}$.

Taking into account the Starling effect, (7.8) becomes

$$\begin{aligned}\sigma_c\dot{\varepsilon}_c - \frac{\partial\left(d(\varepsilon_c)\frac{k_c}{2}(\varepsilon_c^e)^2\right)}{\partial t} &= \mu_c\dot{\varepsilon}_c^2 + \frac{d(\varepsilon_c)(\tau_c)^2}{2k_c}(\alpha|\dot{\varepsilon}_c| + |u|) \\ &\quad + d(\varepsilon_c)\left(\frac{k_0}{2}\frac{\tau_c^2}{k_c^2} - \sigma_0\frac{\tau_c}{k_c}\right)|u|_+ - \dot{\varepsilon}_c d'(\varepsilon_c)\frac{\tau_c^2}{2k_c}, \qquad (7.9)\end{aligned}$$

where in order to satisfy the second principle of thermodynamics $d(\varepsilon_c)$ is chosen so that $\alpha d \geq |d'|$. In the sequel the variations of $d(\varepsilon_c)$ correspond to those depicted in Fig. 50-(ii).

7.1.4 Kinetic interpretation of the contraction law

The Huxley model appears as a conservation law with source term and the Zahalak moment formula (7.2) shares common points with a kinetic description. We have tried to investigate this idea and to obtain a kinetic type interpretation of the Bestel-Sorine contraction law.

In this paragraph, we neglect the Starling effect. Let us introduce the controlled kinetic equation

$$(\mathcal{B}_{myo}), \quad \frac{\partial\psi}{\partial t} + v\frac{\partial\psi}{\partial\zeta} - P + (f+g)\psi = Q, \qquad (7.10)$$

with

$$\psi = k_c\delta(\zeta - \varepsilon_c^e)\delta(v - \dot{\varepsilon}_c),$$
$$P = k_0|u|_+\delta(\zeta - \varepsilon_c^e)\delta(v - \dot{\varepsilon}_c),$$
$$f + g = |u| + \alpha|\dot{\varepsilon}_c|,$$

where δ denotes the Dirac distribution. The collision term $Q = Q(\zeta, t, v)$ chosen here has a special form namely,

$$Q = k_0|u|_+(\varepsilon_{c,0}^e - \varepsilon_c^e)\frac{\partial}{\partial\zeta}\delta(\zeta - \varepsilon_c^e)\delta(v - \dot{\varepsilon}_c),$$

and it satisfies for smooth solutions

$$\int_\zeta Q\ d\zeta = \int_\zeta \zeta Q\ d\zeta = 0, \quad \text{and} \quad \int_\zeta \zeta^2 Q\ d\zeta = k_0|u|_+(\varepsilon_{c,0}^e - \varepsilon_c^e)\varepsilon_c^e. \tag{7.11}$$

Notice that in the kinetic equation (7.10), two levels of microscopic descriptions are embedded since v plays the role of a microscopic velocity and ζ is a microscopic displacement. By analogy with the kinetic description of a flow, k_c plays the role of a water depth, τ_c is similar to a flux and ε_c^e corresponds to the flow velocity. Despite the apparent similarities, relation (7.10) and properties (7.11) are very different from a kinetic description since here we integrate the equations in variable ζ instead of variable v representing the micriscopic velocity.

From the above definitions we have

$$0 = \int_\zeta Q\ d\zeta = \frac{\partial}{\partial t}\left(k_c\delta(v - \dot{\varepsilon}_c)\right) - k_0|u|_+\delta(v - \dot{\varepsilon}_c) + (|u| + \alpha|\dot{\varepsilon}_c|)k_c\delta(v - \dot{\varepsilon}_c).$$

Likewise we have

$$0 = \int_\zeta \zeta Q\ d\zeta = \frac{\partial}{\partial t}\left(k_c\varepsilon_c^e\delta(v - \dot{\varepsilon}_c)\right) - vk_c - \varepsilon_{c,0}^e k_0|u|_+\delta(v - \dot{\varepsilon}_c) + (|u| + \alpha|\dot{\varepsilon}_c|)k_c\varepsilon_c^e\delta(v - \dot{\varepsilon}_c).$$

And a mean in v of the two preceding equations gives the contraction law (7.3). For smooth solutions, the energy balance (7.8) is given calculating

$$\int_v\int_\zeta \frac{\zeta^2}{2}(\mathcal{B}_{myo})d\zeta dv.$$

For the moment, this kinetic interpretation is not used in the discretization scheme.

7.1.5 3d mechanical modeling of the cardiac tissue

Now we describe how the electrically-activated contraction law presented above is used in a 3d continuum mechanics framework formulated for large displacements and strains – as is observed in the actual behavior of the heart.

The definitions and notations used for the description of the mechanical model are the following:

- $\underline{y}$ denotes the displacement field,
- $\underline{\underline{F}}$ the deformation gradient, namely,

$$\underline{\underline{F}} = \underline{\underline{1}} + \underline{\underline{\nabla}}\,\underline{y},$$

- $\underline{\underline{C}}$ the right Cauchy-Green deformation tensor, viz.

$$\underline{\underline{C}} = \underline{\underline{F}}^T \cdot \underline{\underline{F}},$$

- $\underline{\underline{E}}$ the Green-Lagrange strain tensor, i.e.

$$\underline{\underline{E}} = \frac{1}{2}\big(\underline{\underline{C}} - \underline{\underline{1}}\big),$$

- $\underline{\underline{\Sigma}}$ the second Piola-Kirchhoff stress tensor, namely, the stress tensor which is energy-conjugate to $\underline{\underline{E}}$.

We recall that the three classical strain invariants are defined by

$$I_1 = \mathrm{Tr}\,\underline{\underline{C}}, \quad I_2 = \frac{1}{2}\big((\mathrm{Tr}\,\underline{\underline{C}})^2 - \mathrm{Tr}\,\underline{\underline{C}}^2\big), \quad I_3 = \det \underline{\underline{C}}.$$

We will also use the so-called reduced invariants given by

$$\tilde{I}_1 = I_1 J^{-\frac{1}{3}}, \quad \tilde{I}_2 = I_2 J^{-\frac{2}{3}}, \quad J = (I_3)^{\frac{1}{2}}.$$

The rheological model The myofibre constitutive law described above is now incorporated in a rheological model of Hill-Maxwell type [CCG+01, Hil38, RC02], as depicted in Fig. 52-a. The element E_c accounts for the contractile electrically-activated behavior governed by (7.3) and all symbols appearing with index c refer to this element. An elastic material law is used for the series element E_s and a visco-elastic behavior is considered for the parallel branch E_p. The stress-strain law for E_s – which plays an important role during isovolumetric phases – is generally assumed to be linear [MP73b], and we follow this assumption in our modeling. The role of E_p, described in details in Section 7.1.5, is – in particular – to prevent the heart from overstepping certain limits during filling or ejection.

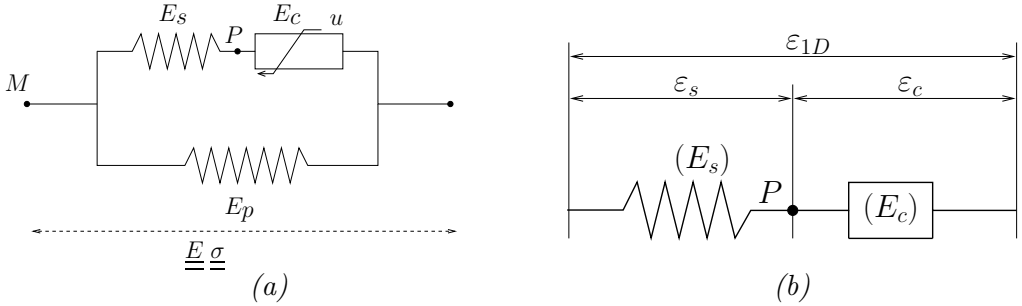

Figure 52: *(a)* Hill-Maxwell rheological model and *(b)* strains in the active branch.

In the active branch the only relevant deformations are those occurring along the direction of the muscle fibres, namely 1D deformations. Denoting by $\underline{n}$ the unit-length vector that represents the fibre direction at any point in the reference configuration, we thus define

$$\varepsilon_{1D} = \sum_{i,j} E_{ij} n_i n_j. \tag{7.12}$$

Because of large deformations, the individual deformations within the active branch (depicted in Fig. 52-b) compose according to a multiplicative – not additive – rule, viz.

$$1 + 2\varepsilon_{1D} = (1 + 2\varepsilon_c)(1 + 2\varepsilon_s), \tag{7.13}$$

and thermodynamical considerations entail that the resulting generated tension is [LT94]

$$\sigma_{1D} = \frac{\sigma_c}{1 + 2\varepsilon_s} = \frac{\sigma_s}{1 + 2\varepsilon_c}. \tag{7.14}$$

Description of the parallel branch We now focus on the description of the parallel element E_p. Considering an isothermal process, the satisfaction of the Clausius-Duhem inequality [TN92] in the absence of dissipation leads to

$$\underline{\underline{\Sigma}}_p = \rho_0 \frac{\partial W^e}{\partial \underline{\underline{E}}},$$

ρ_0 being the density expressed in the reference state and W^e a hyperelastic strain energy potential. When viscosity is considered, the Clausius-Duhem inequality becomes

$$\left(\underline{\underline{\Sigma}}_p - \rho_0 \frac{\partial W^e}{\partial \underline{\underline{E}}} \right) : \dot{\underline{\underline{E}}} \geq 0, \qquad \forall \underline{\underline{E}}, \dot{\underline{\underline{E}}},$$

and a viscous pseudo-potential $W^v(\underline{\underline{E}}, \dot{\underline{\underline{E}}})$ accounting for energy dissipation ought to satisfy

$$\frac{\partial W^v}{\partial \dot{\underline{\underline{E}}}} : \dot{\underline{\underline{E}}} \geq 0, \qquad \forall \dot{\underline{\underline{E}}}. \tag{7.15}$$

This holds – in particular – when W^v is a convex function of $\dot{\underline{\underline{E}}}$ with $\frac{\partial W^v}{\partial \dot{\underline{\underline{E}}}}(\underline{\underline{0}}) = \underline{\underline{0}}$, which are natural assumptions.

Taking dissipation into account we thus have

$$\begin{aligned} \underline{\underline{\Sigma}}_p(\underline{\underline{E}}, \dot{\underline{\underline{E}}}) &= \rho_0 \frac{\partial W^e}{\partial \underline{\underline{E}}} + \frac{\partial W^v}{\partial \dot{\underline{\underline{E}}}} \\ &= \underline{\underline{\Sigma}}^e_p(\underline{\underline{E}}) + \underline{\underline{\Sigma}}^v_p(\underline{\underline{E}}, \dot{\underline{\underline{E}}}). \end{aligned}$$

Two families of material laws are frequently used in the literature for the modeling of soft tissues, namely, Mooney-Rivlin materials and Veronda-Westmann materials [Fun93, Hum02, Kau01, VW70]. In this context W^e appears as a linear combination of the following terms

$$\begin{array}{lll} W^e_1 = \kappa_1(\tilde{I}_1 - 3) & \ldots & \text{neo-Hookean term} \\ W^e_2 = \kappa_2(\tilde{I}_2 - 3) & \ldots & \text{Mooney-Rivlin term} \\ W^e_3 = \kappa_3(e^{\eta(\tilde{I}_1 - 3)} - 1) & \ldots & \text{Veronda-Westmann term.} \end{array} \tag{7.16}$$

We point out that several authors do not restrict the choice of elastic constitutive law to hyperelastic materials and focus on fitting stress-strain curves with experimental data. The most widely used experimental-based stress-strain law is called the "pole-zero law" and has been introduced by Hunter [SH91b, MSCH01], see also [LY98] for an alternative approach. This remark also prevails for the design of the active constitutive law describing the muscle fibres, see [WH99].

In our simulations we have considered a Mooney-Rivlin material, namely,

$$W^e = \kappa_1(\tilde{I}_1 - 3) + \kappa_2(\tilde{I}_2 - 3).$$

Regarding the viscous part of the behavior, we used

$$W^v = \frac{\eta}{2}\dot{\underline{\underline{E}}} : \dot{\underline{\underline{E}}},$$

see also Pioletti *et al.* [PRBL98] for a more complex viscous pseudo-potential function.

The calibration of the parameters appearing in W^e and W^v will be discussed in Section 7.1.7.

3D constitutive equations and equilibrium In the model, we do not consider exact incompressibility and instead the volume variations of the muscle are penalized. The rheological model described above leads to

$$\underline{\underline{\Sigma}} = -pJ\underline{\underline{C}}^{-1} + \underline{\underline{\Sigma}}^e_p(\underline{\underline{E}}) + \underline{\underline{\Sigma}}^v_p(\underline{\underline{E}}, \dot{\underline{\underline{E}}}) + \sigma_{1D}\ \underline{n} \otimes \underline{n}, \tag{7.17}$$

where the symbol $\otimes$ denotes tensorial product, hence the term $\sigma_{1D}\ \underline{n} \otimes \underline{n}$ expresses that active stresses arise along the fibre directions. The first term in Eq. (7.17) corresponds to the volumetric behavior described by

$$W^{vol} = K(J-1) - K\ln J, \quad \frac{\partial W^{vol}}{\partial \underline{\underline{E}}} = -pJ\underline{\underline{C}}^{-1},$$

with $p = K(\frac{1-J}{J})$, K being a large bulk modulus ensuring an approximate incompressibility of the cardiac tissue, see [LT94]. Note that, when the coronary microcirculation is considered – which is not the case here – changes of volumes must instead be related to internal fluid flows.

In addition, in Eq.(7.17) the quantities $\underline{\underline{\Sigma}}^e_p(\underline{\underline{E}})$ and $\underline{\underline{\Sigma}}^v_p(\underline{\underline{E}}, \dot{\underline{\underline{E}}})$ represent the elastic and viscous parts – respectively – in the parallel branch as described above.

Finally, the material behavior is completely described by (7.17), where:

- σ_{1D} can be expressed as a function of $\underline{\underline{E}}$ (through ε_{1D}, see (7.12)) and ε_c using Eqs. (7.13), (7.14), and the series element elastic law, namely,

$$\sigma_{1D} = \frac{\sigma_s}{1+2\varepsilon_c} = \frac{E_s[(\varepsilon_{1D} - \varepsilon_c)/(1+2\varepsilon_c)]}{1+2\varepsilon_c}, \tag{7.18}$$

- $\underline{\underline{E}}$ and ε_c are related by the equilibrium equation in the series branch, viz.

$$\sigma_c \frac{1+2\varepsilon_c}{1+2\varepsilon_{1D}} = \frac{E_s[(\varepsilon_{1D} - \varepsilon_c)/(1+2\varepsilon_c)]}{1+2\varepsilon_c}, \tag{7.19}$$

- σ_c being related to ε_c through the dynamical system (7.3) (where we recall that u is seen as an input).

7.1.6 Other ingredients

In order to build a complete model of the heart contraction, several other components are required such as: a model for the electrical activation, a geometrical model of the muscle including the fibres, a mecanism of opening and closure of the valves, a model for the blood circulation,.... And the preceding models have to be completed with suitable initial and boundary conditions. All these components and the finite element discretization of the full model are described in [11]. W we present hereafter some simulations of the built model.

7.1.7 Numerical simulations

In the results presented hereafter, the time step is taken constant with $\Delta t = 5$ ms. This value is largely determined by the isovolumetric phases durations (roughly 50 ms each). Considering the ejection and filling phases a larger time step could be used, hence an adaptative time step procedure could be introduced.

Calibration of the 3D model A correct calibration of all the parameters used in the model is – of course – very important in order to obtain realistic simulations. The parameters to be calibrated can be divided into three groups:

- The parameters used in the arteries models can be estimated from data concerning pressure variations and phases lengths during a cardiac cycle. For more detailed considerations regarding the calibration of these parameters, see in particular [SWW99, WBDVN69] and the references therein.
- The main two parameters appearing in the contraction law (7.3) are k_0 and σ_0. The quantity σ_0 represents the asymptotic value for τ_c and can be estimated knowing the range of intraventricular blood pressure reached during muscle contraction. In our simulations we used $\sigma_0 = 300$ kPa and $k_0 = 150$ kPa.
- Concerning the calibration of the viscous and passive behaviors of the cardiac tissue, literature data are not as widely available as for soft tissues such as skin and tendons, see [VW70, PR00]. Hence we estimated the parameters c_1, c_2 and η appearing in W^e and W^v so that the filling of the ventricles corresponds to physiological data.

Simulation results We now present some results of simulations carried out with the complete heart model previously described. For animated versions of these results see the web page of the author [mac10].

These results have been obtained after a simulation of several cardiac cycles so that the approximate initial conditions are of no significance. Indeed, the stability of the model is demonstrated by results obtained over a sequence of cycles, which shows that the system rapidly reaches an attractor (limit cycle), whether after initialization or following a modification of the parameters, see Fig. 53.

Fig. 54 shows some classical indicators characteristic of the cardiac function. The quantities displayed are (from left to right and from top to bottom): left ventricle volume variations, blood pressure variations (with P_{lv}, P_{ao} and P_{at} denoting the pressures in the left ventricle, aorta and left atrium, respectively), aortic flow and mitral flow, mitral annulus displacement along the apex-base axis, contractile stress, strains in the fibre direction for a given point of the myocardium. Fig. 55 illustrates the Starling effect. Namely, two P-V cycles for the left ventricle, obtained with two different mitral pressures are plotted demonstrating how the stroke volume increases with the mitral pressure.

We also point out that – since we do not use a mixed displacement-pressure formulation – we only obtain approximate incompressibility of the cardiac tissue by penalizing the volume variations, see Section 7.1.5. Fig. 56 shows the typical volume variations for a sample of tetrahedra during a cardiac cycle.

We finally present simulation results representing a pathological case. As a simplified model of an infarcted heart, we considered reduced values of the contraction parameters k_0 and σ_0 in two given areas corresponding to regions of interest specified by the American Heart Association,

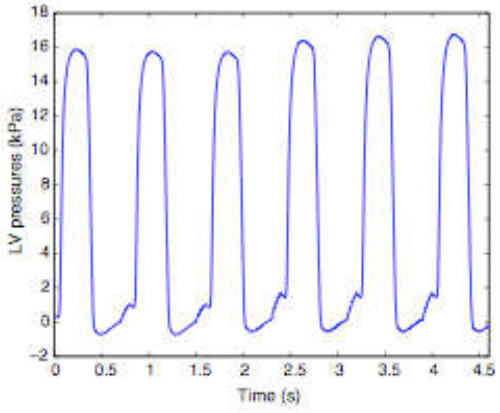

Figure 53: Blood pressure P_{v} in the left ventricle over 6 cycles; a modification of P_{at} in the left compartment is introduced before the fourth cycle.

see Fig. 57. The strains at the end of the ejection are shown in Fig. 58. We note that the tissue stretches – instead of contracting – within the affected areas, as expected. The global indicators of the cardiac function for the pathological case are presented and compared with the reference case in Fig. 59. We observe that the ejected volume and maximum ventricular pressure are significantly reduced in the impaired organ.

7.2 Perfusion in the cardiac muscle [6]

The electro-mechanical activity of the heart muscle needs nutrients and oxygen brought by the blood. So we are also interested in the modeling of blood flows through the beating myocardium, namely cardiac perfusion.

Despite recent advances on the anatomical description and measurements of the coronary tree – see e.g. [SKvdW$^+$08, HWSS09] – and on the corresponding physiological, physical and numerical modeling aspects – see e.g.[WBLS06, SK01, Smi04] – the complete modeling and simulation of blood flows inside the coronaries from the arteries to the veins via the capillaries is still out of reach. Therefore, in order to model blood perfusion in the cardiac tissue, we must limit the description of the detailed flows at a given space scale, and simplify the modeling of the smaller scale flows by aggregating these phenomena into macroscopic quantities, by some kind of "homogenization" procedure. To that purpose, the modeling of the fluid-solid coupling within the framework of porous media appears appropriate.

Poromechanics is a simplified mixture theory where a complex fluid-structure interaction problem is replaced by a superposition of both components, each of them representing a fraction of the complete material at every point. It originally emerged in soils mechanics with the work of Terzaghi [Ter43], and Biot [Bio56, Bio72] later gave a description of the mechanical behavior of a porous medium using an elastic formulation for the solid matrix, and Darcy's law for the fluid flow through the matrix. Finite strain poroelastic models have already been proposed [MNM98, AS98, YS06, Bor06a], albeit with *ad hoc* formulations for which compatibility with thermodynamics laws and incompressibility conditions is not established. Poroelastic models have also been considered in the framework of fluid-structure interaction, e.g. to model blood vessel walls [BQQ], with some extensions including lipid (LDL) [KACH07] and drug [CBBH08, FT09] transport. Other formulations have been proposed with multiple fluid compartments – or a continuum of such

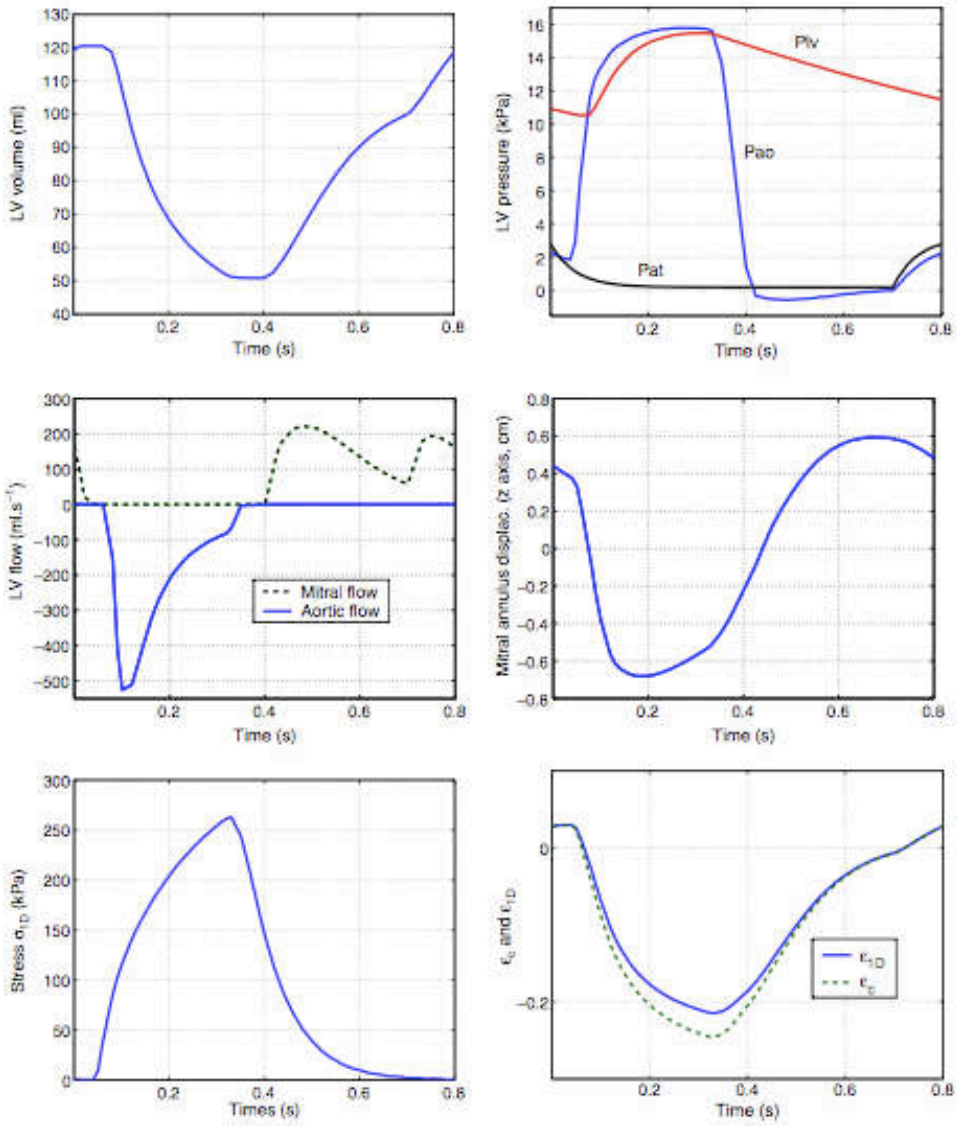

Figure 54: Global indicators of the cardiac function for the left ventricle.

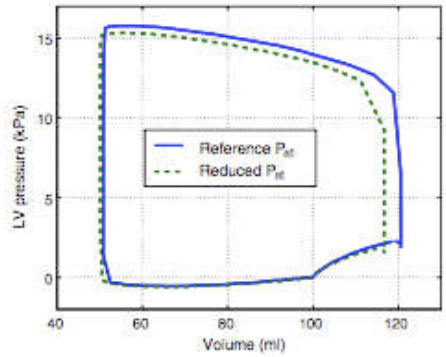

Figure 55: P-V cycle for 2 different mitral pressures (Starling effect).

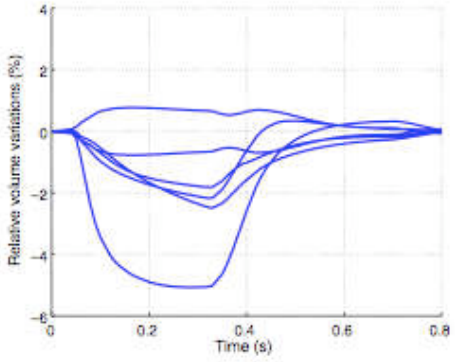

Figure 56: Volume variations along a cardiac cycles for a sample of tetrahedra.

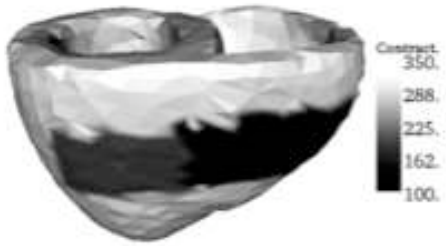

Figure 57: Areas with reduced contractility: $\sigma_0 = 100, 200$ kPa, instead of the reference value $\sigma_0 = 350$ kPa ($k_0 = \sigma_0/2$ in all areas).

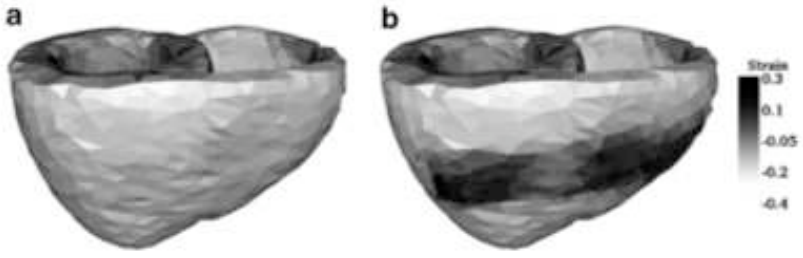

Figure 58: Strain ε_{1D} (end systole), *(a)* reference situation and *(b)* pathological case.

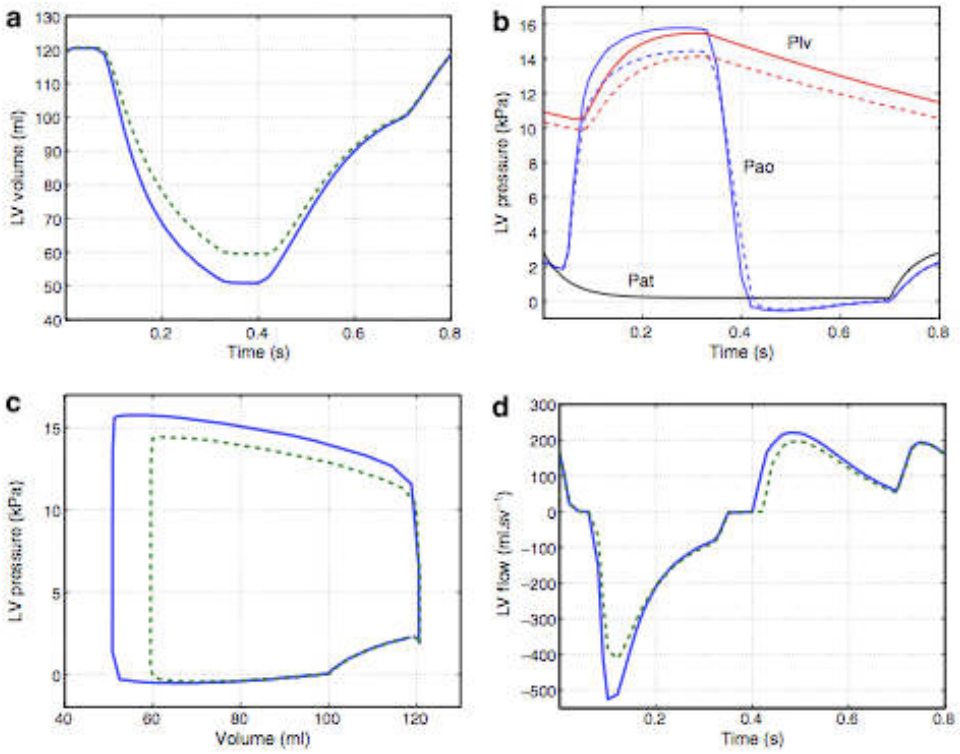

Figure 59: Global indicators of cardiac function (solid line: reference case, dashed line: pathologic case). For the left ventricle, *(a)* volume variations, *(b)* pressions variations *(c)* PV loop, *(d)* LV inflow (> 0) and outflow (< 0).

compartments – coupled with each other and with the solid medium [HvC91a, HvC91b, CR03b], and with applications to the modeling of living tissues [VHJH97], but of course such models are extremely difficult to validate with experimental evidence in practice.

The main contribution of [6] is the derivation of a general poroelastic formulation valid for finite strains and compatible with incompressibility, as these two features are deemed to be important in the modeling of living tissues. We follow the strategy – presented in [Cou95] in a linear framework – of deriving the formulation from an appropriate free energy functional, which is crucial to guarantee that fundamental thermodynamics principles are satisfied. We also propose a numerical procedure to solve the resulting system of equations and we illustrate the behavior of this poroelastic model by several numerical examples.

The governing equations of the model and their discretization are not presented here, see [6]. We present hereafter a test problem illustrating the behavior of this poroelastic model under large deformations.

We present a simulation of the model described above on a three-dimensional analytical geometry that mimics the left ventricle. Fibers are embedded with an orientation that varies nonlinearly across the wall [11]. The activation of the muscle occurs during 0.25 s, after which the muscle relaxes so that the heart beat lasts 0.8 s. The contraction is such that the ejection fraction is normal (around 50%). To investigate the effect of the contraction decoupled from the ventricular pressure, there is no valve in this model and the ventricle is unloaded. On the fluid side, blood cannot enter into or leak from the ventricle (a null flux condition is applied on the whole boundary). Instead, blood enters in the myocardium from a distributed source with $p_a = 2.7\,\text{kPa}$ which corresponds to a typical small artery pressure of 20 mmHg, and leaves through the venous side at a pressure of 10 mmHg modeled as a distributed sink with $p_v = 1.3\,\text{kPa}$. The pressure differential across the capillary bed is thus of 10 mmHg. These values are consistent with literature data for the myocardium and skeletal muscles [ZBS95, KLF99a, FZ75]. The inverse of the volume resistance to flow from the small arteries and into the small veins is $3\,10^{-5}\,\text{Pa}^{-1}\text{s}^{-1}$, chosen so that the average flow rate for the whole myocardium corresponds to 4% of a normal cardiac output [BL01]. The initial blood porosity ϕ_0 is 0.15 [GB90, MNCO$^+$01], representing here the volume fraction of blood in the capillaries, which is ten times larger than the ones of the other small vessels [GN07]. The permeability $K\underline{\underline{1}}$ is isotropic and homogeneous with a scalar value of $2\,10^{-9}\,\text{m}^2\text{Pa}^{-1}\text{s}^{-1}$ [HAvCR92]. The simulation was run with a mesh of 15,000 elements and a time step of 5 ms. Periodicity of the solution was achieved after 3-4 cycles. The number of fixed-point iterations necessary to achieve convergence of a relative residual on the mass m of 10^{-4} was typically 4, and up to 8 at the peak of the contraction.

The resulting time-averaged behavior is a system in which blood flows continuously from the small arteries into the capillaries, and from the capillaries into the small veins, at a flow rate of $4\,\text{mL}\,\text{s}^{-1}$, a mean pressure of 15 mmHg (2 kPa) and a muscle volume of 260 mL. Figure 60 shows the variation in time around this state. During contraction, the volume of the myocardium decreases, while it increases during relaxation. This phenomenon has been reported in [ACY$^+$08] and references herein. The contraction of the fibers induces a rise of the pressure. As a consequence, the flow from the small arteries into the capillaries q_a is considerably reduced - which corresponds to the so called *flow impediment* ([WBLS06] and references herein) - and blood is squeezed out of the capillaries (lowering of m) into the small veins (rise of q_v). During relaxation, the opposite happens: m rises as q_a increases and q_v decreases, filling up the capacitance of the capillaries. The mainly systolic flow in the small arteries and mainly diastolic flow in the small veins are characteristic of the coronary network, and consistent with the measured velocities in small arteries and small veins in the left ventricle given in [GN07].

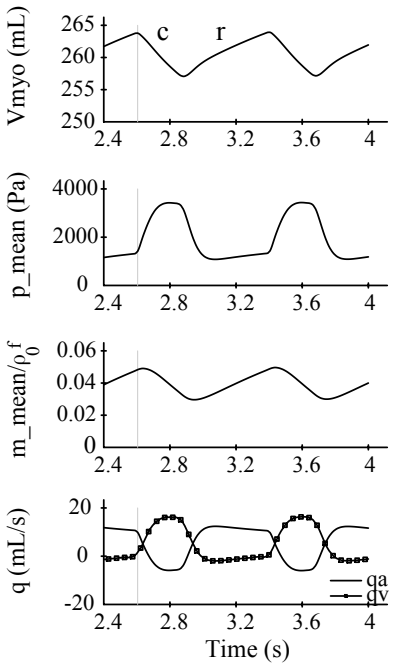

Figure 60: Variations over two cardiac cycles of the volume of the myocardium with the contraction (c) and relaxation (r) phases, the pressure averaged over the volume, the added blood mass averaged over the volume, and the flow rates that come from the small arteries (q_a) and leave into the small veins (q_v).

Furthermore, as can be seen in Figure 61, pressure and mass vary nonlinearly across the myocardium wall. During contraction, pressure, and consequently flows as well, is more affected by the contraction in the subendocardium than in the subepicardium. The model is thus able to reproduce the fact that flow impediment is known to be higher in the subendocardium than in the subepicardium [GFD$^+$91, GN07]. In addition, Figure 62 shows that the solution is heterogeneous in the different regions of the myocardium, which supports the choice of such a three-dimensional model. During the cardiac cycle, the myocardium undergoes large deformations. The displacement of the apex between the relaxed and the contracted states is here of 2.4 cm, which corresponds to 24% of the initial length.

This simulation shows that key phenomena that characterize the cross-talk between myocardium and coronary flow are described by this model. However the former presents several limitations. The capacitance of the arteries and veins is neglected, as a consequence flow in the small arteries is negative during part of the contraction. Nevertheless, negative flows have been recorded in coronary arteries [GN07, GG40]. Furthermore, the pressures in the small arteries and veins are taken constant in time and homogeneous. The pulsatility in the pressure at these levels is usually considered to be negligible [NO05] but these pressures are likely to be inhomogeneous. To improve the model, one could couple it with a distributed network of the larger arteries and veins. Homogeneous and constant inverse resistance parameters as well as a homogeneous reference porosity are chosen

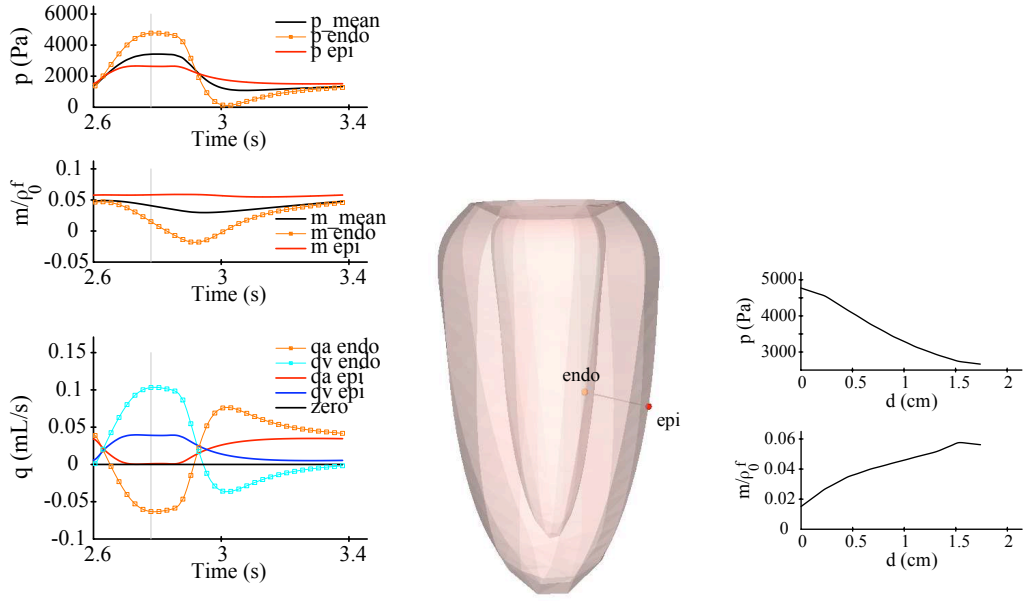

Figure 61: Mean pressure and mass are traced over one cardiac cycle (upper left graphs). Pressure, mass, and arterial and venous flow rates are traced for two different locations - endocardium (endo) and epicardium (epi). Their exact location in the myocardium is shown in the 3D figure. The pressure and mass gradients across the myocardium wall between these two points are represented on the lower right graphs (d is the distance from the endocardium point).

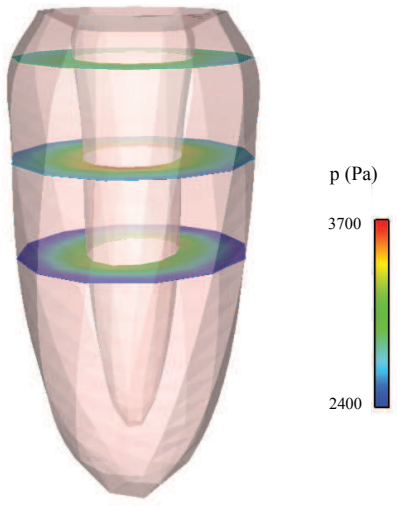

Figure 62: Myocardium with pressure contours shown on three slices.

for simplicity. This is further motivated by the fact that their variations are a matter of debate [WBLS06].

7.3 Model reduction

In biomechanical engineering, the simulations of 3d nonlinear models accounting for large strains and large displacements are costly, hence model reduction techniques are attractive. Model reduction for nonlinear PDEs raises two main issues:

- the design of a reduced basis valid for significant variations of the initial conditions and/or the constitutive parameters of the model,
- the derivation of error estimates between the full simulation results and the reduced ones.

Unlike reduced basis techniques for which costly calculations are carried out offline, we are interested in POD (Proper Orthogonal Decomposition) type techniques, that have proved successful in domains ranging from signal analysis to fluid mechanics. Such techniques enable lighter and shorter online simulations of a PDE based model, and rely on the knowledge of a few complete solutions, often called snapshots, that are supposed to capture the most "characteristic" behaviors of the system. The POD method shows good reductibility and stability in the case of linear parabolic equations, especially its simplest form, the heat equation. We also explored the reduction properties of more complex systems of reaction-diffusion type (e.g. FitzHugh-Nagumo equations), which are nonlinear parabolic, parameter-sensitive and which exhibit a propagation-like behaviour. The usual POD criterion is inappropriate to conveniently reduce an interesting range of solutions and we have proposed extensions of the optimal criterion. We are currently investigating the applications of POD methods on optimality systems and inverse problems with applications to the estimation of mechanical parameters arising in cardiac modeling. The aim is to make Kalman filtering type techniques tractable by reducing the size of the covariance matrices, in particular. This approach raises questions about reduced optimal control problems.

Asven Gariah has begun its PhD (co-supervised by the author) in November 2008, publications on this subject will be submitted soon.

8 Works in progress & outlook

Since the topics mentioned in this document are fascinating with numerous open questions, the main objective of the author in the years to come is to go on these works. Several aspects need to be examined in more details. It seems to the author two axis have to be investigated deepened and two new axis are worth being considered. These four points are described now.

8.1 Numerical tools

All the 2d (x, z) simulations of this document have been carried out with a numerical code developed by the author with the help of M.-O. Bristeau. The code contains all the models: section-averaged, non-hydrostatic, varying density presented in this document. In real life, most of the problems exhibits 3d effects. Some 3d simulations are presented using a Fortran code developed jointly with M.-O. Bristeau. The development of this 3d code will go on and especially the integration of the results contained in [10] leading to a full 3d Navier-Stokes solver.

The characteristic length in time and space of some phenomena e.g. in oceanography is challenging for simulation tools. Indeed the simulation of complex models over large periods and areas using explicit schemes constrained by a CFL condition involving the wave velocity becomes quickly unfeasible. Moreover, we have to keep in mind our objective that is to propose efficient models more easily accessible and robust – for the analysis and the simulation – than the usual Navier-Stokes solvers. A first idea is to introduce a complete or partial rigid lid assumption in order to eliminate the wave velocity from the CFL condition. This has been already tested and the validity domain is significantly reduced. Another idea could be to write the kinetic schemes with irregular Gibbs equilibria (distribution) and where the pressure terms are treated as source terms, and thus leading to a reduced CFL condition. The third possibility could be to propose implicit versions of the kinetic schemes.

The models presented in this document admit a kinetic interpretation which is used to derive the numerical scheme. Indeed, some source terms, especially the pressure source terms but also the wind forces are numerically treated separately and are not based on the kinetic description. We have obtained recently a kinetic scheme for the Saint-Venant system – but also for the other models we have proposed – where all the sources terms are discretized at the kinetic level.

Even if these numerical tools are supplied to colleagues and searchers involved in these topics, the objective is not necessarily to develop a software for free surface flows simulation. We need a numerical tool for the implementation of schemes and we are pleased to propose e.g. subroutines that can be integrated in other codes as done with the industrial code Mascaret (EDF R&D).

8.2 Applied mathematics for life sciences

Modeling, numerical analysis and scientific calculus for life sciences have strongly developed over the past decade. And yet, there is still a lot of work. Indeed ecosystems, organs,... are often far more complex systems than what is usually encountered for example in industry (cars, planes, bridges,...).

Compared to classical engineering structures, we have often to deal in life sciences with active systems – such as muscle – with remodeling and growth terms. As in population dynamics of cells or micro-organisms, the modeling of such systems of transport-reaction type raises important difficulties with hyperbolic features. It seems to the author the approach proposes in this document is not only dedicated to hydraulics and can be useful in other domains.

8.3 Hydrodynamics-biology coupling

In water, there is often not only water. The coupling between

- hydrodynamics,
- population dynamics of plancton and other organisms,
- temperature, salinity,
- light,
- external forcings : Coriolis ans wind effects,

is not well-known and the modeling of such systems with their interactions is complex. The approach presented all along this document with robust, efficient and low-complexity models and schemes can be a promising way to tackle these difficult problems. The work in this direction has begun in the framework of the Nautilus research project [nau10].

8.4 Mathematical analysis

The mathematical analysis of the models arising in fluid mechanics is extremely complex and the results contained in [LPS96, LPT94b] and devoted to the Euler system for compressible gas dynamics and the Saint-Venant system can not be easily extended to more complex models. But it is not fully satisfactory to have, as in this document, only formal estimates of the convergence of the proposed models to the target model.

Two interesting aspects, namely, the hyperbolicity and the existence of entropies – especially for the hydrostatic Euler system – have begun to be investigated with the help of E. Audusse. The results obtained until now are interesting but need be completed and enriched.

8.5 Control, stabilization and data assimilation

The control and stabilization of models arising in fluid mechanics is tricky. For Shallow Water flows, we mention the works of Coron [Cor02, Cor07]. The idea here has been to introduce Luenberger observers in the kinetic interpretation. The use of Luenberger observers (also called nudging technique) in Shallow Water models has been tested by Auroux and Blum [AB05b, AB08] with interesting results but the stability is difficult to achieve.

The cornerstone of the approach we propose is that once embedded in the kinetic formalism, the stability of the Luenberger observers is guaranteed. This is similar to a BGK type relaxation towards the observed quantities. This work is carried out with P. Moireau (INRIA-MACS), the results recently obtained concerning the stabilization, the control of the hydrostatic Navier-Stokes system are promising.

We shortly present a stabilization result recently obtained. We point out that the example we describe now concerns the hydrostatic Navier-Stokes system and not only the Saint-Venant system. The test case is built as follows. Starting from the initial condition given in the upper part of Fig. 63-*(a)*, we first simulate the propagation of a wave in a closed basin with vertical shores. The upper parts of Figs. 63-*(b)* and 63-*(c)* depict the water depth and the velocity field at two different instants of this simulation. Then from this simulation, we extract the water depth for the nodes arround the bump and for 1 out of 50 of the simulation steps. And finally, starting from a

bassin at rest with a modified water depth (lower part of Fig. 63-*(a)*), we apply our stabilization technique with the observation measurements selected before. We observe that quickly (lower part of Figs. 63-*(b)* and 63-*(c)*), the control system reachs the target model.

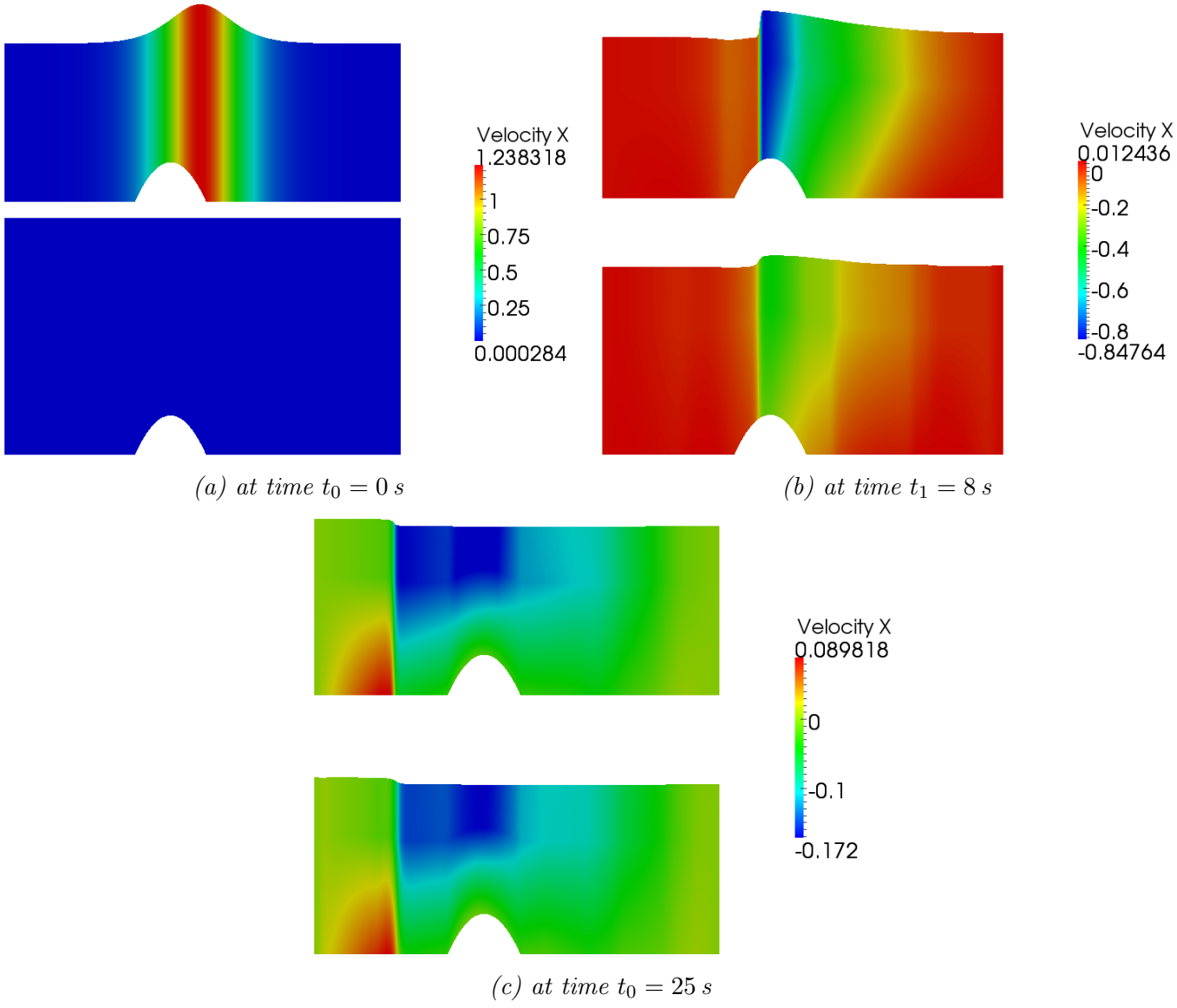

(a) at time $t_0 = 0\,s$

(b) at time $t_1 = 8\,s$

(c) at time $t_0 = 25\,s$

Figure 63: Comparison between the reference state and the simulated state at three different instants.

Bibliography of the author

[1] E. Audusse, F. Benkhaldoun, J. Sainte-Marie, and M. Seaid. Multilayer Saint-Venant Equations over movable beds. *Accpeted for publication in Discrete Contin. Dyn. Syst. Ser. B*, 2010.

[2] E. Audusse, M.-O. Bristeau, M. Pelanti, and J. Sainte-Marie. Approximation of the hydrostatic navier-stokes system for density stratified flows by a multilayer model. kinetic interpretation and numerical validation. *Accepted for publication in J. Comp. Phys.*, 2011.

[3] E. Audusse, M.-O. Bristeau, B. Perthame, and J. Sainte-Marie. A multilayer Saint-Venant system with mass exchanges for Shallow Water flows. Derivation and numerical validation. *ESAIM: M2AN*, 2010.

[4] E. Audusse, M.O. Bristeau, M. Pelanti, and J. Sainte-Marie. A Multilayer Saint-Venant System with variable density for Shallow Water flows. *Submitted to J. Sci. Comp.*, 2010.

[5] M.-O. Bristeau and J. Sainte-Marie. Derivation of a non-hydrostatic shallow water model; Comparison with Saint-Venant and Boussinesq systems. *Discrete Contin. Dyn. Syst. Ser. B*, 10(4):733–759, 2008.

[6] D. Chapelle, J.-F. Gerbeau, J. Sainte-Marie, and I. Vignon-Clementel. A poroelastic model valid in large strains with applications to perfusion in cardiac modeling. *Comp. Mech.*, 46:2010, 91–101.

[7] N. Goutal, M.-O. Bristeau, and J. Sainte-Marie. Numerical simulations of a non-hydrostatic shallow water model. *Submitted to Computers & Fluids*, 2010.

[8] N. Goutal and J. Sainte-Marie. A kinetic interpretation of the section-averaged Saint-Venant system for natural river hydraulics. *Published online : Int. J. Numer. Meth. Fluids*, 2010.

[9] P. Krejci, J. Sainte-Marie, M. Sorine, and J.M. Urquiza. Solutions to muscle fiber equations and their long time behaviour. *Nonlinear Analysis: Real World Applications*, 7(4):535–558, 2006.

[10] J. Sainte-Marie. Vertically averaged models for the free surface Euler system. Derivation and kinetic interpretation. *Accepted for publication in M3AS*, 2010.

[11] J. Sainte-Marie, D. Chapelle, R. Cimrman, and M. Sorine. Modeling and estimation of the cardiac electromechanical activity. *Computers & Structures*, 84:1743–1759, 2006.

[12] M. Sermesant, P. Moireau, O. Camara, J. Sainte-Marie, R. Andriantsimiavona, R. Cimrman, D.-L. Hill, D. Chapelle, and R. Razavi. Cardiac function estimation from mri using a heart model and data assimilation: Advances and difficulties. *Medical Image Analysis*, 10(4):642–656, 2006.

References

[AB03] E. Audusse and M.-O. Bristeau. Transport of pollutant in shallow water flows : A two time steps kinetic method. *ESAIM: M2AN*, 37(2):389–416, 2003.

[AB05a] E. Audusse and M.-O. Bristeau. A well-balanced positivity preserving second-order scheme for shallow water flows on unstructured meshes. *J. Comput. Phys.*, 206(1):311–333, 2005.

[AB05b] D. Auroux and J. Blum. Back and forth nudging algorithm for data assimilation problems. *C. R. Acad. Sci. Paris, Ser. I*, 340:873–878, 2005.

[AB07] E. Audusse and M.-O. Bristeau. Finite-volume solvers for a multilayer Saint-Venant system. *Int. J. Appl. Math. Comput. Sci.*, 17(3):311–319, 2007.

[AB08] D. Auroux and J. Blum. A nudging based data assimilation method; the back and forth nudging algorithm. *Nonlinear Processes in Geophysics*, 15:305–319, 2008.

[ABB+04] E. Audusse, F. Bouchut, M.-O. Bristeau, R. Klein, and B. Perthame. A fast and stable well-balanced scheme with hydrostatic reconstruction for Shallow Water flows. *SIAM J. Sci. Comput.*, 25(6):2050–2065, 2004.

[ABD08] E. Audusse, M.-O. Bristeau, and A. Decoene. Numerical simulations of 3d free surface flows by a multilayer Saint-Venant model. *Internat. J. Numer. Methods Fluids*, 56(3):331–350, 2008.

[ABP00] E. Audusse, M.-O. Bristeau, and B. Perthame. Kinetic schemes for Saint-Venant equations with source terms on unstructured grids. Technical Report 3989, INRIA, Unité de recherche de Rocquencourt, FRANCE, 2000. http://www.inria.fr/rrrt/rr-3989.html.

[ACY+08] Hiroshi Ashikaga, Benjamin A. Coppola, Katrina G. Yamazaki, Francisco J. Villarreal, Jeffrey H. Omens, and James W. Covell. Changes in regional myocardial volume during the cardiac cycle: implications for transmural blood flow and cardiac structure. *Am J Physiol Heart Circ Physiol*, 295(2):H610–618, 2008.

[ADT81] D.N. Arnold, J. Douglas, and V. Thomée. Superconvergence of a Finite Element Approximation to the Solution of a Sobolev Equation in a Single Space Variable. *Mathematics of Computation*, 36(153):53–64, 1981.

[AS98] E.S. Almeida and R.L. Spilker. Finite element formulations for hyperelastic transversely isotropic biphasic soft tissues. *Computer Methods in Applied Mechanics and Engineering*, 151(3-4):513–538, 1998.

[Aud05] E. Audusse. A multilayer Saint-Venant System : Derivation and Numerical Validation. *Discrete Contin. Dyn. Syst. Ser. B*, 5(2):189–214, 2005.

[Bar04] E. Barthelemy. Nonlinear shallow water theories for coastal waves. *Surveys in Geophysics*, 25(3,4):315–337, 2004.

[BBC+05] M. Baudin, C. Berthon, F. Coquel, R. Masson, and Q.H. Tran. A relaxation method for two-phase flow models with hydrodynamic closure law. *Numer. Math.*, 99(3):411–440, 2005.

[BBC+10] P. Bonneton, E. Barthelemy, J.D. Carter, F. Chazel, R. Cienfuegos, D. Lannes, F. Marche, and M. Tissier. Fully nonlinear weakly dispersive modelling of wave transformation, breaking and runup. *Submitted*, 2010. Preprint arXiv:1004.3480.

[BBM72] J.-L. Bona, T.-B. Benjamin, and J.-J. Mahony. Model equations for long waves in nonlinear dispersive systems. *Philos. Trans. Royal Soc. London Series A*, 272:47–78, 1972.

[BC01] M.O. Bristeau and B. Coussin. Boundary Conditions for the Shallow Water Equations solved by Kinetic Schemes. Research Report RR-4282, INRIA, 2001.

[BCS01a] J. Bestel, F. Clément, and M. Sorine. A biomechanical model of muscle contraction. In *Lectures Notes in Computer Science*, volume 2208. Eds W.J. Niessen, M.A. Viergever, Springer, 2001.

[BCS01b] J. Bestel, F. Clément, and M. Sorine. A biomechanical model of muscle contraction. In *Lectures Notes in Computer Science*, volume 2208. Eds W.J. Niessen & M.A. Viergever, Springer-Verlag, 2001.

[BCS02] J.L. Bona, M. Chen, and J.-C. Saut. Boussinesq equations and other systems for small-amplitude long waves in nonlinear dispersive media: Part I. Derivation and linear theory. *J. Nonlinear Sci.*, 12:283–318, 2002.

[BCS04] J.L. Bona, M. Chen, and J.-C. Saut. Boussinesq equations and other systems for small-amplitude long waves in nonlinear dispersive media: Part II. Nonlinear theory. *Nonlinearity*, 17:925–952, 2004.

[BDDV98] A. Bermudez, A. Dervieux, J.A. Desideri, and M.E. Vazquez. Upwind schemes for the two-dimensional shallow water equations with variable depth using unstructured meshes. *Comput. Meth. Appl. Mech. Eng.*, 155(1-2):49–72, 1998.

[BdSV71] A.-J.-C. Barré de Saint-Venant. Théorie du mouvement non permanent des eaux avec applications aux crues des rivières et à l'introduction des marées dans leur lit. *C. R. Acad. Sci. Paris*, 73:147–154, 1871.

[BGH98] T. Buffard, T. Gallouët, and J.-M. Hérard. Un schéma simple pour les équations de saint-venant. *C. R. Acad. Sci. Paris, Série I*, 326:386–390, 1998.

[BGH00] T. Buffard, T. Gallouët, and J.M. Hérard. A sequel to a rough godunov scheme : application to real gases. *Computers and Fluids*, 29(7):813–847, 2000.

[Bio56] M.A. Biot. Theory of propagation of elastic waves in a fluid-saturated porous solid. II higher frequency range. *J. Acoust. Soc. Am.*, 28, 1956.

[Bio72] M. A. Biot. Theory of finite deformations of pourous solids. *Indiana Univ. Math. J.*, 21:597–620, 1972.

[BK09] J. Balbás and S. Karni. A central scheme for shallow water flows along channels with irregular geometry. *ESAIM: M2AN*, 43(2):333–351, mar 2009.

[BL01] R.M. Berne and M.N Levy. *Cardiovascular Physiology.* St Louis, Mosby, 2001.

[BM08] C. Berthon and F. Marche. A positive preserving high order vfroe scheme for shallow water equations: a class of relaxation schemes. *SIAM J. Sci. Comp.*, 30(5):2587–2612, 2008.

[BMCPV03] F. Bouchut, A. Mangeney-Castelnau, B. Perthame, and J.-P. Vilotte. A new model of saint venant and savage-hutter type for gravity driven shallow water flows. *Comptes Rendus Mathematique*, 336(6):531 – 536, 2003.

[BMdL08] F. Bouchut and T. Morales de Luna. An entropy satisfying scheme for two-layer shallow water equations with uncoupled treatment. *M2AN Math. Model. Numer. Anal.*, 42:683–698, 2008.

[Bor06a] R.I. Borja. On the mechanical energy and effective stress in saturated and unsaturated porous continua. *International Journal of Solids and Structures*, 43(6):1764–1786, 2006.

[Bou71a] J.-V. Boussinesq. Théorie de l'intumescence liquide appelée onde solitaire ou de translation se propageant dans un canal rectangulaire. *C. R. Acad. Sci. Paris*, 72:755–759, 1871.

[Bou71b] J.-V. Boussinesq. Théorie générale des mouvements qui sont propagés dans un canal rectangulaire horizontal. *C. R. Acad. Sci. Paris*, 73:256–260, 1871.

[Bou72] J.-V. Boussinesq. Théorie des ondes et des remous qui se propagent le long d'un canal rectangulaire horizontal, en communiquant au liquide contenu dans ce canal des vitesses sensiblement pareilles de la surface au fond. *J. Math. Pures Appl.*, 17:55–108, 1872.

[Bou99] F. Bouchut. Construction of bgk models with a family of kinetic entropies for a given system of conservation laws. *J. Stat. Phys.*, 95:113–170, 1999.

[Bou03] F. Bouchut. Entropy satisfying flux vector splittings and kinetic bgk models. *Numer. Math.*, 94:623–672, 2003.

[Bou04a] F. Bouchut. An introduction to finite volume methods for hyperbolic conservation laws. *ESAIM Proc.*, 15:107–127, 2004.

[Bou04b] F. Bouchut. *Nonlinear stability of finite volume methods for hyperbolic conservation laws and well-balanced schemes for sources*. Birkhäuser, 2004.

[Bou04c] F. Bouchut. A reduced stability condition for nonlinear relaxation to conservation laws. *J. Hyperbolic Differ. Equ.*, 1(1):149–170, 2004.

[BQQ] S. Badia, A. Quaini, and A. Quarteroni. Coupling Biot and Navier–Stokes equations for modelling fluid–poroelastic media interaction. to appear in Journal of Computational Physics.

[Bre99] Y. Brenier. Homogeneous hydrostatic flows with convex velocity profiles. *Nonlinearity*, 12(3):495–512, 1999.

[BV94] A. Bermudez and M.E. Vazquez. Upwind methods for hyperbolic conservation laws with source terms. *Comput. Fluids*, 23(8):1049–1071, 1994.

[BW04] F. Bouchut and M. Westdickenberg. Gravity driven shallow water models for arbitrary topography. *Comm. in Math. Sci.*, 2:359–389, 2004.

[BZ10] F. Bouchut and V. Zeitlin. A robust well-balanced scheme for multi-layer shallow water equations. *Discrete Contin. Dyn. Syst. Ser. B*, 13:739–758, 2010.

[Cau68] L. Caudron. Contribution à l'étude des ondes de Favre. Technical Report HC.032-E230, Laboratoire National d'Hydraulique, Electricité de France, France, 1968.

[CBB06a] R. Cienfuegos, E. Barthélemy, and P. Bonneton. A fourth-order compact finite volume scheme for fully nonlinear and weakly dispersive Boussinesq-type equations. Part I: Model development and analysis. *Internat. J. Numer. Methods Fluids*, 51(11):1217–1253, 2006.

[CBB06b] R. Cienfuegos, E. Barthélemy, and P. Bonneton. A fourth-order compact finite volume scheme for fully nonlinear and weakly dispersive Boussinesq-type equations. Part II: Boundary conditions and validation. *Int. J. Numer. Meth. Fluids*, 53(9):1423–1455, 2006.

[CBBH08] V.M. Calo, N.F. Brasher, Y. Bazilevs, and T.J.R. Hughes. Multiphysics model for blood flow and drug transport with application to patient-specific coronary artery flow. *Comput. Mech.*, 43(1):161–177, 2008.

[CCG+01] D. Chapelle, F. Clément, F. Génot, P. Le Tallec, M. Sorine, and J. Urquiza. A physiologically-based model for the active cardiac muscle. In *Lectures Notes in Computer Science*, volume 2230. Eds T. Katila, I.E. Magnin, P. Clarysse, J. Montagnat, J. Nenonen, Springer-Verlag, 2001.

[CCL+09] R. Chabiniok, D. Chapelle, P. Lesault, A. Rahmouni, and J. Deux. Validation of a biomechanical heart model using animal data with acute myocardial infarction. In *CI2BM09 - MICCAI Workshop on Cardiovascular Interventional Imaging and Biophysical Modelling*, London United Kingdom, 2009.

[CDFNF08] M.-J. Castro Diaz, E.-D. Fernändez-Nieto, and A.-M. Ferreiro. Sediment transport models in shallow water equations and numerical approach by high order finite volume methods. *Computers & Fluids*, 37(3):299–316, 2008.

[CGP+01] F. Coquel, E. Godlewski, B. Perthame, A. In, and P. Rascle. Some new Godunov and relaxation methods for two-phase flow problems. In *Godunov methods (Oxford, 1999)*, pages 179–188. Kluwer/Plenum, New York, 2001.

[CGRGV+04] M.J. Castro, J.A. García-Rodríguez, J.M. González-Vida, J. Macías, C. Parés, and M.E. Vázquez-Cendón. Numerical simulation of two-layer shallow water flows through channels with irregular geometry. *J. Comput. Phys.*, 195(1):202–235, 2004.

[CLL94] G.Q. Chen, C.D. Levermore, and T.-P. Liu. Hyperbolic conservation laws with stiff relaxation terms and entropy. *Comm. Pure Appl. Math.*, 47(6):787–830, 1994.

[CLM10] F. Chazel, D. Lannes, and F Marche. Numerical simulation of strongly nonlinear and dispersive waves using a Green-Naghdi model. *Submitted*, 2010. Preprint arXiv:1004.3436.

[CLTMS11] D. Chapelle, P. Le Tallec, P. Moireau, and M. Sorine. An energy-preserving muscle tissue model: formulation and compatible discretizations. *International Journal of Multiscale Computational Engineering*, 2011. in Press.

[CMP01] M.-J. Castro, J. Macías, and C. Parés. A q-scheme for a class of systems of coupled conservation laws with source term. application to a two-layer 1-D shallow water system. *M2AN Math. Model. Numer. Anal.*, 35(1):107–127, 2001.

[Cor02] J.-M. Coron. Local controllability of a 1-d tank containing a fluid modeled by the shallow water equations. *ESAIM Control Optim. Calc. Var.*, 8:513–554, 2002.

[Cor07] J.-M. Coron. *Control and Nonlinearity.* Mathematical Surveys and Monographs, Vol. 136, American Mathematical Society, 2007.

[Cou95] O. Coussy. *Mechanics of porous continua.* Wiley, New-York, 1995.

[CR03b] R Cimrman and E Rohan. Modelling heart tissue using a composite muscle model with blood perfusion. In Bathe, KJ, editor, *Computational Fluid and Solid Mechanics, 2nd MIT Conference*, pages 1642–1646, 2003.

[CRDN03a] T. Chacon Rebollo, A.D. Delgado, and E.D.F. Nieto. An entropy-correction free solver for non homogeneous shallow water equations. *ESAIM: M2AN*, 37:363–390, 2003.

[CRDN03b] T. Chacon Rebollo, A.D. Delgado, and E.D.F. Nieto. A family of stable numerical solvers for the shallow water equations with source terms. *Comput. Meth. Appl. Math. Eng.*, 192:203–225, 2003.

[CS97] C. R. Chu and C. K. Soong. Numerical simulation of wind-induced entrainment in a stably stratified water basin. *J. Hydraul. Research IAHR*, 35:21–41, 1997.

[DBMS09] A. Decoene, L. Bonaventura, E. Miglio, and F. Saleri. Asymptotic derivation of the section-averaged shallow water equations for river hydraulics. *M3AS*, 19(3):387–417, 2009.

[DBRG07] A. Deponti, L. Bonaventura, G. Rosatti, and G. Garegnani. An accurate and efficient semi-implicit method for section averaged free surface flow modelling. Technical Report 12/2007, MOX - Dipartimento di Matematica, Politecnico Milano, 2007.

[DG09] A. Decoene and J.-F. Gerbeau. Sigma transformation and ALE formulation for three-dimensional free surface flows. *Internat. J. Numer. Methods Fluids*, 59(4):357–386, 2009.

[Din97] M.-W. Dingemans. *Wave propagation over uneven bottoms.* Advanced Series on Ocean Engineering - World Scientific, 1997.

[EGH00] R. Eymard, T. Gallouët, and R. Herbin. Finite volume methods. In *Handbook of numerical analysis, Vol. VII*, Handb. Numer. Anal., VII, pages 713–1020. North-Holland, Amsterdam, 2000.

[EPD08] A. Ern, S. Piperno, and K. Djadel. A well-balanced runge–kutta discontinuous galerkin method for the shallow-water equations with flooding and drying. *Internat. J. for Numerical Methods in Fluids*, 58(4):1–25, 2008.

[FAS05] O.-B. Fringer, S.-W. Armfield, and R.-L. Street. Reducing numerical diffusion in interfacial gravity wave simulations. *Int. J. Num. Meth. Fluids.*, 49:301–329, 2005.

[FLQ03a] L. Formaggia, D. Lamponi, and A. Quarteroni. One-dimensional models for blood flow in arteries. *J. Engrg. Math.*, 47(2-3):251–276, 2003.

[fre09] FreeFem++ home page. http://www.freefem.org/ff++/index.htm, 2009.

[FS04] S. Ferrari and F. Saleri. A new two-dimensional Shallow Water model including pressure effects and slow varying bottom topography. *M2AN Math. Model. Numer. Anal.*, 38(2):211–234, 2004.

[FT09] P.H. Feenstra and C.A. Taylor. Drug transport in artery walls: A sequential porohyperelastic-transport approach. *Computer Methods in Biomechanics and Biomedical Engineering*, 12(3):263–276, 2009.

[Fun93] Y.C. Fung. *Biomechanics: Mechanical Properties of Living Tissues.* Springer-Verlag, 2nd Ed., 1993.

[FZ75] K Fronek and BW Zweifach. Microvascular pressure distribution in skeletal muscle and the effect of vasodilation. *Am J Physiol*, 228(3):791–796, 1975.

[GB90] F. Gonzalez and J. B. Bassingthwaighte. Heterogeneities in regional volumes of distribution and flows in rabbit heart. *Am J Physiol Heart Circ Physiol*, 258(4):H1012–1024, 1990.

[GFD+91] M. Goto, A. E. Flynn, J. W. Doucette, C. M. Jansen, M. M. Stork, D. L. Coggins, D. D. Muehrcke, W. K. Husseini, and J. I. Hoffman. Cardiac contraction affects deep myocardial vessels predominantly. *Am J Physiol Heart Circ Physiol*, 261(5):H1417–1429, 1991.

[GG40] D.E. Gregg and H.D. Green. Registration and interpretation of normal phasic inflow into a left coronary artery by an improved differential manometric method. *Am J Physiol*, 130:114–125, 1940.

[GHS03] T. Gallouët, J.M. Hérard, and N. Seguin. Some approximate godunov schemes to compute shallow-water equations with topography. *Comput. Fluids*, 32:479–513, 2003.

[GL96] J. M. Greenberg and A. Y. Leroux. A well-balanced scheme for the numerical processing of source terms in hyperbolic equations. *SIAM J. Numer. Anal.*, 33(1):1–16, 1996.

[Gla05] P. Glaister. Conservative upwind difference schemes for open channel flows–theory and applications. *Computers & Mathematics with Applications*, 50(1-2):57–72, 2005.

[GLC01] R.-J. Greatbatch, Y. Lu, and Y. Cai. Relaxing the boussinesq approximation in ocean circulation models. *Journal of Atmospheric and Oceanic Technology*, 18(11):1911–1923, 2001.

[GM97] N. Goutal and F. Maurel. In *Proceedings of the 2nd Workshop on dam-break wave simulation*, EDF HE-43/97/016/A, 1997.

[GM02] N. Goutal and F. Maurel. A finite volume solver for 1D shallow-water equations applied to an actual river. *Int. J. Numer. Meth. Fluids*, 38:1–19, 2002.

[GN76] A.E. Green and P.M. Naghdi. A derivation of equations for wave propagation in water of variable depth. *J. Fluid Mech.*, 78:237–246, 1976.

[GN07] D.N. Ghista and E.Y.K. Ng. *Cardiac Perfusion and Pumping Engineering.* World Scientific, 2007.

[God59] S.K. Godunov. A difference method for numerical calculation of discontinuous solutions of the equations of hydrodynamics. *Mat. Sb. (N.S.)*, 47(89):271–306, 1959.

[Gos00] L. Gosse. A well-balanced flux-vector splitting scheme designed for hyperbolic systems of conservation laws with source terms,. *Comput. Math. Appl.*, 39:135–159, 2000.

[Gos01] L. Gosse. A well-balanced scheme using nonconservative products designed for hyperbolic systems of conservation laws with source terms. *Math. Mod. Meth. Appl. Sci.*, 11(2):339–365, 2001.

[GP01] J.-F. Gerbeau and B. Perthame. Derivation of Viscous Saint-Venant System for Laminar Shallow Water; Numerical Validation. *Discrete Contin. Dyn. Syst. Ser. B*, 1(1):89–102, 2001.

[GR96] E. Godlewski and P.-A. Raviart. *Numerical approximations of hyperbolic systems of conservation laws*. Applied Mathematical Sciences, vol. 118, Springer, New York, 1996.

[Gre99] E. Grenier. On the derivation of homogeneous hydrostatic equations. *ESAIM: M2AN*, 33(5):965–970, 1999.

[GS98] N. Goutal and M. Slydowski. Validation d'un schéma volumes finis pour les équations de Saint-Venant bidimensionnelles (in french). Technical Report HE-43/96/077/B, EDF, Direction des études et recherches - LNH, 1998.

[HAvCR92] J. M. Huyghe, T. Arts, D. H. van Campen, and R. S. Reneman. Porous medium finite element model of the beating left ventricle. *Am J Physiol Heart Circ Physiol*, 262(4):H1256–1267, 1992.

[Hel96] D. Helbing. Gas-kinetic derivation of navier-stokes-like traffic equations. *Phys. Rev. E*, 53:2366–2381, 1996.

[Her07] J.-M. Hervouet. *Hydrodynamics of Free Surface Flows: Modelling with the finite element method*. John Wiley & Sons, 2007.

[Hil38] A.V. Hill. The heat of shortening and the dynamic constants in muscle. *Proc. Roy. Soc. London (B)*, 126:136–195, 1938.

[HISW00] R. Hodges, J. Imberger, A. Saggio, and K. B. Winters. Modeling basin-scale internal waves in a stratified lake. *Limnol. Oceanogr.*, 45(7):1603–1620, 2000.

[HKPS95] K. Hutter, T. Koch, C. Plüss, and S. B. Savage. The dynamics of avalanches of granular materials from initiation to runout. II. Experiments. *Acta Mech.*, 109(1-4):127–165, 1995.

[HLvL83] A. Harten, P.D. Lax, and B. van Leer. On upstream differencing and godunov-type schemes for hyperbolic conservation laws. *SIAM Review*, 25(1):35–61, 1983.

[HNS97] P.J. Hunter, M.P. Nash, and G.B. Sands. Computational electromechanics of the heart. In *Computational Biology of the Heart*, pages 345–407. A.V. Panfilov and A.V. Holden Eds, John Wiley & Sons, 1997.

[HO09] G. Holzapfel and R. Ogden. Constitutive modelling of passive myocardium: a structurally based framework for material characterization. *Phil. Trans. R. Soc. A*, 367:3445–3475, 2009.

[HR66] N. S. Heaps and A. E. Ramsbottom. Wind effects on water in a narrow two-layered lake. *Phil. Trans. R. Soc. London A*, 312:391–430, 1966.

[Hum02] J.D. Humphrey. Continuum biomechanics of soft tissues. *Proc. R. Soc. Lond. A*, 459:3–46, 2002.

[Hux57] A.F. Huxley. Muscle structure and theories of contraction. In *Progress in Biophysics and Biological Chemistry*, volume 7, pages 255–318. Pergamon press, 1957.

[HvC91a] J. M. Huyghe and D. H. van Campen. Finite deformation theory of hierarchically arranged porous solids: I. balance of mass and momentum. *Int. J. Engng Sci.*, 33(13):1861–1871, 1991.

[HvC91b] J. M. Huyghe and D. H. van Campen. Finite deformation theory of hierarchically arranged porous solids: Ii. constitutive behaviour. *Int. J. Engng Sci.*, 33(13):1861–1871, 1991.

[HWSS09] P. Horssen, J. P. H. M. Wijngaard, M. Siebes, and J. A. E. Spaan. Improved regional myocardial perfusion measurement by means of an imaging cryomicrotome. In *4th European Conference of the International Federation for Medical and Biological Engineering*, pages 771–774. Springer, 2009.

[Imb98] J. Imberger. *Physical Processes in Lakes and Oceans*. American Geophysical Union, 1998.

[IP90] J. Imberger and J. C. Patterson. Physical limnology. *Adv. Applied Mech.*, 27:303–475, 1990.

[Jan99] J.A. Jankowski. *A non-hydrostatic model for free surface flows, Dissertation*. PhD thesis, Institut fï£¡r Strï£¡mungsmechanik und ERiB, Hannover university, 1999.

[JAP97b] F. Jülicher, A. Ajdari, and J. Prost. Modeling molecular motors. *Reviews of Modern Physics*, 69(4), October 1997.

[Jin01] S. Jin. A steady-state capturing method for hyperbolic systems with geometrical source terms. *M2AN*, 35:631–645, 2001.

[JX95] S. Jin and Z.P. Xin. The relaxation schemes for systems of conservation laws in arbitrary space dimensions. *Comm. Pure Appl. Math.*, 48(3):235–276, 1995.

[KACH07] N. Koshiba, J. Ando, X. Chen, and T. Hisada. Multiphysics simulation of blood flow and LDL transport in a porohyperelastic arterial wall model. *Journal of biomechanical engineering*, 129:374, 2007.

[Kau01] M. Kauer. *Inverse finite element characterization of soft tissues with aspiration*. PhD thesis, Swiss Federal Institute of Techonology, 2001.

[KL02] A. Kurganov and D. Levy. Central-upwind schemes for the saint-venant system. *ESAIM: M2AN*, 36:397–425, 2002.

[KLF99a] Ghassan S. Kassab, Kha N. Le, and Yuan-Cheng B. Fung. A hemodynamic analysis of coronary capillary blood flow based on anatomic and distensibility data. *Am J Physiol Heart Circ Physiol*, 277(6):H2158–2166, 1999.

[KM03] T. Katsaounis and C. Makridakis. Relaxation models and finite element schemes for the shallow water equations. *Hyperbolic Problems : Theory, Numerics, Applications*, pages 621–631, 2003.

[Kra85] C. Kranenburg. Mixed-layer deepening in lakes after wind set-up. *J. Hydraul. Div. ASCE*, 111:334–354, 1985.

[KT00] A. Kurganov and E. Tadmor. New high-resolution central schemes for nonlinear conservation laws and convection-diffusion equations. *J. Comput. Phys.*, 160:214–282, 2000.

[LB09] D. Lannes and P. Bonneton. Derivation of asymptotic two-dimensional time-dependent equations for surface water wave propagation. *Physics of Fluids*, 21(1):9 pages, 2009.

[LeV98] R.-J. LeVeque. Balancing source terms and flux gradients in high-resolution godunov methods: the quasi-steady wavepropagation. *J. Comput. Phys.*, 146(1):346–365, 1998.

[LeV02] R.-J. LeVeque. *Finite Volume Methods for Hyperbolic Problems*. Cambridge University Press, 2002.

[Lio96] P.-L. Lions. *Mathematical Topics in Fluid Mechanics. Vol. 1: Incompressible models.* Oxford University Press, 1996.

[LMGH10] O. Le Métayer, S. Gavrilyuk, and S. Hank. A numerical scheme for the Green-Naghdi model. *Journal of Computational Physics*, 229(6):2034–2045, 2010.

[LP01] R.J. LeVeque and M. Pelanti. A class of approximate Riemann solvers and their relation to relaxation schemes. *J. Comput. Phys.*, 172(2):572–591, 2001.

[LPS96] P.L. Lions, B. Perthame, and P.E. Souganidis. Existence of entropy solutions to isentropic gas dynamics system. *Comm. Pure Appl. Math.*, 49:599–638, 1996.

[LPT94a] P.-L. Lions, B. Perthame, and E. Tadmor. A kinetic formulation of scalar multidimensional conservation laws. *J. AMS*, 7:169–191, 1994.

[LPT94b] P.-L. Lions, B. Perthame, and E. Tadmor. Kinetic formulation of the isentropic gas dynamics and p-systems. *Commun. Math. Physics*, 163:415–431, 1994.

[LT94] P. Le Tallec. *Handbook of Numerical Analysis*, volume 3, chapter Numerical Methods for Nonlinear Three-Dimensional Elasticity, pages 465–622. North-Holland, P.G. Ciarlet and J.L. Lions edition, 1994.

[LY98] D.H. Lin and F.C. Yin. A multiaxial constitutive law for mammalian left ventricular myocardium in steady-state barium contracture or tetanus. *J. Biomech. Eng.*, 120(4):504–517, 1998.

[mac10] Macs team home page. http://www-rocq.inria.fr/MACS/, 2010.

[Mar07] F. Marche. Derivation of a new two-dimensional viscous shallow water model with varying topography, bottom friction and capillary effects. *European Journal of Mechanic /B*, 26:49–63, 2007.

[mas09] Mascaret home page. http://rd.edf.com/edf-fr-accueil/edf-recherche–developpement/logiciels-et-codes/code-mascaret-107043.html, 2009.

[MBNS95a] I. MacDonald, M.J. Baines, N.K. Nichols, and P.G. Samuels. Comparisons of some steady state Saint-Venant solvers for some test problems with analytic solutions. Technical Report 3/95, Dept of Mathematics, University of Reading, 1995. http://www.reading.ac.uk/maths/research/maths-numanalrpts.aspx#1995.

[MBNS95b] I. MacDonald, M.J. Baines, N.K. Nichols, and P.G. Samuels. Steady open channel test problems with analytic solutions. Technical Report 2/95, Dept of Mathematics, University of Reading, 1995. http://www.reading.ac.uk/maths/research/maths-numanalrpts.aspx#1995.

[MGL02] T.J. McDougall, R.J. Greatbatch, and Y. Lu. On conservation equations in oceanography: How accurate are Boussinesq ocean models? *Journal of Physical Oceanography*, 32(5):1574–1584, 2002.

[MM09] J. Marin and J. Monnier. Superposition of local zoom models and simultaneous calibration for 1d-2d shallow water flows. *Math. Comput. Simul.*, 80(3):547–560, 2009.

[MMS02] A. Monti, C. Médigue, and M. Sorine. Short-term modelling of the controlled cardiovascular system. *ESAIM Proc.*, 12:115–128, 2002.

[MNCO$^+$01] K.D. May-Newman, C.L. Chen, R. Oka, R. Haslim, and A.N. DeMaria. Evaluation of myocardial perfusion using three-dimensional myocardial contrast echocardiography. In *Nuclear Science Symposium Conference Record, 2001 IEEE*, volume 3, pages 1691–1694 vol.3, Nov. 2001.

[MNM98] K. May-Newman and A. D. McCulloch. Homogenization modeling for the mechanics of perfused myocardium. *Progress in Biophysics & Molecular Biology*, 69:463–481, 1998.

[Mon85] S. G. Monismith. Wind-forced motions in stratified lakes and their effect on mixed-layer shear. *Limnol. Oceanogr.*, 30(4):771–783, 1985.

[Mon86] S. G. Monismith. An experimental study of the upwelling response of stratified reservoirs to surface shear stress. *J. Fluid Mech.*, 171:407–439, 1986.

[Mor52] C. H. Mortimer. Water movements in lakes during summer stratification; evidence from the distribution of temperature in Windermere. *Phil. Trans. R. Soc. B*, 236:255–404, 1952.

[MP73b] I. Mirsky and W.W. Parmley. Assessment of passive elastic stiffness for isolated heart muscle and the intact heart. *Circul. Research*, 33:233–243, 1973.

[MPV98] B. Mohammadi, O. Pironneau, and F. Valentin. Rough boundaries and wall laws. *Internat. J. Numer. Methods Fluids*, 27(1-4):169–177, 1998.

[MSCH01] P.J. Mulquiney, N.P. Smith, K. Clark, and P.J. Hunter. Mathematical modelling of the ischaemic heart. *Nonlinear Analysis*, 47:235–244, 2001.

[nau10] Nautilus arc home page. http://www-sop.inria.fr/comore/ARC_Nautilus/index.html, 2010.

[NH41] M. Nash and p. Hunter. Computational mechanics of the heart : from tissue structure to ventricular function. *Journal of Elasticity*, 61:2000, 113–141.

[NO05] W.W. Nichols and M.F. O'Rourke. *McDonald's blood flow in arteries.* Hodder Arnold, 2005.

[NT90] H. Nessyahu and E. Tadmor. Non-oscillatory central differencing for hyperbolic conservation laws. *J. Comput. Phys.*, 87:408–463, 1990.

[Nwo93] O. Nwogu. Alternative form of Boussinesq equations for nearshore wave propagation. *Journal of Waterway, Port, Coastal and Ocean Engineering, ASCE*, 119(6):618–638, 1993.

[OI07] P. Okely and J. Imberger. Horizontal transport induced by upwelling in a canyon-shaped reservoir. *Hydrobiologia*, 586:343–355, 2007.

[Ovs79] L. V. Ovsyannikov. Two-layer shallow water models. *Prikl. Mekh. Tekh. Fiz.*, 2:3–14, 1979.

[PBM08] M. Pelanti, F. Bouchut, and A. Mangeney. A roe-type scheme for two-phase shallow granular flows over variable topography. *ESAIM: M2AN*, 42(5):851–885, 2008.

[Per67] D.H. Peregrine. Long waves on a beach. *J. Fluid Mech.*, 27:815–827, 1967.

[Per99] B. Perthame. *An Introduction to Kinetic Schemes for Gas Dynamics.*, chapter An introduction to recent developments in theory and numerics for consevation laws. LNCS. Springer, 1999.

[Per02] B. Perthame. *Kinetic formulation of conservation laws.* Oxford University Press, 2002.

[PR00] D.P. Pioletti and L.R. Rakotomanana. Non linear viscoelastic laws for soft biological tissues. *Eur. J. Mech. A/Solids*, 19:749–759, 2000.

[PRBL98] D.P. Pioletti, L.R. Rakotomanana, J.F. Benvenuti, and P.F. Leyvraz. Viscoelastic constitutive law in large deformations: application to human knee ligaments and tendons. *J. Biomech.*, 31:753–757, 1998.

[PS00] S. Perotto and F. Saleri. Adaptive finite element methods for Boussinesq equations. *Numer. Methods Partial Differential Equations*, 16(2):214–236, 2000.

[PS01] B. Perthame and C. Simeoni. A kinetic scheme for the Saint-Venant system with a source term. *Calcolo*, 38(4):201–231, 2001.

[PT91] B. Perthame and E. Tadmor. A kinetic equation with kinetic entropy functions for scalar conservation laws. *Commun. Math. Phys.*, 136:501–517, 1991.

[RC02] E. Rohan and R. Cimrman. Sensitivity analysis and material identification for activated smooth muscle. *Computer Assisted Mechanics and Engineering Science*, 9:519–541, 2002.

[RHI02] M. Reggio, A. Hess, and A. Ilinca. 3-d multiple-level simulation of free surface flows. *J. Hyd. Res.*, 44(2):413–423, 2002.

[Roe97] P.-L. Roe. Approximate riemann solvers, parameter vectors, and difference schemes. *J. Comput. Phys.*, 135(2):250–258, 1997.

[SCS97] N. J. Shankar, H. F. Cheong, and S. Sankaranarayanan. Multilevel finite-difference model for three-dimensional hydrodynamic circulation. *Ocean Engineering*, 24(9):785–816, 1997.

[SFZ02] S. Soares Frazao and Y. Zech. Undular bores and secondary waves - Experiments and hybrid finite-volume modelling. *Journal of Hydraulic Research*, 40(1):33–43, 2002.

[SH91a] S. B. Savage and K. Hutter. The dynamics of avalanches of granular materials from initiation to runout. I. Analysis. *Acta Mech.*, 86(1-4):201–223, 1991.

[SH91b] B.H. Smaill and P.J. Hunter. Structure and function of the diastolic heart: Material properties of passive myocardium. In *Theory of Heart: Biomechanics, Biophysics, and Nonlinear Dynamics of Cardiac Function*. Springer-Verlag, New-York, 1991.

[SI96] C. Stevens and J. Imberger. The initial response of a stratified lake to a surface shear stress. *J. Fluid Mech.*, 312:39–66, 1996.

[SK01] N.P. Smith and G.S. Kassab. Analysis of coronary blood flow interaction with myocardial mechanics based on anatomical models. *Phil. Trans. R. Soc. Lond. A*, 359:1251–1262, 2001.

[SKvdW+08] Jos Spaan, Christina Kolyva, Jeroen van den Wijngaard, Rene ter Wee, Pepijn van Horssen, Jan Piek, and Maria Siebes. Coronary structure and perfusion in health and disease. *Philosophical Transactions of the Royal Society A*, 366(1878):3137–3153, September 2008.

[Smi04] N.P. Smith. A computational study of the interaction between coronary blood flow and myocardial mechanics. *Physiological Measurement*, 25(4):863–877, 2004.

[ST96] M.J. Salençon and J.M. Thébault. Simulation model of a mesotrophic reservoir (lac de pareloup, france): Melodia, an ecosystem reservoir management model. *Ecological modelling*, 84:163–187, 1996.

[Sto58] J.-J. Stoker. *Water Waves: The Mathematical Theory with Applications*. Wiley-Interscience, 1958.

[SWW99] N. Stergiopulos, B.E. Westerhof, and N. Westerhof. Total arterial inertance as the fourth element of the windkessel model. *Am. J. Physiol.*, 276:H81–H88, 1999.

[Ter43] K. Terzaghi. *Theoretical Soil Mechanics*. John Wiley and Sons, New-York, 1943.

[Tho68] S.-A. Thorpe. On standing internal waves of finite amplitude. *J. Fluid Mech.*, 32:299–319, 1968.

[TI80] R. O. R. Y. Thomson and J. Imberger. Response of a numerical model of a stratified lake to wind stress. In T. Carsten and T. McClimans, editors, *Second International Symposium on Stratified Flows, IAHR, Trondheim, Norway*, pages 562–570, 1980.

[TN92] C. Truesdell and W. Noll. *The non-linear field theories of mechanics, 2nd ed.* Springer, Berlin, 1992.

[Tre94] A. Treske. Undular bores (favre waves) in open channels - experimental studies,. *J. Hydr. Research*, 32(3):355–370, 1994.

[VHJH97] W.J. Vankan, J.M. Huyghe, J.D. Janssen, and A. Huson. A finite element mixture model for hierarchical porous media. *Int. J. Numer. Meth. Engng.*, 40:193–210, 1997.

[Vre79] C. B. Vreugdenhil. Two-layer shallow-water flow in two dimensions, a numerical study. *J. Comput. Phys.*, 33:169–184, 1979.

[VW70] D.R. Veronda and R.A. Westmann. Mechanical characterization of skin-finite deformation. *Journal of Biomechanics*, 3:114–124, 1970.

[Wal99] M.A. Walkley. *A numerical Method for Extended Boussinesq Shallow-Water Wave Equations*. PhD thesis, University of Leeds, 1999.

[WBDVN69] N. Westerhof, F. Bosman, C.J. De Vries, and A. Noordegraaf. Analog study of the human systemic arterial tree. *J. Biomech.*, 2:121–143, 1969.

[WBLS06] Nico Westerhof, Christa Boer, Regis R. Lamberts, and Pieter Sipkema. Cross-Talk Between Cardiac Muscle and Coronary Vasculature. *Physiol. Rev.*, 86(4):1263–1308, 2006.

[Wed12] E. M. Wedderburn. Temperature observations in Loch Earn, with a further contribution to the hydrodynamical theory of the temperature seiche. *Trans. R. Soc. Edin.*, 48:629–695, 1912.

[WH99] J.Z. Wu and W. Herzog. Modelling concentric contraction of muscle using an improved cross-bridge model. *Journal of Biomechanics*, 32:837–848, 1999.

[YKW04] X. Ying, A. A. Khan, and S. S. Y. Wang. Upwind conservative scheme for the saint venant equations. *J.of Hydraul. Eng.*, 130(10):977–987, 2004.

[YS06] Z. Yang and P. Smolinski. Dynamic finite element modeling of poroviscoelastic soft tissue. *Computer Methods in Biomechanics and Biomedical Engineering*, 9(1):7–16, 2006.

[Zah81] G.I. Zahalak. A distribution moment approximation for kinetic theories of muscular contraction. *Mathematical Biosciences*, 55:89–114, 1981.

[ZBS95] D. Zinemanas, R. Beyar, and S. Sideman. An integrated model of LV muscle mechanics, coronary flow, and fluid and mass transport. *Am J Physiol Heart Circ Physiol*, 268(2):H633–645, 1995.